Investigating ER-mitochondria signalling in Amyotrophic Lateral Sclerosis

Hartopp, Naomi

Awarding institution:
King's College London

Investigating Endoplasmic Reticulum-Mitochondria Signalling in Amyotrophic Lateral Sclerosis

Naomi Jade Hartopp

Thesis submitted in fulfilment of the degree of Doctor of Philosophy

2020

Department of Basic and Clinical Neuroscience

Institute of Psychiatry, Psychology and Neuroscience

King's College London

Declaration

I hereby declare that, with the exception of the culture of iPSC-MNs in Chapter 3 and immunoprecipitation of VAPB and PTPIP51 from cells in Chapter 4, all of the work presented in this thesis is my own. iPSC-MN PLA experiments were performed in collaboration with Jenny Greig. Sébastien Paillusson provided recombinant VAPB and Gábor Mórotz carried out immunoprecipitation of VAPB and PTPIP51 from cells for LC-MS/MS in Chapter 4. LC-MS/MS was in collaboration with Steve Lynham at the KCL proteomics facility. This work has not been submitted for any other degree.

Naomi Hartopp
April 2020

Acknowledgements

I would like to thank my first supervisor Professor Chris Miller for giving me the opportunity to work in his lab and for his expertise on this project, and my second supervisor Wendy Noble for her continued support throughout this work and her thoughtful scientific input. My thanks also to my third supervisor Patricia Gomez-Suaga for her guidance. I am grateful for the support and time I have been gifted by my personal tutor Sandrine Thuret, as well as Sarah Mzelinska, Marc-David Ruepp and most recently Sally Marlow, who has been a shining light in the last few months of this work.

Our work as researchers is not possible without patients who donate cells and tissues and I would like to thank them for this. Similarly, our work is made possible by funding bodies and I would like to thank Guy's and St Thomas' Charity for funding this study.

My thanks are extended to the whole Miller lab and many others in the Wohl for continued guidance in the lab. Thank you to Sebastien Paillusson and Gábor Mórotz for providing VAPB and PTPIP51 for mass spectrometry. Dawn Lau made learning PLA an absolute joy and Jenny Grieg has been a wonderful lab partner as well as producing many iPSC-MNs, carrying out some PLA experiments and sharing her stem cell expertise – thank you both. Thanks also to Steve Lynham of the KCL proteomics facility for carrying out multiple LC-MS/MS experiments and patiently sharing his expertise with me. It was a pleasure to learn from all of these people. More thanks than I can express to Lizzie, Charlotte and my wonderful Dad for painstakingly proofreading this work.

I will be forever grateful to Lizzie Glennon, for always being generous with her time and excellent scientific advice, but more importantly for the laughing, crying and cycling together. Lizzie, Ambra, Dawn, Jenny, Sharky and Andrea – thank you for the great fun! To Rachael Evans for making my first three years of living in London an absolute pleasure and to Charlotte Flanagan for being an incredible friend from the day we met, for laughter, ranting and wine, long may these friendships last. Thank you to old school friends, particularly Megan, for keeping me smiling and to flatmates in London, Nick and Abbie, for putting up with me whilst I was writing. I am grateful beyond words to the truly wonderful friends I have made at the Clapham Chasers, "G5" in particular, and too many others to mention, who have time and again helped me to run, swim, cycle, drink and laugh my way through the difficult parts of this process. Thank you to my parents for always, always being there to support me in every way possible. Finally, I would like to dedicate this thesis in memory of my Granddad, David Sylvester, who inspired my path into neuroscience and whose memory still reminds me to enjoy the little things in life.

Abstract

Amyotrophic Lateral Sclerosis (ALS) is a fatal neurodegenerative disease, causing progressive muscle wasting and eventual paralysis. A number of the cellular functions that are disrupted in ALS are mediated by signalling between the endoplasmic reticulum (ER) and mitochondria. This signalling is facilitated by close physical contacts between areas of ER and mitochondrial membranes. The ER membrane protein, VAPB, and the outer mitochondrial membrane protein, PTPIP51, interact to act as tethers, mediating the formation of ER-mitochondria contacts. Transgenic mouse and cellular studies have shown that ER-mitochondria contacts are disrupted by ALS insults, some of which disrupt the VAPB-PTPIP51 interaction via activation of the kinase GSK-3β. However, ER-mitochondria contacts have not been studied in ALS in humans and the mechanism by which GSK-3β disrupts the VAPB-PTPIP51 interaction is yet to be elucidated.

The first hypothesis that underlies this thesis is that damage to ER-mitochondria signalling, involving disruption of the VAPB-PTPIP51 tethers, is a feature of disease in ALS in humans. This was investigated by quantifying the VAPB-PTPIP51 interaction using proximity ligation assays in post-mortem spinal cord tissues from ALS and control cases, and in iPSC-derived motor neurons from control donors and ALS donors carrying familial pathogenic TDP-43 mutations. The VAPB-PTPIP51 interaction was reduced in both ALS post-mortem spinal cord and iPSC-derived motor neurons. VAPB protein levels were reduced in ALS, but other ER-mitochondria proteins investigated were unchanged.

The second hypothesis of this thesis is that GSK-3β phosphorylates VAPB or PTPIP51, reducing their interaction as ER-mitochondria tethers. Recombinant VAPB and PTPIP51 were phosphorylated *in vitro* by GSK-3β and then analysed by mass spectrometry. Novel potential GSK-3β phosphorylation sites were identified in both proteins. Using phospho-mimicking mutants in a cellular GAL4 based 2-hybrid binding assay, one phosphorylation site in VAPB was shown to alter its binding to PTPIP51. To complement these *in vitro* studies, cellular phosphorylation of VAPB and PTPIP51 was also investigated. This involved immunoprecipitation of VAPB and PTPIP51 from cells in which GSK-3β or AMP kinase activities were increased, and mass spectrometry. These studies identified novel phosphorylation sites in both proteins, which may facilitate future studies on the role of the VAPB-PTPIP51 interaction in ER-mitochondria signalling.

In summary, the studies presented in this thesis identify disruption of the VAPB-PTPIP51 ER-mitochondria tethers as a novel feature of ALS in humans and provide insight into a mechanism for this disruption. These studies also provide further support for correcting damage to the VAPB-PTPIP51 interaction as a novel therapeutic target for ALS.

Table of Contents

Table of Figures

Table of Tables

Abbreviations

Amino acids

Single letter code	Abbreviation	Amino Acid
A	Ala	Alanine
C	Cys	Cysteine
D	Asp	Aspartic acid
E	Glu	Glutamic acid
F	Phe	Phenylalanine
G	Gly	Glycine
H	His	Histidine
I	Ile	Isoleucine
K	Lys	Lysine
L	Leu	Leucine
M	Met	Methionine
N	Asn	Asparagine
P	Pro	Proline
Q	Gln	Glutamine
R	Arg	Arginine
S	Ser	Serine
T	Thr	Threonine
V	Val	Valine
W	Trp	Tryptophan
X	N/A	Any amino acid
Y	Tyr	Tyrosine

Other Abbreviations

Aβ	Amyloid Beta
ACC	Acetyl-CoA Carboxylase
AD	Alzheimer's Disease
ADP	Adenosine Diphosphate
AICAR	5-aminoimidazole-4-carboxamide-1-β-D-ribofuranoside
ALS	Amyotrophic Lateral Sclerosis
Ambic	Ammonium Bicarbonate
AMP	Adenosine Monophosphate
Amp	Ampicillin
AMPAR	α-Amino-3-hydroxy-5-Methyl-4-isoxazolepropionic Acid Receptor
AMPK	AMP Kinase
ANOVA	Analysis of Variance
APP	Amyloid Precursor Protein
APS	Ammonium Persulfate
ATF4	Activating Transcription Factor 4
ATP	Adenosine Triphosphate
Bap31	B-cell receptor-associated protein 31
BCA	Bicinchoninic Acid
BDNF	Brain Derived Neurotrophic Factor
BiP	Binding immunoglobulin protein
BSA	Bovine Serum Albumin
CAMKK2	Calcium/Calmodulin Dependent Protein Kinase Kinase 2
CC	Coiled-Coil
CD68	Cluster of Differentiation 68
ChAT	Choline Acetyl Transferase
CHIR	CHIR99021, GSK-3β inhibitor
CNS	Central Nervous System
Ctrl	Control
C9ORF72	Chromosome 9 Open Reading Frame 72
DAB	3,3′- Diaminobenzidine
DAPI	4,6-Diamidine-2-Phenylindole
DBD	DNA binding domain
dbPAF	Database of Phospho-sites in Animals and Fungi
DCTN	Dynactin
DJ-1	Deglycase 1
DMEM	Dulbecco's Modified Eagle Medium
DMSO	Dimethyl Sulfoxide

DNA	Deoxyribonucleic Acid
Dorso	Dorsomorphin, AMPK inhibitor
DPR	Dipeptide Repeat
DRP1	Dynamin Related Protein 1
DTT	Dithiothreitol
EDTA	Ethylenediaminetetraacetic Acid
eIF2α	Eukaryotic Initiation of Translation Factor 2α
ER	Endoplasmic Reticulum
ERAD	ER-Associated Degradation
ERMES	ER-Mitochondria Encounter Structure
FBS	Fetal Bovine Serum
Fis1	Fission Protein 1
FTLD	Frontotemporal Lobar Dementia
FTD	Frontotemporal Dementia
FUS	Fused in Sarcoma
FUNDC1	FUN14 Domain-Containing Protein 1
GDNF	Glia cell line Derived Neurotrophic Factor
GFAP	Glial Fibrillary Acidic Protein
GRP75	Glucose-Regulated Protein 75
GSK-3β	Glycogen Synthase Kinase 3 beta
GST	Glutathione S Transferase
HA	Hemagglutinin
HEK	Human Embryonic Kidney
IAA	Iodoacetamide
IgG	Immunoglobulin
IGF	Insulin-like Growth Factor
IP3R	Inositol Triphosphate Receptor
iPSC	induced Pluripotent Stem Cell
iPSC-MN	induced Pluripotent Stem Cell derived Motor Neuron
IPTG	Isopropyl β- D -1-Thiogalactopyranoside
IRE1a	Inositol-Requiring Enzyme-1a
kDa	Kilo Dalton
KIF5A	Kinesin Family 5A
LB	Luria-Bertani
LC	Liquid Chromatography
LRRK2	Leucine Rich Repeat Kinase 2
MAPK	Mitogen-Activated Protein Kinase
MAM	Mitochondria Associated ER Membranes

MIGA2	Mitoguardin 2
Mmm1	Maintenance of Mitochondrial Morphology Protein 1
MND	Motor Neuron Disease
MOSPD2	Motile Sperm Domain Containing Protein-2
MS/MS	Tandem Mass Spectrometry
MSP	Motile Sperm Protein
MW	Molecular Weight
m/z	Mass to Charge Ratio
NLR	NOD-like Receptor
NPC	Nuclear Pore Complex
NSE	Neuron Specific Enolase
OD	Optical Density
OPTN	Optineurin
ORP	Oxysterol Binding Protein-Related Protein
PACS-2	Phosphofurin Acid Cluster Sorting Protein 2
PBS	Phosphate Buffered Saline
PC	Phosphatidylcholine
PD	Parkinson's Disease
PDI	Protein Disulfide Isomerase
PDZD8	PDZ Domain-containing Protein 8
PE	Phosphatidylethanolamine
PERK	Protein Kinase R-like ER Kinase
PFA	Paraformaldehyde
PINK1	PTEN-induced Kinase 1
PLA	Proximity Ligation Assay
PMD	Post-mortem Delay
Presenilin	PSN
PS	Phosphatidylserine
PTPIP51	Protein Tyrosine Phosphatase Interacting Protein 51 kDa
RA	Retinoic Acid
Ri	ROCK inhibitor
RIPA	Radio-Immunoprecipitation Assay
RM	Reaction Mix
RNA	Ribonucleic Acid
ROCK	Rho-associated Protein Kinase
ROS	Reactive Oxygen Species
RRBP1	Ribosome-Binding Protein 1
SAG	Smoothened Agonist

SB	SB431542, Activin Inhibitor
SDS	Sodium Dodecyl Sulfate
SDS-PAGE	SDS-Polyacrylamide Gel Electrophoresis
S.e.m.	Standard Error of the Mean
SOD1	Superoxide Dismutase
SQSTM1	Sequestosome 1
SYNJ2BP	Synaptojanin 2 Binding Protein
TA	Trans-Activating
TAR	Transactivating Response Element
TBK-1	TANK-Binding Kinase 1
TBS	Tris-Buffered Saline
TDP-43	TAR DNA Binding Protein 43 kDa
TEMED	N,N,N`,N`-Tetramethyl Ethylenediamine
TM	Transmembrane
TOM20	Translocase of Outer Membrane 20 kDa
TPR	Tetratricopeptide Repeat
TRAK	Trafficking Kinesin Protein
UAS	Upstream Activating Sequence
UPR	Unfolded Protein Response
VAPB	Vesicle Associated Membrane Protein Associated Protein B
VCP	Valosin-Containing Protein
VDAC	Voltage Dependant Anion Channels
WT	Wild Type
XBP1	X-Box Binding Protein 1

Chapter 1: Introduction

1.1 Amyotrophic Lateral Sclerosis

1.1.1 Clinical overview

Amyotrophic Lateral Sclerosis (ALS) is the most common cause of adult-onset motor neuron disease (MND), thought to account for 80-90 % of MND cases (Yedavalli et al., 2018). The disease is characterised by the degeneration of upper and lower motor neurons which leads to the atrophy and progressive paralysis of muscles. ALS is a fatal neurodegenerative disease and paralysis of respiratory muscles typically causes patient fatality within 2 – 5 years of diagnosis (Ringel et al., 1993). Most cases of ALS are thought to be sporadic, occurring in patients with no family history of the disease; approximately 5-10 % are diagnosed as familial cases of ALS (Mathis et al., 2019).

The clinical symptoms of ALS are largely heterogeneous. The majority of ALS cases, approximately 80 %, are categorised as limb onset disease in which patients present first with weakness in a specific limb which eventually progresses to various other muscles. The other 20 % are categorised as bulbar onset in which facial, pharyngeal or respiratory muscles are affected first, leading to symptoms such as sialorrhea, facial weakness and dysphagia. Bulbar onset cases tend to progress more quickly due to the importance of the muscle groups affected early on in the disease. Most patients will develop bulbar symptoms at some stage of disease progression (Tiryaki and Horak, 2014). Clinical variation also arises from the contribution of upper or lower motor neuron degeneration. Upper motor neurons originate in the motor cortex and transmit signals to the lower motor neurons in the spinal cord which directly innervate muscle fibres. Degeneration of lower motor neurons leads to rapid atrophy of the muscles due to denervation of the fibres. This presents clinically as progressive muscle weakness. Degeneration of upper motor neurons presents as muscle spasticity caused by a lack of motor signal transmission (Tiryaki and Horak, 2014).

There is currently no cure or effective disease modifying treatment for ALS. Treatment primarily focuses on alleviating the clinical symptoms such as treating dysphagia or respiratory difficulties. There are only two approved drugs for the treatment of ALS, Riluzole and Edaravone (Jaiswal, 2019). Riluzole blocks the release of the neurotransmitter glutamate, reducing neuronal excitotoxicity which can contribute to cell death in damaged cells. Riluzole can only modestly extend life, or the time until a patient requires mechanical ventilation (Hinchcliffe and Smith, 2017; Miller et al., 2003). Edaravone is a free radical scavenger thought to minimise oxidative stress and also offers only modestly improved survival time for ALS patients (Group and Group, 2017; Rothstein, 2017; Yoshino, 2019).

Approximately 15 % of patients with ALS also display some of the clinical symptoms of frontotemporal dementia (FTD) (Ringholz et al., 2005; Woollacott and Rohrer, 2016). FTD is the most prevalent subtype of frontotemporal lobar dementia (FTLD) and is characterised by degeneration of neurons in the frontal and temporal cortex (Mann and Snowden, 2017). FTD can present clinically with a variety of changes in behaviour including social disinhibition, apathy and obsessive behaviours which develop into progressive loss of executive function. Reports suggest that up to 40 % of patients with FTLD display motor symptoms, with the majority of these being FTD patients displaying the clinical symptoms of ALS (Bang et al., 2015). As well as clinical features, ALS and FTD share some genetic and pathological features which lead to the reference of a spectrum disorder, ALS/FTD. It is worth noting this overlap because it suggests that therapeutic targets may also be shared between the two diseases. The work in this thesis however focuses on ALS because the donors from which cells and tissues were used were clinically diagnosed with ALS rather than FTD.

1.1.2 Genetics of Amyotrophic Lateral Sclerosis

Mutations in more than 30 genes have been identified as likely to cause ALS and mutations in almost another 100 genes are thought to increase the likelihood of developing ALS (Wroe et al., 2008). A full list of ALS-associated genes can be found at https://alsod.ac.uk. ALS is genetically as well as clinically heterogeneous; various clinical symptoms can be caused by the same genetic mutation and likewise different genetic backgrounds can give rise to similar clinical symptoms (Tiryaki and Horak, 2014).

The first identified genetic cause of familial ALS was a mutation in *SOD1* (Rosen et al., 1993), encoding the protein Cu/Zn superoxide dismutase (SOD1). SOD1 catalyses the conversion of the free radical superoxide (O_2^-) into either oxygen or hydrogen peroxide, thus protecting the cell against oxidative stress (Sangwan and Eisenberg, 2016). Across familial and sporadic cases of ALS, more than 180 mutations have been found in the gene encoding the protein SOD1. It is not yet known if all of these are causative for the disease and many may be risk factors. Some have been shown to cause misfolding and aggregation of the protein (Sangwan and Eisenberg, 2016).

Intronic hexanucleotide repeat expansions (GGGGCC) in the *C9ORF72* gene cause a third of European ALS cases. In the wild-type (WT) gene, up to 30 hexanucleotide repeats may be found but expansions of hundreds or more are found in patients, causing autosomal dominantly inherited ALS (DeJesus-Hernandez et al., 2011; Renton et al., 2011). The protein encoded by *C9ORF72* is predicted to be a guanine nucleotide exchange factor with proposed activity in processes including autophagy and vesicle

trafficking (Iyer et al., 2018). However, the extent of its physiological function in ALS is not yet fully understood. The *C9ORF72* repeat expansion is transcribed into extended repeats of RNA that undergo non-ATG mediated translation to form five different polypeptides of two repeating amino acids (poly-GR, -PR, -GA, -PA, -GP); these are known as dipeptide repeats (DPRs) (Mori et al., 2013a). Loss of function, toxic gain of function, the formation of RNA foci and toxicity of some of the DPRs have been investigated as mechanisms arising from the *C9ORF72* repeat expansion (Iyer et al., 2018), but the mechanism of disease is still not fully understood.

Several ALS-causing mutations have been identified in the gene encoding Trans-Active Response (TAR) DNA-binding protein of 43 kDa (TDP-43), *TARDBP.* More than 30 point mutations, including M337V and G298S, have been identified in ALS patients (Gitcho et al., 2008; Kabashi et al., 2008; Rutherford et al., 2008; Sreedharan et al., 2008; Van Deerlin et al., 2008). Together these mutations account for approximately 5 % of familial ALS cases. TDP-43 is an RNA binding protein with roles in splicing and the regulation of translation. Mutations in *TARDBP* cause autosomal dominantly inherited ALS and a large proportion of the mutations are found in the glycine-rich region of the protein which mediates the binding of TDP-43 to RNA; these mutations therefore affect TDP-43 translational and splicing regulation functions (Kabashi et al., 2008; Pesiridis et al., 2009; Sreedharan et al., 2008). Point mutations in the gene *FUS,* which encodes another RNA binding protein, Fused in Sarcoma (FUS), also cause ALS (Kwiatkowski et al., 2009; Neumann et al., 2019; Vance et al., 2009). Both autosomal dominant and recessive mutations in *FUS* have been found. Like TDP-43, FUS is an RNA binding protein which functions to regulate splicing and translation of a large number of transcripts. Mutations in FUS are primarily found in the C-terminal region of the protein, which is responsible for the targeting of FUS to the nucleus, these mutations therefore cause mislocalisation of the protein (Kwiatkowski et al., 2009; Vance et al., 2009).

Mutations have also been identified in ALS patients in a number of other genes. These genes encode proteins which function in autophagy, such as Optineurin (OPTN) (Belzil et al., 2011; Del Bo et al., 2011; Maruyama et al., 2010; Naruse et al., 2012; Tumer et al., 2012; van Blitterswijk et al., 2012) and TANK-binding kinase 1 (TBK-1) (Cirulli et al., 2015; Freischmidt et al., 2015), axonal transport, such as Dynactin (DCTN) (Munch et al., 2005; Munch et al., 2004) and Kinesin family 5A (KIF5A) (Brenner et al., 2018), and signalling between the endoplasmic reticulum (ER) and mitochondria, such as Vesicle associated membrane protein associated protein B (VAPB) (Kanekura et al., 2006) and Sigma-1 receptor (Sigma1R) (Al-Saif et al., 2011; Luty et al., 2010).

DCTN is a component of the molecular motor complex dynein/dynactin, which facilitates the movement of cargos along microtubules in the axon. Mutations in the *DCTN1* gene are thought to affect its interaction with the molecular motor dynein and are autosomal dominantly inherited (Munch et al., 2005; Munch et al., 2004). OPTN is an autophagy receptor and is phosphorylated by TBK-1 (Morton et al., 2008). OPTN and TBK-1 are recruited to damaged mitochondria in order to facilitate mitophagy. ALS-related mutations in either OPTN or TBK-1 disrupt this process (Moore and Holzbaur, 2016). VAPB is an integral ER membrane protein and plays a role in the ER unfolded protein response (UPR) and signalling between the ER and mitochondria. A dominantly inherited point mutation in VAPB, P56S, leads to familial ALS (Nishimura et al., 2004). The P56S mutation causes mutant VAPB to aggregate and sequester WT VAPB, causing a loss of VAPB function (Kanekura et al., 2006). *Sigma1R* mutations are autosomal recessive and produce unstable forms of the protein, altering its function at contact sites between the ER and mitochondria (Gregianin et al., 2016). The role of these proteins in ER-mitochondrial signalling and ALS will be discussed in more detail in section 1.2.

1.1.3 Pathology of Amyotrophic Lateral Sclerosis

ALS is characterised by cytoplasmic inclusions of ubiquitinated proteins. In 97 % of cases, these inclusions are formed of ubiquitinated and phosphorylated TDP-43 (Arai et al., 2006; Neumann et al., 2006). As stated above, TDP-43 is an RNA binding protein which functions in mRNA splicing and the regulation of mRNA translation (Buratti and Baralle, 2001; Neumann et al., 2006). In healthy cells, TDP-43 is primarily localised to the nucleus of the cell. However, in ALS TDP-43 is ubiquitinated and hyperphosphorylated and is found aggregated in both the nucleus and the cytoplasm (Arai et al., 2006; Hasegawa et al., 2008; Neumann et al., 2006).

Approximately 2 % of ALS cases, also including familial and sporadic cases, display cytoplasmic inclusions of the protein SOD1. These inclusions are positive for ubiquitin. Accumulations of phosphorylated neurofilaments and several chaperones are also seen in SOD1 ALS (Ince et al., 1998; Kato et al., 2000; Stewart et al., 2006). Some of the remaining cytoplasmic inclusions in ALS cases are formed of the protein FUS (Vance et al., 2009). In ALS cases caused by C9ORF72 mutations, inclusions contain DPRs (Ash et al., 2013; Mori et al., 2013a; Mori et al., 2013b), and in some cases the hallmark ubiquitinated and phosphorylated TDP-43 (Arai et al., 2006; Hasegawa et al., 2008; Neumann et al., 2006). Post-mortem studies also identify inflammation as an ALS pathology. Glial activation, as measured by staining of markers for activated astrocytes (glial fibrillary acidic protein, GFAP) and activated microglia (cluster of differentiation 68,

CD68), is found in ALS patient tissue and is a correlate of disease (Brettschneider et al., 2012).

1.1.4 Pathological mechanisms in Amyotrophic Lateral Sclerosis

1.1.4.1 Protein misfolding and aggregation and damage to autophagy

Abnormal accumulations of disease-related proteins are features of numerous neurodegenerative diseases. Misfolding and ubiquitination of pathological proteins can induce aggregation and lead to the formation of pathological inclusions. Autophagy is the process by which misfolded or damaged proteins are degraded and recycled and damage to autophagy is another feature of ALS which is believed to contribute to the formation of pathological inclusions (Guo et al., 2018).

The major hallmark protein pathologies in ALS patients are cytoplasmic inclusions of TDP-43, FUS or SOD1 in motor neurons. Many ALS causing mutations increase the propensity of these proteins to misfold whilst other mutations increase the mislocalisation of pathological proteins to the cytoplasm. These features suggest a role for misfolding and aggregation in the pathogenesis of the disease. ALS causing mutations are also found in proteins in the autophagic pathway, such as OPTN, Sequestosome 1 (SQSTM1), TBK1 and C9ORF72 are reported to disrupt the process of autophagy, contributing to the ubiquitination and build-up of pathological proteins (Guo et al., 2018). Enhancing autophagic pathways clears inclusions to an extent and is reported to reduce pathogenesis (Castillo et al., 2013; Chen et al., 2015; Mandrioli et al., 2018; Zhang et al., 2014). The activation of heat shock proteins, which act as protein folding chaperones, reduces TDP-43 aggregation and these have also been found sequestered in neuronal inclusions in ALS (Chang et al., 2013). This finding further implicates protein misfolding in the formation of pathological inclusions. Misfolding and subsequent aggregation of proteins can be damaging in itself but can also lead to reductions in the normal function of the sequestered proteins.

1.1.4.2 Nucleocytoplasmic trafficking damage

Nucleocytoplasmic trafficking is the process by which proteins are shuttled between the cytoplasm and the nucleus across the nuclear membrane. This transport occurs via a complex of proteins which form a pore in the nuclear envelope known as the nuclear pore complex (NPC). Importins facilitate protein transport across the NPC. The specificity of the NPC to allow certain proteins to be transported into the nucleus relies on various receptors on the surface of the pore and a hydrogel-like structure within the lumen of the pore which mediates exclusion of certain molecules based on their size (Kim and Taylor, 2017).

Two hallmark ALS proteins, TDP-43 and FUS, are shuttled between the nucleus and the cytoplasm via the NPC, and there is evidence that this trafficking is damaged in ALS. Mutations in the nuclear localisation sequence of FUS account for approximately half of the ALS-related mutations found in the gene (Ling et al., 2013). In ALS pathology, a deficit of disease-related proteins such as TDP-43 in the nucleus and a build-up in the cytoplasm, suggests that the net movement across the NPC is shifted in the cytoplasmic direction (Chou et al., 2018). In studies of ALS patient cells and tissue, components of the nuclear pore are mislocalised and the expression of importins is reduced (Neumann et al., 2012; Nishimura et al., 2010; Takeuchi et al., 2013; Zhang et al., 2015b). This evidence indicates a role for damaged nucleocytoplasmic trafficking of proteins in ALS pathogenesis.

1.1.4.3 RNA Toxicity

RNA toxicity can arise via the sequestration of RNA and RNA binding proteins such as splicing and transcription factors. Certain RNA and RNA-binding proteins are sequestered in response to stress; these accumulate to form non-membrane bound organelles known as stress granules (Vance et al., 2013). The formation of stress granules occurs by a dynamic and reversible process known as liquid-liquid phase separation. It is thought that the sequestration of RNA and proteins in these granules reversibly reduces the activity of cellular process such as translation to preserve energy during the stress response. Dissociation of these granules then releases sequestered RNA and proteins, allowing these processes to resume (Baradaran-Heravi et al., 2020; Mandrioli et al., 2019; Vance et al., 2013).

Many of the genes and proteins related to ALS, including TDP-43 and FUS, are RNA-binding proteins involved in the processing of RNA and are sequestered into stress granules (Baradaran-Heravi et al., 2020; Vance et al., 2013; Zhang et al., 2018). Certain ALS-related mutations in proteins including TDP-43, FUS and Ataxin2 reduce the speed with which stress granules dissociate and increase their susceptibility to irreversible aggregation. This traps crucial RNA and RNA processing components in the stress granule, prolonging and enhancing the stress response of the cell (Zhang et al., 2018).

1.1.4.4 Axonal transport dysfunction

Organelles, proteins and other molecules in the cell require transport to their site of function; these sites can often be distant from their site of production. Motor neurons are the largest cells in the human body with axons of up to 1 m in length (Shaw, 1999). This creates potentially huge distances between soma and synapses and makes these cells highly reliant on the transport of cargos through axons. Axonal transport is driven by the

molecular motors kinesin and dynein which move along microtubules. Kinesins facilitate most anterograde transport; that from the cell body towards the synapse. Dynein facilitates most retrograde transport; from synapses to the cell body (Guedes-Dias and Holzbaur, 2019; Saxton and Hollenbeck, 2012; Sleigh et al., 2019).

Damage to axonal transport is well reported in several models of ALS. In particular, disruption to the transport of mitochondria is commonly seen. The expression of Miro1, which mediates the binding of mitochondria to axonal transport motors, is decreased in ALS patient spinal cord tissue (Zhang et al., 2015a). Mutations in genes encoding components of the molecular motors responsible for axonal transport have been reported in ALS patients. These include DCTN, a subunit of the dynein complex and the molecular motor subunit KIF5A, (Brenner et al., 2018; Munch et al., 2005; Munch et al., 2004; Nicolas et al., 2018). Mitochondrial transport in axons is impaired in cells expressing ALS-causing mutants, including in TDP-43, VAPB and SOD1 (Moller et al., 2017; Morotz et al., 2012; Wang et al., 2013). Transgenic mouse models of ALS also show reduced expression of Miro1 and reduced numbers of mitochondria in axons, indicating transport deficits (Vande Velde et al., 2011; Zhang et al., 2015a).

1.1.4.5 Excitotoxicity

Excitotoxicity refers to damage caused to neurons due to overstimulation by neurotransmitters, which eventually leads to neuronal death. In ALS, excitotoxicity occurs due to excessive glutamatergic neurotransmission in motor neurons. This leads to an influx of ions such as calcium, which if not properly buffered leads to activation of calcium-induced apoptotic pathways. There are a number of mechanisms thought to lead to increased glutamate excitability of motor neurons in ALS (Blasco et al., 2014).

Glutamate receptors including α-amino-3-hydroxy-5-methyl-4-isoxazolepropionic acid receptors (AMPARs) on the surface of motor neurons modulate calcium influx into the cell. Astroglia protect against excitotoxicity by removing glutamate from the extracellular neuronal environment, reducing the concentration of glutamate available to neurons and therefore reducing the capacity for stimulation (Starr and Sattler, 2018). Motor neurons derived from ALS patient induced pluripotent stem cells (iPSCs) and motor neurons from ALS mouse models show increased permeability of AMPARs to calcium. Glutamate uptake activity of astroglia is also reduced in ALS models. This combination reduces the calcium buffering ability of neurons and increases their susceptibility to calcium-induced cell death (Selvaraj et al., 2018; Starr and Sattler, 2018). Further evidence that glutamate excitotoxicity is a pathogenic mechanism in ALS is that Riluzole, one of only two

approved treatments for ALS, acts by inhibiting glutamatergic neurotransmission (Hinchcliffe and Smith, 2017; Miller et al., 2003).

1.1.4.6 Inflammation

Neuroinflammation is an inflammatory response within the central nervous system which stimulates the production of inflammatory molecules such as cytokines and activates microglia and astrocytes. Neuroinflammation is a protective response in healthy physiology but activation of neuroinflammation has been reported in a number of neurodegenerative diseases including ALS. It is now widely hypothesised that neuroinflammation begins as a protective response to neurodegenerative disease insults but becomes a damaging process during the course of the disease (Geloso et al., 2017; Komine and Yamanaka, 2015).

In post-mortem patient tissue, glial activation, as measured by staining of GFAP and CD68 to indicate activated astrocytes and microglia respectively is a correlate of disease (Brettschneider et al., 2012). Imaging in ALS patients has shown that markers for activated glia are present early in disease and correlate with motor symptoms (Cagnin et al., 2004; Corcia et al., 2012; Turner et al., 2004). Glial activation is also a feature in a number of transgenic models of ALS including mutant SOD1 transgenic mice; in these mice microglial activation occurs before the onset of symptoms (Jara et al., 2017; Liao et al., 2012; McCauley and Baloh, 2019). In addition, mutant OPTN transgenic mice that model aspects of ALS display some necrosis which can be an inflammation-induced form of cell death (Ito et al., 2016). Finally, there is evidence of an increased systemic inflammatory response in ALS. Some transgenic mouse models of ALS display downregulated regulatory T cells and ALS patient blood is found to have increased levels of inflammatory markers and dysfunctional regulatory T cells (Beers et al., 2017; Zhao et al., 2012).

1.1.4.7 Mitochondrial dysfunction and oxidative stress

Damage to mitochondria results in bioenergetic deficiency due to impaired mitochondrial membrane potential, reduced electron transport chain activity and in turn reduced generation of ATP. A large body of work points to damage to mitochondria as a pathogenic mechanism in ALS. ALS patient tissue shows reduced oxidative phosphorylation indicative of defective ATP production (Jiang et al., 2015). ALS mutant proteins including FUS, TDP-43 and Valosin-containing protein (VCP) cause reduced ATP production and morphological damage to mitochondria which is seen in animal and cell models of ALS (Jiang et al., 2015).

Oxidative stress refers to the damage caused to cellular processes by free radicals and reactive oxygen species (ROS). ROS are produced by mitochondria and in healthy cells they can act as signalling molecules that are eventually converted to stable molecules. In damaged cells, mitochondrial dysfunction leads to ROS being produced in greater quantities and converted to stable molecules less efficiently. SOD1 catalyses the dismutation of the free radical species superoxide into hydrogen peroxide. Increased ROS are found in ALS mouse models including C9ORF72, TDP-43 and FUS models and in turn, oxidative damage has been shown to enhance the aggregation of FUS and TDP-43, suggesting a potential feed-forward loop for damage in ALS (Jiang et al., 2015; Smith et al., 2017). Finally Edaravone, an approved treatment for ALS, acts as a scavenger of free radicals to reduce oxidative stress (Group and Group, 2017; Rothstein, 2017; Smith et al., 2017; Yoshino, 2019).

1.1.4.8 ER stress and the unfolded protein response

The ER UPR is a pathway activated in response to ER stress and is caused by the accumulation and misfolding of proteins in the ER. There are three pathways of the UPR which together aim to alleviate ER stress and to return proteostasis to normal levels. The first pathway involves activation of Protein kinase R (PKR)-like ER kinase (PERK) and Eukaryotic initiation of translation factor 2α (eIF2α) and leads to decreased global translation to reduce ER protein load. This same pathway also activates Activating Transcription Factor (ATF) 4, to increase the expression of genes involved in autophagy so as to clear misfolded proteins. The second pathway involves dimerization of Inositol-requiring enzyme-1a (IRE1a) and activates alternative splicing to produce the active form of X-Box Binding Protein 1 (XBP1) which in turn increases the expression of protein folding chaperone genes and genes involved in ER-associated degradation (ERAD). The third pathway involves proteolysis of the transcription factor ATF 6 to enhance the expression of ERAD related genes (Bernales et al., 2006; Kanekura et al., 2009).

As in many neurodegenerative diseases, dysfunction of the UPR is implicated in the pathogenesis of ALS. Misfolded or aggregated proteins such as TDP-43 and FUS, are hallmarks of the disease and indicate UPR dysfunction (Walker and Atkin, 2011). The expression of various UPR genes including VAPB are altered in ALS patient tissues and inhibiting UPR pathways reduced disease progression in a transgenic mouse model of ALS (Anagnostou et al., 2010; Jiang et al., 2014; Scheper and Hoozemans, 2015). Perhaps most compelling is the evidence that mutations in VAPB, which functions in the UPR, cause ALS in humans (Gkogkas et al., 2008; Suzuki et al., 2009; Walker and Atkin, 2011).

1.1.4.9 ER-mitochondrial signalling damage

The ER serves vital functions in the cell, including folding of proteins, storage of calcium and the UPR. The primary function of mitochondria is the generation of energy in the form of ATP. Many of the functions of ER and mitochondria require communication between these two organelles. There is now evidence that ER-mitochondria signalling and communications are disrupted in several neurodegenerative diseases including ALS (Csordas et al., 2006; Lau et al., 2018; Paillusson et al., 2016; Rowland and Voeltz, 2012). Damage to ER-mitochondria signalling is the focus of this work and is therefore discussed in detail below.

1.2 ER-mitochondrial signalling

1.2.1 ER-mitochondrial signalling regulates a number of fundamental cellular processes

As mentioned above, some of the primary roles of the ER include protein and lipid synthesis and the storage of calcium. Likewise, mitochondria control important cellular functions, especially the generation of energy in the form of ATP via oxidative phosphorylation, apoptosis and calcium signalling. Many ER and mitochondrial functions require communication between the two organelles. In order to facilitate these communications, ER and mitochondria are physically tethered to form close contacts (10 to 30 nm distances). The regions of ER associated with mitochondria are known as mitochondria-associated ER membranes (MAM) (Csordas et al., 2006; Lau et al., 2018; Paillusson et al., 2016; Rowland and Voeltz, 2012). Below, the major functions of ER-mitochondria contacts and signalling are discussed.

1.2.1.1 Calcium signalling and ATP production

ATP production by the mitochondria is critically dependant on calcium, because this stimulates the activity of the calcium dependant dehydrogenase enzymes in the tricarboxylic acid cycle (Griffiths and Rutter, 2009). The ER is the primary source of intracellular calcium, from where it is released at ER-mitochondria contact sites via Inositol trisphosphate receptors (IP3Rs). Calcium uptake into the mitochondria occurs via Voltage dependant anion channels (VDACs) in the outer mitochondrial membrane and the mitochondrial calcium uniporter (Csordas et al., 2006; Lau et al., 2018; Paillusson et al., 2016; Rowland and Voeltz, 2012).

For the efficient transfer of calcium, the concentration of calcium ions at the mitochondrial membrane must be sufficiently high. IP3Rs are clustered at ER-mitochondria contact sites, aided by the chaperone Sigma1R (Hayashi and Su, 2007; Ryskamp et al., 2019) and interact with VDAC, as mediated by the molecular chaperone glucose-regulated

protein 75 (grp75) (Szabadkai et al., 2006). Areas of IP3R clustering enable high local calcium concentrations when calcium is released from the ER. This enhances the efficiency with which the required calcium concentration for uptake is reached and increases both the speed and amount of calcium transfer from ER to mitochondria (Giacomello et al., 2010; Lau et al., 2018; Paillusson et al., 2016).

Whilst delivery of calcium to mitochondria is beneficial in stimulating ATP production, excessive delivery of calcium to mitochondria can be detrimental. This is because excessively high levels of mitochondrial calcium stimulate opening of the mitochondrial permeability transition pore which stimulates signals for apoptosis (Hurst et al., 2017).

1.2.1.2 Phospholipid biosynthesis

The ER is the major site of lipid production and this represents another function facilitated by close contact between the ER and the mitochondria (Rowland and Voeltz, 2012). Several of the most abundant phospholipids including Phosphatidylserine (PS), Phosphatidylethanolamine (PE) and Phosphatidylcholine (PC) are synthesised in an as yet undefined multistep process involving various enzymes. A number of the synthase enzymes involved in these steps reside at MAM or the inner mitochondrial membrane. Some lipid synthesis therefore relies on efficient exchange of precursor lipids between the ER and mitochondria and close contacts between ER and mitochondria facilitate this exchange (Filadi et al., 2017; Rusinol et al., 1994; Stone and Vance, 2000; Vance, 1990). As an example, synthesis of PE and PC which are the two most abundant phospholipids in mammalian cells commences in MAM via conversion of phosphatidic acid to PS by phosphatidylserine synthase. This is then transported to mitochondria and converted to PE which is transported to MAM for conversion to PC which is in turn transported back to mitochondria (Rowland and Voeltz, 2012).

1.2.1.3. Mitochondrial biogenesis

ER-mitochondria contact sites also regulate mitochondrial biogenesis and division. Mitochondria with damaged DNA fuse with other mitochondria to enable recombining of this DNA to generate a complete and correct mitochondrial genome. Mitofusin 1 and 2 regulate mitochondrial fusion and reside at ER-mitochondria contact sites (Chen et al., 2003; Cosson et al., 2012; de Brito and Scorrano, 2008; Koshiba et al., 2004; Leal et al., 2016; Naon et al., 2016).

In addition, FUN14 Domain-Containing Protein 1 (FUNDC1) plays a crucial role in mitochondrial turnover by recruiting Dynamin related protein 1 (DRP1) during mitophagy to enable mitochondrial fission. FUNDC1 is also enriched at MAM (Wu et al., 2016a; Wu

et al., 2016b). Mitochondrial division has been found to occur in close association with the ER and it is thought that ER tubules physically aid division by wrapping around and constricting mitochondria along with actin filaments (Friedman et al., 2011; Korobova et al., 2013). Finally, mitochondrial DNA (mtDNA) synthesis occurs at ER-mitochondria contact sites. There is evidence for a role for these contacts in the coupling of mtDNA replication with mitochondrial division to ensure the correct distribution of mtDNA (Lewis et al., 2016).

1.2.1.4 Mitochondria and ER trafficking and transport

ER-mitochondria contact is also implicated in the transport of both organelles along axons. Mitochondria and ER are transported along microtubules anterogradely by the molecular motor kinesin-1. Attachment of mitochondria to the kinesin-1 motor is mediated by binding of the outer mitochondrial membrane protein Miro-1 to Trafficking Kinesin Proteins (TRAKs) which interact with kinesin-1 (Macaskill et al., 2009; Saotome et al., 2008). Miro-1 is a calcium sensing protein found localised at ER-mitochondria contact sites (Kornmann et al., 2011). Calcium causes Miro-1 to detach from KIF5A of the kinesin motor, preventing further movement of mitochondria along the microtubules (Macaskill et al., 2009). Since Miro-1 is found at ER-mitochondria contact sites and these contacts mediate local calcium concentrations, it is likely that ER-mitochondria contacts affect the transport of mitochondria via Miro-1. In addition to this, mitochondria and ER have been shown to remain in contact during transport along microtubules (Friedman et al., 2010). Together this evidence suggests that ER-mitochondria contacts play a role in the co-transport of the organelles.

1.2.1.5 Inflammasome formation

ER-mitochondria contacts sites are also implicated in the formation of inflammasomes. The inflammasome is a multiprotein oligomer of the immune system which activates inflammatory responses (Gross et al., 2011; Missiroli et al., 2018). Tissue and cell damage are sensed by pattern recognition receptors such as the NOD-like receptors (NLRs) which are a part of the innate immune system and form an inflammasome. This complex of NLRs stimulates the cleavage of interleukin 1β into its active form to induce the activation of an inflammatory response (Gross et al., 2011). One of these NLRs, known as NLRP3 localises to ER-mitochondria contact sites and recent research has found that the cell stressors such as ROS, produced by the mitochondria, stimulate relocation of NLRP3 to ER-mitochondria contact sites (Zhou et al., 2011). ER-mitochondria contacts are therefore implicated in inflammatory responses.

1.2.1.6 Proteostasis; the ER unfolded protein response and autophagy

Proteostasis is the balance of protein synthesis, folding, modification and degradation that is required to maintain the correct expression levels of functional proteins within the cell. The ER plays an important role in proteostasis, being responsible for the correct folding of proteins and responding to abnormal proteostasis through the UPR.

As detailed above the UPR is a cellular response which is induced due to an accumulation of unfolded proteins in the ER (Bernales et al., 2006; Kanekura et al., 2009). A number of ER resident protein folding chaperones including Binding immunoglobulin protein (BiP), calnexin, calreticulin and the Sigma1R require calcium for their chaperone activity and are found to be localised to ER-mitochondria contact sites (Hayashi and Su, 2007; Simmen et al., 2010). Moreover, VAPB which is an ER-mitochondria tethering protein, has been shown to modulate the UPR (Gkogkas et al., 2008; Kanekura et al., 2006). There is also evidence that ER-mitochondria contacts and related bioenergetics are crucial for regulating whether the UPR acts to restore proteostasis or stimulates apoptotic pathways (Bravo et al., 2011; Cardenas et al., 2010).

Autophagy is a degradative process for proteins that is used to recycle obsolete cellular constituents and remove damaged organelles and protein aggregates. It involves transport of damaged proteins and organelles to an organelle known as the aggresome. Elimination of damaged substrates at the aggresome then involves their delivery to lysosomes via autophagosomes, where lysosomal enzymes digest the components so that their individual components (e.g. amino acids) can be recycled by the cell (Nixon et al., 2013; Rubinsztein et al., 2012).

A number of lines of evidence support the idea that ER-mitochondria contacts regulate autophagy. Firstly, autophagosomes have been shown to form at ER-mitochondria contact sites (Hamasaki et al., 2013). Secondly, inhibition of the delivery of calcium to the mitochondria by IP3Rs located at MAM, induces autophagy (Cardenas and Foskett, 2012; Cardenas et al., 2010; Gomez-Suaga et al., 2017a; Sarkar et al., 2005). Finally, experimental manipulation of ER-mitochondria contact sites has been shown to regulate autophagy (Gomez-Suaga et al., 2017b; Hamasaki et al., 2013; Mao et al., 2019). However, not all of these results are consistent, with some studies showing that increasing ER-mitochondria contacts and signalling stimulates, whereas others show that it inhibits, autophagosome formation (Gomez-Suaga et al., 2017b; Hamasaki et al., 2013; Mao et al., 2019).

1.2.2 ER-mitochondrial signalling is mediated by tethering proteins

Studies investigating the ER and mitochondria by electron microscopy identified ER-mitochondria contact sites. These studies revealed the presence of structures which appear to act as physical tethers between the membranes of the two organelles (Csordas et al., 2006; Csordas et al., 2010; Lau et al., 2018; Paillusson et al., 2016). Further studies have identified ER and mitochondrial proteins which interact to form these structures and some of which specifically function as tethers between ER and mitochondria. Proteins found at ER-mitochondria contact sites are shown in Figure 1.1. VAPB and PTPIP51 (dark red and dark blue) are the focus of this thesis and the rationale for this, including discussion of the current knowledge about each of the ER-mitochondria resident proteins, is discussed below.

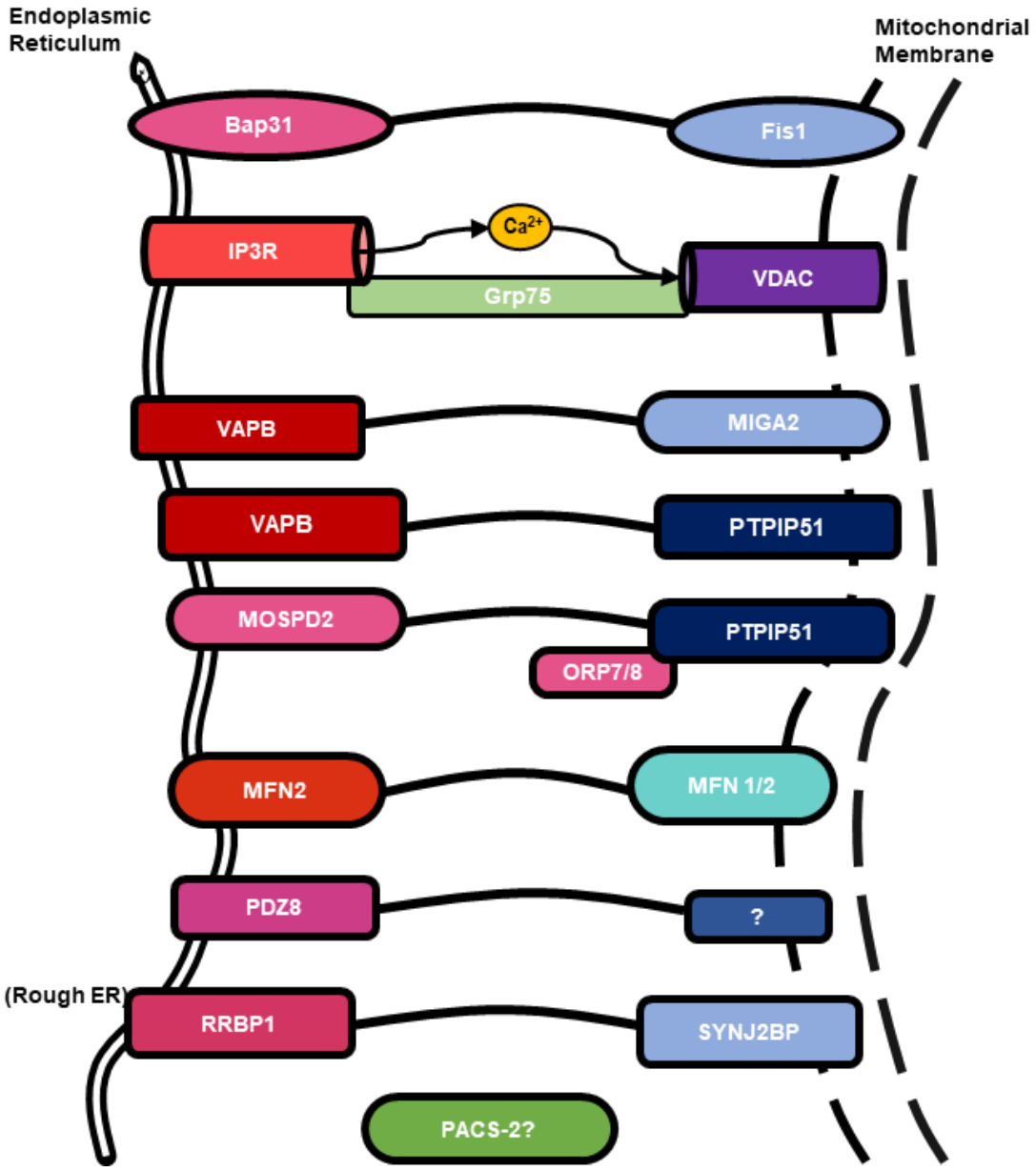

Figure 1.1: Protein interactions found at ER-mitochondria contact sites

In yeast, proteins of the ER-mitochondria encounter structure (ERMES) act as tethers (Kornmann et al., 2009). The ER protein PDZ domain containing protein 8 (PDZD8) has recently been proposed as an ortholog of the ERMES protein Maintenance of mitochondrial morphology protein 1 (Mmm1) (Hirabayashi et al., 2017). Knock down of PDZ in mammalian cells significantly reduced ER-mitochondria contacts, however rescue of broken ER-mitochondria contacts by PDZ8 has not yet been evidenced so it cannot be concluded that PDZ8 directly tethers the two organelles. In addition, current studies are yet to identify a mitochondrial interacting partner for PDZ8.

Mitofusin-2 has been proposed a number of times as a physical tether of ER-mitochondrial membranes (de Brito and Scorrano, 2008; Naon et al., 2016). Mitofusin-2 is found in both ER and mitochondrial membranes and is able to form homodimers between the two membranes as well as binding to Mitofusin-1 in the mitochondrial membrane. However, more recent studies have shown that knockdown of Mitofusin-2 does not reduce the contact between ER and mitochondrial membranes and as such there is question over the role of Mitofusin proteins in ER-mitochondria contacts (Cosson et al., 2012; Filadi et al., 2015; Leal et al., 2016; Wang et al., 2015).

As previously discussed, IP3Rs reside in the ER membrane and VDACs reside in the mitochondrial membrane. Both proteins are found to be enriched at sites of ER-mitochondrial membrane contact and interact via glucose-regulated protein 75 (Grp75) (Rapizzi et al., 2002; Szabadkai et al., 2006), making them a likely ER-mitochondria tether. However, studies in which IP3R is knocked out showed no effect on the presence of ER-mitochondria contacts, as would be expected if IP3R-VDAC binding did indeed tether the two membranes (Csordas et al., 2006). A more recent study, in which all three isoforms of IP3R are addressed, has revisited the possibility that IP3R-VDAC interactions tether ER and mitochondrial membranes (Bartok et al., 2019). There is still no consensus as to whether this interacting pair act to provide structure and regulate the presence of ER-mitochondria contacts or solely function to exchange calcium at MAM.
ER protein B-cell receptor-associated protein 31 (Bap31) and mitochondrial membrane protein Fission protein 1 (Fis1) form complexes at ER-mitochondrial membranes and facilitate signalling to induce apoptosis (Iwasawa et al., 2011). Whether these proteins act as tethers or act solely as signalling molecules at contact sites is not yet known.

Likewise, Phosphofurin acid cluster sorting protein 2 (PACS-2) is enriched at ER-mitochondria contacts and depletion of the protein results in reduced ER-mitochondria contacts (Simmen et al., 2005). However, PACS-2 depletion causes fragmentation of mitochondria which could be responsible for the reduction in ER-mitochondria contact

(Simmen et al., 2005). PACS-2 is also involved in organelle trafficking and signalling to the nucleus (Atkins et al., 2014; Youker et al., 2009). It is not yet clear how these functions relate to ER-mitochondria signalling and it remains possible that PACS-2 plays a functional rather than structural role at ER-mitochondria contact sites.

A further proposed tether involves the outer mitochondrial membrane protein Synaptojanin 2 binding protein (SYNJ2BP) which has been shown to interact with Ribosome-binding protein 1 (RRBP1). This interaction mediates contact sites between mitochondria and rough ER membranes (Hung et al., 2017). The SYNJ2BP-RRBP1 interaction may be a specific ER-mitochondria tether for rough ER.

1.2.2.1 VAPB and PTPIP51 ER-mitochondria tethers

Finally, an interaction between the integral ER membrane protein VAPB and the outer mitochondrial membrane protein Protein tyrosine phosphatase interacting protein of 51 kDa (PTPIP51) has been identified as a tether between ER and mitochondria. Tethering between VAPB and PTPIP51 is the focus of this thesis.

VAPB is anchored into the ER membrane by a C-terminal ER-targeting sequence and its N-terminus projects into the cytosol. VAPB also comprises an alpha helical coiled-coil domain and an N-terminal motile sperm protein (MSP) domain which is structurally similar to the *C. elegans* major sperm protein (Figure 1.2) (De Vos et al., 2012). PTPIP51 is anchored into the outer mitochondrial membrane by an N-terminal mitochondrial targeting sequence and its C-terminus projects into the cytosol. PTPIP51 also comprises an alpha-helical coiled-coil domain, four low complexity regions and a C-terminally located tetratricopeptide repeat (TPR) domain (Figure 1.3) (De Vos et al., 2012). TPR domains are known protein-protein interaction domains (Lau et al., 2018).

Figure 1.2: Domain structure of VAPB. MSP, motile sperm domain. CC, coiled-coil domain. TM, transmembrane domain.

Figure 1.3: Domain structure of PTPIP51. TM, transmembrane domain. CC, coiled-coil domain. TPR, tetratricopeptide repeat domain.

Work from our group identified VAPB and PTPIP51 as direct binding partners using both recombinant and *in vitro* assays including yeast-two hybrid, immunoprecipitation and glutathione S transferase (GST)-pull downs (De Vos et al., 2012; Stoica et al., 2014). There is much evidence that this interaction forms a physical tether between areas of ER and mitochondrial membranes and mediates ER-mitochondrial signalling. In cells, VAPB and PTPIP51 co-localise at sites of ER-mitochondria contact (Stoica et al., 2014). More importantly, knockdown of either VAPB or PTPIP51 significantly reduces the contact between ER and mitochondrial membranes, as measured in electron microscopy studies. Knockdown of both proteins together reduces this contact even further and over expression of either protein increases the amount of mitochondrial membrane in contact with ER (Morotz et al., 2012; Stoica et al., 2014).

Altering the expression of VAPB or PTPIP51 also affects downstream function of ER-mitochondria membrane contact. This is evidenced by studies of calcium transfer in which reduced expression of either VAPB or PTPIP51 leads to a significant increase in the lag time between ER calcium release and mitochondrial calcium uptake. These studies also show significantly reduced mitochondrial calcium concentration overall, suggesting not only a slower but also a less efficient transfer of calcium from the ER to the mitochondria (De Vos et al., 2012; Morotz et al., 2012; Stoica et al., 2014). These experiments confirm that binding between VAPB and PTPIP51 is necessary for the contact between ER and mitochondrial membranes and identifies them as tethering molecules which mediate ER-mitochondrial signalling. Importantly, other studies have also identified VAPB and PTPIP51 as ER-mitochondria tethering proteins (Di Mattia et al., 2018; Galmes et al., 2016; Huttlin et al., 2015; Puri et al., 2019; Qiao et al., 2017; Yang et al., 2018).

There is also evidence that VAPB and PTPIP51 may interact with other ER and mitochondrial proteins to function as tethers. VAPB binds to the outer mitochondrial membrane protein Mitoguardin 2 (MIGA2). PTPIP51 has been shown to bind to Oxysterol binding protein-related proteins ORP5 and ORP8 which are also found at ER-mitochondria contact sites, and a VAPB homologue termed Motile sperm domain containing protein-2 (MOSPD2) (Di Mattia et al., 2018; Freyre et al., 2019; Galmes et al., 2016).

In mediating ER-mitochondria contact, VAPB-PTPIP51 binding is also expected to regulate some of the functions reliant on ER-mitochondria signalling that are discussed in 1.2.1. In addition to the evidence already discussed of the role for VAPB-PTPIP51 in calcium exchange, there is emerging evidence that they regulate functions including autophagy, energy metabolism, and in particular mitochondrial ATP production (Gomez-Suaga et al., 2017b; Paillusson et al., 2017). Importantly, VAPB-PTPIP51 interactions have been shown to be dynamic which is an important feature when considering whether an interaction acts to regulate dynamic cellular processes. In response to stimulating synaptic activity, VAPB-PTPIP51 binding increases (Gomez-Suaga et al., 2019) and it can be considered that this is to stimulate ATP production for the energy dependant activity of synapses.

How the dynamics of VAPB-PTPIP51 binding is mediated has not yet been fully elucidated. However, Glycogen synthase kinase 3 beta (GSK-3β) activity has been found to affect the VAPB-PTPIP51 interaction. Activation of GSK-3β inhibits VAPB-PTPIP51 binding and reduces ER-mitochondria contacts, whilst inhibition of GSK-3β stimulates VAPB-PTPIP51 binding and ER-mitochondria contacts (Stoica et al., 2014; Stoica et al., 2016). The mechanism by which GSK-3β affects the interaction is as yet unknown and investigating this mechanism forms part of this thesis.

1.2.3 ER-mitochondrial signalling in neurodegenerative disease

Alzheimer's disease (AD), Parkinson's disease (PD) and ALS are major neurodegenerative diseases and yet there are currently no effective treatments for them. There is therefore a pressing need for novel drug targets for these diseases. Many physiological processes within the cell are disrupted in AD, PD and ALS including mitochondrial function, the ER UPR, axonal transport, autophagy, calcium homeostasis, lipid metabolism and the inflammatory response. Disruption to these cellular functions indicates disease mechanisms which are common amongst this particular set of diseases.

As discussed in 1.2.1 and 1.2.2, signalling between the ER and mitochondria is necessary for a number of cellular functions, including some of those processes that are disrupted in neurodegenerative diseases. There is emerging evidence that ER-mitochondria contacts are altered in various neurodegenerative diseases, suggesting disruption to these contact sites as a potential common disease mechanism, and a potential novel therapeutic target.

Perhaps the two most convincing lines of evidence that ER-mitochondrial signalling plays a role in neurodegenerative disease is that genetic mutations in proteins facilitating ER-mitochondria contacts can cause ALS and that correcting ER-mitochondrial signalling is protective in models of disease. Mutations in the ER-mitochondria tether VAPB and the IP3R chaperone Sigma1R which is enriched at ER-mitochondria contacts have been found to cause ALS (Al-Saif et al., 2011; Bernard-Marissal et al., 2015; De Vos et al., 2012; Hayashi and Su, 2007; Luty et al., 2010; Nishimura et al., 2004; Watanabe et al., 2016). Similarly, increasing ER-mitochondria contacts by expression of tethering protein VAPB is protective in alpha-synuclein cell models of PD and in a mutant SOD1 model of ALS (Kim et al., 2016; Paillusson et al., 2017).

There is much evidence that ER-mitochondria contacts and signalling are disrupted in AD, PD and most convincingly in ALS. This evidence suggests the potential for novel therapeutic targets and is discussed below.

1.2.3.1 Alzheimer's Disease

AD is a late onset neurodegenerative disease. It is characterised by extracellular accumulations of the protein amyloid beta (Aβ) and cytoplasmic accumulation of the protein tau in the brain (Goedert and Spillantini, 2006). Aβ is formed by cleavage of Amyloid precursor protein (APP) by enzymes known as β-secretase and γ-secretase. Presenilin-1 and -2 (PSN1 and2) are the catalytic components of γ-secretase and some familial forms of Alzheimer's disease are caused by mutations in presenilin proteins or APP (Goedert and Spillantini, 2006; Schellenberg and Montine, 2012).

Presenilin proteins are found to be enriched at sites of ER-mitochondria membrane contact (Area-Gomez et al., 2009) and Aβ peptides are reported to be produced at ER-mitochondria contact sites (Schreiner et al., 2015). There is much experimental evidence that ER-mitochondria contacts and signalling are altered in AD, but there is not yet a clear consensus as to the direction of this effect.

Animal and cell studies of AD-mutant PSN2 have shown conflicting effects, with some reporting increases in ER-mitochondrial colocalization and others reporting reduced mitochondrial calcium uptake as would be expected in response to a decrease in ER-mitochondria contact (Area-Gomez et al., 2012; Kipanyula et al., 2012). Aβ and APP cell and animal models have also reported both increased and disrupted ER-mitochondria contacts (Del Prete et al., 2017; Hedskog et al., 2013; Martino Adami et al., 2019). In addition, cell models mimicking the biggest genetic risk factor for AD, ApoE4 also appear to increase ER-mitochondrial signalling (Tambini et al., 2016).

Differences in the sensitivity with which ER-mitochondria contact or co-localisation may account for some of the discrepancies between studies, as may the use of different assays and quantification methods (Paillusson et al., 2016). It is however clear that ER-mitochondria contacts are altered in AD. Finally, work in our lab, alongside that described in this thesis, has found that ER-mitochondria contacts as measured by VAPB-PTPIP51 binding, are reduced in the brains of early AD patients (manuscript in submission).

1.2.3.2 Parkinson's Disease

PD is a neurodegenerative disease characterised by intraneuronal inclusions of the protein alpha-synuclein and loss of dopaminergic neurons. A number of genetic causes of PD have been identified. These include mutations in alpha-synuclein, Leucine rich repeat kinase 2 (LRRK2) and mitochondrial proteins PTEN-induced kinase 1 (PINK1), Parkin and Deglycase (DJ-1) (Balestrino and Schapira, 2020; Simon et al., 2020).

There are a number of studies pointing to the disruption of ER-mitochondrial signalling in PD. For example, the major protein contributing to PD pathology, alpha-synuclein, is found to be enriched at ER-mitochondria contact sites (Guardia-Laguarta et al., 2014; Paillusson et al., 2017). It has also been shown that alpha-synuclein disrupts contacts at these sites by binding to the ER-mitochondrial tether VAPB and thereby reducing its interaction with the tethering protein PTPIP51 (Paillusson et al., 2017). PD-related mutations in alpha-synuclein also lead to disruption of ER-mitochondria contacts (Guardia-Laguarta et al., 2014). Indeed, neurons generated from iPSCs derived from PD patients harbouring alpha-synuclein triplication displayed reduced ER-mitochondrial membrane tethering when compared to iPSC-neurons derived from control donors (Paillusson et al., 2017).

LRRK2 mutations, which cause most familial PD, have been shown to modulate ER-mitochondria signalling (Toyofuku et al., 2019). Notably, LRRK2 mutant G2019S, which is one of the most common mutations, causing 2 % of PD, stimulates degradation of

some ER-mitochondrial tethering proteins by E3 ubiquitin ligase activity. G2019S mutant LRRK2 therefore reduces ER-mitochondria contacts (Toyofuku et al., 2019). PD-related mutations are also found in the protein DJ-1 which itself is found at ER-mitochondria contacts. PD-related mutation in DJ-1 alters its interaction with IP3R3-Gpr75-VDAC and in turn disrupts ER-mitochondria contacts (Liu et al., 2019).

There is currently contrasting evidence on the role of Parkin in ER-mitochondria contacts in PD. Fibroblasts from humans with mutations in the gene encoding Parkin have been reported to display increased ER-mitochondria contacts in one study (Gautier et al., 2016) and reduced ER-mitochondria contacts in another (Basso et al., 2018). *In vitro,* Parkin knock down experiments have shown reductions in ER-mitochondria contacts and damage to mitochondria (Cali et al., 2013b). Changes in ER-mitochondria contacts have also been found to affect the regulation of mitophagy in PD (Gelmetti et al., 2017; Puri et al., 2019). Whilst there is not yet a consensus on the precise effect, there is much evidence that ER-mitochondrial signalling is altered in PD.

1.2.3.3 Amyotrophic Lateral Sclerosis

Evidence that ER-mitochondria contacts are affected in neurodegenerative disease is perhaps strongest in the case of ALS. There is a detailed body of evidence showing that VAPB-PTPIP51 interactions and consequently ER-mitochondrial signalling are disrupted in both *in vitro* and *in vivo* models of ALS.

Overexpression of either WT or familial disease causing mutant TDP-43 reduces the extent of ER-mitochondria contacts, as measured in electron microscopy studies. Upon stimulation of neurons over-expressing WT or ALS-mutant TDP-43, ER-mitochondria calcium transfer is reduced, indicating disruption to a major function of ER-mitochondria contacts. Co-immunoprecipitation studies show that this effect is due to reduced binding between VAPB and PTPIP51 (Stoica et al., 2014).

Similarly, overexpression of both WT and ALS-mutant FUS disrupts ER-mitochondria contacts as measured by electron microscopy and calcium transfer in cell and transgenic animal models. This effect is caused by reduced VAPB-PTPIP51 binding, as shown directly by immunoprecipitation and by proximity ligation assays (PLAs), which stain for proteins in close proximity (Stoica et al., 2016). Evidence that both WT and mutants of TDP-43 or FUS disrupt ER-mitochondria contacts aligns with evidence that over-expression of WT or mutant TDP-43 or FUS cause disease in transgenic mice (Mitchell et al., 2015; Mitchell et al., 2013; Tsao et al., 2012).

The mechanism by which TDP-43 and FUS alter ER-mitochondria contacts in ALS is yet to be fully identified, but initial studies have indicated a role for kinases in regulating the binding of ER-mitochondria tethering proteins. The ubiquitously expressed serine threonine kinase GSK-3β is activated by TDP-43 and FUS and in turn disrupts ER-mitochondrial signalling by reducing the binding between VAPB and PTPIP51 (Stoica et al., 2014; Stoica et al., 2016).

In humans, the most direct indication for a role of ER-mitochondrial signalling in disease is the identification of point mutations in the ER-mitochondrial tether VAPB, which cause ALS (Nishimura et al., 2004). ALS-causing mutant VAPB P56S has increased affinity for PTPIP51 *in vitro*, however evidence suggests that mutant VAPB sequesters WT VAPB, reducing the overall amount of functional VAPB in patients (Teuling et al., 2007). Furthermore, it has been shown *in vivo* that overexpression of VAPB slows impairment of motor neurons (Kim et al., 2016), though the mechanism by which VAPB is protective is not yet fully understood. VAPB expression is reduced in iPSC-derived neurons from ALS patients harbouring the VAPB P56S mutation (Mitne-Neto et al., 2011) and importantly, VAPB expression is reduced in the spinal cord of sporadic ALS patients (Anagnostou et al., 2010).

As previously discussed, Sigma1R acts as a chaperone to induce IP3R clustering at ER-mitochondria contact sites and therefore enhances the efficiency of calcium transfer (Bernard-Marissal et al., 2015; Hayashi and Su, 2007). Loss of function mutations in Sigma1R have been reported to cause cases of familial ALS (Al-Saif et al., 2011; Bernard-Marissal et al., 2015; Dreser et al., 2017; Gregianin et al., 2016; Luty et al., 2010; Ullah et al., 2015) and polymorphisms in IP3R have been linked to ALS in patients (van Es et al., 2007). The gene encoding Sigma1R resides on chromosome 9, and as such it has been suggested that the mutations found to cause ALS may be linked to C9ORF72, also found on chromosome 9 (Belzil et al., 2013), but recent studies have confirmed the role of Sigma1R mutations in ALS and identified reduced ER-mitochondria signalling (Bernard-Marissal et al., 2015; Gregianin et al., 2016; Watanabe et al., 2016).

Mutations in the SOD1 gene were the first to be identified as a cause of familial ALS. ALS-mutant SOD1 also disrupts ER-mitochondria signalling (Watanabe et al., 2016), although the mechanisms by which this occurs are as yet unclear. However, ALS-mutant SOD1 is thought to interact with VDAC1 and affect its ability to act as a channel for the transfer of molecules such as ATP and calcium across the mitochondrial membrane (Israelson et al., 2010). Similarly, mutant SOD1 has been shown to cause loss of

Sigma1R at ER-mitochondria contacts, affecting ER-mitochondria signalling (Watanabe et al., 2016).

This body of evidence indicates ER-mitochondria contacts as a potential therapeutic target for ALS. However, ER-mitochondria contacts have yet to be investigated in human ALS patients, and the mechanisms by which ER-mitochondria contacts are disrupted in ALS are yet to be elucidated.

1.3 Hypothesis and study aims

As detailed above, ER-mitochondria signalling regulates many of the functions which are damaged in ALS. Much evidence shows that these ER-mitochondria contacts, and the tethering interaction between VAPB and PTPIP51, are themselves disrupted in ALS. To date, this evidence only exists in animal and cell models of the disease. GSK-3β has been identified as a mediator of VAPB-PTPIP51 binding but the full mechanism by which VAPB-PTPIP51 binding is damaged in ALS is yet to be elucidated. As such, there are two hypotheses underlying this thesis; firstly, that ER-mitochondria contacts are disrupted in humans with ALS and secondly that VAPB-PTPIP51 binding is regulated by phosphorylation including via GSK-3β.

There are many studies in cell and transgenic animal models of ALS including TDP-43, FUS and SOD1 models, in which ER-mitochondria signalling is linked to familial ALS (Bernard-Marissal et al., 2015; Israelson et al., 2010; Stoica et al., 2014; Stoica et al., 2016; Watanabe et al., 2016). This body of evidence suggests that ER-mitochondria contacts are a potential therapeutic target for disease. However, ER-mitochondria signalling is yet to be studied in human versions of the disease and there is a particular lack of information about the approximately 90-95 % of ALS cases which are not familial. Therefore, the first hypothesis of this thesis was that ER-mitochondria contacts, as mediated by VAPB-PTPIP51 binding, are disrupted in human ALS.

Firstly, this hypothesis was addressed by measuring the expression and binding of VAPB and PTPIP51 in post-mortem spinal cord samples from sporadic ALS patients and control donors. VAPB and PTPIP51 protein levels and binding were measured by immunoblotting and PLAs. Secondly, to test this hypothesis in familial ALS, motor neurons derived from iPSCs (iPSC-MNs) from control donors and two ALS patients carrying TDP-43 mutations were investigated.

Studies of ER-mitochondria contacts in TDP-43 and FUS models of ALS have found that VAPB-PTPIP51 binding is disrupted by TDP-43 and FUS via activation of GSK-3β

(Stoica et al., 2014; Stoica et al., 2016). The mechanism by which GSK-3β reduces VAPB-PTPIP51 binding is as yet unknown. However, as GSK-3β is a ubiquitously expressed kinase and phosphorylation is a common regulator of protein-protein interactions. The second hypothesis of this thesis was therefore that GSK-3β phosphorylates either VAPB or PTPIP51 to disrupt their binding affinity.

To test this hypothesis, firstly recombinant VAPB and PTPIP51 were incubated with GSK-3β and analysed for phosphorylation sites by mass spectrometry. Secondly, to identify phosphorylation in cells, VAPB and PTPIP51 isolated from cells overexpressing GSK-3β were analysed for phosphorylation sites by mass spectrometry.

The overall aims of this study were to support the idea that correcting damaged ER-mitochondria contacts is a novel therapeutic target for ALS and to begin to identify the mechanism by which ALS pathology disrupts these contacts.

Chapter 2: Materials and Methods

2.1 Materials

Unless otherwise stated, chemicals were purchased from Sigma Aldrich (Dorset, UK), cell culture reagents were purchased from ThermoFisher Scientific (Loughborough, UK) and cell culture plates and flasks were from Corning (Amsterdam, The Netherlands). Ultrapure water used in solutions and buffers was from a Milli-Q purification system (Merck Millipore; Watford, UK). Sterilisation of solutions for molecular biology and cell culture was carried out by autoclaving at 121 °C and 101 kPa for 20 min.

2.1.1 Antibodies

Antibodies were purchased from Cell Signalling Technology (Leiden, The Netherlands), Sigma Aldrich, Dako (Cambridge, UK), Jackson Immunoresearch (Ely, UK), Merck Millipore (Watford, UK), Abcam (Cambridge, UK), Santa Cruz (Heidelberg, Germany), ThermoFisher Scientific, Atlas (Bromma, Sweden), Synaptic Systems (Goettingen, Germany) and Gentex (Hsinchu City, Taiwan) and are detailed in Table 2.1. Primary antibodies against VAPB and PTPIP51 made "in house" were raised in rabbits or rats by immunization with glutathione S-transferase (GST)-VAPB(1-220) and GST-PTPIP51(36-470), respectively as previously described (De Vos et al., 2012).

Table 2.1. Antibodies used in this study

Primary Antibodies

Antibody	Supplier	Monoclonal / Polyclonal Species	Concentration		Cat no.
			Immuno-blot	ICC/ PLA	
ACC	Cell Signalling Technology	Polyclonal Rabbit	1:1000	-	3662
Phospho-ACC (Ser79)	Cell Signalling Technology	Polyclonal Rabbit	1:2000	-	3661
AMPKα	Cell Signalling Technology	Polyclonal Rabbit	1:1000	-	2532
Phospho-AMPKα (Thr172)	Cell Signalling Technology	Monoclonal Rabbit	1:2000	-	40H9
ChAT	Merck Millipore	Polyclonal Goat	-	1:500	AB144
GSK-3β	Cell Signalling Technology	Monoclonal Rabbit	1:1000	-	D5C5Z

HA	Cell Signalling Technology	Monoclonal Mouse	(Immuno-precipitation 1:500)	-	6E2
IP3R3	Atlas	Polyclonal Rabbit	1:2000	1:200	HP A003915
IP3R3	Merck Millipore	Polyclonal Rabbit	-	1:200	AB9076
Myc	Cell Signalling Technology	Monoclonal Mouse	(Immuno-precipitation 1:500)	-	9B11
NSE	Dako	Monoclonal Mouse	1:10000	-	MO837
PDI	Thermo fisher	Monoclonal Mouse	1:2000	-	RL77
PTPIP51	In-house	Rat	-	1:200	N/A
PTPIP51	Gentex	Polyclonal Rabbit	1:2000	-	GTX54674
PTPIP51	Atlas	Polyclonal Rabbit	1:2000	-	HP A009975
Sigma1R	Santa Cruz	Monoclonal Mouse	1:1000	-	sc-166392
TOM20	Santa Cruz	Polyclonal Rabbit	1:2000	-	sc-11415
VAPB	In-house	Rabbit	1:2000	1:200	N/A
VAPB	Abcam	Polyclonal Rabbit	1:2000	-	ab103638
VDAC	Abcam	Monoclonal Mouse	1:2000	1:200	ab14734

Secondary Antibodies

Antibody	Supplier	Monoclonal /Polyclonal Species	Conc.	Conjugate	Cat no.
Mouse IgG	Dako	Rabbit	1:5000	HRP	0447
Rabbit IgG	Dako	Polyclonal Goat	1:5000	HRP	0448
Goat IgG	Invitrogen	Polyclonal Donkey	1:500	Alexa 488	A11055

PLA Probes

Antibody	Supplier	Monoclonal /Polyclonal Species	Conc. PLA	Conjugate	Cat no.
Rat IgG	Jackson Immuno	Polyclonal Donkey	Conjugated to PLA Probe-maker PLUS		712-005-153
Rabbit MINUS	Sigma Aldrich	Polyclonal Donkey	1:5	Duolink PLUS	DUO92005
Mouse PLUS	Sigma Aldrich	Polyclonal Donkey	1:5	Duolink MINUS	DUO92001
Probe maker PLUS	Sigma Aldrich	-	Conjugated to Rat IgG		DUO92009

2.1.2 Plasmids

E-Coli expression vectors pET28A-His-VAPB(1-220) and pGEX5X-PTPIP51(36-470) used to produce recombinant protein were as previously described (Stoica et al., 2014). Mammalian expression vectors were pCIneo control vector from Addgene (Massachusetts, USA) and amino-terminal myc-tagged VAPB (myc-VAPB) and carboxy-terminal HA-tagged PTPIP51 (HA-PTPIP51) in pCIneo as previously described (De Vos et al., 2012).

Mammalian expression vectors expressing full length GAL4 (pSG4+), GAL4-DNA binding domain (DBD, pM1) and VP16 DNA trans-activation domain (pVP16) were generated by Dr. Sarah Müller using vectors previously described (Sadowski et al., 1992; Sadowski et al., 1988). Renilla luciferase pRL-CMV and firefly luciferase pG5-luc vectors were from Promega (Hampshire, UK). Expression vectors for GAL4 DBD-VAPB(1-220) (pM1-VAPB(1-220)) and VP16-PTPIP51(36-470) were produced by Dr. Sarah Müller (unpublished work) using previously described plasmids (De Vos et al., 2012). pCDNA3.1 was from ThermoFisher and pCDNA3.1-GSK-3β-WT was from Addgene (Massachusetts, USA).

2.1.3 Human cells and tissue

2.1.3.1 Post-mortem tissue

Post-mortem spinal cord tissue for human studies was provided by the Medical Research Council Neurodegenerative Disease Brain Bank at King's College London. All tissue collection and processing were carried out under the regulations and licensing of the Human Tissue Authority, and in accordance with the Human Tissue Act, 2004. Human spinal cord tissue from 17 ALS and 17 control donors were provided (Table 2.2). All but three samples, which came from thoracic spinal cord, were from the lumbar region of the spinal cord. Patients were clinically diagnosed with ALS and diagnoses were confirmed by the brain bank by post-mortem identification of TDP-43 pathology. With the exception of two patients, who harboured a *C9ORF72* repeat expansion, ALS-causing mutations were not reported in any other cases. Controls were age-matched and free of the clinical symptoms of ALS at time of death. One control donor was found to have TDP-43 inclusions in their amygdala and hippocampus, but not in motor neurons in spinal cord. Aside from this, TDP-43 pathology was not reported in any control tissue. Two control donors displayed stage III Braak pathology, twelve displayed stage I-II, and three were not classified. Braak pathology above II was not reported in any ALS cases.

For proximity ligation assays, 7 µm paraffin wax embedded sections of post-mortem lumbar or thoracic spinal cord were provided. For immunoblotting, frozen spinal cord tissue from the same donors were provided.

Table 2.2: Demographics of donors of human post-mortem spinal cord

Group	Unique Identifier	Sex	Age (years)	Post-mortem Delay (hrs)
Control	C1	M	105	25
Control	C2	F	73	27
Control	C3	F	77	21
Control	C4	M	84	53
Control	C5	M	65	26
Control	C6	M	85	55
Control	C7	M	63	23
Control	C8	F	99	32
Control	C9	M	78	24
Control	C10	M	82	24
Control	C11	F	92	9
Control	C12	M	97	44
Control	C13	F	84	34
Control	C14	F	92	22.5
Control	C15	F	89	41
Control	*C16	M	81	18
Control	*C17	M	79	47
ALS	A1	M	68	78
ALS	**A2	M	57	94
ALS	A3	M	69	52.5
ALS	A4	M	76	51

ALS	A5	M	68	73
ALS	*A6	F	73	70
ALS	A7	F	90	34
ALS	**A8	F	59	74
ALS	A9	F	72	53
ALS	A10	M	54	69
ALS	A11	M	77	66
ALS	A12	F	86	77
ALS	A13	F	80	36.5
ALS	A14	M	73	41.5
ALS	A15	F	69	64
ALS	A16	M	74	70
ALS	A17	M	71	58

*Thoracic spinal cord

2.1.3.2 iPSC-MNs

Motor neurons differentiated from patient iPSCs from two control donor and two ALS donor cell lines were kindly provided by the laboratory of Professor Chris Shaw (King's College London), who originally received both ALS patient cell lines and one control cell line (33D6) from Professor Siddharthan Chandran (University of Edinburgh) and the other control line (M135) from Professor Jack Price (King's College London). Patient cells were from two unrelated males, one aged 52 and harbouring the M337V mutation in TDP-43 and the other aged 64 and harbouring the G298S mutation. Control cells were from two unrelated males, one (33D6) aged 56 and the other (M135) in his 40s.

2.1.4 Immunostaining and Assays

Duolink *in situ* proximity ligation assay kits (brightfield and orange) including *in situ* wash buffers, ligase and polymerase enzymes and buffers, blocking solutions and antibody diluents, Duolink PLA probes, and Mayer's Haematoxylin were all purchased from Sigma-Aldrich. Xylene and ethanol were from VWR (Lutterworth, UK). NOVA red peroxidase substrate kit and ABC Vectastain were from VECTOR (Peterborough, UK) Clearvue mountant XYL, for mounting tissue sections, was from ThermoFisher Scientific. Fluorescence mountant, for mounting cells, was from Dako. Dual Glo Luciferase Assay System, including lysis buffer, luciferase substrates and luciferase inhibitor solution, was from Promega.

2.1.5 Cell culture

2.1.5.1 Stem cell culture and differentiation into iPSC-MNs

Geltrex, Essential 8 Flex Medium (E8 Flex), Rho-associated protein kinase (ROCK) inhibitor Revitacell (100x), StemPro Accutase Cell Dissociation Reagent, Dulbecco's Modified Eagle Medium (DMEM) / F12 with GlutaMAX, Neurobasal medium, N2 supplement (10x), B27 supplement (10x), β-mercaptoethanol (0.01%) and Retinoic Acid (RA) were from ThermoFisher Scientific. SB431542 Activin Inhibitor (SB) and CHIR99021 GSK3 inhibitor (CHIR) were from Cambridge Biosciences (Cambridge, UK). Dorsomorphin AMPK inhibitor (Dorso) and Smoothened Agonist (SAG) were from Merck, ROCK inhibitor (Ri) Y-27632 was from Stem Cell Technologies and DAPT from Cell Guidance Systems (Cambridge, UK). Recombinant human Brain-Derived Neurotrophic Factor (BDNF), Glial cell line-Derived Neurotrophic Factor (GDNF) and Insulin-like Growth Factor (IGF) were from Peptrotech (London, UK). Versene (Ethylenediaminetetraacetic acid (EDTA) in phosphate buffered saline (PBS)) was from Lonza (Basel, Switzerland). Laminin isolated from Engelbreth-Holm-Swarm murine sarcoma (basement membrane), L-Ascorbic Acid 2-Phosphate (AA2P), Poly-L-ornithine (0.01 %) and Puromycin were from Sigma Aldrich.

2.1.5.2 Cell line culture

DMEM containing 4.5 g/l glucose and 1mM sodium pyruvate, Trypsin-EDTA solution (0.05 % (v/v)/ 0.02 % (v/v) in PBS) and Opti-MEM reduced serum medium were from Life Technologies. Fetal Bovine Serum (FBS) and L-glutamine (200 mM) were from GE Healthcare (Buckinghamshire, UK). Fugene 6 transfection reagent was from Promega. PHERAstar FSX Microplate Reader was from BMG Labtech (Aylesbury, UK).

2.1.6 Molecular biology

2.1.6.1 Immunoblotting and immunoprecipitation

BCA protein assay kit was from Bio-Rad (Watford, UK). cOmplete protease inhibitor cocktail (EDTA free) and phosphatase inhibitor cocktail (PhosStop) were both from Roche (Welwyn Garden City, UK). Novex 4 – 12 % Tris-Glycine gels and nitrocellulose membranes were from ThermoFisher Scientific. For casting "home-made" gels, Mini-PROTEAN Tetra Cell Casting set was from Bio-Rad and 30 % Acrylamide-bis-acrylamide 37:5:1 stabilised solution was from Geneflow (Litchfield, UK). Molecular weight marker used was PageRuler Plus Prestained Protein Ladder 10 to 250 kDa from ThermoFisher Scientific. Dried milk powder and Bovine Serum Albumin (BSA) were from Sigma Aldrich. Enhanced chemiluminescent blotting reagent and Protein G Sepharose Fast Flow beads were from GE healthcare. The ChemiDoc XRS+ imaging system used to visualise immunoblots was from Bio-Rad.

2.1.6.2 Plasmid production and mutagenesis

Luria-Bertani (LB) agar, LB broth, nuclease free water and the NanoDrop 1000 Spectrophotometer used for measuring DNA concentration were from ThermoFisher Scientific. HiSpeed plasmid purification midi kits were from Qiagen (Manchester, UK). Quick change XL site directed mutagenesis kit and XL-Blue *E.coli* were from Agilent Technologies (Cheshire, UK). Library efficiency *E.coli* DH5α were from Thermofisher Scientific.

2.1.6.3 Protein purification, recombinant protein and cell treatments

E.coli BL21 (DE3) were from Agilent. GraviTrap nickel column and Glutathione Sepharose 4B beads were from GE healthcare. Spectrophotometer was a Jenway 6300. Recombinant GSK-3β (P6040S) was from New England Biolabs and AMPK activator A-769662 was from Cell Guidance Systems.

2.1.7 Mass Spectrometry

EASY NanoLC system for liquid chromatography (LC) and Orbitrap Velos Pro for electrospray ionisation and mass spectrometry were both from ThermoFisher Scientific.

2.1.8 Primers

For mutagenesis of pCIneo-myc-VAPB and pM1-VAPB(1-220) the following primers were used to generate:

pCIneo-myc-/pM1- VAPB-T143A
Forward: AATAAAATTATATCCGCAACTGCATCAAAGACAGAAACACCAATAGTG
Reverse: CACTATTGGTGTTTCTGCCTTTGATGCAGTTGTGGATATAATTTTATT

pCIneo-myc-/pM1- VAPB-T143D
Forward: AATAAAATTATATCCGACACTGCATCAAAGACAGAAACACCAATAGTG
Reverse: CACTATTGGTGTTTCGTCCTTTGATGCAGTTGTGGATATAATTTTATT

pCIneo-myc-/pM1- VAPB-T148A
Forward: AATAAAATTATATCCACAACTGCATCAAAGGCAGAAACACCAATAGTG
Reverse: CACTATTGGTGTTTCTGTCTTTGATGCAGTTGCGGATATAATTTTATT

pCIneo-myc-/pM1- VAPB-T148D
Forward: AATAAAATTATATCCACAACTGCATCAAAGGACGAAACACCAATAGTG
Reverse: CACTATTGGTGTTTCTGTCTTTGATGCAGTGTCGGATATAATTTTATT

2.1.9 Common reagents

Phosphate Buffered Saline

0.01 M phosphate buffer

0.0027 M KCl

0.137 M NaCl

pH 7.4

Tris Buffered Saline

50 mM Tris-HCL

150 mM NaCl

pH 7.4

RIPA Buffer

50 mM Tris-HCl

150 mM NaCl

1 mM EDTA

1 % (v/v) Triton X-100

0.5 % (w/v) sodium deoxycholate

0.1 % (w/v) sodium dodecyl sulfate (SDS)

pH 7.4

cOmplete protease inhibitor cocktail

Phosphatase inhibitor (PhosStop)

5x Lamelli Sample Buffer

62.5 mM Tris-HCl (pH6.8)

2 % (w/v) SDS

5 % (v/v) β-mercaptoethanol

10 % (v/v) Glycerol

Touch bromophenol blue

Resolving Gels

Resolving master mix: 500 mM Tris pH 8.8, 1.5 % SDS in ultrapure H_2O

Table 2.3 Polyacrylamide resolving gel recipes for SDS-PAGE

Component	**8 % Gel**	**10 % Gel**	**12 % Gel**
Resolving master mix	6 ml	6 ml	6 ml
30 % (v/v) Acrylamide-bis-acrylamide	2.4 ml	3 ml	3.6 ml
10 % (w/v) Ammonium persulfate (APS)	90 µl	90 µl	90 µl
N,N,N`,N`-Tetramethyl ethylenediamine (TEMED)	3.6 µl	3.6 µl	3.6 µl
RO water	0.6 ml	N/A	N/A

Note that APS and TEMED are added only immediately before pouring

Stacking Gel

3.75 ml stacking master mix (150 mM Tris pH 6.8, 1.2 % SDS in ultrapure H_2O)

0.75 ml 30 % (v/v) Acrylamide-bis-acrylamide

45 µl 10 % (w/v) APS

4.5 µl TEMED

SDS-PAGE Running Buffer 1L

3 g Tris

13 g Glycine

10 ml 10 % (w/v) SDS

in ultrapure H_2O

Buffered to pH 8.3

SDS-PAGE Transfer Buffer 1L

3 g Tris

13 g Glycine

200 ml methanol

in ultrapure H_2O

Stripping Buffer 500 ml

7.5 g Glycine

0.5 g SDS

5 ml Tween 20

in ultrapure H_2O

Buffered to pH 2.2

2.2 Methods

2.2.1 Preparation of frozen human spinal cord tissue

Frozen post-mortem spinal cord tissue was homogenized at 100 mg/ml in RIPA buffer using a Bio-Gen PRO200 rotor-stator homogeniser (Pro Scientific, Connecticut, USA) for 20 sec, with samples maintained on ice throughout. Tissue was sonicated 3 times for 3 sec (Output 3, 10 sec on a Sonics Vibra Cells (Jencons PLS, East Grinstead, UK)) and returned to ice between each sonication. After sonication, samples were centrifuged for 13 000 x g with an Eppendorf 5415R desktop centrifuge (Eppendorf, Hamburg, Germany) at 4 ^{o}C for 20 min and supernatant collected in fresh tubes. The protein concentration of each sample was determined as described in section 2.2.2. RIPA buffer was used to normalise the protein concentration of samples and 5x lamelli sample buffer was added to each sample to bring it to a final concentration of 2.5 mg/ml.

2.2.2 Determining protein concentrations

Protein concentrations were determined using a Promega BCA assay kit. Briefly, BSA was diluted in RIPA buffer to produce eights standards of concentration range 0-2 mg/ml. Samples were diluted 1:1 in RIPA buffer. 10 µl of sample or standard was added per well to a 96-well plate (ThermoNunc, Roskilde, Denmark) in triplicate. As per manufacturer's instructions, BCA Reagents A and B were diluted 50:1 A:B and 200 µL was added to each well, prior to incubation for 30 min at 37 ^{o}C in the dark. The absorbance of the purple reaction product at 562 nm was determined with a PHERAstar microplate reader. Absorbance of each protein standard was plotted against concentration to create a standard curve. The protein concentration of each sample was determined using the line equation of the standard curve, $y=mx+b$, where y is absorbance, m is line gradient, b is the intersect on the y axis and x is protein concentration.

2.2.3 Production of plasmid DNA

LB agar (32 g/l) and LB broth (20 g/l) were sterilised by autoclaving and ~10 ml LB agar containing 100 µg/ml filter-sterilised ampicillin (LB-amp) for selection of plasmid vectors, was poured into sterile petri dishes and allowed to set. Plates were stored at 4 ^{o}C until use and for no more than one month.

DH5α *E.coli* were transformed with plasmid DNA for expression and purification as follows. 50 µl aliquots of Library Efficiency DH5α *E.coli* cells were thawed on ice, mixed gently and transferred to 1.5 ml Eppendorf tubes. ~5 ng plasmid DNA was added and tubes incubated on ice for 30 min before a 45 sec heat shock in a water bath at 42 ^{o}C. Eppendorfs were incubated on ice for a further 2 min before the addition of 950 µl pre-warmed LB broth and incubation at 37 ^{o}C for 1 hr with shaking at 225 rpm on a rotary

shaker. 20 - 200 µl LB containing transformed cells was streaked on LB-amp plates and bacteria were grown overnight at 37 ºC. 5 ml LB broth containing 100 µg/ml filter-sterilised ampicillin was inoculated with a single bacterial colony from LB-amp plates and incubated at 37 ºC for 8 hrs with shaking at 225 rpm. 1 ml of this starter culture was used to inoculate 50 ml LB broth containing 100 µg/ml filter-sterilised ampicillin and these cultures were grown overnight at 37 ºC. At this stage, in order to make stable stocks of cells expressing plasmids of interest, 0.75 ml 50 % glycerol was added to 0.75 ml overnight culture containing *E.coli* DH5α expressing the plasmid, and these were snap frozen and stored at -80 ºC as a glycerol stock. These stocks could be streaked onto LB agar plates each time more of the plasmid was needed.

Plasmid purification was carried out using a HiSpeed plasmid purification midi kit (Qiagen) as per the manufacturers' instructions. 50 ml overnight culture was centrifuged at 4 300 x g for 30 min in a Beckman Allegra centrifuge (Beckman Coulter, Indianapolis, USA). Supernatant was removed and the bacterial pellet resuspended in 3 ml resuspension buffer. 3 ml lysis buffer was added and tubes were gently mix by repeated inversion prior to addition of 5 ml neutralisation buffer. Samples were centrifuged at 4 300 x g for 30 min and the supernatant was applied to the binding column provided with the kit, to which DNA binds. Vacuum suction was applied to empty the column. The columns were washed by adding 5 ml wash buffer followed by vacuum suction, and then 20 ml wash buffer, followed by vacuum suction. Bound DNA was eluted in 500 µl DNAse free water. The concentration of plasmid DNA was quantified by measuring absorbance at 260 nm using a NanoDrop 1000 spectrophotometer. The 260/280 nm absorbance ratio was used to determine DNA purity: pure DNA has a ratio of 1.8. Plasmid DNA was stored at -20 °C until required.

2.2.4 Mutagenesis

Site directed mutagenesis was carried out using the QuikChange II Site-Directed Mutagenesis Kit (Qiagen) as per manufacturer's instructions. Briefly, reactions were set up to undergo PCR as follows; 50 ng of WT plasmid DNA to be mutated, 125 ng of forward and reverse primers (as per 2.1.8), 1 µl of dNTP, 5 µl of reaction buffer provided with the kit, nuclease free water to a total of 50 µl and 1 µl of *PfuUltra* High Fidelity DNA polymerase. PCR was carried out beginning with a 95 ºC 30 sec step, followed by 18 amplification cycles of the following:

95 ºC for 30 sec

55 ºC for 1 min

68 ºC for 6 min

1 µl *Dpn* I restriction enzyme was added to each reaction for 1 hr at 37 ºC. XL-1 Blue Competent *E.coli* were transformed with 1µl of the PCR reaction as described in section 2.2.3 for DH5α *E.coli.* 20 - 200 µl LB containing transformed cells was streaked on LB-amp plates and bacteria were grown overnight at 37 ºC. Multiple lots of 5 ml LB broth containing 100 µg/ml filter-sterilised ampicillin were inoculated with single bacterial colonies from the LB-amp plate and incubated at 37 ºC for 8 hrs with shaking at 225 rpm. Plasmids were extracted from these cultures using the Qiagen HiSpeed plasmid purification kit as described in section 2.2.3. Plasmids were sequenced by SourceBioscience (Nottingham, UK) and this sequence was aligned with the wild type sequence to identify colonies containing the correct mutation.

2.2.5 Cell culture

Cell culture was carried out under sterile conditions in a class II microbiological hood and cells were cultured in a humidified incubator at 37 ºC with 5 % CO_2.

2.2.5.1 iPSC culture and iPSC-MN differentiation

Stem cell culture and differentiation was carried out by Dr. Jenny Greig. iPSCs were grown in E8 Flex medium with Revitacell (1/100) on 6-well plates coated with Geltrex. Cells were passaged 1 in 6 or as appropriate twice each week and media was typically replaced a minimum of twice each week or as required. For passaging, media was aspirated, cells were washed in PBS and 1 ml versene was applied to each well until cells detached from each other, but not fully from the well. Versene was carefully removed and cells washed with PBS very gently so as not to detach cells from the well. E8 flex with Revitacell was then used to wash cells, remove them from the surface of the well and resuspend for replating. Media was replaced with E8 Flex without Revitacell 24 hrs after passaging.

iPSCs from two healthy controls and two ALS cases, with either a M337V or G298S mutation in TDP-43 were differentiated into motor neurons by Dr. Jenny Greig, following a protocol adapted from Maury et al. (2015), briefly as follows and in Figure 2.1. The differentiation protocol was started when iPSCs reached ~ 70 % confluency. Cells were first washed with PBS and then detached from the well using 1 ml Accutase + 20 µM Ri. Cells were resuspended in E8 Flex with Revitacell, counted using a Nucelocounter NC-3000 and briefly centrifuged. The cell pellet was resuspended in base media (1:1 DMEM/F12 + GlutaMAX : Neurobasal with 1 % (v/v) N2, 1 % (v/v) B27, 0.01 % (v/v) β-mercaptoethanol, 0.5 µM AA2P) containing 40 µM SB, 2 µM Dorso, 1 µM CHIR and 5 µM Ri and cells were plated in 96-well plates at $1x10^5$ cells per well. Plates were centrifuged at 200 x g in a Universal 320R centrifuge (Hettich, Massachusetts, USA) for

4 min with low brake and incubated overnight to allow the formation of embryoid bodies (EBs). EBs were transferred to 6-well plates in fresh base media containing SB, Dorso, CHIR and Ri as before and this was considered Day 0. After 48 hrs (Day 2), media was replaced with fresh base media containing SB, Dorso, CHIR, Ri, 1μM RA and 0.5 mM SAG. This media was replaced every 48 hrs or as required. On Day 7, media was replaced with base media containing only 1 μM RA and 0.5 mM SAG and on Day 9, media was replaced with base media containing 10 μM DAPT.

On Day 11, EBs were dissociated by transferring to a 15 ml falcon tube, removal of supernatant, washing with PBS and addition of 1 ml pre-warmed Accutase. Cells were warmed at 37 ^{o}C for 5 – 10 min, resuspended in base media, centrifuged and the cell pellet re-suspended in base media + 20 ng/ml BDNF, GDNF, IGF and 10 μM DAPT (maturation media). Cells were transferred in maturation media to 24-well plates containing 13 mm coverslips which had previously been coated with 50 μg/ml poly-L-ornithine in PBS for 1 hr at 37 ^{o}C followed by 40 μg/ml laminin in DMEM/F12 for 3 hrs at 37 ^{o}C. Half of the media in each well was replaced every 48 hrs or more often as necessary. iPSC-MNs were fixed 22 days after EB formation by the addition of 16 % (w/v) paraformaldehyde (PFA) (Sigma Aldrich, Dorset, UK) to media to allow a final concentration of 4 % PFA. Media was then gently removed and replaced with fresh 4 % PFA in PBS, in which cells were incubated for 15 min. PFA was removed and cells were stored in PBS at 4 ^{o}C until use in proximity ligation assays.

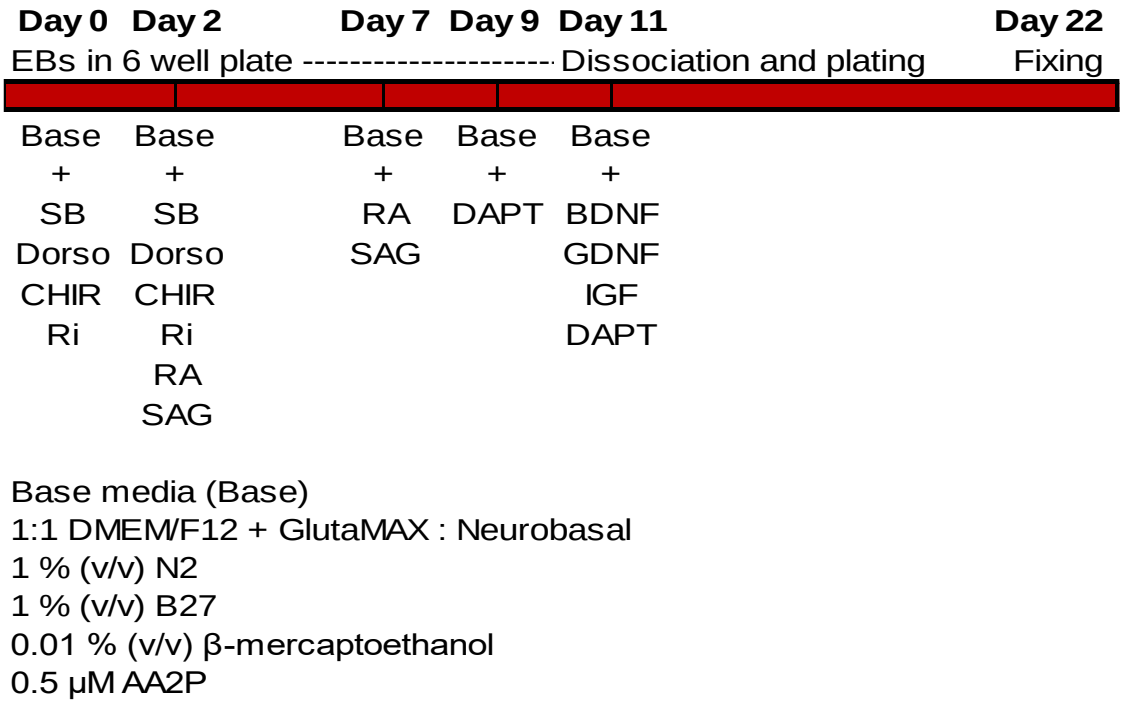

Figure 2.1: Diagram of iPSC-MN differentiation timeline

2.2.5.2 Cell line culture

HEK-293 cells were cultured in 75cm^2 flasks in DMEM containing 4.5 g/l glucose and 1mM sodium pyruvate, supplemented with 10 % (v/v) FBS and 1 % (v/v) glutaMAX. Cells were passaged every 3 or 4 days as appropriate, at ~ 80 % confluency. For passaging, media was aspirated and cells were washed with PBS before pre-warmed Trypsin-EDTA solution (0.05 % (v/v)/ 0.02 % (v/v) in phosphate buffered saline; PBS) was added in a volume sufficient to cover the base of the flask for ~3 min until cells detached from the flask. Pre-warmed culture media was added to dilute trypsin to 1/10, solution was triturated to produce a single cell suspension and the appropriate amount of cell suspension, usually containing 1/6 of the starting cell number, was transferred to a new flask. Cells were plated in 24-well plates or 100 mm dishes and cells were harvested on ice by removal of media and scraping in appropriate lysis buffer.

2.2.5.3 Cell line transfection and treatment with compounds

Cells were transfected using Opti-MEM and Fugene 6. For each well of a 24-well plate, 2 µl Fugene 6 was added to 50 µl Opti-MEM and, separately, plasmid DNA totalling 1 µg was added to 50 µl Opti-MEM. Opti-MEM containing DNA and Fugene 6 were incubated separately for 5 min before being mixed and incubated for 20 min. The DNA-transfection reagent complexes were added to each well, and cells were lysed or fixed as appropriate 24 hrs after transfection.

AMPK inhibitors 5-aminoimidazole-4-carboxamide-1-β-D-ribofuranoside (AICAR) and A-769662 were made to stock concentrations of 10 mM in Dimethyl sulfoxide (DMSO), which were stored for up to 1 month at -20 ^{o}C and were diluted 1:100 to 100 mM in fresh cell culture media when required. The same volume of the vehicle control (DMSO) was diluted in cell culture media. Media was aspirated from cells and replaced with media containing either AICAR, A-769662 or DMSO for 2 hrs before cells were collected for analysis.

2.2.6 SDS-PAGE and Immunoblotting

Samples were boiled for 5 min at 98 ^{o}C using a digital DM-100 dry bath (Jencons PLS, East Grinstead, UK) and centrifuged at 31 400 x g for 60 sec with a Spectrafuge 24D centrifuge (Jencons PLS) before separation. 8, 10 or 12 % (v/v) polyacrylamide resolving gels were made as per Table 2.3 in Mini-PROTEAN Tetra Cell Casting sets, with isopropanol added on top to prevent drying. Once resolving gel was set, isopropanol was removed and stacking gel was added with a well comb in place and allowed to set. Samples were separated by SDS-polyacrylamide gel electrophoresis (SDS-PAGE) on “home-made” polyacrylamide gels alongside a PageRuler Plus Prestained Protein

Ladder to allow determination of protein size. Post-mortem human spinal cord samples were separated by SDS-PAGE using Novex 4-12 % Tris-glycine gels. Running buffer was the same for both commercial and “home-made” gels and was made as detailed in section 2.1.9. Proteins were electrophoresed at 120 V for 1.5 – 2 hrs, until the dye front reached the bottom of the gel.

After separation by SDS-PAGE, proteins were transferred to Protran nitrocellulose membranes (0.45 µm pore; G.E. Healthcare) using a Bio-Rad Transblot system (for “home-made”) or Invitrogen X-Cell blot II (for precast gels) transfer systems. Transfers were carried out at 120 V for 1.5 hrs or at 30 V overnight to improve transfer efficiency when of large proteins, such as IP3R. After transfer, non-specific antibody binding was reduced by incubating membranes in blocking solution. Blocking solution was Tris–HCl-buffered saline (TBS, pH 7.3) and 0.1 % (v/v) Tween-20 containing either 5 % (w/v) BSA (for probing for TOM20, IP3R3, GSK-3β and AMPK) or 5 % (w/v) non-fat dried milk powder (for probing all other proteins), for 1 hr at room temperature. Membranes were incubated with primary antibodies in blocking buffer overnight at 4 ^{o}C with rocking. After washing three times for 5-10 min with TBS containing 0.1 % Tween-20 (TBS-T), membranes were incubated with appropriate secondary antibodies diluted in blocking buffer for 1 hr at room temperature with rocking. After washing again three times in TBS-T, membranes were processed for chemiluminescent detection. Membranes were incubated for 5 min in either a 1:1 dilution of ECL blotting reagents 1 and 2 (GE Healthcare) or Luminata Forte detection reagent (ThermoFisher). Chemiluminescent signals were detected with a Bio-Rad ChemiDoc imaging system. With the exception of western blots of immunoprecipitated protein, a housekeeping protein was also immunoblotted to allow for normalisation of protein loading in each well. Where the housekeeping protein is of a similar molecular weight to the protein of interest (for example, PDI and NSE), antibodies were stripped from the membrane after detection of bands for the protein of interest by incubation in stripping buffer for 10 min followed by 3 x 10 min washes in PBS. The immunoblot process was then repeated from the stage of blocking with antibodies for the housekeeping protein. For proteins of sufficiently different sizes (for example TOM20 and PTPIP51), membranes were cut between these sizes to allow incubation of the same membrane in different antibodies. Optical density (OD) of each band was measured using ImageJ. For each sample, the OD of the band of the protein of interest was normalised to the OD for the loading control. A mean OD value for the control samples was calculated and OD values for each sample were then normalised to the mean OD value for controls.

2.2.7 Immunostaining

Wax was removed from embedded tissue sections by heating at 60 ^{o}C for 20 min in an oven followed by 2 x 2 min washes in xylene. A re-hydration series of 2 x 2 min immersions in 99 % (v/v) ethanol and 1 x 2 min wash in 95 % (v/v) ethanol was performed followed by 10 min immersion in running tap water. Antigen retrieval was carried out using 10 mM sodium citrate, pH 6.0, in RO water by heating sections in antigen retrieval solution to boiling and then simmering in a microwave. The time and power taken to reach and maintain boiling varies dependant on microwave and volume of buffer, but for 2 – 4 sections in ~100 ml buffer, high power (in an 800W machine) was used for 6 min, followed by medium power for 12 min. Sections were washed in running tap water for 5 min. At this stage, a hydrophobic pen was used to encircle the tissue so that minimal amounts of reagent were required to sufficiently cover the tissue. Endogenous peroxidase activity was blocked using 2.5 % (v/v) hydrogen peroxide in methanol for 5 min at room temperature. Non-specific antibody binding was blocked by incubating sections in blocking buffer (TBS, pH 7.6, containing 1 % (v/v) donkey serum, 0.15 % (v/v) Tween-20) for 1 hr at room temperature.

Sections were then incubated with primary antibody diluted in blocking buffer (TBS pH 7.6, 1 % (v/v) donkey serum, 0.15 % (v/v) Tween-20) overnight at 4 ^{o}C. Sections were washed three times with PBS before the addition of appropriate secondary antibodies, also diluted in blocking buffer (TBS pH 7.6, 1 % (v/v) donkey serum, 0.15 % (v/v) Tween-20) for 1 hr at room temperature. Sections were again washed three times in PBS and biotinylated secondary antibody were bound by avidin/biotinylated enzyme complexes using ABC vector kits (Vector labs, Peterborough, UK) as per the manufacturer's instructions. To detect the signal, 0.5 mg/mL 3,3′- diaminobenzidine (DAB) in TBS containing 0.05 % (v/v) H_2O_2 was applied for 2 min. Sections were washed in PBS before Mayer's Haematoxylin was used for 2 min to counterstain nuclei and sections were transferred to tap water to remove remaining solutions. After 10 min in running tap water, sections were de-hydrated by immersion for 1 x 2 min in 95 % (v/v) ethanol, 2 x 2 min in 99 % (v/v) ethanol, 1 x 10 min in xylene, and glass coverslips were mounted using ClearVue XYL mounting media.

2.2.8 Proximity ligation assay

2.2.8.1 Post-mortem spinal cord sections

Wax removal, re-hydration, antigen retrieval and peroxidase blocking steps were carried out as for immunostaining with the exception that the antigen retrieval step was longer due to the increased volume of buffer needed for a larger number of slides; for 2 x ~300

ml buffer (2 containers each holding 17 sections), high power in an 800 W machine was used for 6 min, followed by medium power for 15 min.

Proximity ligation assays were performed using Duolink *In Situ* Brightfield detection reagents (Sigma-Aldrich), essentially as described by the manufacturer. As for immunostaining, a hydrophobic pen was used to encircle the tissue and minimise the amount of reagent required. After peroxidase blocking as above, sections were washed for 2 x 5 min in PLA wash buffer A before blocking for 1 hr at 37 ^{o}C in 1 drop of PLA blocking buffer. All steps at 37 ^{o}C were performed in a humidified slide chamber. After blocking, sections were incubated with 50 µl of both primary antibodies in PLA antibody diluent for 1 hr at 4 ^{o}C. Sections were washed twice for 5 min in PLA wash buffer A, followed by incubation for 1 hr at 37 ^{o}C in 50 µl PLA probe diluent containing PLA probes corresponding to each primary antibody and conjugated to complimentary oligonucleotides (one PLUS and one MINUS, both Duolink). Sections were washed twice for 5 min in PLA wash buffer A followed by incubation for 30 min at 37 ^{o}C with the ligase provided, diluted 1:40 in 1 x PLA ligase buffer in nuclease free water. Sections were washed twice for 5 min in PLA wash buffer A followed by incubation for 2 hrs at 37 ^{o}C with polymerase diluted 1:80 in 1 x amplification buffer in nuclease free water. Sections were washed twice for 2 min in wash buffer A followed by incubation with 1 x brightfield detection reagent in nuclease free water. Sections were washed twice for 2 min in wash buffer A before development of the PLA signal. NOVA red substrate kit reagents 1, 2, 3, 4 were diluted 1/62, 1/100, 1/100, 1/62 respectively, mixed, and applied to the tissue for 2 min. Sections were washed two more times for 2 min in buffer A and then counterstained in Mayer's Haematoxylin for 2 min and washed in running tap water for 10 min. De-hydration and mounting of sections was carried out as described for immunostaining; 95 % ethanol, 99 % ethanol and xylene immersions followed by mounting of glass coverslips using ClearVue XYL.

Sections were imaged using an Olympus slide scanner VS120 with Brightfield mode, generating an automated maximal projection of 11 z planes through the depth of the tissue with a 40 x lens and 0.95 numerical aperture. Motor neurons were identified by eye based on their distinct morphology; large, round nuclei only found in the ventral horn grey matter of the spinal cord. PLA signals were quantified as the number of dots per motor neuron. Using Visopharm (v2018.4) software each motor neuron was manually outlined and an APP was created using the Author module to automatically detect and count the number of PLA dots within outlined areas. Raw PLA signals were plotted and PLA signals for each individual were also plotted against the normalised VAPB protein amounts, as determine by western blotting, for the same individual.

2.2.8.2 iPSC-MNs

Cells were fixed in 4 % (v/v) PFA in PBS for 15 min at room temperature, quenched of autofluorescence using 0.05 M NH_4Cl in PBS for 15 min and permeabilised using 0.2 % Triton-X in PBS for 3 min. Proximity ligation was performed using Duolink *In Situ* Orange detection reagents following the same protocol as for post-mortem tissue sections, with the exception that incubation with polymerase and amplification buffer was performed for 100 min. Coverslips were incubated in the humidified chamber cell side down onto ~40 µl of each reagent spotted on parafilm. After amplification, all steps were carried out protected from light to prevent any loss of fluorescent signal. Cells were washed 1 x 10 min in wash buffer B, 1 x 10 min in 0.1 wash buffer B and 1 x 10 min in PBS before counterstaining and mounting on to slides using fluorescent mountant (Dako).

Counterstaining for ChAT in iPSC-MNs was performed at the end of the protocol by incubation with anti-ChAT in PBS overnight at 4 ^{o}C, followed by three washes in PBS and incubation in secondary antibody in PBS at room temperature for 1 hr. After counterstaining, coverslips were incubated with 4,6-diamidine-2-phenylindole (DAPI) followed by two washes in PBS and were mounted onto slides with fluorescent mounting medium. Images were taken at multiple depths through each ChAT-positive iPSC-MN on a Leica light microscope with Leica CTR500 camera using a 40 x objective or a Nikon A1R confocal microscope with Nikon A1 plus camera using a 60 x objective and 1.4 numerical aperture (Nikon A1R images presented). Maximum intensity projections of image stacks were generated using the stack focuser plugin of ImageJ (for Leica images) or NIS Elements software (for Nikon A1R images) and proximity ligation signals, counted as the number of dots per cell soma, were quantified using the Particle Analysis function of ImageJ.

2.2.9 Luciferase assay

For luciferase experiments, HEK-293 cells were transfected in 24 well plates as described in section 2.2.5.3 with plasmid DNA totalling 1 µg per well; 0.3 µg firefly luciferase, 0.3 µg VP16-PTPIP51(36-470) and 0.3 µg pM1-VAPB(1-220) WT or mutant. In addition, renilla was transfected at 0.1 µg per well due to the strength of its signal. Luciferase assays were performed 24 hrs after transfection using the Dual-Glo Luciferase Assay System (Promega) as per the manufacturers' instructions. Briefly, for a 24 well plate, cell media was aspirated, and cells were lysed in 50 µl Dual-Glo Luciferase assay reagent, made by diluting Dual-Glo Luciferase Substrate in Dual-Glo Luciferase Buffer, for 10 min at room temperature. Cell lysate was transferred to an opaque 96-well plate and firefly luminescence signal was measured using a PHERAstar

plate reader at 560 nm. 25 µl Dual-Glo Stop & Glo assay reagent, made by diluting Dual-Glo Stop & Glo Substrate 1:100 in Dual-Glo Stop & Glo Buffer, was added to each well to inhibit firefly luminescence signal and after 10 min renilla signal was measured using a PHERAstar plate reader at 480 nm. Firefly luciferase signals were normalised to the signal given by the transfection control renilla and were compared to the control WT signal. The mean of at least three biological replicates was calculated for each experiment.

2.2.10 Immunoprecipitation

For the analysis of VAPB and PTPIP51 phosphorylation in cells, VAPB and PTPIP51 were immunoprecipitated from HEK293 cells by Dr. Gábor Mórotz. HEK-293 cells were plated in 100 mm dishes and transfected at ~70 % confluency as described in section 2.2.5.2 with 4 µg pCIneo-Myc-VAPB or pCIneo-HA-PTPIP51 and 4 µg control vector or pCDNA3.1- GSK-3β per well. 24 hrs after transfection, cells were lysed in 500 µl cold PBS containing 1 % (v/v) Triton-X 100 and protease inhibitors and incubated at 4 ^{o}C for 1 hr on a rotary shaker. Cell lysate was then centrifuged at 6 100 x g for 1 min and 20 µl supernatant was taken as “input” of the immunoprecipitation. The remaining lysate was incubated with 2 µl Myc (for VAPB immunoprecipitation) or HA (for PTPIP51 immunoprecipitation) antibody on a rotary shaker at 4 ^{o}C overnight. Protein-G-sepharose beads (Sigma Aldrich) were washed by suspending in 10 ml PBS, centrifuging at 3000 x g for 1 min and replacing PBS. After three washes, PBS was removed and to generate a 50 % slurry of beads 384 µl PBS containing 0.1 % (v/v) Triton X-100 was added for every 500 µl of beads. Antibodies were allowed to bind the beads by the addition of 25 µl of this 50 % Protein-G-sepharose bead slurry to each 500 µl lysate/antibody mixture for 2 hrs at 4 ^{o}C on a rotary shaker. Following three x washes in PBS containing 0.1 % (v/v) Triton X-100, centrifuging at 3000 x g for 1 min between each wash to remove unbound proteins, the supernatant was discarded and the immunoprecipitated proteins were prepared for SDS–PAGE by eluting them from sepharose beads by the addition of laemmli sample buffer and heating at 98 °C for 5 min. Immunoprecipitated proteins were separated by SDS–PAGE as described in section 2.2.6, on 10 or 12 % acrylamide gels depending on the size of the protein to be resolved and were processed for mass spectrometry as described below (section 2.2.12).

2.2.11 Production of recombinant protein and in vitro phosphorylation

Recombinant VAPB and PTPIP51 were produced for incubation with recombinant kinase and subsequent analysis by mass spectrometry. Recombinant histidine tagged VAPB(1-220) was prepared by Dr. Sébastien Paillusson by expression of pET28A-His-VAPB(1-220) in *E.coli* BL21 (DE3) according to the manufacturers’ instructions, with the exception

that expression was induced with 0.4 mM Isopropyl β- D -1-thiogalactopyranoside (IPTG) for 3 hrs at 37 ºC. Recombinant protein was purified on a GraviTrap nickel column and eluted with 500mM imidazole.

GST-PTPIP51(36-470) was expressed in *E.Coli* DH5α because PTPIP51 was found to degrade less in these cells than in *E.Coli* BL21 (DE3). *E.Coli* DH5α cells were transformed with pGEX51, encoding GST, or pGEX51-PTPIP51(36-470) as described in section 2.2.3 and grown overnight. 5 ml of overnight cultures were used to inoculate 100 ml LB broth. These 100 ml cultures were grown at 37 ºC until they reached an optical density of 0.6-0.8. Cultures were then induced to express the protein using 1 mM IPTG and incubated at 18 ºC overnight. This lower temperature was used to further minimize degradation. An uninduced control culture was also grown at 18 ºC overnight. Bacterial cultures were centrifuged at 4 ºC at 4 300 x g for 30 min and the pellet was resuspended in lysis buffer (50 mM Tris pH 7.7, 150 mM KCl, 0.1 % Triton X 100 with 1 mM dithiothreitol (DTT, added fresh just before use). After 30 min incubation on ice, cell lysates were sonicated using 2, 20 sec pulses at 40 % duty cycle, with 60 sec on ice between each pulse to cool down the sample. After sonication, 1 ml of both induced and uninduced lysate was centrifuged at 31 400 x g for 1 min, supernatant was removed, and the cell pellet lysed in 1 x laemmli sample buffer ready for separation by SDS-PAGE. The remainder of the lysate was centrifuged at 4 ºC at 4 000 x g for 20 min and supernatant collected.

For each sample (GST and GST-PTPIP51(36-470)), 200 µl glutathione sepharose beads were washed by suspending in 10 ml PBS, centrifuging at 750 x g for 3 min and replacing PBS. After three washes, beads were re-suspended in 200 µl PBS. 400 µl glutathione-sepharose beads in PBS were added to the supernatant of each bacterial cell lysate and incubated at 4 ºC for 90 min on a rotary shaker. Beads were then washed as previously, three times with PBS, and re-suspended in 200 µl PBS. 20 µl of these GST-bound glutathione beads were diluted with 20 µl 2 x laemmli sample buffer ready for separation by SDS-PAGE. The remaining beads were centrifuged (750 x g, 3 min) and resuspended in glutathione buffer (25 mM glutathione, 50 mM Tris, 200 mM NaCl) for 1 hr at 4 ºC to elute the recombinant protein from the beads. Purified recombinant protein was stored at -80 ºC until required.

The approximate concentration of recombinant protein was determined by running samples alongside BSA standards of known concentrations (1 – 10 µg) on an SDS-PAGE gel. After separation, the gel was fixed for 1 hr in 50 % (v/v) methanol and 10 % (v/v) glacial acetic acid, and stained for 2 hrs in 50 % (v/v) methanol, 1 % (v/v) glacial

acetic acid and 0.1 % (w/v) Coomassie Brilliant Blue. Gels were de-stained in ultrapure H_2O overnight. Protein concentrations were determined by matching band intensities of recombinant protein to BSA bands. Once an approximate concentration of purified protein was determined, 6 µg His-VAPB(1-220) or GST-PTPIP51(36-470) were incubated for 16 hrs at 30 ^oC with 1 µl (500 units) commercial recombinant rabbit GSK-3β in the buffer provided, supplemented with 200 µM ATP. The phosphorylation reaction was stopped by the addition of laemmli sample buffer. Samples were separated by SDS-PAGE as described in section 2.2.6, on 10 or 12 % acrylamide gels depending on the size of the protein to be resolved and were processed for mass spectrometry as described below (section 2.2.12).

2.2.12 Mass spectrometry

Recombinant or *in vitro* proteins to undergo mass spectrometry were separated by SDS–PAGE on 10 or 12 % acrylamide gels, as described in section 2.2.6. Proteins were fixed in the gel by incubation in fixing buffer containing 50 % (v/v) methanol and 10 % (v/v) glacial acetic acid for 1 hr at room temperature. Proteins were then stained by incubation in imperial protein stain for 2 hrs at room temperature and de-stained in ultrapure H_2O overnight, also at room temperature. Proteins bands were excised and stored in ultrapure H_2O at 4 ^oC until further processing.

Peptide processing and subsequent liquid chromatography with tandem mass spectrometry (LC-MS/MS) were carried out by Mr. Steven Lynham at the KCL Proteomics Facility. Peptide processing was carried out on proteins whilst they remained in the gel and three bands of each protein were pooled for analysis. Briefly, after removing water in which they were stored, gel pieces were washed for 10 min in a sufficient amount of 100 mM Ammonium Bicarbonate (Ambic) to cover them. Gel pieces were then washed twice in acetonitrile and dried for 5 min in a SpeedVac. Gel pieces were rehydrated in 1 mM DTT (1 mM DTT in 100 mM Ambic) at 56 ^oC for 30 min to chemically block cysteine residues by reduction. Gel pieces were again washed with acetonitrile, followed by incubation in 55 mM Iodoacetamide (IAA, 55 mM in 100 mM Ambic) in the dark for 20 min at room temperature to form stable carbamidomethyl derivatives. Following a further two washes in acetonitrile to completely destain and dehydrate, gel pieces were dried in a SpeedVac for 10 min. Gel pieces were rehydrated with trypsin (30 µl Trypsin in 0.1 % (v/v) trifluoracetic acid diluted in 200 µl 50 mM Ambic) for 20 min at 4 ^oC. Unabsorbed trypsin was removed and replaced with 50 mM Ambic to maintain hydration of gel pieces, which were incubated for 2 hrs at 37 ^oC and then at room temperature overnight. After digestion, peptides were extracted from the gel by three 5 min washes at 37 ^oC with 50 mM Ambic followed by acetonitrile. Peptides were

dried in a SpeedVac and re-suspended in 10 µL of 50 mM ammonium bicarbonate for analysis.

Peptides were separated by liquid chromatography on an EASY NanoLC system, using reversed phase chromatography on a 75 µm C18 column and eluted at a flow rate of 300 nl/min over 60 min in a linear gradient of acetonitrile in 0.1 % formic acid. The eluate was ionized by electrospray ionization, ions were fragmented by collision induced fragmentation and the mass to charge ratio of fragment ions was detected using a linear trap quadrupole. This ionisation, fragmentation and detection were carried out in an Orbitrap Velos Pro. Raw data was processed in Proteome Discoverer (v1.4) and an in-house database containing VAPB or PTPIP51 as appropriate was used to assign peptide spectra in Mascot software. Spectra were visualised in Scaffold 4 (v4.7.2). Analysis of b- and y- ion series was performed manually to confirm or reject assignment of phosphorylation sites. b- and y- series ions are created by fragmentation of peptides at the peptide bond between amino acids; b-ions are generated when the ion is retained on the N-terminal fragment and y-ions are generated when the ion is retained on the C-terminal fragment. Correct assignment of phosphorylation was confirmed where there was sufficient coverage of b- and y- ions and loss of phosphoric acid (mass loss of 98, indicative of phosphorylation) was found on specific b- and y- ions such that there was only one possible position of phosphorylation in the full peptide.

2.2.13 Statistical Analysis

Statistical analyses were carried out using GraphPad Prism. Data was tested for normal distribution using D'Agostino & Pearson normality test and $p > 0.05$ was considered to represent normally distributed data. Non-parametric tests were used where data was not normally distributed ($p < 0.05$). Raw data for post-mortem delay (PMD) and age and normalised data western blots and PLA were plotted for control and ALS cases. Normally distributed data were analysed by unpaired two-tailed t-test and data which was not normally distributed were analysed by the non-parametric alternative Mann-Whitney test. PLA data and VAPB protein amounts for each individual were also plotted against each other and against raw PMD and age data for each individual. These data were analysed by Pearson's correlation. Luciferase data was analysed by ANOVA and Tukey post-hoc test. $p < 0.05$ was considered statistically significant for all analyses.

Chapter 3: ER-mitochondria contacts are reduced in ALS patients

3.1 Introduction

3.1.1. ER-mitochondria signalling in animal and cell models of ALS

As detailed in chapter 1, signalling between ER and mitochondria facilitates a number of the cellular processes that are damaged in neurodegenerative diseases including calcium exchange and ATP production, and correcting ER-mitochondria interactions may therefore represent a therapeutic target. Signalling between these organelles is mediated by tethering between the ER membrane protein VAPB and mitochondrial membrane protein PTPIP51 (Lau et al., 2018).

The VAPB-PTPIP51 interaction is disrupted in animal and cell models of ALS. Expression of WT or ALS-causing mutant forms of either TDP-43 or FUS reduce VAPB-PTPIP51 interactions in cultured cells and this reduction is also seen in transgenic mouse models expressing WT and mutant forms of TDP-43 and FUS (Stoica et al., 2014; Stoica et al., 2016). As a result, disrupted ER-mitochondria contacts, reduced calcium exchange between ER and mitochondria and reduced ATP production are also observed in these models (Stoica et al., 2014; Stoica et al., 2016). However, neither ER-mitochondrial signalling nor VAPB-PTPIP51 binding has yet been investigated in ALS in humans.

3.1.2 Measuring ER-mitochondria contacts in ALS donor tissues

Human diseases of the central nervous system (CNS) present a major challenge to investigate because the affected tissues are largely inaccessible in humans. CNS tissues obtained post-mortem and peripheral cells re-programmed to neuronal lineages provide two potential solutions to this challenge.

3.1.2.1 Post-mortem spinal cord tissues

Studies of human neurodegenerative diseases using post-mortem CNS tissue have identified pathological hallmarks of diseases such as ALS. For example, TDP-43 was identified as the ubiquitinated disease protein that accumulates in affected neurons in both ALS and FTD (Neumann et al., 2006) prior to discovery of disease-causing mutations in the *TARDBP* gene that encodes TDP-43 (Sreedharan et al., 2008). This can be considered evidence that post-mortem disease tissue is a valuable resource for investigating disease mechanisms. For the studies described in this Chapter, the London Medical Research Council Neurodegenerative Diseases Brain Bank provided post-mortem samples of spinal cord from ALS and control donors.

3.1.2.2 Induced pluripotent stem cell-derived motor neurons

Differentiated patient-derived iPSCs are now relatively well characterised as *in vitro* models of disease (Egawa et al., 2012; Ghaffari et al., 2018; Guo et al., 2017), and this approach allows the study of various different cell types, including neurons which cannot be directly sampled from patients. Cells derived from iPSC retain the exact genetic identity of donors, potentially including as yet unidentified variants that contribute to disease.

In this Chapter, VAPB-PTPIP51 interactions were examined in motor neurons differentiated from human iPSCs (iPSC-MNs), from control donors and from donors with ALS-causing mutations. The two ALS donors had familial forms of ALS, rather than the more common sporadic type of disease represented in our post-mortem tissue samples. Both donors harbour ALS-causing mutations in the *TARDP* gene that lead to single amino acid substitutions in the TDP-43 protein, M337V (Corrado et al., 2009; Rutherford et al., 2008; Sreedharan et al., 2008) and G298S (Nozaki et al., 2010; Van Deerlin et al., 2008). Both of these mutations are found in exon 6 of *TARDP,* which codes a glycine rich domain and a C-terminal domain (Pesiridis et al., 2009). The G298S mutation resides in the glycine rich domain of TDP-43, which is responsible for alternative splicing regulation (Van Deerlin et al., 2008). The M337V mutation resides in the C-terminal domain and is reported to promote increased fragmentation of TDP-43 to produce C-terminally truncated TDP-43 fragments (Sreedharan et al., 2008). The protein region coded by Exon 6 is also known to be important for mediating the interactions of TDP-43 with other RNA binding proteins (Berning and Walker, 2019). iPSC-MNs harbouring the M337 or G298S mutations in TDP-43 have previously been investigated. These studies found that M337V and G298S iPSC-MNs display reduced neurite length as well as increased amounts of insoluble TDP-43 relative to control lines (Bilican et al., 2012; Egawa et al., 2012). The latter findings are in-line with the accumulations of TDP-43 found in the post-mortem tissues of a majority of ALS patients (Ling et al., 2013; Van Deerlin et al., 2008), while the former suggest that these TDP-43 mutations are damaging to motor neuron health.

Dr. Jenny Greig, a collaborator on this project, differentiated iPSCs generated from patient and control donor fibroblasts into motor neurons. For this study, an adapted protocol was used which promotes maturation of iPSCs into motor neurons as determined by electrophysiological activity and expression of choline acetyl transferase (ChAT), the enzyme responsible for the synthesis of the neurotransmitter acetylcholine. In iPSC-derived motor neuron cells, an immature action potential can be stimulated at 17 days *in vitro* and ChAT expression and mature action potential firing are observed at

31 days of culture (Maury et al., 2015). In the studies described in this Chapter, iPSC-motor neurons were grown to 22 days *in vitro* at which point ChAT is expressed in 65 – 80 % of cells (unpublished data, Jenny Greig e-thesis). In our hands, this timepoint gave the best compromise between maturity of motor neurons and their *in vitro* survival. Dr. Greig previously characterised the M337V and G298S iPSC-MNs used here and found in both lines that localisation of TDP-43 is unaltered, but TDP-43 levels are increased compared to that in iPSC-MNs from control donors (unpublished data, Jenny Greig e-thesis).

3.1.2.3 Proximity ligation assays

To investigate ER-mitochondria contacts in post-mortem spinal cord and iPSC-MNs from humans with ALS, this study uses proximity ligation assays to detect VAPB-PTPIP51 interactions. Proximity ligation assays detect two proteins of interest that are in close proximity, between 10 and 40 nm (Alam, 2018; Soderberg et al., 2006). Briefly, primary antibodies to the two proteins of interest, raised in different host species, are applied to the cells or tissue. In this case in-house rabbit VAPB and in-house rat PTPIP51 antibodies are used. Species-specific secondary antibodies conjugated to complimentary oligonucleotides are then applied and these two oligonucleotides are ligated when proteins of interest are sufficiently close to each other. For Brightfield PLA, as used for tissue sections, rolling amplification using the ligated oligonucleotides as a primer is followed by addition of detection reagents containing horse radish peroxidase-linked nucleotides which hybridize to the amplification product. These oligonucleotides enzymatically convert NOVA red substrate to produce visible red-brown dots at areas of interaction between proteins of interest. PLAs were used in their brightfield format in human tissue because, in our hands, this generates the strongest signal-background and a nuclear counterstain is sufficient to identify motor neurons on the basis of their morphology. For fluorescent detection, as used on iPSC-MNs, the rolling amplification occurs with fluorescently labelled nucleotides and no extra detection step is required. In this case, a fluorescent dot indicates an interaction between the two proteins. PLAs were used in their fluorescent format for iPSC-MN studies to enable both nuclear and ChAT counterstaining to ensure that analysis was specific to cells that had been successfully differentiated into motor neurons.

PLAs have previously been used by our group to examine VAPB-PTPIP51 interactions in neuronal cell lines, rodent primary neurons, mouse brain, and iPSC-neurons (Gomez-Suaga et al., 2017b; Gomez-Suaga et al., 2019; Paillusson et al., 2017; Stoica et al., 2014; Stoica et al., 2016).

3.1.3 Aims of this chapter

The aim of this chapter was to investigate the hypothesis that ER-mitochondria contacts are disrupted in human ALS. Evidence from human tissues is critical to support the idea that strategies which correct ER-mitochondria contacts will have benefit for the treatment of ALS.

Firstly, VAPB and PTPIP51 protein amounts were measured in post-mortem spinal cord tissue by immunoblotting for VAPB and PTPIP51. Motor neurons in post-mortem spinal cord tissue from the same donors were assessed by PLA to allow measurement of interactions between the ER-mitochondria tethers VAPB and PTPIP51. Secondly, VAPB-PTPIP51 interactions were measured by PLA in iPSC-MNs harbouring ALS-causative M337V or G298S mutations in comparison to unrelated control iPSC-MNs.

3.2 Results

3.2.1 VAPB levels are reduced in ALS donor tissue

Previous studies have found that VAPB-PTPIP51 binding is disrupted in animal and cell models of ALS, and that this reduction in tethering is not caused by a reduction in the protein levels of either VAPB or PTPIP51 (Stoica et al., 2014; Stoica et al., 2016). However, there are reports that VAPB protein levels are reduced in sporadic ALS spinal cord relative to controls (Anagnostou et al., 2010) and that iPSC-MNs carrying ALS-causing mutant forms of VAPB show reduced levels of VAPB protein relative to iPSC-MNs from non-affected siblings (Mitne-Neto et al., 2011). This study therefore first investigated VAPB and PTPIP51 protein expression in our samples of post-mortem spinal cord by immunoblotting. Samples were homogenised in RIPA buffer, sonicated, centrifuged and protein concentration was measured by BCA assay as described in 2.2.1 and 2.2.2. Protein concentration was normalised to 2.5 mg/ml protein in Laemmli sample buffer before boiling for 5 min.

It was first important to identify primary antibodies with sufficient specificity. Several antibodies against VAPB and PTPIP51 were tested in a small set of three control and three ALS samples (Figure 3.1). VAPB was detected by an “in house” anti-VAPB, produced as described (De Vos et al., 2012) and a commercial anti-VAPB antibody from Abcam. Two different anti-PTPIP51 antibodies were tested: one sourced from Gentex and the other from Atlas. The molecular mass of VAPB is 33 kDa and it is predicted to display a single band at this molecular weight (MW) on immunoblot. The molecular mass of PTPIP51 is 51 kDa but it is predicted to display a single band closer to 70 kDa on immunoblot. Neuron specific enolase (NSE) was used as a loading control and has a predicted MW of 47 kDa.

The in-house VAPB antibody produced a single band at the expected MW of 33 kDa (Figure 3.1A). The VAPB antibody from Abcam produced a doublet at approximately 33 kDa as well as non-specific bands at 37 kDa, 55 kDa and 70 kDa (Figure 3.1B). The in-house VAPB antibody is therefore used throughout the rest of this work. The anti-PTPIP51 antibody sourced from Gentex produced the expected band at just below 70 kDa but also some strong non-specific bands at 35kDa (Figure 3.1C). The anti-PTPIP51 antibody sourced from Atlas also produced the expected band at 70 kDa and only faint non-specific bands at 35 kDa (Figure 3.1D) and is therefore used throughout the rest of this work.

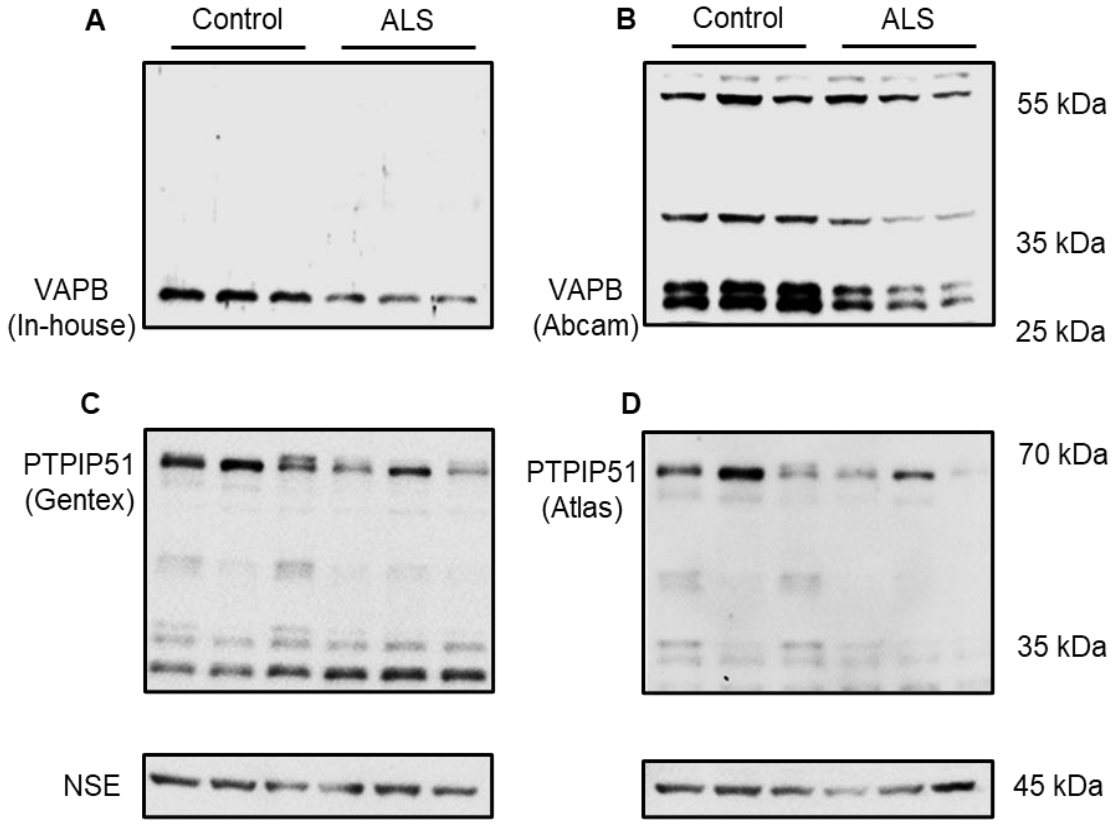

Figure 3.1: Antibody optimisation for VAPB and PTPIP51 antibodies. Immunoblots of human spinal cord homogenate probed with A) In-house VAPB antibody, B) VAPB antibody sourced from Abcam, C) PTPIP51 antibody sourced from Gentex and D) PTPIP51 antibody sourced from Atlas. Corresponding NSE blots for A) and C) (bottom left panel) and B) and D) (bottom right panel) are shown. N=1 experiment, 3 control and 3 ALS cases.

Having selected primary antibodies against VAPB and PTPIP51, post-mortem spinal cord samples from 17 control and 17 ALS donors, prepared as described above, were immunoblotted. All but three samples, which came from thoracic spinal cord, were from the lumbar region of the spinal cord. Samples from the thoracic spinal cord are indicated in results. Clinical ALS diagnosis was confirmed by the Brain Bank through histopathological identification of TDP-43 pathology in motor neurons in all but one case. The cases did not include any that showed FUS or SOD1 pathology. Two ALS cases were subsequently found to have repeat expansions in C9ORF72 and are indicated in results, but no other donor carried additional ALS-causing mutations. One control donor displayed TDP-43 inclusions in the hippocampal formation and amygdala, but all control donors were confirmed as suitable for this study by both a lack of clinical ALS diagnosis and the absence of TDP-43, FUS, SOD1 or C9ORF72 pathology in motor neurons.

Summary demographics of the cases are displayed in Table 3.1. Samples were selected by the Brain Bank based on the best possible match between gender, age, and post-mortem delay (PMD) between control and ALS samples. However, some differences in these parameters were subsequently found. Samples are well-matched based on sex. There was however a significant difference in PMD: the average PMD for control samples was 30.91 (+/- 12.89) hrs compared to an average of 62.44 (+/-16.06) hrs for ALS samples (Figure 3.2A). Control samples came from significantly older donors with an average age of 83.82 (+/- 11.28) years compared to an average age in ALS cases of 73.12 (+/- 8.96) years (Figure 3.2B). Age and PMD are therefore assessed in relation to results of interest throughout this work to account for any potential influences of these variables.

Table 3.1: Summary demographics of post-mortem spinal cord tissue donors

	Control	ALS
Number of cases	17	17
Male	10	10
Female	7	7
Age (years)	63 - 105	56 - 90
Average Post-mortem Delay (Hrs)	9 - 55	34 - 94
C9ORF72	0	2

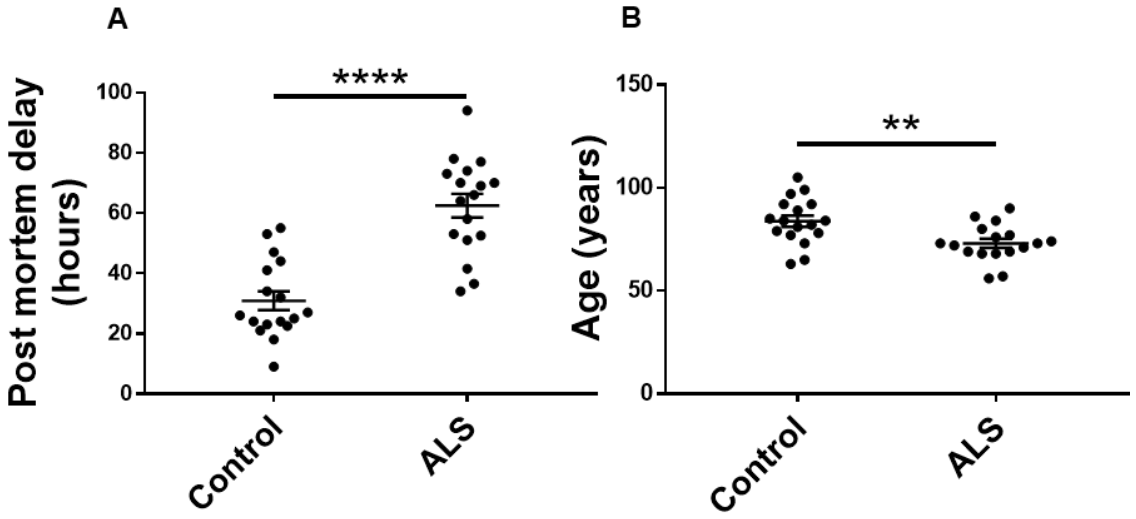

Figure 3.2: Differences in age and post-mortem delay between control and ALS cases. A) Hrs of post-mortem delay and B) age in years are plotted for each control and ALS donor from which post-mortem spinal cord tissue samples were obtained. N = 17 control and 17 ALS cases. Age and post-mortem delay were normally distributed as tested using D'Agostino & Pearson normality test, $p > 0.05$. As such, data were analysed by the parametric unpaired two-tailed t-test, error bars are s.e.m., ****$p<0.0001$, **$p=0.004$.

VAPB and PTPIP51 protein levels were measured in control and ALS donor samples by immunoblotting. One ALS sample consistently showed bands at higher than expected molecular weights for each protein and was therefore excluded from all analyses. One control sample showed no PTPIP51 band and was therefore also excluded. Loss of neurons occurs in the spinal cord of ALS patients (Rosler et al., 2000) and therefore a general loss of neuronal proteins may also be expected in spinal cord lysates. To account for this, the neuronal protein NSE was measured in all samples and amount of protein of interest was normalised to NSE level in the same sample. Samples were run across two gels, with 8 control and 8 ALS samples on one gel, and 9 control and 9 ALS samples on the other. Samples were loaded alternating between control and ALS to reduce the risk of any potential uneven antibody exposure. For figures 3.3 and 3.4, representative samples, 7 control and 7 ALS, were chosen and the centre 5 control and 5 ALS samples on the immunoblot are shown. A single blot was cut to probe for PTPIP51 and TOM20, followed by stripping and re-probing for NSE. VAPB and PDI were probed on separate blots but also stripped and re-probed for NSE since they are of similar molecular weight.

VAPB levels were found to be significantly reduced in ALS spinal cord compared to that in control spinal cord (Figure 3.3A). In contrast, there was no change in the levels of PTPIP51 in spinal cord tissue between ALS and control spinal cord samples (Figure 3.3B). To determine if this reduction in the amount of VAPB is specific or results from loss of total ER in ALS spinal cord, the expression of an ER marker, protein disulfide isomerase (PDI), was measured by immunoblotting in the same samples. PDI has a predicted molecular mass of 57kDa. Similarly, the expression of a 20kDa mitochondrial marker, translocase of outer mitochondrial membrane 20 (TOM20), was measured to indicate whether the amount of mitochondria is altered in ALS samples. One control sample showed no TOM20 band and was therefore excluded from the analysis. The protein levels of PDI and TOM20 were also normalised to that of NSE for each sample. There was no change in the amount of the ER marker PDI (Figure 3.3C), suggesting that the amount of ER, and therefore other ER proteins, is maintained in the ALS tissues. Overall, these data suggest a selective loss of VAPB in sporadic ALS spinal cord, in agreement with Anagnostou et al. (2010). Interestingly, levels of the mitochondrial marker TOM20 were found to be increased in ALS samples relative to controls (Figure 3.3D), which suggests that there is an increase in either mitochondrial number or mitochondrial protein content in ALS spinal cord.

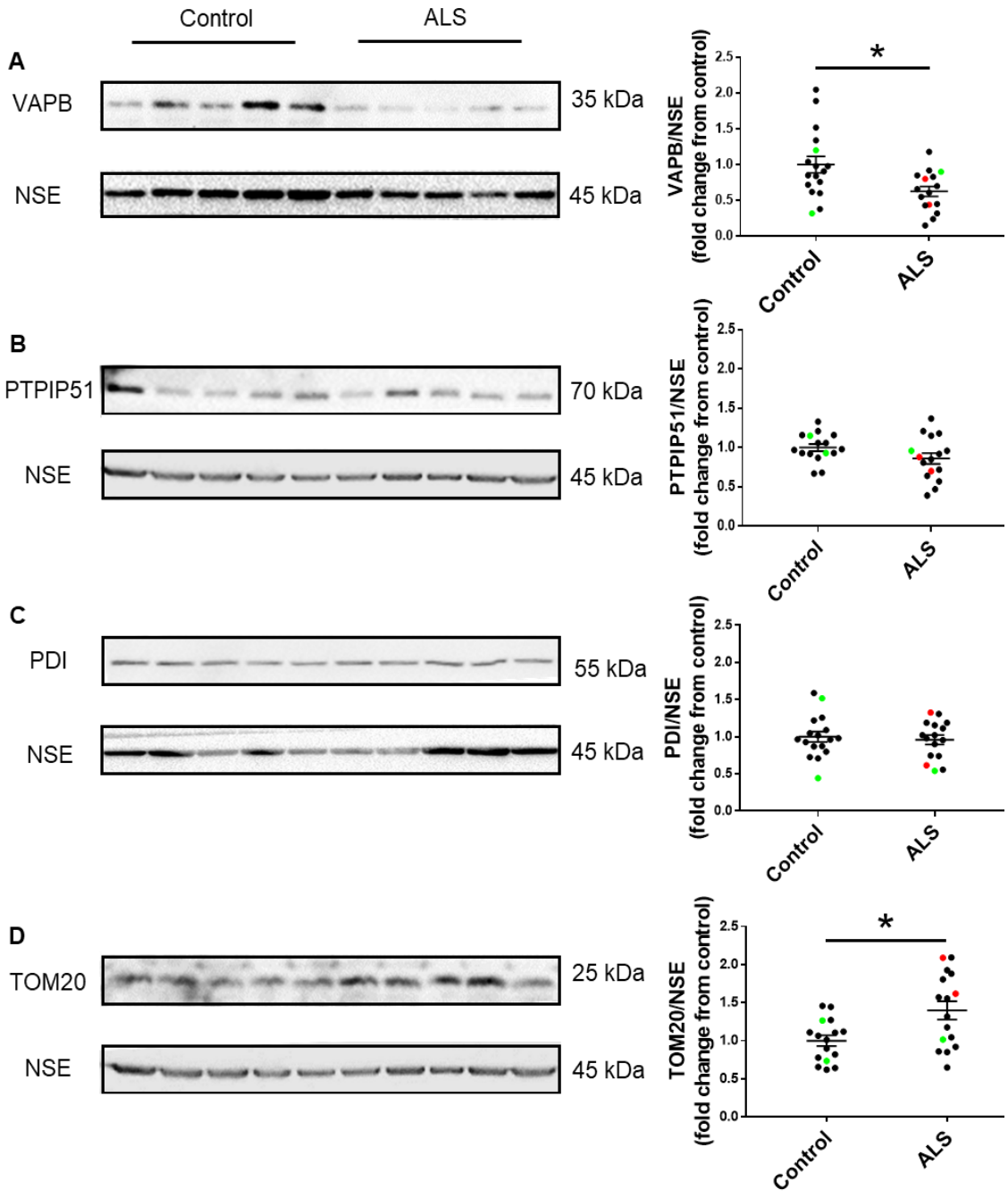

Figure 3.3: Levels of ER and mitochondrial proteins in post-mortem spinal cord tissue from control and ALS donors. Representative immunoblots of NSE and A) VAPB, B) PTPIP51, C) PDI and D) TOM20 in control and ALS spinal cord. Graphs show quantification of MAM-related protein levels in the different samples following normalisation to NSE levels. Thoracic spinal cord samples are indicated in green and C9ORF72 cases are indicated in red. The levels of each protein in control and ALS data sets were normally distributed as tested using D'Agostino & Pearson normality test, $p > 0.05$. As such, data were analysed by the parametric unpaired two-tailed t-test. N=16-17, error bars are s.e.m., *$p<0.05$.

3.2.2 Levels of IP3R, VDAC and Sigma1R are unaltered in ALS donor tissue

In addition to VAPB and PTPIP51, which represent structural tethers between ER and mitochondria, this study investigated interacting pairs of proteins at ER-mitochondria contact sites that are proposed to have important functional roles in this location, but that may not have a direct role in tethering ER and mitochondria (Lau et al., 2018). One of the major functions facilitated by ER-mitochondria contacts is the transfer of calcium from the ER, where it is stored, into the mitochondria where it is used in the production of ATP (Paillusson et al., 2016). IP3R-VDAC interactions via Grp75 mediate this exchange of calcium between the two organelles: calcium is released from the ER via IP3R and enters the mitochondria via VDAC (Paillusson et al., 2016; Szabadkai et al., 2006). There are three isoforms of IP3R that interact with VDAC to form contacts between the ER and mitochondria, IP3R1 and IP3R3 being the most well studied in this respect (Ivanova et al., 2014). Unpublished data from our lab investigating IP3R1 and IP3R3 showed that IP3R1 was most abundant in the brain and IP3R3 was most abundant in the spinal cord, and as such, IP3R3 was studied. The Sigma1R, an ER protein enriched in MAM, binds to IP3Rs in the membrane of the ER and is thought to mediate IP3R clustering in the membrane to facilitate IP3R-mediated delivery of calcium from ER stores to mitochondria. Interestingly, loss-of-function mutations in Sigma1R are linked with familial ALS and FTD (Al-Saif et al., 2011; Belzil et al., 2013; Bernard-Marissal et al., 2015; Luty et al., 2010) and Sigma1R agonists have shown benefits in mouse models of ALS/FTD (Mancuso et al., 2012; Ono et al., 2014; Ryskamp et al., 2019). Calcium exchange is not only one of the major functions of ER-mitochondrial signalling but is also known to be disrupted in a number of neurodegenerative diseases (Bernard-Marissal et al., 2018; Cali et al., 2013a; Krols et al., 2016). We therefore chose to investigate whether IP3R, VDAC or Sigma1R protein levels are altered in human ALS donor spinal cord.

IP3R3, VDAC and Sigma1R levels were measured in control and ALS spinal cord samples by immunoblotting and protein amounts were normalised to NSE, as described above. Sigma1R was probed on the same blot as VAPB, above, by cutting the membrane to probe with separate antibodies. NSE was probed on the same section as VAPB, after stripping. IP3R and VDAC were probed on separate blots, and the VDAC blot was stripped and re-probed for NSE. IP3R3 has a calculated molecular weight of 304 kDa but is expected to produce a band at 260 kDa. VDAC and Sigma1R have molecular weights of 31 and 25 kDa, respectively. Quantification of this data showed that there was no significant difference in the levels of IP3R3, VDAC or Sigma1R in ALS relative to control spinal cord (Figure 3.4 A, B and C respectively).

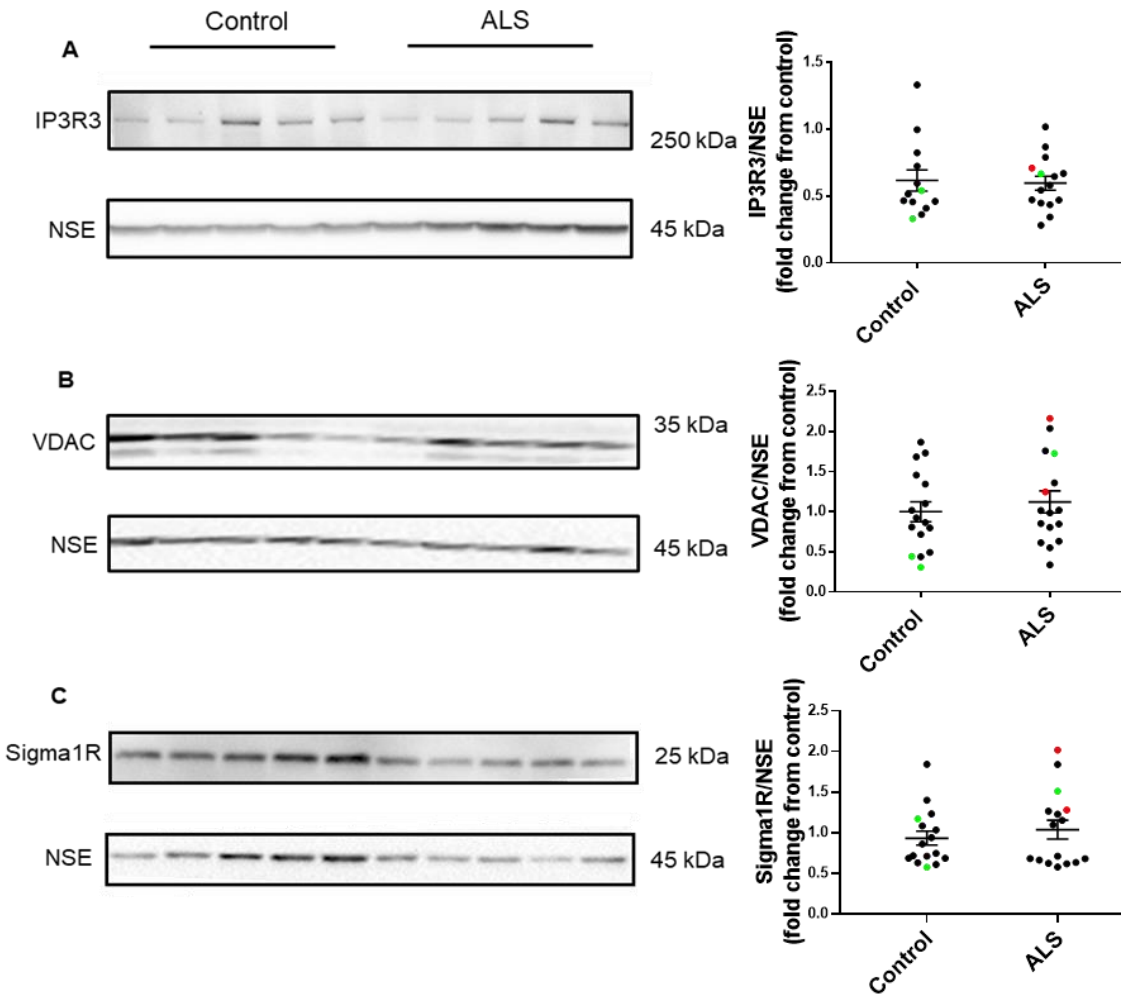

Figure 3.4: Levels of MAM related proteins in post-mortem spinal cord tissue from control and ALS donors. Representative immunoblots of NSE and A) IP3R3, B) VDAC and C) Sigma1R in control and ALS spinal cord. Graphs show quantification of MAM-related protein levels in the different samples following normalisation to NSE levels. Thoracic spinal cord samples are indicated in green and C9ORF72 cases are indicated in red. The levels of VDAC in control and ALS data sets were normally distributed as tested using D'Agostino & Pearson normality test, $p > 0.05$ and were therefore analysed by unpaired two-tailed t test. The levels of IP3R and Sigma1R in Control and ALS data sets were not normally distributed as tested using D'Agostino & Pearson normality test, $p < 0.05$ and were therefore analysed by the non-parametric Mann-Whitney test. Error bars are s.e.m.

3.2.3 VAPB-PTPIP51 interactions are reduced in ALS donor tissue

Having confirmed that there is a loss of VAPB, but not general ER proteins, and an increase in some mitochondrial proteins (but not PTPIP51) in human ALS donor tissue, the next aim in this study was to determine if the tethering between VAPB and PTPIP51, which mediates ER-mitochondrial signalling, is disrupted in ALS donor tissue. Previous studies have shown a reduction in the binding between VAPB and PTPIP51 in cell and animal models of ALS (Stoica et al., 2014; Stoica et al., 2016), and so it was hypothesised that this tethering interaction would be reduced in ALS spinal cord motor neurons relative to controls. In order to investigate this, PLAs, as previously described (Stoica et al., 2016), were used to measure VAPB-PTPIP51 interactions in spinal cord sections from the same control and ALS cases used for immunoblotting.

In the first instance, immunohistochemistry was performed on spinal cord tissue with in-house VAPB and PTPIP51 antibodies as previously used on tissue sections (Stoica et al., 2016). Each antibody was used at concentrations of 1/200, 1/800 and 1/3200 to identify a suitable concentration for use in proximity ligation assays on tissue sections. The anti-VAPB antibody showed strong labelling at a concentration of 1/200, weak labelling at 1/800 and no labelling was apparent when used at 1/3200 (Figure 3.5A). The anti-PTPIP51 antibody showed strong immunolabelling when used at concentrations of 1/200 and 1/800 and weak labelling at 1/3200 (Figure 3.5B). Therefore, antibodies were used in PLA experiments at concentrations of 1/200 for VAPB and PTPIP51.

PLAs using the VAPB and PTPIP51 antibodies used in this study have previously been published (Stoica et al., 2014; Stoica et al., 2016). To confirm the specificity of the technique in human spinal cord tissue, control PLA experiments were carried out. This involved conditions in which neither or only a single primary antibody was applied, in order to detect any non-specific binding of either primary antibody to other proteins in the tissue, and to test the specificity of the PLA signals. Sections were therefore incubated with all reagents required for successful PLA and either both primary antibodies, neither primary antibody, VAPB primary antibody only, or PTPIP51 antibody only (Figure 3.6). PLA signal (red dots) was only detected in the condition in which both antibodies were applied, confirming that the signal is specific and is able to identify regions of VAPB and PTPIP51 interactions.

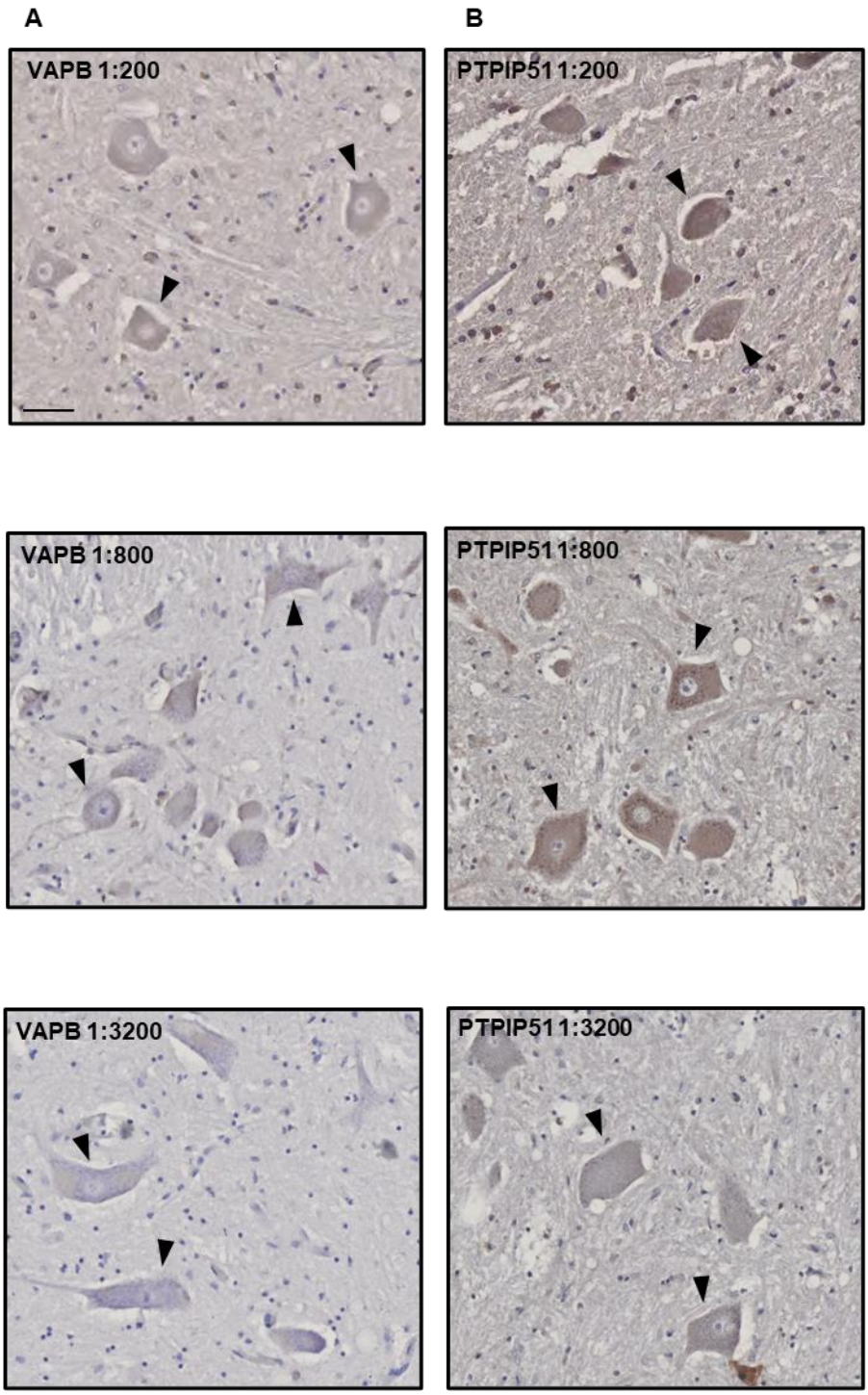

Figure 3.5: Determining optimum antibody concentrations for immunolabelling in spinal cord. VAPB (A) and PTPIP51 (B) antibodies were used to immunolabel human spinal cord tissue sections at concentrations of 1:200, 1:800 and 1:3200. Examples of motor neurons are indicated by arrows. N=1 experiment, scale bar=50 μm.

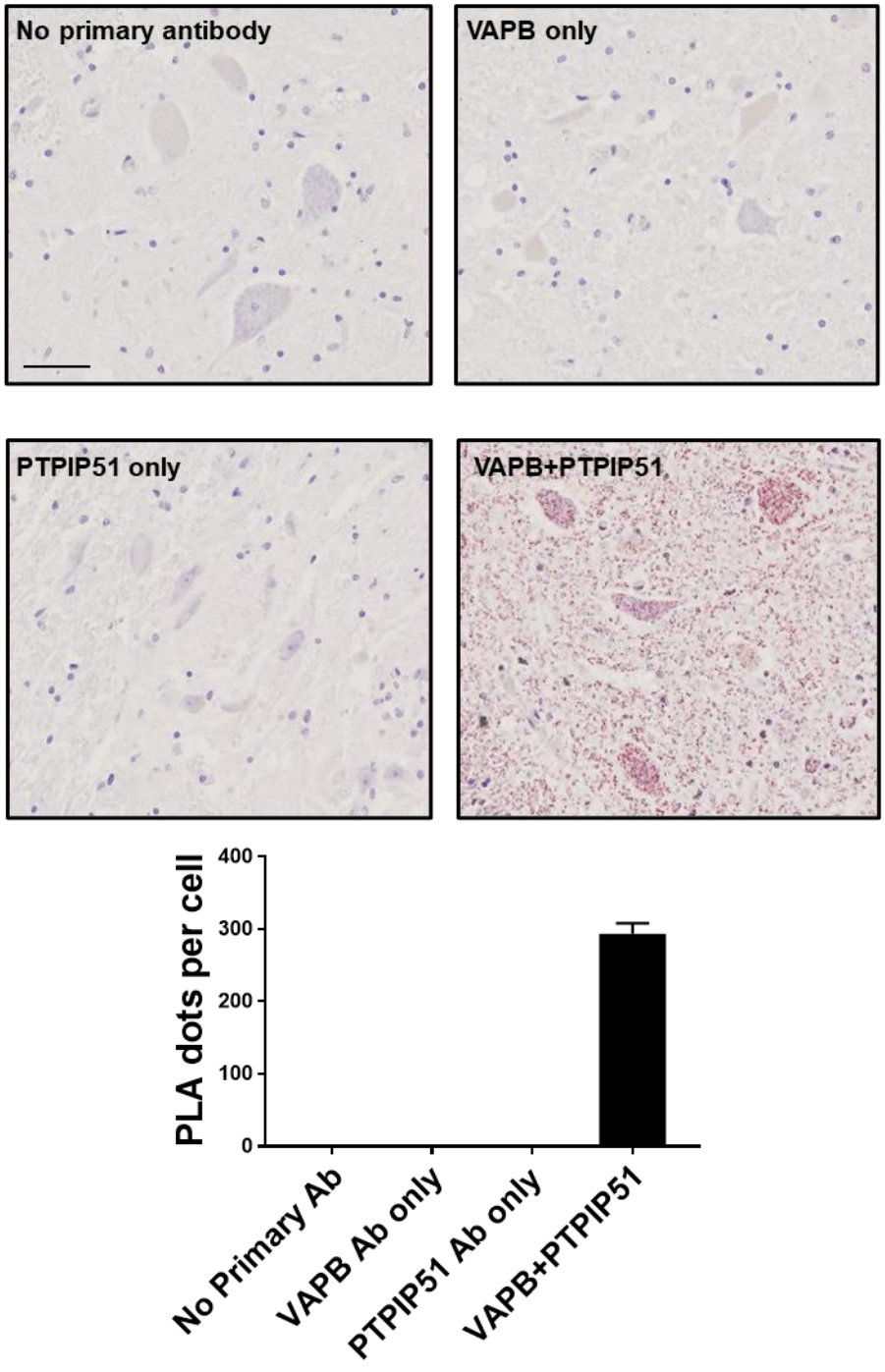

Figure 3.6: Control experiments demonstrating the specificity of VAPB-PTPIP51 PLAs in post-mortem spinal cord sections. Controls involved omission of VAPB (PTPIP51 only), PTPIP51 (VAPB only), or both VAPB and PTPIP51 primary antibodies (no primary Ab). Graph shows PLA signals per motor neuron in the different conditions. N=1 experiment, 20-96 cells per antibody condition, error bars are s.e.m. Scale bar=50 μm.

Having established the optimum concentration of VAPB and PTPIP51 antibodies for use in PLAs on spinal cord sections, and demonstrated that the PLA signals are specific, VAPB-PTPIP51 PLAs were then carried out on spinal cord sections from the 17 ALS and 17 control cases used above for immunoblotting. Sections were also stained with haematoxylin to detect nuclei. One control and one ALS section showed no PLA signal, and one ALS tissue section did not display discernible motor neurons, so quantification of PLA signals was conducted on the remaining 16 control and 15 ALS sections. Motor neurons were identified in the ventral horn on the basis of their size and morphology as in other studies (Arai et al., 2006; Vance et al., 2009) and the number of PLA dots per motor neuron was counted. Plasticity in the size of motor neurons has previously been reported, with an increase in soma size in affected regions of ALS mice in early disease, and a decrease in soma size at end stage disease, compared to that of healthy control mice (Dukkipati et al., 2018). However, no difference in size was found between the soma of healthy and ALS motor neurons in humans, likely given that the size of a motor neuron soma can vary greatly (Toft et al., 2005). To account for possible variations in soma size, the number of PLA signals in each motor neuron soma was normalised to its size. The number of PLA dots per cell area was significantly reduced in motor neurons of ALS spinal cord compared to those in the motor neurons of control sections (Control 100 % +/- 4.7; ALS 83 % +/- 6.4. Raw data are PLA dots per cell: Control 240 +/- 24; ALS 174 +/- 15) (Figure 3.7) as determined by a two-tailed t-test ($p = 0.026$). These data indicate that the number of VAPB-PTPIP51 interactions is reduced in ALS spinal cord, and therefore that ER-mitochondria communication is disrupted in ALS.

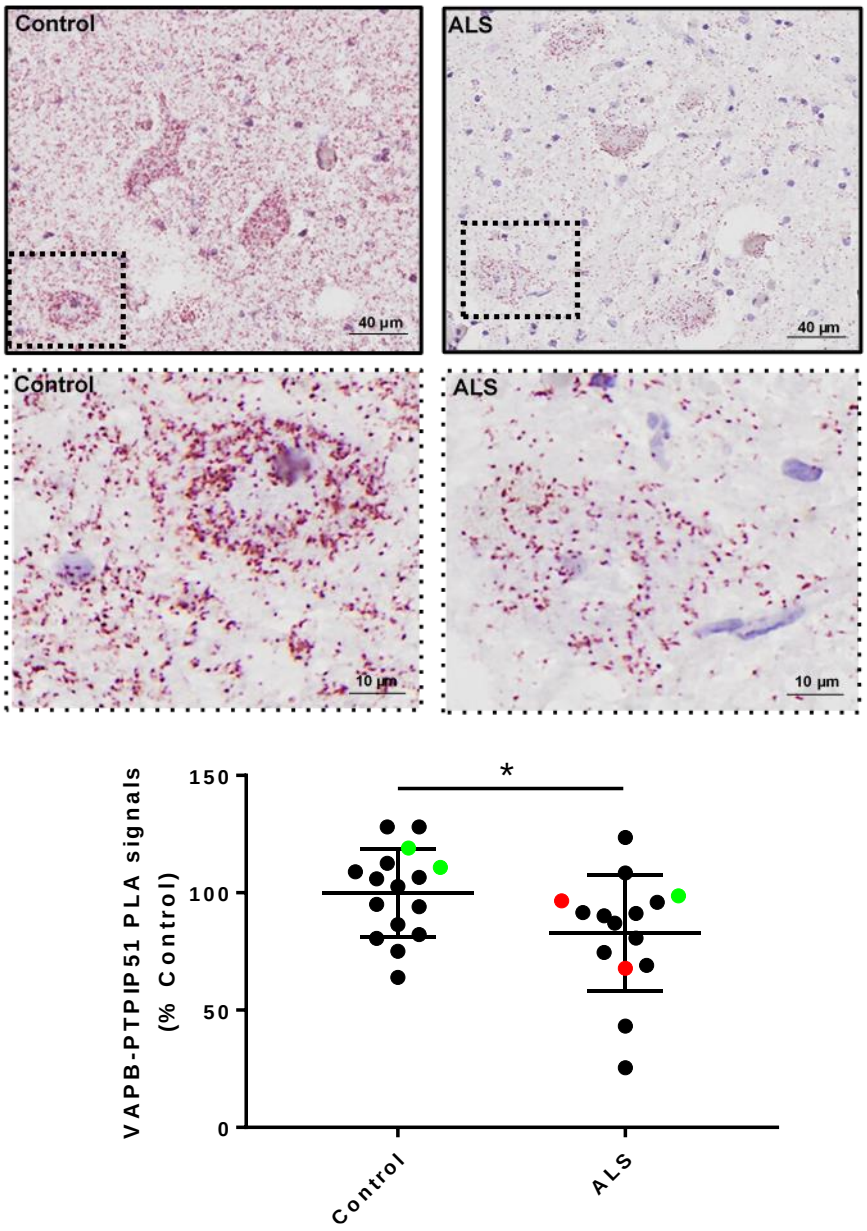

Figure 3.7: VAPB-PTPIP51 interactions are reduced in ALS spinal cord motor neurons. Representative images of VAPB-PTPIP51 PLAs in motor neurons of control and ALS donor spinal cord sections are shown. Top panel shows low magnification and bottom panel shows higher magnification insets of the areas indicated by dotted lines. VAPB-PTPIP51 signal numbers were normalised to the size of each cell to correct for any shrinkage of neurons in the ALS cases. Data was then normalised to controls. Graph shows mean number of VAPB-PTPIP51 PLA signals per area of motor neuron for each case as a percentage of the mean for control cases. Thoracic spinal cord samples are indicated in green and C9ORF72 cases are indicated in red. There was an average of 240 signals per cell in controls and 174 signals per cell in ALS tissue. n = 16 control, n = 15 ALS: 20 – 208 motor neurons per case. The number of PLA signals were normally distributed as tested using D'Agostino & Pearson normality test, $p > 0.05$ and were therefore analysed by unpaired two-tailed t-test, error bars are s.e.m., *p=0.037. Scale bars; 40 µm (top panel) and 10 µm (bottom panel).

3.2.4 VAPB level does not correlate with VAPB-PTPIP51 interactions

Given that VAPB protein is reduced in ALS spinal cord tissue, it is possible that the reduction of VAPB-PTPIP51 interactions seen in ALS donor tissue is caused by lower VAPB protein amounts in the same tissue. In order to investigate this hypothesis, the level of VAPB protein was correlated with VAPB-PTPIP51 PLA signal in sections from the same case (Figure 3.8). If the interaction between VAPB and PTPIP51 were altered based on changes in VAPB protein amount alone, a strong positive correlation would be expected. However, there was no significant correlation between protein levels of VAPB and PLA signal number ($r = -0.106$, $p=0.58$) (Figure 3.8A). Similarly, there was no correlation between VAPB amounts and VAPB-PTPIP51 PLA signals when ALS or control groups were examined alone (ALS $r = 0.045$, $p=0.11$; control $r = -0.444$, $p=0.87$) (Figure 3.8A where black dots represent control and red dots ALS cases). This suggests that changes in VAPB protein amounts alone are not sufficient to cause the reduction in VAPB-PTPIP51 interactions identified in ALS spinal cord.

As there were significant differences in age and post-mortem delay between the post-mortem ALS and control spinal cord tissue samples used in this study, these factors were also investigated in relation to VAPB protein amounts and VAPB-PTPIP51 PLAs. As mentioned above, should either age or PMD affect levels of VAPB protein or VAPB-PTPIP51 interactions, a correlation with levels of VAPB or PLA signal would be expected. In fact, neither age nor PMD delay correlated with levels of VAPB protein or PLA signal and this remained the case whether groups were considered individually or as a whole (Figure 3.8B-E where black dots represent control and red dots represent ALS cases, summarised in Table 3.2). These results suggest that regardless of age or PMD, the amount of VAPB protein is reduced in ALS donor spinal cord and that, independently of the levels of VAPB, the interaction between VAPB and PTPIP51 is disrupted in ALS donor spinal cords. Taken together these data are strongly indicative that ER-mitochondria interactions are disrupted in human ALS.

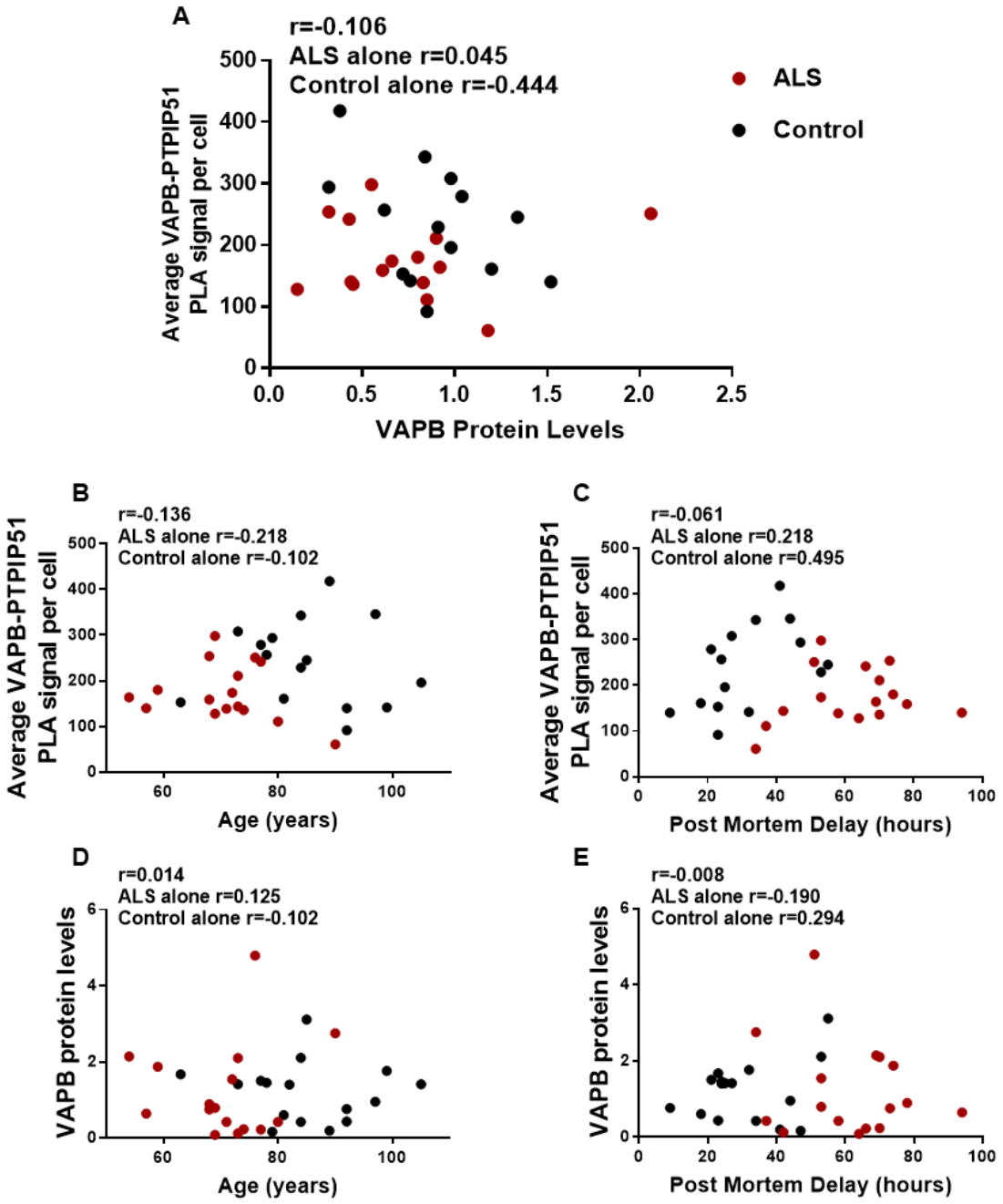

Figure 3.8: VAPB protein levels, age and PMD do not correlate with PLA signal. A) VAPB protein levels normalised to NSE for each individual were plotted against the mean number of VAPB-PTPIP51 PLA signals per cell for each individual. The mean number of VAPB-PTPIP51 PLA signals per cell were plotted against B) Age and C) PMD. VAPB protein levels normalised to NSE were also plotted against D) Age and E) PMD. Data was analysed by Pearson's correlation. R values, calculated for control and ALS subgroups, and for all cases are shown. $P > 0.05$ for all r values.

Table 3.2: Correlation coefficients for donor post-mortem spinal cord tissues

	VAPB level Age	VAPB level PMD	PLA Signal Age	PLA Signal PMD	VAPB level PLA Signal
Control	-0.102	0.294	-0.102	0.495	-0.444
ALS	0.125	-0.190	-0.218	0.218	0.045
All cases	0.014	-0.008	-0.316	-0.061	-0.106

p>0.05 for all correlations

3.2.5 VAPB-PTPIP51 interactions are reduced in iPSC-MNs from ALS donors harbouring mutations in TDP-43

Having confirmed that VAPB-PTPIP51 interactions are reduced in post-mortem ALS spinal cord compared to control tissues, this work next aimed to investigate the VAPB-PTPIP51 interaction in a second model with direct relevance to human disease. Therefore, VAPB-PTPIP51 interactions were studied in iPSC-MNs derived from two ALS patients harbouring either the M337V or G298S ALS-causative mutation in TDP-43, and two unrelated control donors.

Firstly, the specificity of the PLA method in control iPSC-MNs was investigated (Figure 3.9). ChAT is a marker for motor neurons (Maury et al., 2015; Oda, 1999) and so cultured cells were counter stained for ChAT (green) to confirm differentiation of iPSCs into motor neurons. ChAT staining was strong and diffuse in cell soma, with some small puncta, as seen in Figures 3.9 – 3.11. As expected, ChAT also clearly stained cell processes, thought this staining was less strong than in the cell soma. The percentage of ChAT stained cells was not quantified in these experiments but was deemed to be similar to previous experiments by our collaborator, Jenny Greig who reported 65 – 80 % ChAT staining (Jenny Greig e-thesis). Controls were carried out as before, including neither primary antibody, VAPB primary antibody only, PTPIP51 antibody only or both primary antibodies (Figure 3.9). No PLA signal (red dots) was detected when no primary antibodies were applied (not shown) or when only a single antibody was used. PLA signal was only detected in the condition in which both antibodies were applied, showing that the signal is specific to points of interaction between the VAPB and PTPIP51 proteins in iPSC-MNs. Coverslips showing populations of cells with very large soma, indicating glia cell populations, were excluded since it was considered that this might affect VAPB-PTPIP51 binding and introduce a variable other than patient versus control cells. These populations showed PLA signal and would be interesting in future investigation.

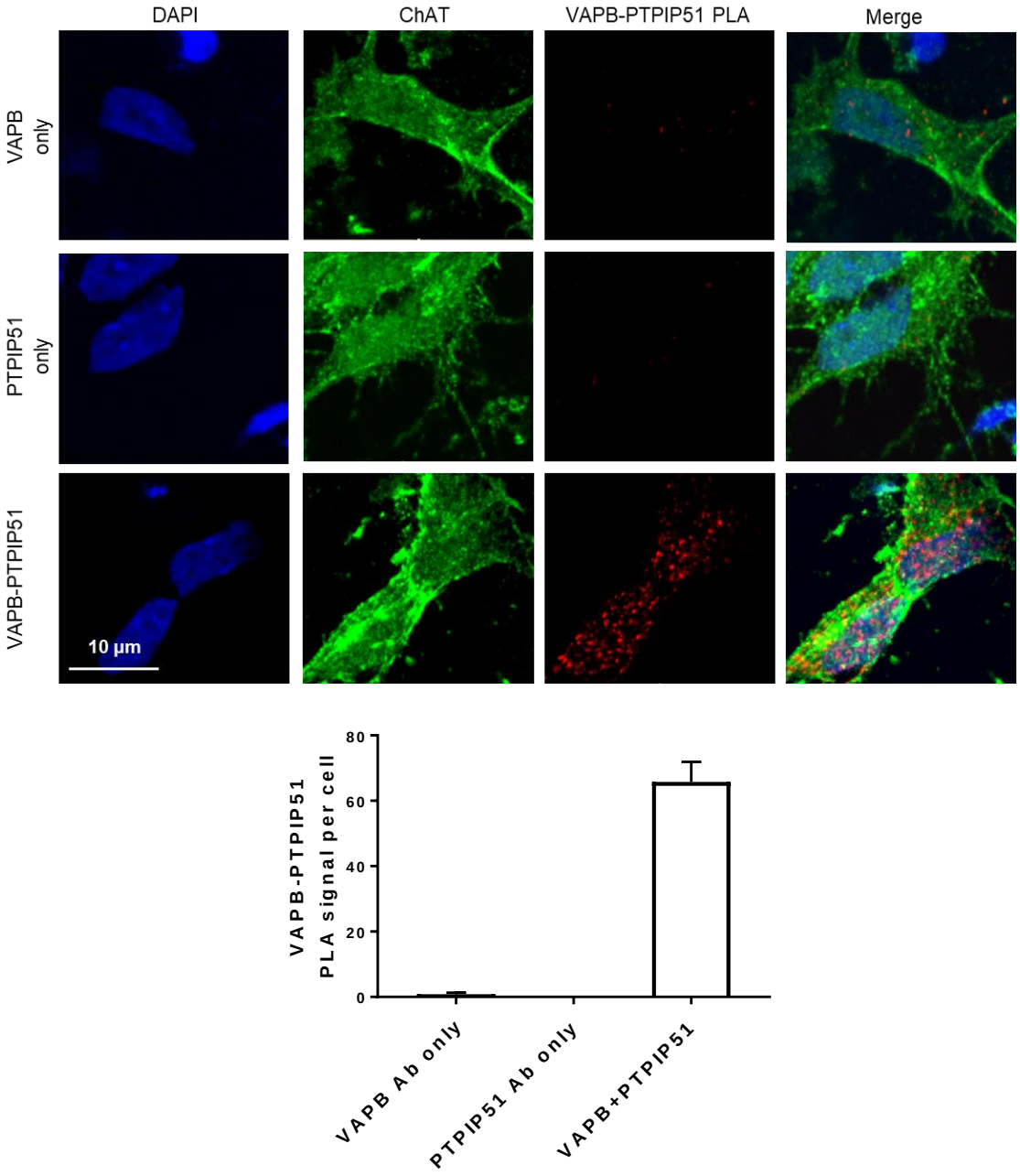

Figure 3.9: Control experiments demonstrating the specificity of VAPB-PTPIP51 PLAs in iPSC-MNs. Controls involved omission of VAPB (PTPIP51 only), PTPIP51 (VAPB only), or both VAPB and PTPIP51 primary antibodies (not shown). Cells were immunolabelled with an antibody against choline acetyl transferase (ChAT) to identify cells that had differentiated into motor neurons. Panels show DAPI (blue), ChAT (green), PLA (red) and Merge from left to right, respectively. Graph shows VAPB-PTPIP51 PLA signals per iPSC-MN in the different conditions. N=1 experiment, 20-96 cells per condition, error bars are s.e.m. Scale bar, 10 µm.

To determine whether the VAPB–PTPIP51 interaction is disrupted in ALS patient material, proximity ligation assays were used to examine the VAPB-PTPIP51 interaction in iPSC-MNs from ALS patients with either M337V or G298S point mutations in TDP-43, and unrelated controls without ALS.

Firstly, iPSC-MNs from an ALS patient donor harbouring an M337V mutation in TDP-43 were investigated in comparison to iPSC-MNs from an unrelated healthy donor. VAPB-PTPIP51 PLA was carried out as above and PLA signals were quantified specifically in motor neurons that display ChAT immunolabelling. PLA signals were quantified per motor neuron and normalised to the surface area of the motor neuron soma to account for any differences in cell size. PLA signals per area of motor neuron were found to be significantly reduced in ALS patient iPSC-MNs as compared to control iPSC-MNs ($p<0.0001$) (Figure 3.10). PLA signal in iPSC-MNs from TDP-43-M337V ALS donors was on average 49 % lower than PLA signal in iPSC-MNs from control donors (Figure 3.10).

Next, iPSC-MNs from an ALS patient donor harbouring a G298S mutation in TDP-43 were investigated compared to iPSC-MNs from another unrelated control donor. VAPB-PTPIP51 PLA and quantification was carried out as described above. PLA signals were found to be significantly reduced in TDP-43-G298S iPSC-MNs ALS in comparison to those in control iPSC-MNs ($p=0.0011$) (Figure 3.11). PLA signal in iPSC-MNs from TDP-43-G298S ALS donors was on average 40 % lower than PLA signal in iPSC-MNs from control donors (Figure 3.11). Taken together these data indicate a disruption of VAPB-PTPIP51 binding in ALS patient material, further indicating that ER-mitochondria interactions are lost in ALS.

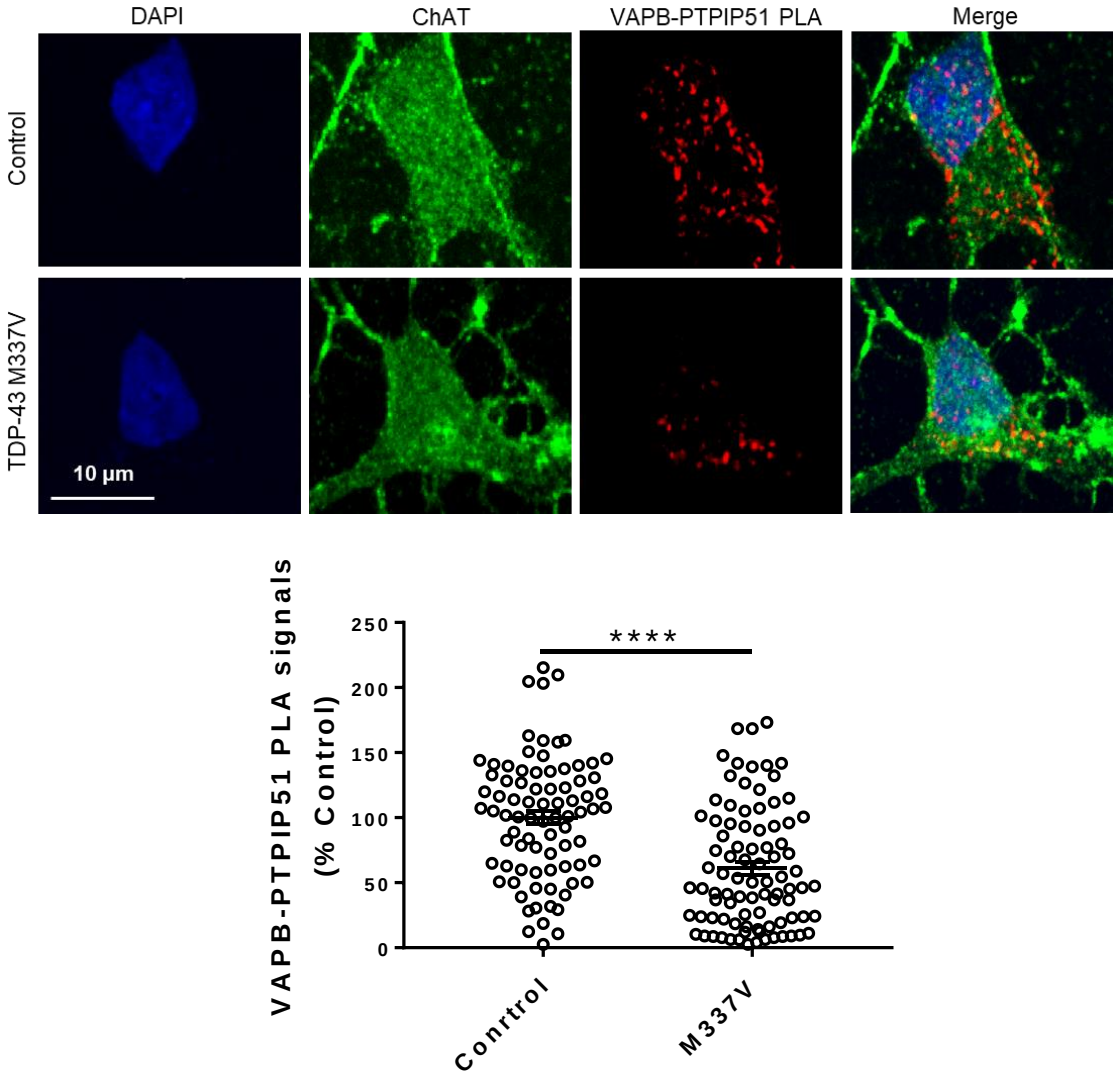

Figure 3.10: The VAPB-PTPIP51 interaction is reduced in iPSC-MNs derived from ALS patients harbouring the TDP-43 M337V mutation. Representative images of VAPB-PTPIP51 PLAs in iPSC-MNs derived from a control donor and an ALS patient harbouring a TDP-43 M337V mutation are shown. Cells were also immunolabelled using an antibody against choline acetyl transferase (ChAT) to identify motor neurons. Panels show DAPI (blue), ChAT (green), PLA (red) and Merge from left to right, respectively. Graph shows mean number of VAPB-PTPIP51 PLA signals per area of motor neuron as a percentage of control. The number of neurons analysed were N=3 biological replicates, including 13 – 53 cells from each experiment. PLA signals in ALS samples were not normally distributed as tested using D'Agostino & Pearson normality test, $p < 0.05$ and data was therefore analysed by the non-parametric Mann-Whitney test, error bars are s.e.m., ****p<0.0001. Scale bar, 10 µm.

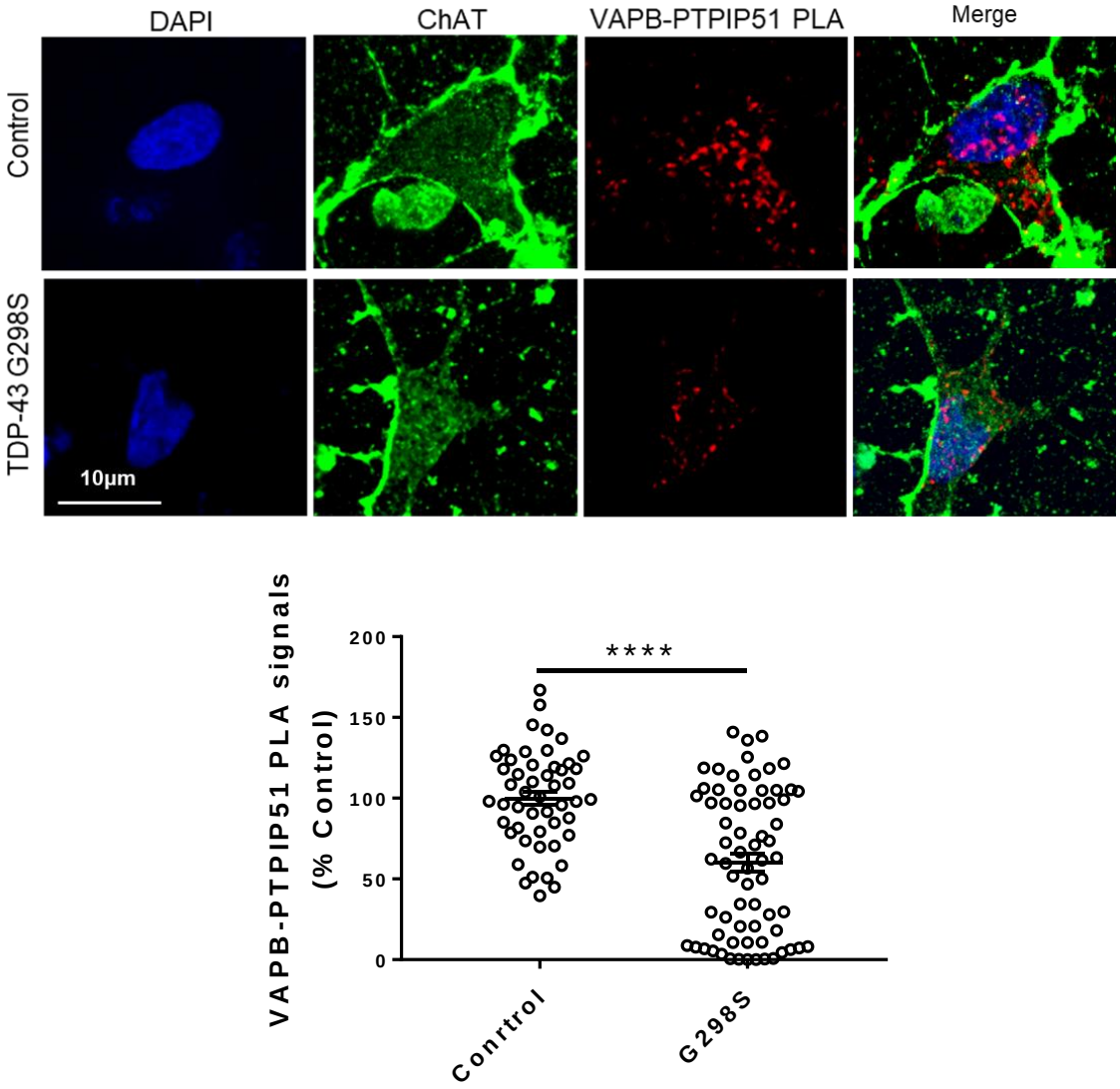

Figure 3.11: The VAPB-PTPIP51 interaction is reduced in iPSC-MNs derived from ALS patients harbouring the TDP-43 G298S mutation. Representative images of VAPB-PTPIP51 PLAs in iPSC-MNs derived from control donors and ALS patients harbouring a TDP-43 G298S mutation are shown. Cells were counter-stained for choline acetyl transferase (ChAT) to identify motor neurons. Panels show DAPI (blue), ChAT (green), PLA (red) and Merge from left to right, respectively. Graph shows mean number of VAPB-PTPIP51 PLA signals per area of motor neuron as a percentage of control. The numbers of neurons analysed were N= 3 biological replicates, 10 – 32 cells from each experiment. PLA signals in ALS samples were not normally distributed as tested using D'Agostino & Pearson normality test, $p < 0.05$ and data was therefore analysed by the non-parametric Mann-Whitney test, error bars are s.e.m., ****$p<0.0001$. Scale bar, 10 µm.

3.3 Discussion

3.3.1 Summary of results

In line with the hypothesis of this chapter, this work has found that the interaction between VAPB and PTPIP51 is reduced in motor neurons in human ALS spinal cord tissues and iPSC-MNs compared to controls. VAPB protein amounts are reduced in ALS spinal cord but did not correlate with disrupted VAPB-PTPIP51 interactions in these samples. The amount of the ER marker PDI was unchanged from controls indicating that the change in VAPB is not solely a result of ER loss. No change in the protein amount of PTPIP51 was detected between ALS and control spinal cord tissue, but levels of the mitochondrial marker TOM20 were increased in ALS tissue. There was no change in the levels of other ER-mitochondria associated proteins, namely IP3R, VDAC or Sigma1R in ALS donor tissue compared to controls. These results strongly indicate that the reduced interactions between VAPB-PTPIP51 observed in these samples is specific and indicates disrupted ER-mitochondria interactions in ALS.

3.3.2 ER protein levels in post-mortem ALS spinal cord

The finding in this work that VAPB protein levels are reduced in the spinal cord of ALS donors complements previously published data (Anagnostou et al., 2010). This finding also fits with reports that expression of the P56S ALS-causing mutation in VAPB reduces VAPB protein levels and loss of VAPB function (Kanekura et al., 2006; Mitne-Neto et al., 2011), suggesting that reduced VAPB functionality is involved in ALS pathogenesis. Interestingly, in contrast to the findings in spinal cord, VAPB protein levels are reported to accumulate in denervated muscle tissue of ALS donors (Jesse et al., 2017). Taken together, these observations highlight cell-type differences in ALS and could indicate that gene therapy to upregulate VAPB in brain may not be a feasible strategy in ALS, unless we develop a better understanding of the causes of ALS up- and down-regulation in specific tissues.

In the work presented here, the levels of other ER resident proteins, PDI and IP3R, were similar in control and ALS spinal cord tissues. This suggests that the change seen in VAPB protein is not due to a reduction in the overall amount of ER in ALS spinal cord. It has previously been reported that the amount of PDI, which is considered a marker of ER stress, is increased in ALS (Atkin et al., 2008; Ilieva et al., 2007). These published studies investigated only 5 – 8 individuals including some earlier onset ALS cases which may explain the differences between these studies and the work presented here. The average age of ALS donors in the previous reports was 59 and 63 years respectively, compared to an average age of 72 years in this study. Interestingly, Anagnostou et al. (2010) found that VAPB protein amounts are only significantly lower in ALS cases that

show rapid progession from diagnosis to death (1-3 years) and not in patients surviving 4 – 20 years with ALS. These observations raise questions about the possibility that there are differing mechanisms in disease depending on age at disease onset, and the speed of progression. It would be interesting therefore to consider differences in VAPB, PDI, and other ER-stress markers in early- and late-onset ALS in which rate of disease progression is known, and also to compare sporadic and familial ALS cases.

3.3.3 Mitochondrial protein levels in post-mortem ALS spinal cord

TOM20 is a constituent member of a complex found in the outer membrane of mitochondria that is responsible for importing mitochondrial proteins from cytosol into the intermembrane space of mitochondria (Mori and Terada, 1998). It is used in this study as a mitochondrial marker and its protein levels were found to be increased in ALS spinal cord. It may be speculated that elevated TOM20 amounts indicates increased numbers of mitochondria or increased production of mitochondrial proteins. However, the levels of other mitochondrial proteins, PTPIP51 and VDAC, were found to be unchanged between control and ALS donors which argues against this conclusion. Therefore, the observed increase in TOM20 expression in ALS tissue is surprising, especially since mitochondrial dysfunction is heavily implicated in ALS (Jiang et al., 2015).

A study of mitochondria in spinal cord from two ALS cases with SOD1 mutations also reported an increase in the amounts of TOM20, as well as an increase in the amounts of other mitochondrial import proteins (Li et al., 2010). A hypothesis to explain these observations, consistent with reports that mitochondria are defective in ALS, would be that enhanced expression of mitochondrial proteins represents a compensatory mechanism for dysfunctional mitochondria. This is supported by the finding of Li et al. (2010) in SOD1 transgenic mice, who showed that despite increased levels of TOM proteins generally, the import activity of mitochondria in the ALS model is reduced, suggesting dysfunction of the TOM complex. The hypothesis could be investigated by measuring import activity and mitochondrial protein amounts at various time points during ALS progression: if decreased import activity occurred first, it may indicate that increased protein expression is a compensatory response. Measuring whether or not experimental impairment of TOM20 activity, for example by genetic editing, results in increased mitochondrial protein levels would serve to show whether impaired TOM20 activity alone is sufficient to drive an increase in protein levels. Although PTPIP51 and VDAC protein levels were not found to be higher in ALS than control tissues in this study, Li et al. (2010) also found increases in the amount of other mitochondrial proteins such as respiratory complex I proteins, despite decreased complex I activity (Li et al., 2010).

There are also reports that mitophagy, the process by which mitochondria are degraded and recycled, is disrupted in ALS (Davis et al., 2018; Hong et al., 2012) and this is in-keeping with findings of ALS-causing mutations in genes involved in autophagy such as TBK-1 and OPTN (Oakes et al., 2017). Dysfunctional mitophagy leads to aberrant accumulation of mitochondria (Evans and Holzbaur, 2019) and therefore mitophagy could also be investigated as a potential cause of increased TOM20 protein levels in ALS.

3.3.4 Sigma1R protein levels in post-mortem ALS spinal cord

This study also investigated the levels of proteins involved in calcium signalling between the ER and mitochondria. IP3R and VDAC interact at MAM to facilitate efficient exchange of calcium (Csordas et al., 2006; Rowland and Voeltz, 2012) and the Sigma 1R mediates the clustering of IP3Rs at MAM to generate localised high calcium concentrations (Hayashi and Su, 2007; Ryskamp et al., 2019). IP3R3, VDAC and Sigma1R protein levels in spinal cord were found to be unchanged between ALS and control tissues in this study. IP3R3 was investigated in this study due to its relative abundance in the spinal cord compared to the other well studied isoform, IP3R1. More recently however, isoform 2 has been reported as the most efficient coupler for ER-mitochondria calcium transfer, although all three isoforms carry out this role (Bartok et al., 2019). It would therefore be worthwhile to investigate the protein levels of IP3R2, and its interaction with VDAC, in ALS spinal cord.

ALS-causing mutations have been found in Sigma1R (Al-Saif et al., 2011; Luty et al., 2010) but since these mutations are thought to be loss of function mutations (Bernard-Marissal et al., 2015; Dreser et al., 2017; Gregianin et al., 2016), altered Sigma1R protein amounts are not necessarily expected. It has been reported that Sigma1R protein levels are increased in denervated muscle tissue of ALS donors (Jesse et al., 2017), as discussed previously for VAPB. Increased VAPB levels in denervated muscle tissue (Jesse et al., 2017) and decreased VAPB levels in spinal cord in ALS (Anagnostou et al., 2010) further indicates that there may be cell/tissue specific alterations in MAM proteins in ALS that are worthy of further investigation.

3.3.5 Reduced VAPB-PTPIP51 interactions in post-mortem ALS spinal cord

The finding in this chapter that VAPB-PTPIP51 interactions are reduced in human ALS spinal cord and iPSC-MNs provides valuable validation of previous studies showing reduced interactions between these proteins in animal and cell models of ALS (Stoica et al., 2014; Stoica et al., 2016). Previous studies have shown that reducing VAPB-PTPIP51 interactions, by genetically ablating VAPB or PTPIP51 expression, reduces

ER-mitochondrial membrane contacts and subsequently ER-mitochondrial signalling (De Vos et al., 2012). The data therefore leads to the conclusion that ER-mitochondrial signalling is disrupted in ALS. To further confirm this conclusion, post-mortem tissue may be used in EM studies to measure ER and mitochondrial membrane contacts directly. The methods employed in this chapter could be used to investigate the interaction of IP3R and VDAC, which are responsible for the transfer of calcium at ER-mitochondria contact sites (Szabadkai et al., 2006), in ALS tissues. This could provide further confirmation that there is disruption of ER-mitochondrial signalling in ALS.

It may be considered that reduced VAPB protein amounts explain the reduction in VAPB-PTPIP51 interactions observed in ALS spinal cord. However, VAPB protein amounts did not correlate with number of VAPB-PTPIP51 PLA signals in the same samples. This suggests that levels of VAPB does not account entirely for the reduced VAPB-PTPIP51 binding in ALS cells, and that another, as yet unknown, mechanism contributes to this reduced interaction. This is supported by findings in animal models in which VAPB-PTPIP51 binding is decreased in ALS without any corresponding changes in VAPB protein (Stoica et al., 2014; Stoica et al., 2016). It may be hypothesised therefore that there is a change in the affinity of VAPB to PTPIP51 in ALS motor neurons. Previous studies have shown that TDP-43 and FUS reduce VAPB-PTPIP51 interaction via activation of the kinase GSK-3β (Stoica et al., 2014; Stoica et al., 2016). GSK-3β phosphorylates a wide range of proteins in the cell and as such it is possible that VAPB or PTPIP51 is a target, either directly or indirectly, of GSK-3β. Phosphorylation can act as a modulator of protein interactions and therefore it can be hypothesised that phosphorylation of either VAPB or PTPIP51 disrupts their interaction and therefore ER-mitochondria contacts. This potential mechanism is investigated in the next chapter of this study.

The majority of ALS cases investigated here were sporadic and had no identified ALS-causing mutations. Two ALS cases had repeat expansions in C9ORF72. The amount of VAPB and PTPIP51 proteins and extent of VAPB-PTPIP51 interactions in these cases were not apparently different compared to the other ALS cases examined. Therefore, there was not sufficient justification to remove them from our data set. The ALS donors were significantly younger at death than non-disease controls, but samples from these cases were exposed to significantly longer post-mortem delays than control donors. These variables were correlated with VAPB protein amounts and PLA signal to gauge the extent that such variables might contribute to the results. No correlation was identified between either age or post-mortem delay with VAPB amounts or VAPB-PTPIP51 PLA signals. This does not completely rule out potential effects of age and post-mortem delay

on our investigations but does indicate that factors besides these two variables are involved in the differences in ER-mitochondria interactions observed between ALS and control donor tissues.

Finally, post-mortem ALS tissues are generally collected at the very end stages of disease, with varying levels of post-mortem delay, which can cause variability in protein degradation and tissue integrity. Therefore, post-mortem tissues do not necessarily represent only tissue changes caused by disease. However, major pathological findings in post-mortem tissue have paved the way for the discovery of mutations which cause ALS. For tissues such as the CNS, post-mortem analyses remain one of the most accessible ways of measuring disease related changes in an inaccessible tissue.

3.3.6 Reduced VAPB-PTPIP51 interactions in ALS patient-derived iPSC-MNs

Measurement of PLA signal in iPSC-MNs allowed investigation of ALS in a human tissue model that is not subject to post-mortem stress and using cells from patients harbouring mutations in TDP-43 that cause familial forms of ALS. VAPB-PTPIP51 interactions were found to be reduced in iPSC-MNs derived from patients with two different TDP-43 mutations (M337V and G298S), providing further support for the idea that disruption of VAPB-PTPIP51 binding reduces ER-mitochondria interactions in ALS.

At 21 days of iPSC-MN differentiation, our collaborator on this work (Dr. Greig) reports increased TDP-43 levels in both M337V and G298S iPSC-MNs, and that formation of TDP-43 aggregates is found only in M337V cells at this timepoint (unpublished data, Jenny Greig e-thesis). Therefore, reduced VAPB-PTPIP51 interactions do not appear to be related to the emergence of TDP-43 aggregates since PLA signals were similarly reduced in both iPSC-MN lines. This might suggest that disrupted ER-mitochondria interactions occur early in disease development. End stage disease in humans shows reduced VAPB protein levels as well as reduced ER-mitochondria interactions, however, mouse studies find reduced ER-mitochondria but unaltered VAPB or PTPIP51 protein levels. This supports, but does not confirm, a hypothesis that ER-mitochondria contact is an early pathological disease mechanism. This hypothesis could be investigated effectively by studying transgenic mouse models of ALS at various time points before and after symptom onset. Parallel studies of iPSC-MNs differentiated for different lengths of time would also go some way to ascertaining the stage at which ER-mitochondria contacts are disrupted.

Some criticisms have been made over the use of iPSC-derived cells, particularly in age-related neurodegenerative diseases. For example, epigenetic profiles are usually

disrupted during the de-differentiation process and since epigenetic marks confer many age-related properties of cells (Guo et al., 2017), this is an issue when studying neurodegenerative diseases for which age is a risk factor. As for all cell culture studies, the surrounding environment of the cells does not recapitulate that of human brain, lacking other neural cell types and the many extracellular factors that can affect cell responses. In addition, this study compares just two patient iPSC lines as a result of availability, and so individual (within group) differences impact results very strongly and make comparisons with controls difficult. Isogenic control lines in which the ALS-causing mutation, in this case M337V or G298S in TDP-43, is edited to the wild-type sequence, would overcome some of these issues by enabling the comparison of cells from the same donor. Editing is carried out after de-differentiation to iPSCs, such that changes in epigenetic profiles during the de-differentiation process, although still disrupted, are consistent between cell lines (Ghaffari et al., 2018). Most importantly, isogenic cell lines eliminate individual genetic differences between control and mutant cells, besides the ALS-causing mutation (Guo et al., 2017). Moreover, motor neurons derived from patient iPSCs also enable the study of disease development and progression, unlike post-mortem tissues.

To further strengthen findings from human ALS tissues described here, VAPB-PTPIP51 interactions could be studied in human material from more common familial forms of ALS, including those with disease-causing mutations in SOD1 and C9ORF72. Nevertheless, finding the same results in human tissues with sporadic and familial forms of ALS strongly supports the premise that disrupted ER-mitochondria contacts are a pathological feature of ALS. This is supported by the notion that ER-mitochondrial signalling mediates a number of common mechanisms disrupted in ALS and neurodegenerative disease more widely (Paillusson et al., 2016). In addition, our group have found reduced VAPB-PTPIP51 interactions in early Braak stage post-mortem AD brain (Lau et al., manuscript in submission) supporting the hypothesis that defective ER-mitochondrial interactions occur early in different types of neurodegenerative diseases. Together these results suggest ER-mitochondria contacts should be considered as a potential therapeutic target for ALS.

Chapter 4: Identification of phosphorylation sites in VAPB and PTPIP51

4.1 Introduction

4.1.1. ER-mitochondrial signalling is disrupted by TDP-43 and FUS by GSK-3β activation

The work in Chapter 3 showed that ER-mitochondria tethering by VAPB-PTPIP51 binding is reduced in the motor neurons of human ALS patients. This work confirms previous studies suggesting that the VAPB-PTPIP51 interaction is a potential therapeutic target for the treatment of ALS.

As discussed in detail in Chapter 1, VAPB-PTPIP51 binding is disrupted by ALS-related proteins TDP-43 and FUS. This disruption is mediated by activation of GSK-3β (Stoica et al., 2016; Stoica et al., 2014). Two small molecule inhibitors of GSK-3β, CHIR99021 and AR-A014418, were used to study its role in ER-mitochondrial signalling and found that GSK-3β inhibition increases VAPB-PTPIP51 binding and rescues the effect of WT and ALS-mutant FUS on ER-mitochondria tethering and calcium signalling (Stoica et al., 2016). This indicates a potential role for GSK-3β kinase activity in the disruption of ER-mitochondria contact functions and in turn in the pathogenesis of ALS. However, the mechanism by which GSK-3β affects the binding of VAPB and PTPIP51 is yet to be established.

4.1.2 GSK-3β is a serine/threonine kinase implicated in neurodegenerative disease

GSK-3β is a serine/threonine kinase which phosphorylates a large number of substrates in the cell (Kaidanovich-Beilin and Woodgett, 2011). Phosphorylation is one of the primary post translational modifications known to alter protein-protein interactions within the cell. Phosphorylation also occurs dynamically, meaning that it can modulate interactions reversibly, as would be necessary in the case of regulating ER-mitochondria contacts which respond to dynamic cellular processes. The work in this chapter therefore hypothesises that GSK-3β disrupts VAPB-PTPIP51 binding by phosphorylating VAPB and/or PTPIP51.

There are two isoforms of glycogen synthase kinase, GSK-3α and GSK-3β. Both isoforms are ubiquitous and highly expressed in the central nervous system. Both GSK-3 isoforms are involved in a wide range of cellular processes including differentiation, proliferation and apoptosis and they signal in a variety of pathways, including Notch and Wnt signalling (Kaidanovich-Beilin and Woodgett, 2011). GSK-3 is one of few proteins with high basal activity, regulated by inhibitory phosphorylation. For GSK-3β, phosphorylation at tyrosine residue 216 is thought to enhance activity whilst inhibitory phosphorylation occurs primarily at residue serine 9, but can also occur at threonine 43, serine 389 and threonine 390 (Kaidanovich-Beilin and Woodgett, 2011). This regulation

occurs via a number of diverse pathways, including mitogen-activated protein kinase (MAPK) and Akt, but is also reported to occur by autophosphorylation. Additionally, GSK-3β can be regulated by the formation of complexes, such as in the Wnt signalling pathway, or through localisation, although these are less fully understood. GSK-3β has numerous substrates in the cell. Mostly these substrates undergo priming phosphorylation prior to phosphorylation by GSK-3β, such that there is phosphorylation 4 or 5 residues C-terminal to the GSK-3β target site (Doble and Woodgett, 2003; Forde and Dale, 2007; Kaidanovich-Beilin and Woodgett, 2011; Luo, 2012; Wu and Pan, 2010).

GSK-3β is implicated in neurodegenerative diseases, for example in AD due to its activity as a tau kinase, and inhibition of the kinase has been found to be neuroprotective (Doble and Woodgett, 2003). In ALS, small molecule inhibitors of GSK-3β have been found to improve motor neuron survival and reduce symptoms in cell and animal models (Caldero et al., 2010; Feng et al., 2008; Fornai et al., 2008; Koh et al., 2007), though it should be noted that these results were not reproducible in female mice (Pizzasegola et al., 2009). Reduced activity of the GSK-3 inhibitor Akt (which phosphorylates GSK-3β on serine-9) has been reported in ALS patient tissue and prior to symptom onset in the SOD1 mutant mouse model of ALS. Overexpression of Akt in this model reduced motor neuron death (Dewil et al., 2007). Additionally, GSK-3 inhibitors were identified in a screen for kinase inhibitors which reduce the formation of TDP-43-positive stress granules (Moujalled et al., 2013). Despite efforts to inhibit GSK-3β in neurodegenerative disease treatment, trials have not yet been successful; perhaps due to the difficulty in targeting one isoform over another and the extent of pathways in which GSK-3β is a crucial component. Identifying a mechanism downstream of GSK-3β in ALS pathogenesis may therefore provide a drug target with greater selectivity.

4.1.3 AMP-activated Kinase is a master regulator of cellular energy metabolism

AMP-activated kinase (AMPK) has been shown to phosphorylate the ER protein VAPA, as identified in a study of cellular phospho-proteomic changes occurring during exercise (Hoffman et al., 2015). VAPA is a homologue of VAPB and unpublished work from our group shows that VAPA binds to PTPIP51. The protein sequences of VAPA and VAPB are highly conserved and the site phosphorylated by AMPK in VAPA, serine residue 164, is conserved in VAPB at serine residue 158 in humans and other species (Figure 4.1).

AMPK is a major metabolic regulator of the cell. It is activated in response to reduced energy levels and phosphorylates substrates to stimulate processes which increase the production of ATP (Carling, 2017; Hardie et al., 2012). AMPK is a complex of three subunits. The α-subunit contains the protein's catalytic kinase domain and is also the

site of activating phosphorylation, threonine residue 172. Thr172 is phosphorylated by Calcium/Calmodulin Dependent Protein Kinase Kinase 2 (CAMKK2), in response to high cellular calcium levels, activating AMPK. AMPK is also activated by low cellular energy levels, as indicated by high cellular levels of AMP as compared to that of ATP. The γ-subunit binds to AMP, ADP or ATP and therefore senses the AMP/ADP:ATP ratio as a measure of cellular energy. The β-subunit contains a glycogen binding domain which is thought to act as another energy sensing mechanism. The β-subunit also completes the AMPK complex by interacting with both α- and γ- subunits (Carling, 2017; Hardie et al., 2012).

AMPK has also been linked to ALS, though the significance of this link is yet to be established. AMPK activity is reported to be upregulated in one model of ALS (Liu et al., 2015), but this is a model using wild-type TDP-43 and in an ALS-causing mutant TDP-43 model AMPK activity is reduced (Perera et al., 2014). Very little is known about the role of AMPK in ALS, but these studies suggest that dysregulation of AMPK activity may be involved in pathogenesis. Treatment with an AMPK activator, Latrepirdine, has been found to delay symptom onset in a SOD1 ALS mouse model when administered prior to the onset of symptoms (Coughlan et al., 2015). This AMPK activator has also been investigated in clinical trials for AD and other neurodegenerative disease but with mixed efficacy (Cano-Cuenca et al., 2014).

Given that AMPK is activated in response to reduced cellular energy and increased cellular calcium levels, and that ER-mitochondria contacts facilitate mitochondrial calcium uptake and ATP production, it is possible to hypothesise that AMPK plays a role in the regulation of ER-mitochondria contacts. This chapter therefore also investigates the hypothesis that AMPK phosphorylates VAPB or PTPIP51 to modulate their tethering of ER-mitochondrial membranes.

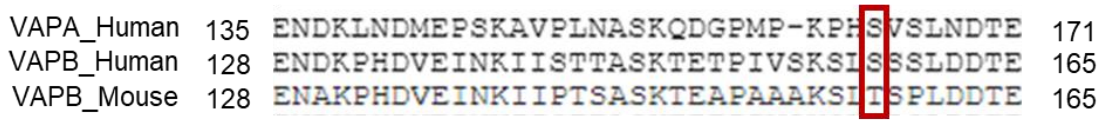

Figure 4.1: AMPK phosphorylation site in VAPA is conserved in VAPB in humans. Alignment of a section of the sequence of human VAPA, human VAPB and mouse VAPB. AMPK phosphorylation site is circled in red; it is conserved between VAPA and VAPB in humans. In mice the corresponding residue is threonine, which can also be phosphorylated.

4.1.4 Aims of this chapter

In order to investigate the hypothesis that GSK-3β phosphorylates VAPB or PTPIP51, this work first phosphorylated recombinant VAPB or PTPIP51 with GSK-3β *in vitro*. LC-MS/MS was then used to identify GSK-3β phosphorylation sites in either protein.

To confirm the presence of these *in vitro* sites in cells, and to identify novel sites of phosphorylation, VAPB and PTPIP51 were immunoprecipitated from cells and analysed by LC-MS/MS. Further, to enhance the likelihood of confirming target GSK-3β phosphorylation sites identified *in vitro*, VAPB and PTPIP51 were immunoprecipitated from cells transfected with GSK-3β, so as to increase its cellular activity. Finally, to enhance the likelihood of identifying the predicted AMPK phosphorylation site, or other potential AMPK target residues, VAPB and PTPIP51 were immunoprecipitated from cells treated with an AMPK activator and analysed by LC-MS/MS.

4.2 Results

4.2.1 Identification of GSK-3β phosphorylation sites in recombinant PTPIP51

To investigate the hypothesis that GSK-3β disrupts VAPB-PTPIP51 binding by phosphorylation, this study sought to identify target sites in recombinant protein isolated from *E.coli*. First, PTPIP51 was to be incubated with recombinant GSK-3β *in vitro* to allow phosphorylation in an environment with no other kinases present.

Recombinant PTPIP51 without the mitochondrial targeting transmembrane domain and fused to GST (GST-PTPIP51(36-470)) was produced as described in 2.2.11. To phosphorylate PTPIP51 with GSK-3β, 6 µg GST-PTPIP51(36-470) was incubated for 16 hrs at 30 ^{o}C with commercially sourced recombinant GSK-3β and an excess of ATP. PTPIP51 without the transmembrane domain was used because membrane spanning domains are not expected to be phosphorylated as they reside in the membrane and are insoluble and therefore difficult to isolate from *E.coli*. Reactions containing either the buffer and ATP reaction mix (RM) alone, RM and GST-PTPIP51(36-470), RM and GSK-3β or RM, GST-PTPIP51(36-470) and GSK-3β were performed. After 16 hrs, samples were separated using SDS-PAGE and stained with imperial protein stain as described in 2.2.12 (Figure 4.2). GST-PTPIP51(36-470) has a molecular weight of approximately 75 kDa and is expected to show a band at a slightly higher molecular weight, as PTPIP51 itself does. GSK-3β has a predicted molecular weight of 47 kDa. Commercially sourced GSK-3β is expected to show a band at approximately 55 kDa and contains the *E.coli* protein GroE chaperone with a molecular weight of 90 kDa. Reactions containing RM, GST-PTPIP51(36-470) and GSK-3β were carried out in triplicate to ensure sufficient protein was available for mass spectrometry and to enable detection of phosphorylation.

Recombinant protein corresponding to GST-PTPIP51(36-470) which had been incubated with GSK-3β was excised from the gel for mass spectrometric analysis. Although mass spectrometry is a sensitive technique, phosphorylation occurs reversibly and in small proportions. Therefore, to ensure that a sufficient amount of protein to enable the detection of phosphopeptides was generated, three bands of the protein were excised and pooled for processing and mass spectrometry. Recombinant protein was prepared for LC-MS/MS as detailed in 2.2.12. Briefly, the protein was digested with trypsin, cysteine residues were reduced and stabilised and peptides were then extracted for LC-MS/MS analyses.

Peptides corresponding to recombinant PTPIP51(36-470) and providing sequence coverage of 79 % of the full-length human protein were identified by LC-MS/MS (Figure 4.3). Only one site of phosphorylation was identified in PTPIP51. The fragmentation spectra of the corresponding phosphopeptide localized this phosphorylation to serine residue S77 (Figure 4.4). Phosphorylation at S77 has not been reported in any large-scale mass spectrometry data curated in either of two online repositories, the database of Phospho-sites in Animals and Fungi (dbPAF) and Phosphosite (see http://www.phosphosite.org/home). Additionally, this serine residue at position 77 is not conserved between the human, mouse or rat protein, suggesting little likelihood of this residue having a regulatory function in such a fundamental cellular process as ER-mitochondrial signalling.

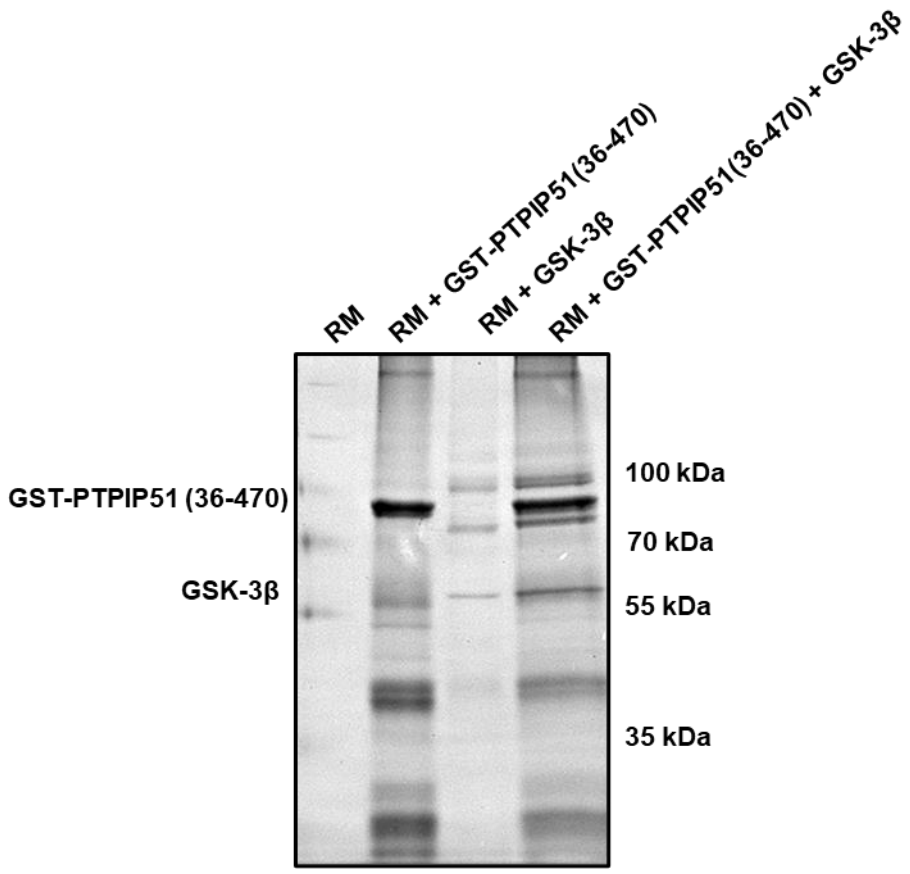

Figure 4.2: *In vitro* phosphorylation of GST-PTPIP51(36-470) by GSK-3β. GST-PTPIP51(36-470) was incubated with commercial GSK-3β. Reactions containing RM alone, RM + GST-PTPIP51(36-470), RM + GSK-3β and RM + GSK-3β + GST-PTPIP51(36-470) were incubated for 16 hrs at 30 ^{0}C. Proteins were separated by SDS-PAGE and visualised using imperial protein stain. Reactions without recombinant PTPIP51 enabled distinction between PTPIP51 and proteins contained in the RM or contaminants of commercial GSK-3β. Molecular mass markers are indicated on the right.

A)

MSRLGALGGARAGLGLLLGTAAGLGFLCLLYSQRWKRTQRHGRSQSLPNSLDYTQTSDPG
RHVMLLRAVPGGAGDA**S**VLPSLPREGQEKVLDRLDFVLTSLVALRREVEELRSSLRGLAGEI
VGEVRCHMEENQRVARRRRFPFVRERSDSTGSSSVYFTASSGATFTDAESEGGYTTANAE
SDNERDSDKESEDGEDEVSCETVKMGRKDSLDLEEEAASGASSALEAGGSSGLEDVLPLL
QQADELHRGDEQGKREGFQLLLNNKLVYGSRQDFLWRLARAYSDMCELTEEVSEKKSYAL
DGKEEAEAALEKGDESADCHLWYAVLCGQLAEHESIQRRIQSGFSFKEHVDKAIALQPENPM
AHFLLGRWCYQVSHLSWLEKKTATALLESPLSATVEDALQSFLKAEELQPGFSKAGRVYISK
CYRELGKNSEARWWMKLALELPDVTKEDLAIQKDLEELEVILRD

B)

Peptide Sequence	**Peptide m/z**	**Modification**
^{68}AVPGGAGDA**pS**VLPSLPR^{84}	822.41^{2+}	pS77

Figure 4.3: PTPIP51 is phosphorylated by GSK-3β *in vitro* at residue S77. (A) Sequence of full length human PTPIP51 with the MS/MS sequence coverage of 79 %, obtained after trypsin digestion of GST-PTPIP51(36-470), shown as underlined. One *in vitro* GSK-3β phosphorylation site was identified (S77), shown in red. (B) PTPIP51 phosphopeptide obtained by MS/MS sequencing with corresponding mass/charge (m/z) ratio. Phosphorylated residue shown in red.

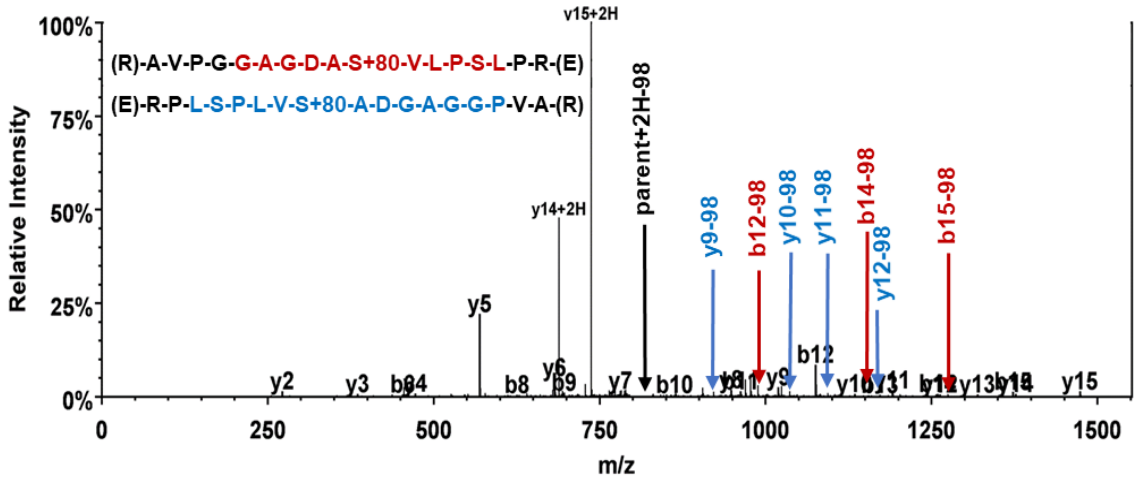

Figure 4.4: Identification of PTPIP51 S77 as a potential GSK-3β phosphorylation site by LC-MS/MS. Tandem mass spectrometry spectrum of the PTPIP51 phosphopeptide ^{68}AVPGGAGDApSVLPSLPR^{84} (m/z 822.41^{2+}) fragment ion series after collision induced dissociation. The m/z of the ions is plotted against intensity and the detected ions of the b- (red) and y- (blue) ion collision series are indicated in the sequence of the peptide (top left). A loss of 98, indicating a constant neutral loss of phosphoric acid, from the parent ion is present at m/z 773.46^{2+} and is indicative of either a serine or threonine phosphorylation on the peptide. Loss of phosphoric acid from b-12, b-14 and b-15 and y-9, y-10, y-11 and y-12 (indicated by arrows on the spectrum) localize this phosphorylation to S77 (highlighted red in peptide sequence).

4.2.2 Identification of GSK-3β phosphorylation sites in recombinant VAPB

Having investigated phosphorylation of PTPIP51 by GSK-3β, this study next sought to identify GSK-3β target phosphorylation sites in recombinant VAPB. As above, VAPB was to be incubated with recombinant GSK-3β to allow phosphorylation in an environment with no other kinases present.

Recombinant protein corresponding to the cytoplasmic domain of VAPB with a histidine tag (His-VAPB(1-220)) was produced as described in 2.2.11. To phosphorylate VAPB with GSK-3β, 6 µg His-VAPB(1-220) was incubated for 16 hrs at 30 ^{o}C with commercially sourced recombinant GSK-3β and an excess of ATP. Reactions containing either the buffer and ATP reaction mix (RM) alone, RM and His-VAPB(1-220), RM and GSK-3β or RM, His-VAPB(1-220) and GSK-3β were performed (Figure 4.5). After 16 hrs, samples were separated using SDS-PAGE and stained with imperial protein stain as described in 2.2.12. VAPB has a predicted molecular weight of 33 kDa and, as in section 4.2.1, GSK-3β was predicted to show a band at 55 kDa with GroE chaperone at 90 kDa. Reactions containing RM, His-VAPB(1-220) and GSK-3β were carried out in triplicate to ensure sufficient protein was available for mass spectrometry and to enable detection of phosphorylation. Recombinant protein was prepared for LC-MS/MS as detailed in 2.2.12.

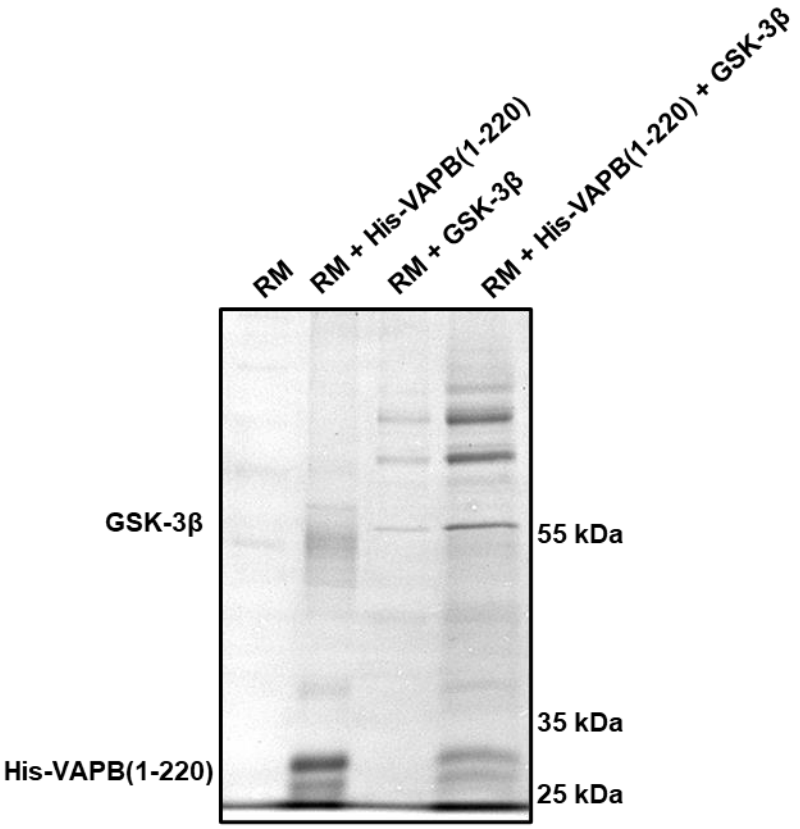

Figure 4.5: *In vitro* phosphorylation of His-VAPB(1-220) by GSK-3β. His-VAPB(1-220) was incubated with commercial GSK-3β. Reactions containing RM alone, RM + His-VAPB(1-220), RM + GSK-3β and RM + GSK-3β + His-VAPB(1-220) were incubated for 16 hrs at 30 ^{0}C. Proteins were separated by SDS-PAGE and visualised using imperial protein stain. Reactions without recombinant VAPB enabled distinction between VAPB and proteins contained in the RM or contaminants of commercial GSK-3β. Molecular mass markers are indicated on the right.

Peptides corresponding to recombinant His-VAPB(1-220) and providing sequence coverage of 85 % of the full-length human protein were identified by LC-MS/MS (Figure 4.6). Three sites of phosphorylation were identified (Figure 4.6) in His-VAPB(1-220). Fragmentation spectra of the corresponding phosphopeptides localized phosphorylation to threonine residues T143, T148 and T150 (Figures 4.7, 4.8, 4.9 respectively). All three of these residues reside between the MSP domain and the coiled coil domain of VAPB.

GSK-3β commonly targets proteins that are pre-phosphorylated at a priming residue located 4 or 5 residues C-terminal to the site of GSK-3β phosphorylation (Doble and Woodgett, 2003). Priming of GSK-3β substrates is usually carried out by a different kinase, therefore such priming is not replicated in these *in vitro* conditions and it is possible that some GSK-3β sites were not detected in this study. However, phosphorylation at residues T143 and T148 fit the consensus sequence for GSK-3β phosphorylation, with T148 potentially acting as a priming site for phosphorylation at T143. It is possible that the close proximity and high concentration of enzyme and substrate in these *in vitro* conditions, as well as the lack of any inhibitory regulation or alternative substrates, allows GSK-3β to phosphorylate residues which are susceptible to phosphorylation but might normally be phosphorylated by a different kinase *in vivo*. Large scale mass spectrometry data from four studies have reported phosphorylation at VAPB-T143, and one study has reported phosphorylation at VAPB-T148, as curated in the dbPAF, supporting the result that these residues undergo phosphorylation. T150 has also been found to be phosphorylated (see http://www.phosphosite.org/) but this site is not conserved between humans, mice and rats. As ER-mitochondrial signalling mediates many fundamental cellular functions and has been observed in experiments in mice, it would be considered that regulatory mechanisms are conserved between species. This project therefore focusses on residues T143 and T148, which are conserved, as the most likely candidates for the regulation of ER-mitochondria contacts.

A)

MAKVEQVLSLEPQHELKFRGPFTDVVTTNLKLGNPTDRNVCFKVKTTAPRRYCVRPNSGIIDA
GASINVSVMLQPFDYDPNEKSKHKFMVQSMFAPTDTSDMEAVWKEAKPEDLMDSKLRCVFEL
PAENDKPHDVEINKIISTTASKTETPIVSKSLSSSLDDTEVKKVMEECKRLQGEVQRLREENKQF
KEEDGLRMRKTVQSNSPISALAPTGKEEGLSTRLLALVVLFFIVGVIIGKIAL

B)

Peptide Sequence	**Peptide m/z**	**Residue**
^{121}CVFELPAENDKPHDVEINKIIS**pT**TASKTETPIVSK^{155}	998.50^{4+}	T143
^{140}IISTTASK**pT**ETPIVSK^{155}	585.98^{3+}	T148
^{121}CVFELPAENDKPHDVEINKIISTTASKTE**pT**PIVSK^{155}	998.50^{4+}	T150
^{140}IISTTASKTE**pT**PIVSK^{155}	878.46^{2+}	T150

Figure 4.6: VAPB is phosphorylated by GSK-3β *in vitro* at residues T143, T148 and T150. (A) Sequence of full length human VAPB with the MS/MS sequence coverage of 85 %, obtained after trypsin digestion of His-VAPB(1-220), shown as underlined. Three *in vitro* GSK-3β phosphorylation sites were identified (T143, T148, T150), shown in red. (B) VAPB phosphopeptides obtained by MS/MS sequencing with their mass/charge (m/z) ratios. Phosphorylated residues shown in red.

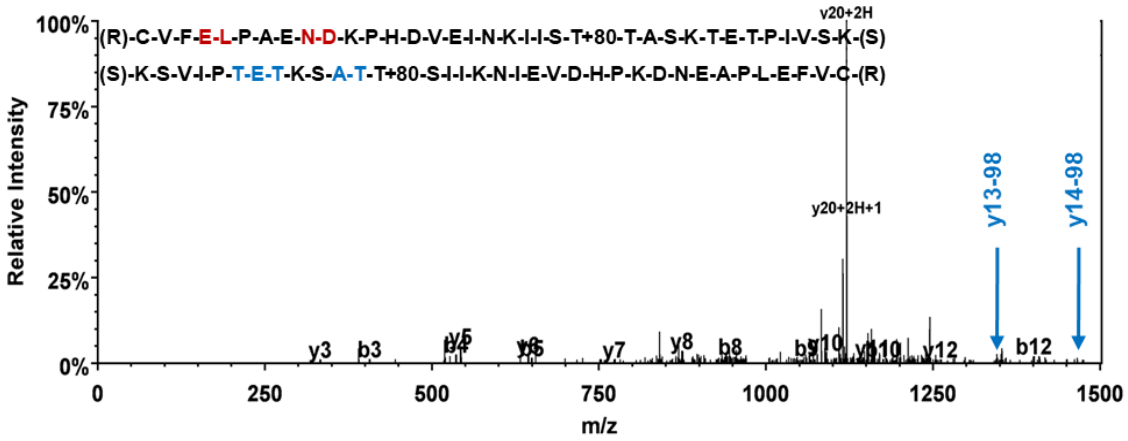

Figure 4.7: Identification of VAPB T143 as a potential GSK-3β phosphorylation site by LC-MS/MS. Tandem mass spectrometry spectrum of the VAPB phosphopeptide ^{121}CVFELPAENDKPHDVEINKIISpTTASKTETPIVSK^{155} (m/z 998.50^{4+}) fragment ion series after collision induced dissociation. The m/z of the ions is plotted against intensity and the detected ions of the b- (red) and y- (blue) ion collision series are indicated on the sequence of the peptide (top left). A constant neutral loss of 98, phosphoric acid, from the parent ion indicative of serine or threonine phosphorylation was not detected on the peptide. However, loss of phosphoric acid from y-13 and y-14, (indicated by arrows on the spectrum), but not y-12, y-10, y-8 or y-7, indicates phosphorylation of T143.

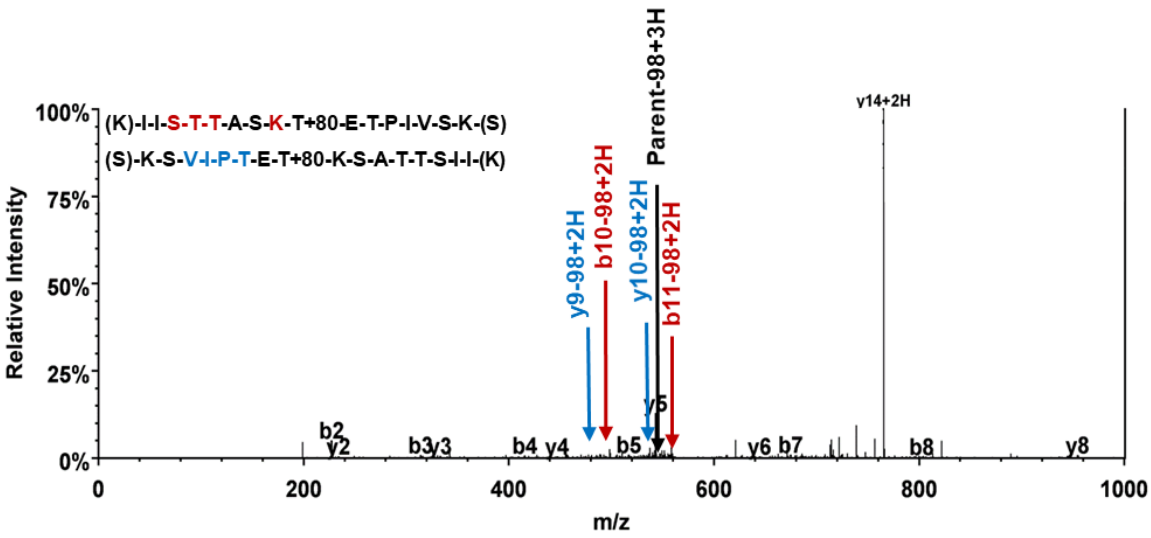

Figure 4.8: Identification of VAPB T148 as a potential GSK-3β phosphorylation site by LC-MS/MS. Tandem mass spectrometry spectrum of the VAPB phosphopeptide ^{140}IISTTASKpTETPIVSK^{155} (m/z 585.98^{3+}) fragment ion series after collision induced dissociation. The m/z of the ions is plotted against intensity and the detected ions of the b- (red) and y- (blue) ion collision series are indicated on the sequence of the peptide (top left). A constant neutral loss of phosphoric acid, 98, from the parent ion was present at m/z 553.26^{3+} and is indicative of either a serine or threonine phosphorylation on the peptide. Loss of phosphoric acid from the doubly charged b-10, b-11 and y-9, y-10 ions (indicated by arrows on the spectrum) localize this phosphorylation to T148.

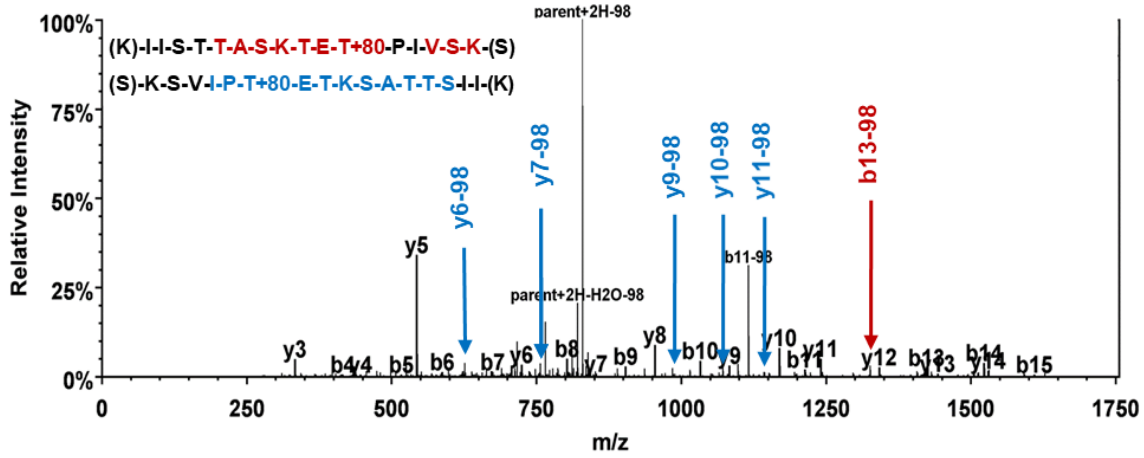

Figure 4.9: Identification of VAPB T150 as a potential GSK-3β phosphorylation site by LC-MS/MS. Tandem mass spectrometry spectrum of the VAPB phosphopeptide ^{140}IISTTASKTEpTPIVSK^{155} (m/z 878.46^{2+}) fragment ion series after collision induced dissociation. The m/z of the ions is plotted against intensity and the detected ions of the b- (red) and y- (blue) ion collision series are indicated on the sequence of the peptide (top left). A constant neutral loss of phosphoric acid, 98, from the parent ion was present at m/z 829.65^{2+} and is indicative of either a serine or threonine phosphorylation on the peptide. Loss of phosphoric acid from b-13 and y-6, y-7, y-9, y-10 and y-11 ions (indicated by arrows on the spectrum) localize this phosphorylation to T150.

4.2.3 Modification of VAPB at GSK-3β phosphorylation sites affects VAPB-PTPIP51 binding

To determine whether phosphorylation by GSK-3β at T143 and T148 in VAPB affect its binding to PTPIP51, phosphomutants of VAPB were generated. T143 and T148 were mutated either to alanine, to prevent phosphorylation, or to aspartate, to mimic constitutive phosphorylation. This approach has been used in many studies (see for e.g. (Ackerley et al., 2003; Eidenmuller et al., 2001)). These mutations were introduced into a construct of VAPB for use in a mammalian GAL4 2-hybrid assay which measures the strength of interaction between VAPB and PTPIP51 using a luciferase readout.

This assay uses a firefly luciferase reporter gene under the control of the upstream activating sequence (UAS) promoter, activated by GAL4. GAL4 comprises a DNA binding domain (DBD) and a trans-activating (TA) domain. The DBD and a viral protein which acts as a strong trans-activator, VP16, can be expressed separately and when coming into contact with each other will drive firefly luciferase expression. To facilitate the measurement of VAPB-PTPIP51 binding, this study used constructs expressing the cytoplasmic domains of VAPB and PTPIP51, VAPB(1-220) and PTPIP51(36-470), fused to the GAL4 DBD and VP16 trans-activator respectively to drive firefly luciferase expression upon binding (Figure 4.10). A construct expressing renilla luciferase under a constitutively active promoter was used as a transfection efficiency control. Renilla luciferase emits light at a different wavelength and in response to different substrates to firefly luciferase and the two signals can therefore be distinguished.

In the first instance, to confirm the specificity of the GAL4 2-hybrid assay system for quantifying VAPB-PTPIP51 binding, the assay was performed with DBD-VAPB(1-220)-WT and VP16-PTPIP51(36-470), with the positive control of full length GAL4 and several negative controls. Negative controls include DBD-VAPB(1-220) and VP16-PTPIP51(36-470) transfected with the corresponding domains of GAL4 not conjugated to the corresponding VAPB or PTPIP51 protein to ensure that both constructs are required to induce firefly luciferase expression.

HEK-293 cells were transfected with the GAL4-UAS-luciferase construct either alone or with DBD, VP16, DBD+VP16, DBD-VAPB(1-220)+VP16, VP16-PTPIP51(36-470)+DBD, DBD-VAPB(1-220)+VP16-PTPIP51(36-470) or full length GAL4 as a positive control. Cells were also transfected with the transfection control renilla luciferase. Expression of GAL4 or DBD-VAPB(1-220)+VP16-PTPIP51(36-470) induced strong firefly luciferase signals (Figure 4.11) compared to controls, demonstrating the validity of the assay for monitoring PTPIP51-VAPB binding.

Next, HEK-293 cells were transfected with constructs expressing renilla and firefly luciferase, VP16-PTPIP51(36-470) and either DBD-VAPB(1-220)-WT, DBD-VAPB(1-220)-T143A, DBD-VAPB(1-220)-T143D, DBD-VAPB(1-220)-T148A or DBD-VAPB(1-220)-T148D. After 24 hrs of transfection cells were lysed and firefly luciferase signals, followed by renilla signals, were assayed. Firefly luciferase signals were normalised to renilla signals and then to that of VAPB(1-220)-WT. VAPB(1-220)-T148D displayed significantly reduced binding to PTPIP51(36-470) when compared to WT-VAPB control ($p=0.028$) in these assays, suggesting that phosphorylation at this residue reduces the ability of VAPB to bind to PTPIP51 (Figure 4.12).

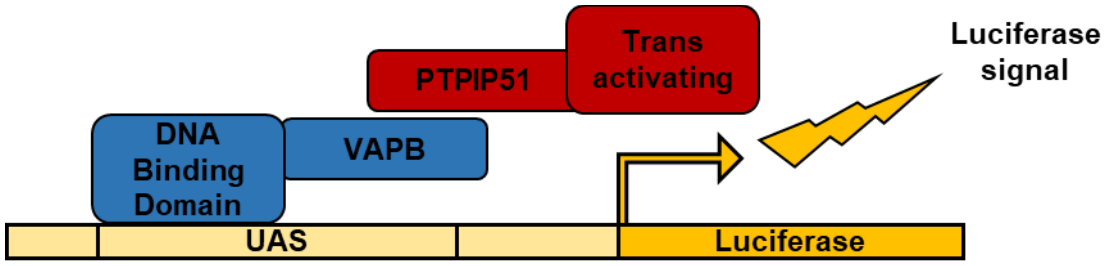

Figure 4.10: Diagram of the basis of the mammalian cell GAL4 2-hybrid assay system for quantifying VAPB-PTPIP51 binding. Luciferase expression is under the control of the GAL4-UAS promoter. Binding of VAPB(1-220), which is conjugated to the DNA binding domain of GAL4, to PTPIP51(36-470), which is conjugated to the trans-activating protein VP16, brings VP16 into close proximity to the promoter enabling it to induce firefly luciferase expression. Measurement of the firefly luciferase signal enables quantification of VAPB-PTPIP51 binding.

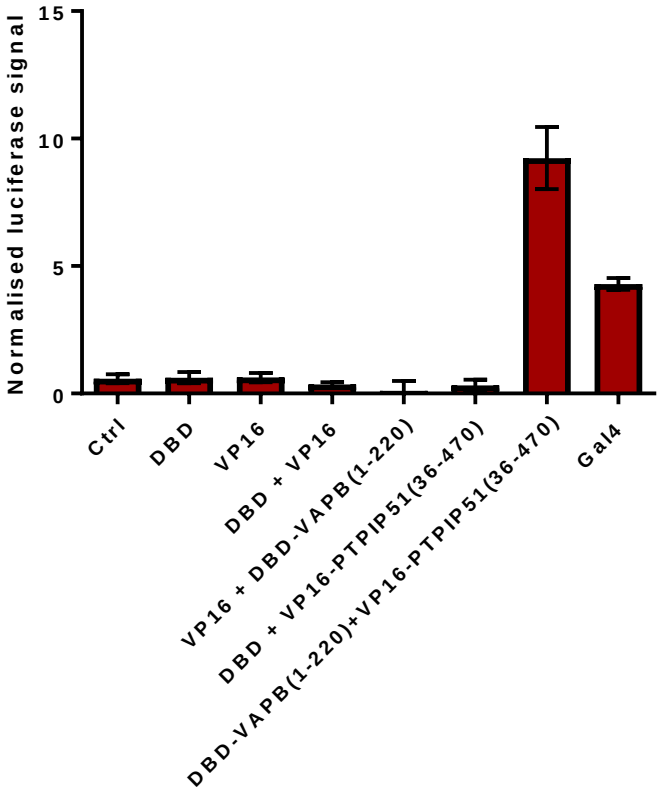

Figure 4.11: Control experiment to demonstrate the validity of the mammalian cell GAL4 2-hybrid assay for monitoring the VAPB-PTPIP51 interaction. Cells were transfected with renilla and firefly luciferase with either control vector (Ctrl), GAL4-DBD, DBD, VP16, DBD+VP16, VP16 + DBD-VAPB(1-220), DBD+VP16-PTPIP51(36-470), DBD-VAPB+VP16-PTPIP51(36-470), or full length GAL4 as a positive control. Cells were lysed 24 hrs after transfection, luciferase signals were measured and firefly luciferase signal normalised to renilla signals. DBD-VAPB(1-220)+VP16-PTPIP51(36-470) and full length GAL4 induced firefly luciferase expression. N = 1 experiment, 4 replicates. Error bars are s.e.m.

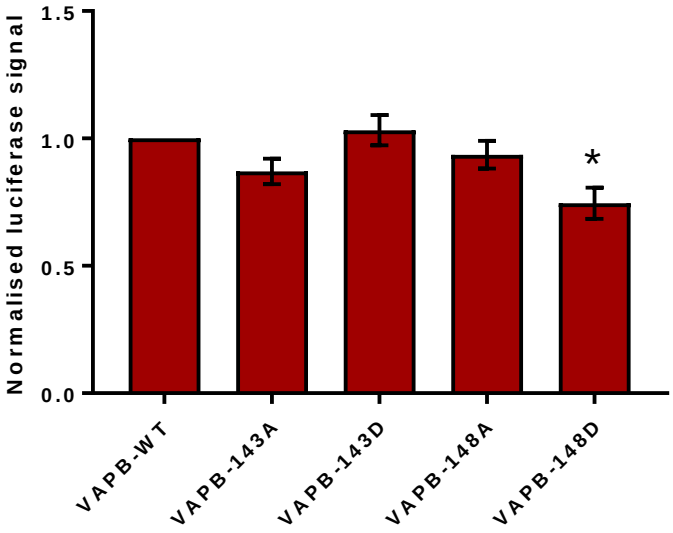

Figure 4.12: Modification of T148D in VAPB reduces binding to PTPIP51 in the mammalian cell GAL4 2-hybrid assay. Cells were transfected with constructs of renilla and firefly luciferase, VP16-PTPIP51(36-470) and either DBD-VAPB(1-220) -WT, -T143A, -T143D, -T148A or -T148D. Cells were lysed 24 hrs after transfection, luciferase signals were measured and firefly luciferase signal normalised to renilla. DBD-VAPB(1-220)-T148D produced significantly lower luciferase signal as compared to DBD-VAPB-WT control. Data analysed by one-way ANOVA and Tukey post hoc test. n = 3 biological replicates of 4 samples each. * = $p<0.05$. Error bars are s.e.m.

4.2.4 Identification of phosphorylation sites in VAPB in cells in which GSK-3β is activated by overexpression

The identification of phosphorylation sites in recombinant proteins as described above is useful to identify sites phosphorylated directly by GSK-3β. However, it is also important to confirm the presence of phosphorylation at these sites in cells, where the factors that affect phosphorylation *in vivo*, such as phosphatases and kinase inhibitors, are present. For this reason, phosphorylation of VAPB and PTPIP51 was studied by mass spectrometry of VAPB and PTPIP51 purified from transfected cells. VAPB and PTPIP51 were purified by immunoprecipitation and SDS-PAGE. To maximise the likelihood of identifying GSK-3β phosphorylation target sites, VAPB and PTPIP51 were co-transfected with either control vector or GSK-3β to increase kinase activity.

Firstly, full length VAPB with an N-terminal myc tag was exogenously expressed in HEK-293 cells with either control vector (Ctrl) or a construct expressing GSK-3β. Cells were lysed 24 hrs after transfection and a small sample was probed for GSK-3β to ensure over-expression in the GSK-3β transfected cells (Figure 4.13A) Endogenous GSK-3β has a predicted molecular weight of 47 kDa and bands were seen at this weight. Myc-VAPB was immunoprecipitated from both samples via the myc tag and proteins were separated by SDS-PAGE. To maximise the amount of protein for analysis, the experiment was carried out in triplicate and myc-VAPB from all three samples for each condition was excised from the imperial stained SDS-PADE gel (Figure 4.13B) for mass spectrometric analysis. More myc-VAPB, as indicated by stronger bands at 33kDa, was found in cells over-expressing GSK-3β. This may be considered to indicate that GSK-3β increases levels of VAPB, increases global protein expression, or that there are more cells in the GSK-3β over-expression condition which may be caused by GSK-3β or may be an experimental difference. Increased global protein amounts are also seen in GSK-3β over-expressing cells in Figure 2.24, though to a lesser extent. Western blot for VAPB with a loading control, or a cell count, could be used to identify the cause of this difference. Gels bands of myc-VAPB were prepared, including digestion of the protein with trypsin, for LC-MS/MS which was carried out at the King's College London Proteomics facility as detailed in 2.2.12.

A)

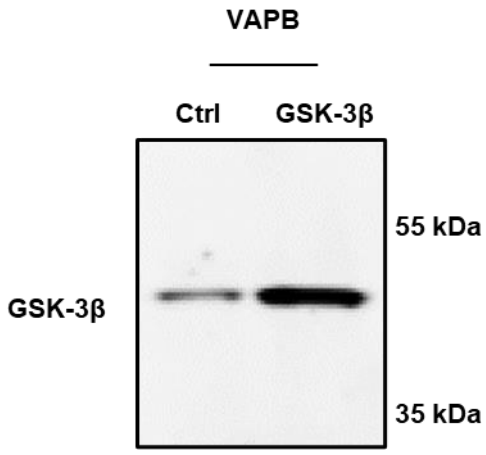

B)

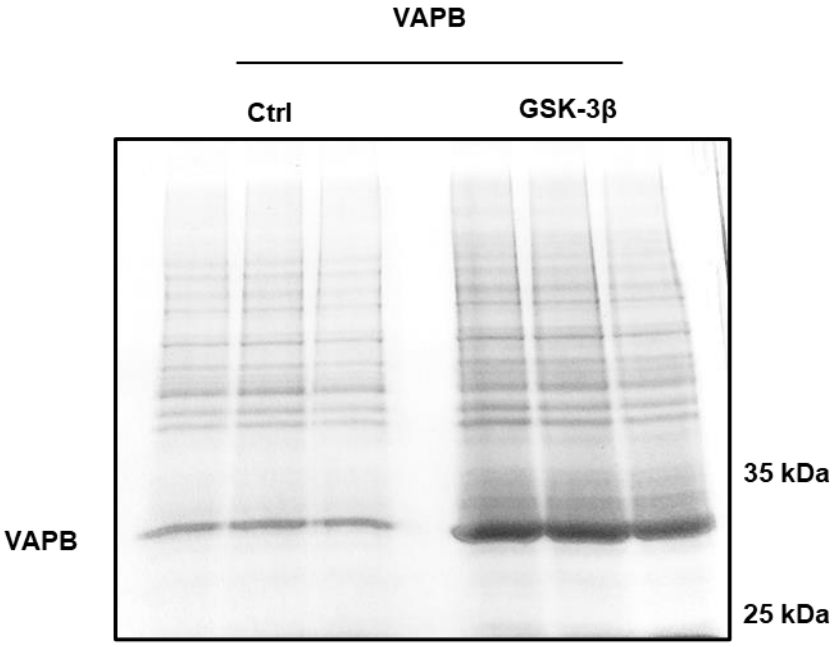

Figure 4.13: Overexpression of GSK-3β and purification of Myc-VAPB for LC-MS/MS analysis of phosphorylation. HEK-293 cells were transfected with Myc-VAPB and either control vector or GSK-3β. Cells were lysed 24 hrs after transfection and a sample was probed for GSK-3β expression by immunoblot (A). Myc-VAPB was immuno-precipitated using a Myc antibody, separated on an SDS-PAGE gel and stained with imperial protein stain (B). The positions of GSK-3β and VAPB are shown and molecular mass markers are shown on the right.

LC-MS/MS of myc-VAPB isolated from cells expressing only endogenous GSK-3β identified peptides corresponding to myc-VAPB and provided sequence coverage of 76 % of the full-length human protein (Figure 4.14). Six individual sites of phosphorylation were identified and analysis of the corresponding fragmentation spectra of these phosphopeptides confirmed the localisation of phosphorylation to threonine reside T144 and serine residues S154, S156, S158, S159 and S160.

LC-MS/MS of myc-VAPB isolated from cells over-expressing exogenous GSK-3β identified peptides corresponding to myc-VAPB and provided sequence coverage of 86 % of the full-length human protein (Figure 4.15). Five individual sites of phosphorylation were identified and analysis of the corresponding fragmentation spectra of these phosphopeptides confirmed the localisation of phosphorylation to threonine reside T150 and serine residues S146, S156, S158 and S160. One doubly phosphorylated peptide was identified, with phosphorylation at both S156 and S160 residues.

One representative fragmentation spectrum is shown for one phosphopeptide representing each phosphorylation site found in VAPB either from cells expressing only endogenous GSK-3β or from cells overexpressing GSK-3β. Spectra are shown for residues T144, S146, T150, S154, S156, S158, S159 and S160 in figures 4.16, 4.17, 4.18, 4.19, 4.20, 4.21, 4.22 and 4.23 respectively.

Phosphorylation at residues S146 and T150 was found in VAPB from cells over-expressing GSK-3β but not in VAPB from control cells. VAPB residues T143 and T148, as identified in the recombinant experiments carried out earlier in the chapter, were not found to be phosphorylated in VAPB from cells. Whilst this does not rule out phosphorylation of these residues by GSK-3β, it does mean that more experiments would need to be carried out to confirm them as targets of GSK-3β.

A)

MAKVEQVLSLEPQHELKFRGPFTDVVTTNLKLGNPTDRNVCFKVKTTAPRRYCVRPNSGIIDA
GASINVSVMLQPFDYDPNEKSKHKFMVQSMFAPTDTSDMEAVWKEAKPEDLMDSKLRCVFE
LPAENDKPHDVEINKIISTTASKTETPIVSKSLSSSLDDTEVKKVMEECKRLQGEVQRLREENK
QFKEEDGLRMRKTVQSNSPISALAPTGKEEGLSTRLLALVVLFFIVGVIIGKIAL

B)

Peptide Sequence	**Peptide m/z**	**Phosphorylated Residue**
^{140}IIST**pT**ASKTETPIVSK^{155}	878.46^{2+}	T144
^{148}TETPIV**pS**KSLSSSLDDTEVKK^{168}	782.06^{3+}	S154
^{140}IISTTASKTETPIVSK**pS**LSSSLDDTEVK^{167}	1006.51^{3+}	S156
^{156}SL**pS**SSLDDTEVKK^{168}	744.85^{2+}	S158
^{148}TETPIVSKSLS**pS**SLDDTEVK^{167}	1108.53^{2+}	S159
^{156}SLSS**pS**LDDTEVKK^{168}	744.85^{2+}	S160

Figure 4.14: Phosphorylation sites identified in VAPB isolated from cells expressing only endogenous GSK-3β. (A) Sequence of full length human VAPB with the MS/MS sequence coverage of 76 % shown as underlined. Six phosphorylation sites were identified (T144, S154, S156, S158, S159, S160), shown in red. (B) VAPB phosphopeptides obtained by MS/MS sequencing with their mass/charge (m/z) ratios. Phosphorylated residues shown in red.

A)

MAKVEQVLSLEPQHELKFRGPFTDVVTTNLKLGNPTDRNVCFKVKTTAPRRYCVRPNSGIIDAG
ASINVSVMLQPFDYDPNEKSKHKFMVQSMFAPTDTSDMEAVWKEAKPEDLMDSKLRCVFELP
AENDKPHDVEINKIISTTA**S**KTE**T**PIVSK**S**L**S**S**S**LDDTEVKKVMEECKRLQGEVQRLREENKQFK
EEDGLRMRKTVQSNSPISALAPTGKEEGLSTRLLALVVLFFIVGVIIGKIAL

B)

Peptide Sequence	Peptide m/z	Phosphorylated Residue
^{140}IISTTA**pS**KTETPIVSK^{155}	878.46^{2+}	S146
^{140}IISTTASKTE**pT**PIVSK^{155}	878.46^{2+}	T150
^{148}TETPIVSK**pS**LSS**pS**LDDTEVK^{167}	1148.52^{2+}	S156, S160
^{148}TETPIVSK**pS**LSSSLDDTEVKK^{167}	739.36^{3+}	S156
^{156}SL**pS**SSLDDTEVKK^{168}	496.90^{3+}	S158
^{156}SLSS**pS**LDDTEVKK^{168}	744.85^{2+}	S160

Figure 4.15: Phosphorylation sites identified in VAPB isolated from cells overexpressing GSK-3β. (A) Sequence of full length human VAPB with the MS/MS sequence coverage of 86 % shown as underlined. Five phosphorylation sites were identified (S146, T150, S156, S158, S160), shown in red. (B) VAPB phosphopeptides obtained by MS/MS sequencing with their mass/charge (m/z) ratios. One doubly phosphorylated peptide was identified, with phosphorylation at both S156 and S160 residues. Phosphorylated residues shown in red.

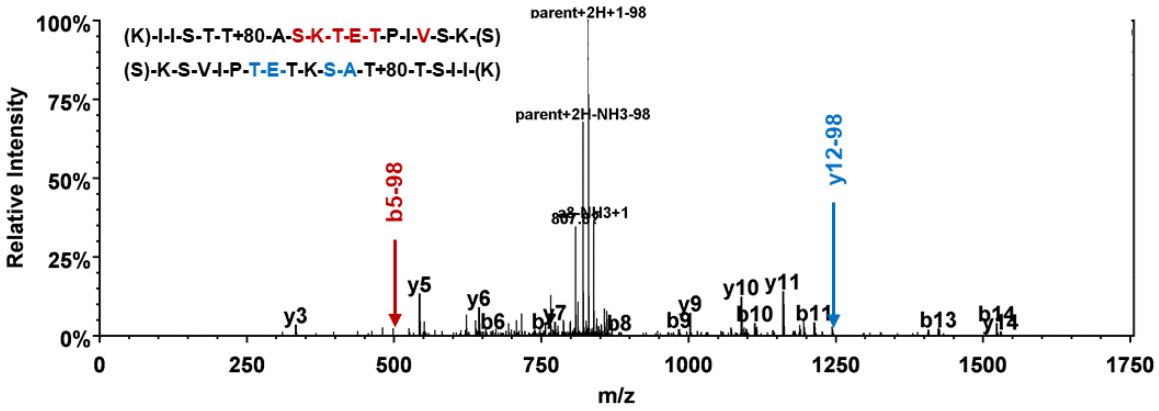

Figure 4.16: Identification of VAPB T144 as a phosphorylation site by LC-MS/MS. Tandem mass spectrometry spectrum of the VAPB phosphopeptide ^{140}IIST**pT**ASKTETPIVSK^{155} (m/z 878.46^{2+}) fragment ion series after collision induced dissociation. The m/z of the fragment ions is plotted against intensity and the detected ions of the b- (red) and y- (blue) ion collision series are indicated on the sequence of the peptide (top left). A constant neutral loss of phosphoric acid, 98, from the parent ion was present at m/z 829.90^{2+} and is indicative of either a serine or threonine phosphorylation on the peptide. Loss of phosphoric acid from the b-5 and y-12 ions (indicated by arrows on the spectrum), localize this phosphorylation to T144.

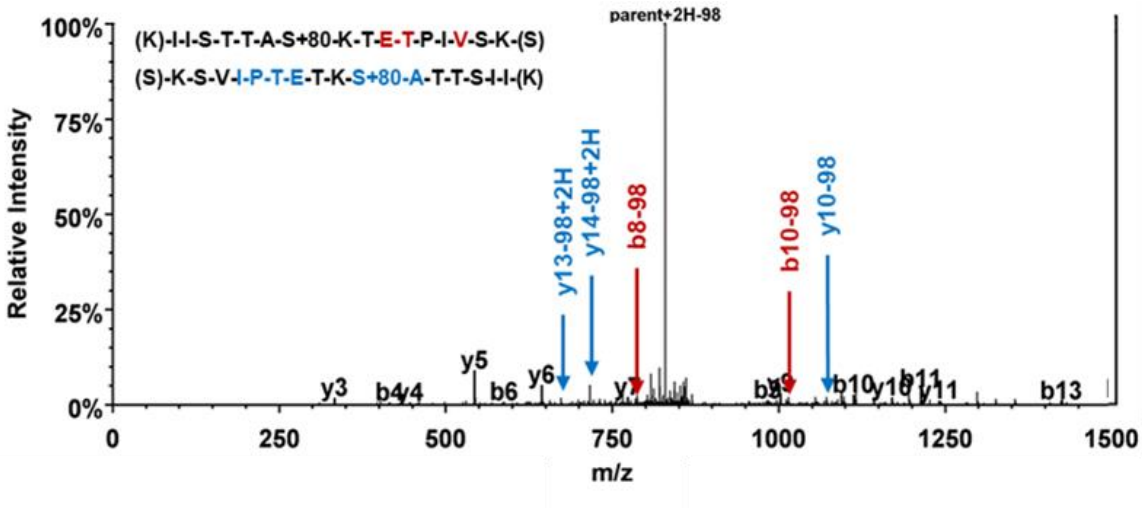

Figure 4.17: Identification of VAPB S146 as a phosphorylation site by LC-MS/MS. Tandem mass spectrometry spectrum of the VAPB phosphopeptide ^{140}IISTTApSKTETPIVSK^{155} (m/z 878.46^{2+}) fragment ion series after collision induced dissociation. The m/z of the fragment ions is plotted against intensity and the detected ions of the b- (red) and y- (blue) ion collision series are indicated on the sequence of the peptide (top left). A constant neutral loss of phosphoric acid, 98, from the parent ion was present at m/z 829.71^{2+} and is indicative of either a serine or threonine phosphorylation on the peptide. Loss of phosphoric acid from the y-10 ion, the doubly charged y-13 and y-14 ions (indicated by arrows on the spectrum) and the b-8 and b-10 ions, localize this phosphorylation to S146.

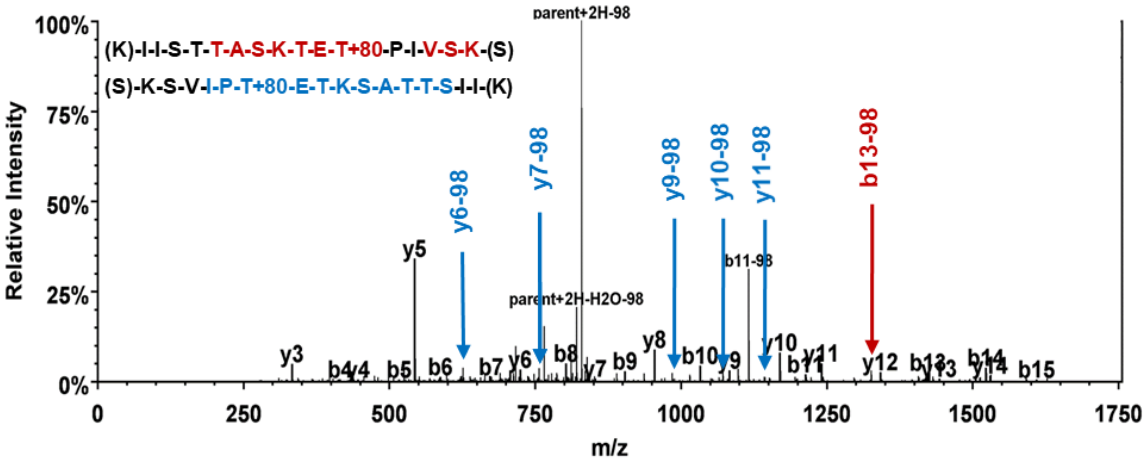

Figure 4.18: Identification of VAPB T150 as a phosphorylation site by LC-MS/MS. Tandem mass spectrometry spectrum of the VAPB phosphopeptide ^{140}IISTTASKTEpTPIVSK^{155} (m/z 878.46^{2+}) fragment ion series after collision induced dissociation. The m/z of the fragment ions is plotted against intensity and the detected ions of the b- (red) and y- (blue) ion collision series are indicated on the sequence of the peptide (top left). A constant neutral loss of phosphoric acid, 98, from the parent ion was present at m/z 830.20^{2+} and is indicative of either a serine or threonine phosphorylation on the peptide. Loss of phosphoric acid was detected at the b-13 ion. Loss of phosphoric acid from the sequence tag y-6 to y-11 ions (indicated by arrows on the spectrum), but not from y-3 to y-5 ions, localize this phosphorylation to T150.

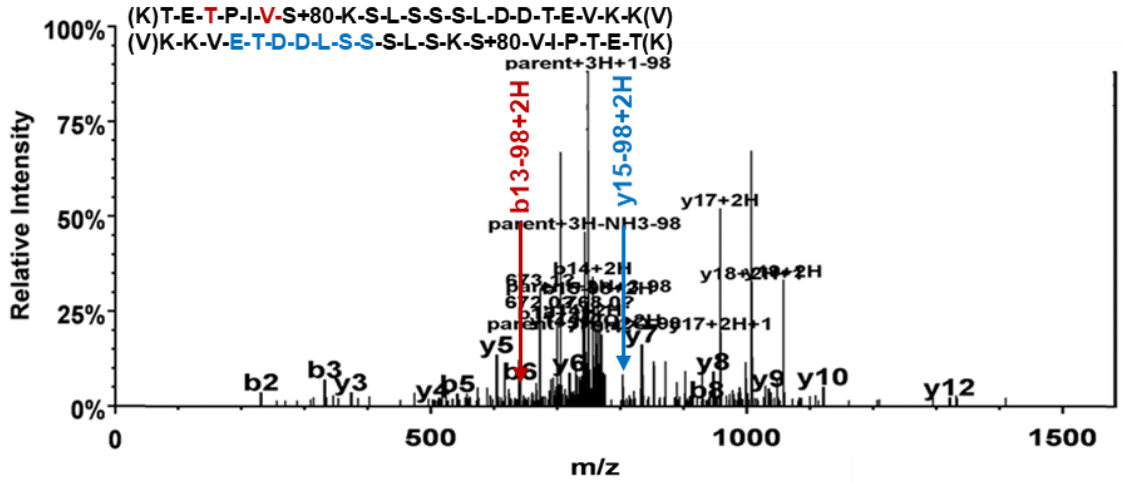

Figure 4.19: Identification of VAPB S154 as a phosphorylation site by LC-MS/MS. Tandem mass spectrometry spectrum of the VAPB phosphopeptide ^{148}TETPIVpSKSLSSSLDDTEVKK^{168} (m/z 782.06^{3+}) fragment ion series after collision induced dissociation. The m/z of the ions is plotted against intensity and the detected ions of the b- (red) and y- (blue) ion collision series are indicated on the sequence of the peptide (top left). A constant neutral loss of phosphoric acid, 98, from the parent ion was present at m/z 749.62^{3+} and is indicative of either a serine or threonine phosphorylation on the peptide. Loss of phosphoric acid from doubly charged b-13 and y-15 ions (indicated by arrows on the spectrum), but not y-5 to y-10 or y-12, localize this phosphorylation to S154.

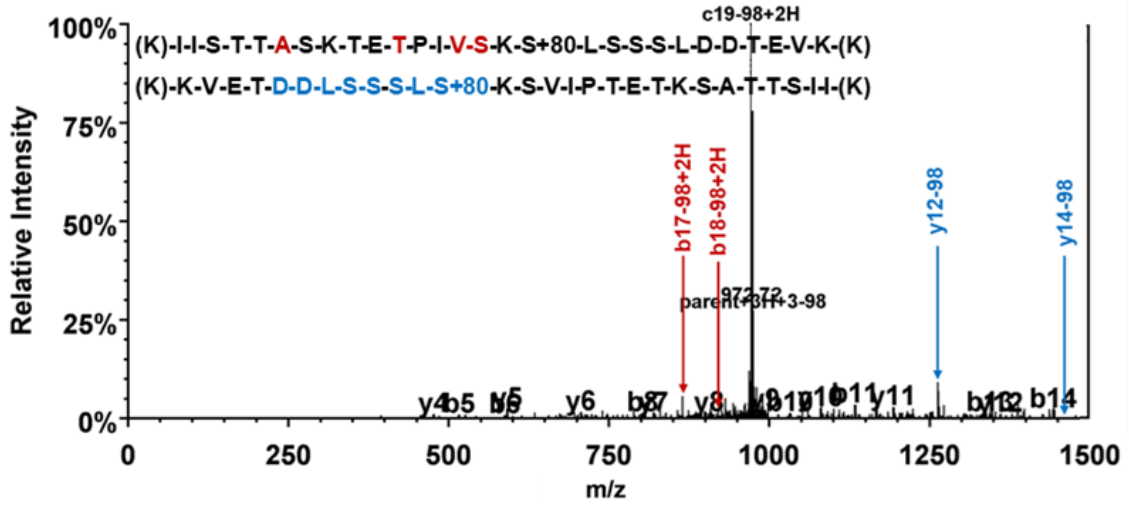

Figure 4.20: Identification of VAPB S156 as a phosphorylation site by LC-MS/MS. Tandem mass spectrometry spectrum of the VAPB phosphopeptide ^{140}IISTTASKTETPIVSKpSLSSSLDDTEVK^{167} (m/z 1006.51^{3+}) fragment ion series after collision induced dissociation. The m/z of the ions is plotted against intensity and the detected ions of the b- (red) and y- (blue) ion collision series are indicated on the sequence of the peptide (top left). A constant neutral loss of phosphoric acid, 98, from the parent ion was present at m/z 974.32^{3+} and is indicative of either a serine or threonine phosphorylation on the peptide. Loss of phosphoric acid from y-12 and y-14 but not y-11 ions, and from doubly charged b-17 and b-18 ions, (indicated by arrows on the spectrum) localize this phosphorylation to S156.

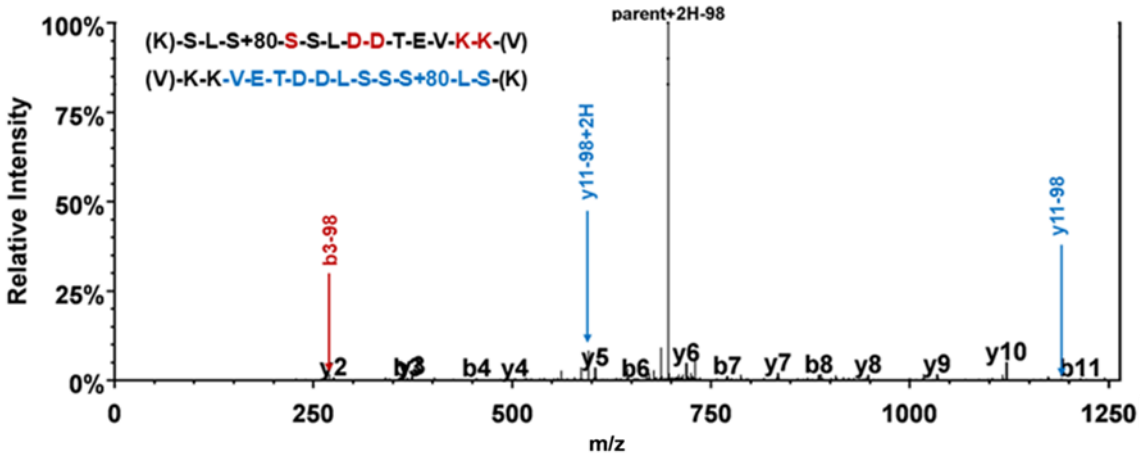

Figure 4.21: Identification of VAPB S158 as a phosphorylation site by LC-MS/MS. Tandem mass spectrometry spectrum of the VAPB phosphopeptide ^{156}SLpSSSLDDTEVKK^{168} (m/z 744.85^{2+}) fragment ion series after collision induced dissociation. The m/z of the ions is plotted against intensity and the detected ions of the b- (red) and y- (blue) ion collision series are indicated on the sequence of the peptide (top left). A constant neutral loss of phosphoric acid, 98, from the parent ion was present at m/z 696.06^{2+} and is indicative of either a serine or threonine phosphorylation on the peptide. Loss of phosphoric acid from b-3 and both singly and doubly charged y-11 ions, (indicated by arrows on the spectrum) localize this phosphorylation to S158.

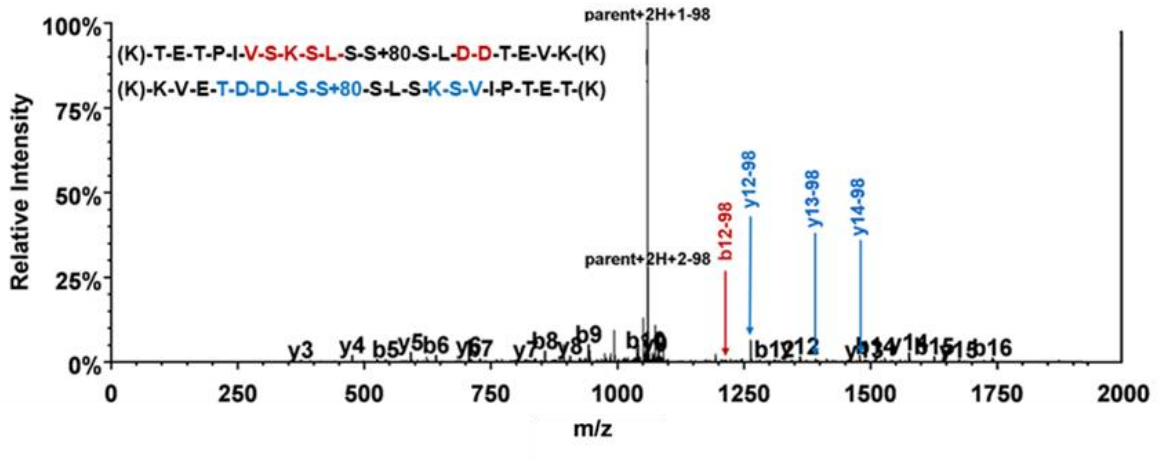

Figure 4.22: Identification of VAPB S159 as a phosphorylation site by LC-MS/MS. Tandem mass spectrometry spectrum of the VAPB phosphopeptide ^{148}TETPIVSKSLSpSSLDDTEVK^{167} (m/z 1,108.53^{2+}) fragment ion series after collision induced dissociation. The m/z of the ions is plotted against intensity and the detected ions of the b- (red) and y- (blue) ion collision series are indicated on the sequence of the peptide (top left). A constant neutral loss of phosphoric acid, 98, from the parent ion was present at m/z 1059.90^{2+} and is indicative of either a serine or threonine phosphorylation on the peptide. Loss of phosphoric acid from b-12, but not b-5 to b-11 ions, and from y-12 to y-14 ions, (indicated by arrows on the spectrum) localize this phosphorylation to S159.

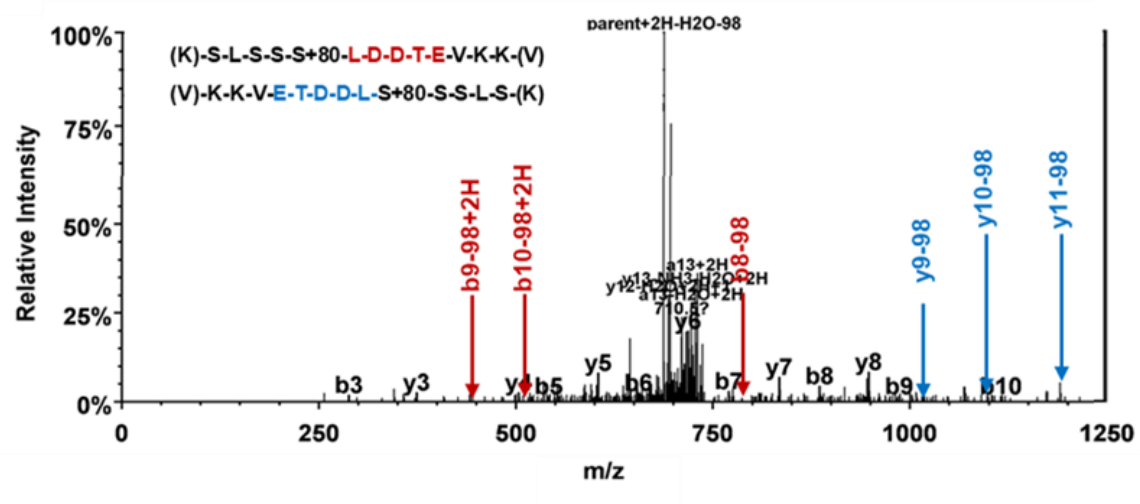

Figure 4.23: Identification of VAPB S160 as a phosphorylation site by LC-MS/MS. Tandem mass spectrometry spectrum of the VAPB phosphopeptide ^{156}SLSSpSLDDTEVKK^{168} (m/z 744.85^{2+}) fragment ion series after collision induced dissociation. The m/z of the ions is plotted against intensity and the detected ions of the b- (red) and y- (blue) ion collision series are indicated on the sequence of the peptide (top left). A constant neutral loss of phosphoric acid, 98, from the parent ion was present at m/z 696.13^{2+} and is indicative of either a serine or threonine phosphorylation on the peptide. Loss of phosphoric acid from singly charged b-8 and doubly charged b-9 and b-10 ions, and from y-9 to y-11 ions, (indicated by arrows on the spectrum) localize this phosphorylation to S160.

4.2.5 Identification of phosphorylation sites in PTPIP51 in cells in which GSK-3β is activated by overexpression

In a similar fashion to the experiments described above for VAPB, cellular phosphorylation of PTPIP51 was studied to identify phosphorylation sites in cells. Full length PTPIP51 with a C-terminal HA tag was exogenously expressed in HEK-293 cells with either control vector (Ctrl) or vector expressing GSK-3β: overexpression of GSK-3β was conducted to increase the possibility of identifying GSK-3β phosphorylation sites. Cells were lysed 24 hrs after transfection and a small sample was probed for GSK-3β by immunoblot to check for over-expression in the GSK-3β transfected cells (Figure 4.24). GSK-3β expression was detected in cells overexpressing GSK-3β, but endogenous GSK-3β was not detected. This is likely due to the small amount of cell lysis sample used to check for GSK-3β. PTPIP51-HA was immunoprecipitated from both samples via the HA tag and proteins were separated by SDS-PAGE and stained with imperial protein stain (Figure 4.24). As above, the experiment was carried out in triplicate and PTPIP51-HA bands from all three samples were excised for mass spectrometric analysis. Gel bands of isolated PTPIP51-HA were prepared, including digestion of the protein with trypsin, as detailed in 2.2.12 for LC-MS/MS which was carried out at the King's College London Proteomics facility.

A)

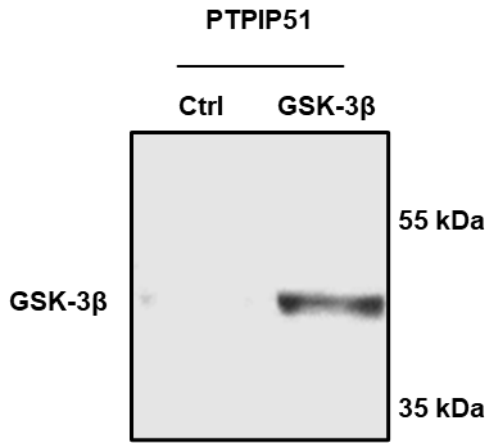

B)

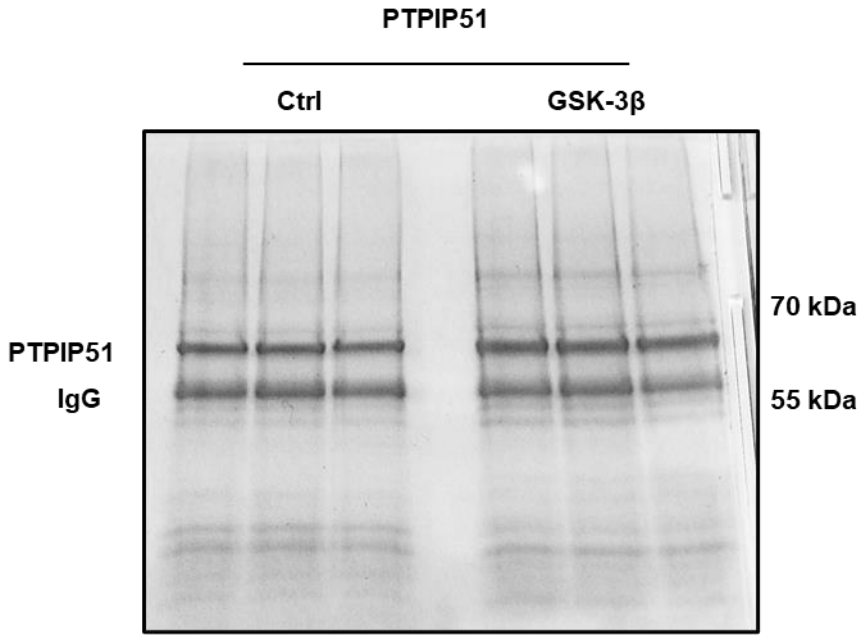

Figure 4.24: Overexpression of GSK-3β and purification of PTPIP51-HA for LC-MS/MS analysis of phosphorylation. HEK-293 cells were transfected with PTPIP51-HA and either control vector or GSK-3β. Cells were lysed 24 hrs after transfection and a sample was probed for GSK-3β expression by immunoblot (A). PTPIP51-HA was immunoprecipitated using a HA antibody, separated on an SDS-PAGE gel, and stained with imperial protein stain (B). The positions of GSK-3β, PTPIP51 and Immunoglobulin heavy chain (IgG) are shown and molecular mass markers are shown on the right.

LC-MS/MS of PTPIP51-HA isolated from cells expressing only endogenous GSK-3β identified peptides corresponding to PTPIP51-HA and provided sequence coverage of 82 % of the full-length human protein (Figure 4.25). Twelve individual sites of phosphorylation were identified and analysis of the corresponding fragmentation spectra of these phosphopeptides confirmed the localisation of phosphorylation to threonine resides T54 and T56 and serine residues S44, S46, S50, S57, S77, S81, S193, S225, S272 and S285. Doubly phosphorylated peptides were identified, corresponding to phosphorylation at S44 and S46, S44 and S50, S46 and S57, S46 and S50.

LC-MS/MS of PTPIP51-HA isolated from cells over-expressing exogenous GSK-3β identified peptides corresponding to PTPIP51-HA and provided sequence coverage of 83 % of the full-length human protein (Figure 4.26). Ten individual sites of phosphorylation were identified and analysis of the corresponding fragmentation spectra of these phosphopeptides confirmed the localisation of phosphorylation to serine residues S44, S46, S50, S57, S77, S81, S193, S212, S285 and to tyrosine residue Y284. Doubly phosphorylated peptides were identified, corresponding to phosphorylation at S44 and S50, S46 and S57, S46 and S50. One triply phosphorylated peptide was identified, with phosphorylation at residues S44, S46, S50. Phosphorylation at residue S212 was found in PTPIP51 from cells over-expressing GSK-3β but not in PTPIP51 from control cells.

One representative fragmentation spectrum is shown for one phosphopeptide representing each phosphorylation site found in PTPIP51, either from cells expressing only endogenous GSK-3β or from cells overexpressing GSK-3β. Spectra are shown for residues S44, S46, S50, T54, T56, S57, S77, S81, S193, S212, S225, Y284, S285 in figures 4.27, 4.28, 4.29, 4.30, 4.31, 4.32, 4.34, 4.35, 4.36, 4.37, 4.38, 4.39 and 4.40 respectively.

A)

MSRLGALGGARAGLGLLLGTAAGLGFLCLLYSQRWKRTQRHGRSQSLPNSLDYTQTSDPG
RHVMLLRAVPGGAGDASVLPSLPREGQEKVLDRLDFVLTSLVALRREVEELRSSLRGLAGEI
VGEVRCHMEENQRVARRRRFPFVRERSDSTGSSSVYFTASSGATFTDAESEGGYTTANAES
DNERDSDKESEDGEDEVSCETVKMGRKDSLDLEEEAASGASSALEAGGSSGLEDVLPLLQ
QADELHRGDEQGKREGFQLLLNNKLVYGSRQDFLWRLARAYSDMCELTEEVSEKKSYALDG
KEEAEAALEKGDESADCHLWYAVLCGQLAEHESIQRRIQSGFSFKEHVDKAIALQPENPMAH
FLLGRWCYQVSHLSWLEKKTATALLESPLSATVEDALQSFLKAEELQPGFSKAGRVYISKCY
RELGKNSEARWWMKLALELPDVTKEDLAIQKDLEELEVILRD

B)

Peptide Sequence	Peptide m/z	Modification
^{41}HGR**pS**Q**pS**LPNSLDYTQTSDPGR^{61}	826.01^{3+}	S44, S46
^{41}HGR**pS**QSLPNSLDYTQTSDPGR^{61}	799.36^{3+}	S44
^{41}HGR**pS**QSLPN**pS**LDYTQTSDPGR^{61}	1238.52^{2+}	S44, S50
^{41}HGRSQ**pS**LPNSLDYTQTSDPGR^{61}	1198.54^{2+}	S46
^{44}SQ**pS**LPNSLDYTQT**pS**DPGR^{61}	1063.43^{2+}	S46, S57
^{44}SQSLPN**pS**LDYTQTSDPGR^{61}	1023.45^{2+}	S50
^{44}SQSLPNSLDYTQ**pT**SDPGR^{61}	1023.45^{2+}	T56
^{44}SQ**pS**LPN**pS**LDYTQTSDPGR^{61}	1063.43^{2+}	S46, S50
^{44}SQSLPNSLDY**pT**QTSDPGR^{61}	683.63^{3+}	T54
^{68}AVPGGAGDA**pS**VLPSLPR^{84}	822.41^{2+}	S77
^{68}AVPGGAGDASVLP**pS**LPR^{84}	822.41^{2+}	S81
^{188}DSDKE**pS**EDGEDEVSCETVK^{206}	1119.42^{2+}	S193
^{210}KDSLDLEEEAASGAS**pS**ALEAGGSSGLEDVLPLLQQADELHR^{250}	1430.01^{3+}	S225
^{268}LVYG**pS**RQDFLWR^{279}	810.39^{2+}	S272
^{283}AY**pS**DMCELTEEVSEK^{297}	907.35^{2+}	S285

Figure 4.25: Phosphorylation sites identified in PTPIP51 isolated from cells expressing endogenous GSK-3β. (A) Sequence of full length human PTPIP51 with the MS/MS sequence coverage of 82 % shown as underlined. Twelve phosphorylation sites were identified, shown red and detailed in B) under “Modification”. (B) PTPIP51 phosphopeptides obtained by MS/MS sequencing with their mass/charge (m/z) ratios and position of phosphorylation. Phosphorylated residues shown in red.

A)

MSRLGALGGARAGLGLLLGTAAGLGFLCLLYSQRWKRTQRHGRSQSLPNSLDYTQTSDPGRH
VMLLRAVPGGAGDASVLPSLPREGQEKVLDRLDFVLTSLVALRREVEELRSSLRGLAGEIVGEV
RCHMEENQRVARRRRFPFVRERSDSTGSSSVYFTASSGATFTDAESEGGYTTANAESDNERD
SDKESEDGEDEVSCETVKMGRKDSLDLEEEAASGASSALEAGGSSGLEDVLPLLQQADELHR
GDEQGKREGFQLLLNNKLVYGSRQDFLWRLARAYSDMCELTEEVSEKKSYALDGKEEAEAALE
KGDESADCHLWYAVLCGQLAEHESIQRRIQSGFSFKEHVDKAIALQPENPMAHFLLGRWCYQV
SHLSWLEKKTATALLESPLSATVEDALQSFLKAEELQPGFSKAGRVYISKCYRELGKNSEARWW
MKLALELPDVTKEDLAIQKDLEELEVILRD

B)

Peptide Sequence	Peptide m/z	Modification
^{41}HGR**pS**QSLPNSLDYTQTSDPGR^{61}	799.36^{3+}	S44
^{41}HGR**pS**QSLPN**pS**LDYTQTSDPGR^{61}	826.02^{3+}	S44, S50
^{41}HGR**pS**Q**pS**LPN**pS**LDYTQTSDPGR^{61}	1278.50^{2+}	S44, S46, S50
^{41}HGRSQ**pS**LPNSLDYTQTSDPGR^{61}	1198.53^{2+}	S46
^{44}SQ**pS**LPNSLDYTQT**pS**DPGR^{61}	1063.43^{2+}	S46, S57
^{44}SQSLPN**pS**LDYTQTSDPGR^{61}	1023.45^{2+}	S50
^{44}SQSLPNSLDYTQT**pS**DPGR^{61}	1023.45^{2+}	S57
^{44}SQ**pS**LPN**pS**LDYTQTSDPGR^{61}	1063.43^{2+}	S46, S50
^{68}AVPGGAGDA**pS**VLPSLPR^{84}	822.41^{2+}	S77
^{68}AVPGGAGDASVLP**pS**LPR^{84}	822.41^{2+}	S81
^{188}DSDKE**pS**EDGEDEVSCETVK^{206}	1119.42^{2+}	S193
^{210}KD**pS**LDLEEEAASGASSALEAGGSSGLEDVLPLLQQADELHR^{250}	1430.01^{3+}	S212
^{283}A**pY**SDMCELTEEVSEK^{297}	907.35^{2+}	Y284
^{283}AY**pS**DMCELTEEVSEKK^{298}	907.35^{2+}	S285

Figure 4.26: Phosphorylation sites identified in PTPIP51 isolated from cells overexpressing exogenous GSK-3β. (A) Sequence of full length human PTPIP51 with the MS/MS sequence coverage of 83 % shown as underlined. Ten phosphorylation sites were identified, shown red and detailed in B) under “Modification”. (B) PTPIP51 phosphopeptides obtained by MS/MS sequencing with their mass/charge (m/z) ratios and position of phosphorylation. Phosphorylated residues shown in red.

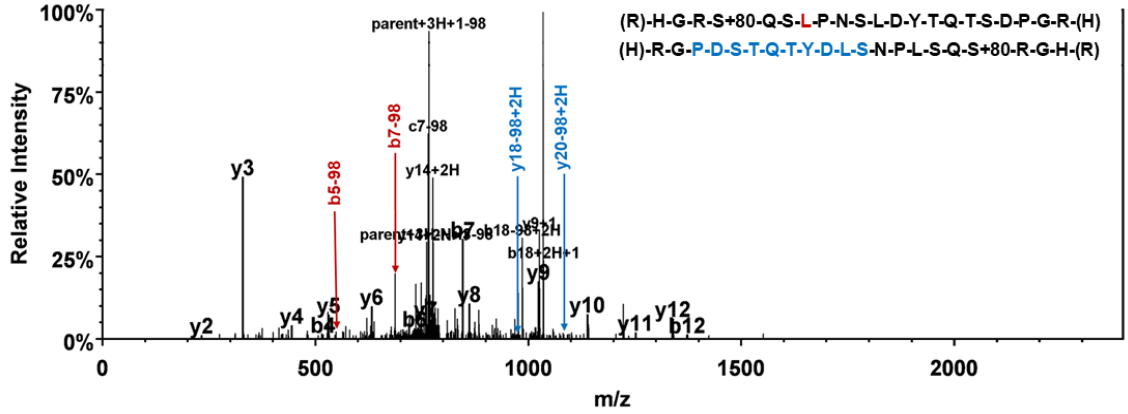

Figure 4.27: Identification of PTPIP51 S44 as a phosphorylation site by LC-MS/MS. Tandem mass spectrometry spectrum of the PTPIP51 phosphopeptide ^{41}HGRpSQSLPNSLDYTQTSDPGR^{61} (m/z 799.36^{3+}) fragment ion series after collision induced dissociation. The m/z of the ions is plotted against intensity and the detected ions of the b- (red) and y- (blue) ion collision series are indicated in the sequence of the peptide (top left). A loss of 98, indicating a constant neutral loss of phosphoric acid, from the parent ion is present at m/z 767.12^{3+} and is indicative of either a serine or threonine phosphorylation on the peptide. Loss of phosphoric acid from b-5 and b-7 ions, and from doubly charged y-18 and y-20 ions (indicated by arrows on the spectrum), localize this phosphorylation to S44 (highlighted red in peptide sequence).

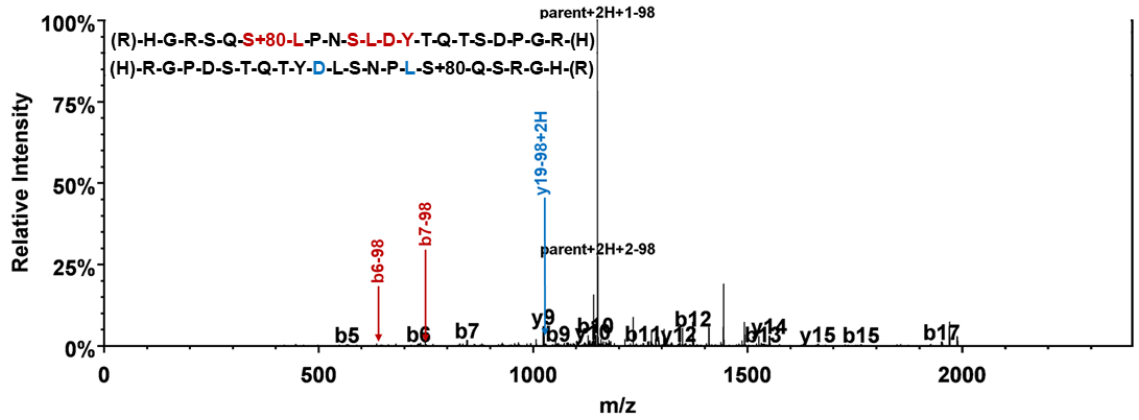

Figure 4.28: Identification of PTPIP51 S46 as a phosphorylation site by LC-MS/MS. Tandem mass spectrometry spectrum of the PTPIP51 phosphopeptide ^{41}HGRSQpSLPNSLDYTQTSDPGR^{61} (m/z 1198.53^{2+}) fragment ion series after collision induced dissociation. The m/z of the ions is plotted against intensity and the detected ions of the b- (red) and y- (blue) ion collision series are indicated in the sequence of the peptide (top left). A loss of 98, indicating a constant neutral loss of phosphoric acid, from the parent ion is present at m/z 1149.89^{2+} and is indicative of either a serine or threonine phosphorylation on the peptide. Loss of phosphoric acid from the doubly charged y-19 ion and from b-6 and b-7 ions, but not from the b-5 ion, (indicated by arrows on the spectrum), localize this phosphorylation to S46 (highlighted red in peptide sequence).

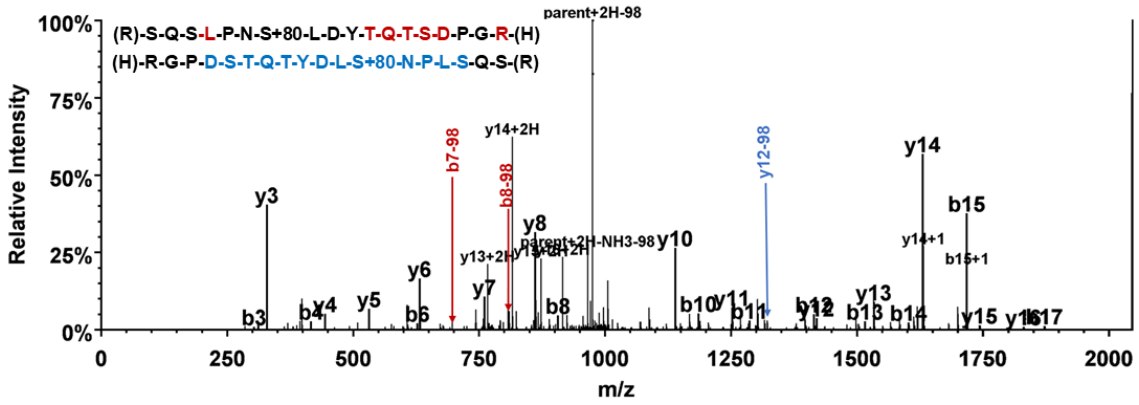

Figure 4.29: Identification of PTPIP51 S50 as a phosphorylation site by LC-MS/MS. Tandem mass spectrometry spectrum of the PTPIP51 phosphopeptide ^{44}SQSLPNpSLDYTQTSDPGR^{61} (m/z 1023.45^{2+}) fragment ion series after collision induced dissociation. The m/z of the ions is plotted against intensity and the detected ions of the b- (red) and y- (blue) ion collision series are indicated in the sequence of the peptide (top left). A loss of 98, indicating a constant neutral loss of phosphoric acid, from the parent ion is present at m/z 974.65^{2+} and is indicative of either a serine or threonine phosphorylation on the peptide. Loss of phosphoric acid from b-7 and b-8 ions, but not from the b-1, b-2 or b3 ions, and from y-12 but not y-16 ions (indicated by arrows on the spectrum), localize this phosphorylation to S50 (highlighted red in peptide sequence).

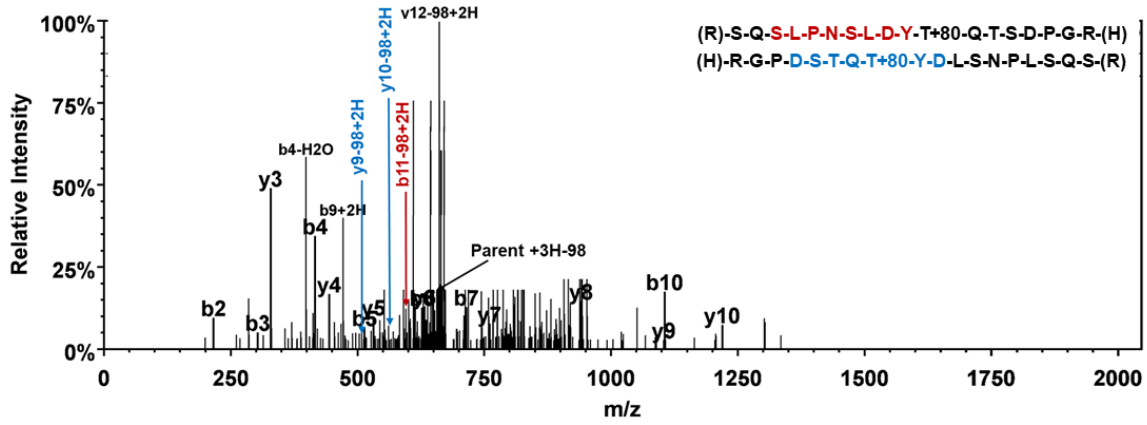

Figure 4.30: Identification of PTPIP51 T54 as a phosphorylation site by LC-MS/MS. Tandem mass spectrometry spectrum of the PTPIP51 phosphopeptide ^{44}SQSLPNSLDYpTQTSDPGR^{61} (m/z 682.63^{3+}) fragment ion series after collision induced dissociation. The m/z of the ions is plotted against intensity and the detected ions of the b- (red) and y- (blue) ion collision series are indicated in the sequence of the peptide (top left). A loss of 98, indicating a constant neutral loss of phosphoric acid, from the parent ion is present at m/z 650.25^{3+} and is indicative of either a serine or threonine phosphorylation on the peptide. Loss of phosphoric acid from doubly charged b-11 and doubly charged y-9 and y-10 ions (indicated by arrows on the spectrum), localize this phosphorylation to T54 (highlighted red in peptide sequence).

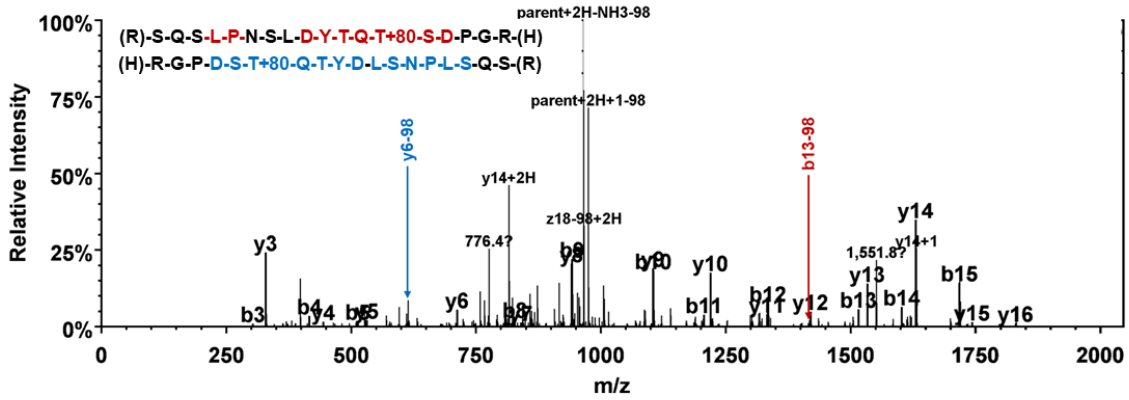

Figure 4.31: Identification of PTPIP51 T56 as a phosphorylation site by LC-MS/MS. Tandem mass spectrometry spectrum of the PTPIP51 phosphopeptide ^{44}SQSLPNSLDYTQpTSDPGR^{61} (m/z 1023.45^{2+}) fragment ion series after collision induced dissociation. The m/z of the ions is plotted against intensity and the detected ions of the b- (red) and y- (blue) ion collision series are indicated in the sequence of the peptide (top left). A loss of 98, indicating a constant neutral loss of phosphoric acid, from the parent ion is present at m/z 965.75^{2+} and is indicative of either a serine or threonine phosphorylation on the peptide. Loss of phosphoric acid from b-13 and y-6 ions (indicated by arrows on the spectrum), localize this phosphorylation to T56 (highlighted red in peptide sequence).

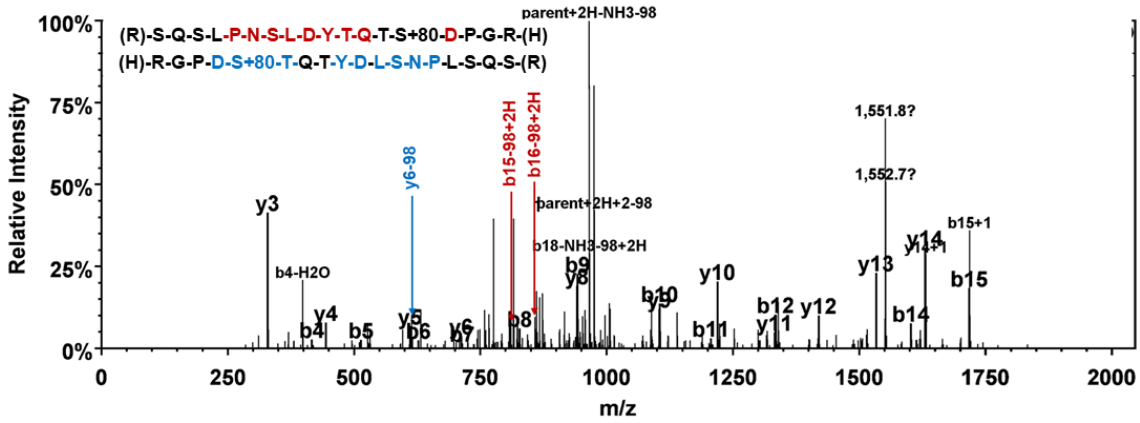

Figure 4.32: Identification of PTPIP51 S57 as a phosphorylation site by LC-MS/MS. Tandem mass spectrometry spectrum of the PTPIP51 phosphopeptide ^{44}SQSLPNSLDYTQTpSDPGR^{61} (m/z 1023.45^{2+}) fragment ion series after collision induced dissociation. The m/z of the ions is plotted against intensity and the detected ions of the b- (red) and y- (blue) ion collision series are indicated in the sequence of the peptide (top left). A loss of 98, indicating a constant neutral loss of phosphoric acid, from the parent ion is present at m/z 974.80^{2+} and is indicative of either a serine or threonine phosphorylation on the peptide. Loss of phosphoric acid from y-6 and doubly charged b-15 and b-16 ions, but not from b-4 to b-12 ions (indicated by arrows on the spectrum), localize this phosphorylation to S57 (highlighted red in peptide sequence).

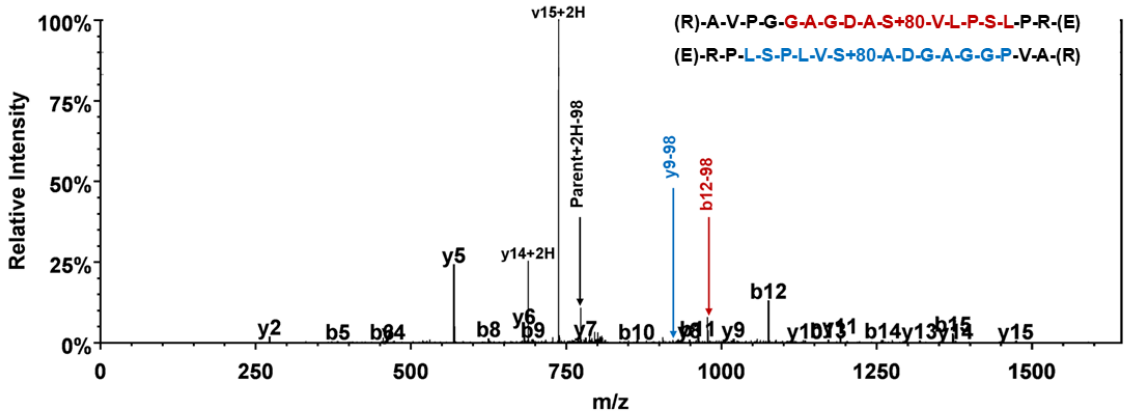

Figure 4.33: Identification of PTPIP51 S77 as phosphorylation site by LC-MS/MS. Tandem mass spectrometry spectrum of the PTPIP51 phosphopeptide ^{68}AVPGGAGDApSVLPSLPR^{84} (m/z 822.41^{2+}) fragment ion series after collision induced dissociation. The m/z of the ions is plotted against intensity and the detected ions of the b- (red) and y- (blue) ion collision series are indicated in the sequence of the peptide (top left). A loss of 98, indicating a constant neutral loss of phosphoric acid, from the parent ion is present at m/z 773.56^{2+} and is indicative of either a serine or threonine phosphorylation on the peptide. Loss of phosphoric acid from b-12 and y-9 ions (indicated by arrows on the spectrum), localize this phosphorylation to S77 (highlighted red in peptide sequence).

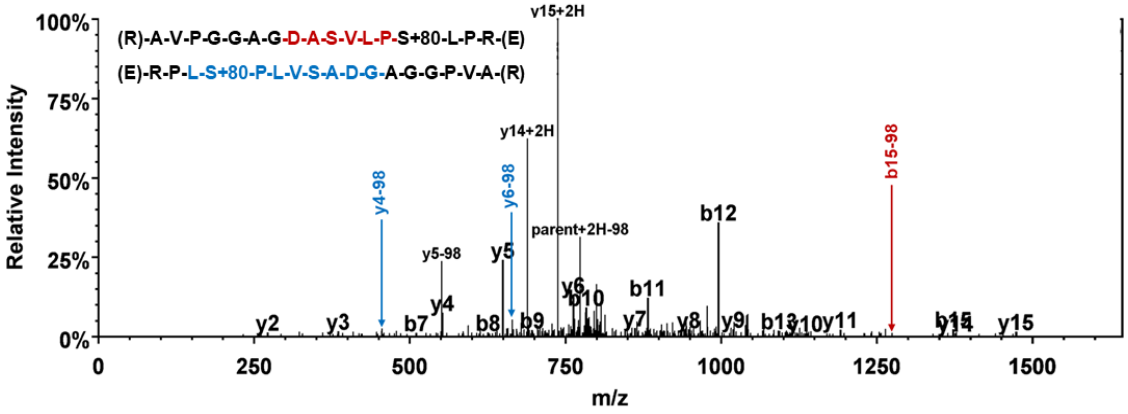

Figure 4.34: Identification of PTPIP51 S81 as phosphorylation site by LC-MS/MS. Tandem mass spectrometry spectrum of the PTPIP51 phosphopeptide ^{68}AVPGGAGDASVLPpSLPR^{84} (m/z 822.41^{2+}) fragment ion series after collision induced dissociation. The m/z of the ions is plotted against intensity and the detected ions of the b- (red) and y- (blue) ion collision series are indicated in the sequence of the peptide (top left). A loss of 98, indicating a constant neutral loss of phosphoric acid, from the parent ion is present at m/z 773.57^{2+} and is indicative of either a serine or threonine phosphorylation on the peptide. Loss of phosphoric acid from b-15 and y-4 and y-6 ions (indicated by arrows on the spectrum), localize this phosphorylation to S81 (highlighted red in peptide sequence).

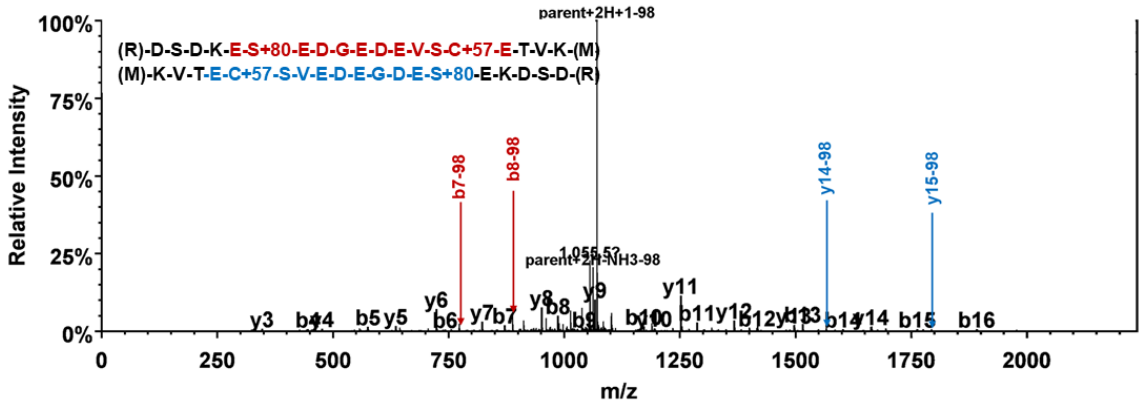

Figure 4.35: Identification of PTPIP51 S193 as phosphorylation site by LC-MS/MS. Tandem mass spectrometry spectrum of the PTPIP51 phosphopeptide ^{188}DSDKEpSEDGEDEVScETVK^{206} (m/z 1119.42^{2+}) fragment ion series after collision induced dissociation. The m/z of the ions is plotted against intensity and the detected ions of the b- (red) and y- (blue) ion collision series are indicated in the sequence of the peptide (top left). A loss of 98, indicating a constant neutral loss of phosphoric acid, from the parent ion is present at m/z 1070.76^{2+} and is indicative of either a serine or threonine phosphorylation on the peptide. Loss of phosphoric acid from b-7 and b-8, y-14 and y-15 ions (indicated by arrows on the spectrum), localize this phosphorylation to S193 (highlighted red in peptide sequence).

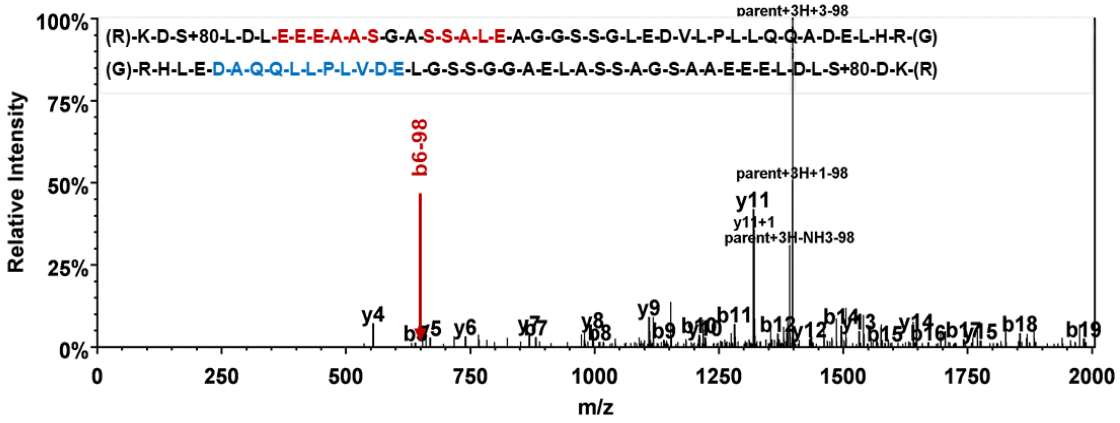

Figure 4.36: Identification of PTPIP51 S212 as a phosphorylation site by LC-MS/MS. Tandem mass spectrometry spectrum of the VAPB phosphopeptide ^{210}KDpSLDLEEEAASGASSALEAGGSSGLEDVLPLLQQADELHR^{250} (m/z 1430.01^{3+}) fragment ion series after collision induced dissociation. The m/z of the fragment ions is plotted against intensity and the detected ions of the b- (red) and y- (blue) ion collision series are indicated on the sequence of the peptide (top left). A constant neutral loss of phosphoric acid, 98, from the parent ion was present at m/z 1398.27^{3+} and is indicative of either a serine or threonine phosphorylation on the peptide. Loss of phosphoric acid at the b-6 ion (indicated by arrows on the spectrum), localizes this phosphorylation to S212.

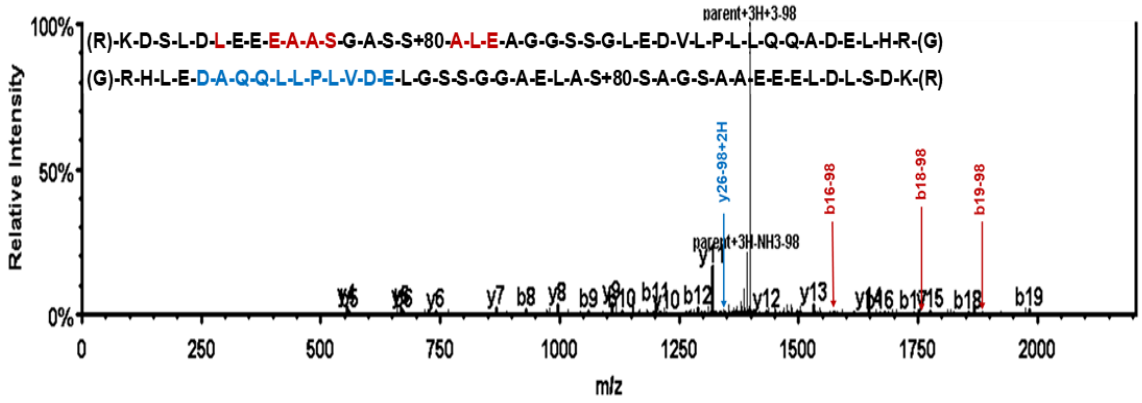

Figure 4.37: Identification of PTPIP51 S225 as a phosphorylation site by LC-MS/MS. Tandem mass spectrometry spectrum of the VAPB phosphopeptide ^{210}KDSLDLEEEAASGASpSALEAGGSSGLEDVLPLLQQADELHR^{250} (m/z 1430.01^{3+}) fragment ion series after collision induced dissociation. The m/z of the fragment ions is plotted against intensity and the detected ions of the b- (red) and y- (blue) ion collision series are indicated on the sequence of the peptide (top left). A constant neutral loss of phosphoric acid, 98, from the parent ion was present at m/z 1398.07^{3+} and is indicative of either a serine or threonine phosphorylation on the peptide. Loss of phosphoric acid at the doubly charged y-26 ion and the b-16, b-18 and b-19 ions (indicated by arrows on the spectrum), localizes this phosphorylation to S225.

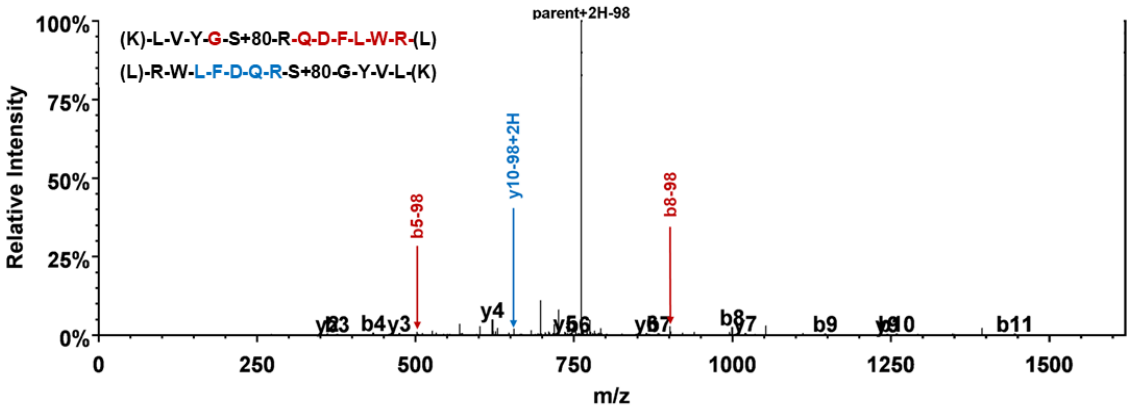

Figure 4.38: Identification of PTPIP51 S272 as a phosphorylation site by LC-MS/MS. Tandem mass spectrometry spectrum of the VAPB phosphopeptide ^{268}LVYGpSRQDFLWR^{279} (m/z 810.39^{2+}) fragment ion series after collision induced dissociation. The m/z of the fragment ions is plotted against intensity and the detected ions of the b- (red) and y- (blue) ion collision series are indicated on the sequence of the peptide (top left). A constant neutral loss of phosphoric acid, 98, from the parent ion was present at m/z 761.60^{2+} and is indicative of either a serine or threonine phosphorylation on the peptide. Loss of phosphoric acid at the doubly charged y-10 ion and the b-5 and b-8 ions (indicated by arrows on the spectrum), localizes this phosphorylation to S272.

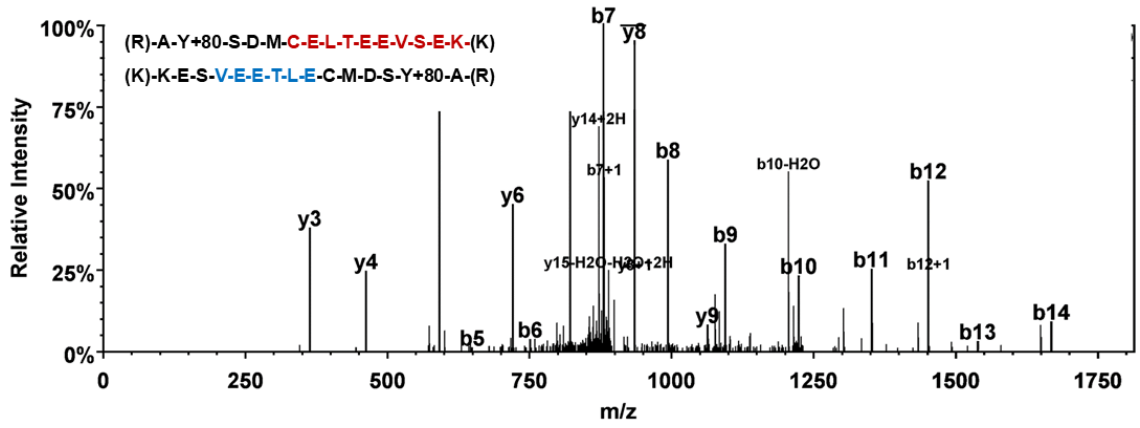

Figure 4.39: Identification of PTPIP51 Y284 as a phosphorylation site by LC-MS/MS. Tandem mass spectrometry spectrum of the VAPB phosphopeptide ^{283}ApYSDMCELTEEVSEK^{297} (m/z 907.35^{2+}) fragment ion series after collision induced dissociation. The m/z of the fragment ions is plotted against intensity and the detected ions of the b- (red) and y- (blue) ion collision series are indicated on the sequence of the peptide (top left). No constant neutral loss from the parent ion was detected, implying that neither serine nor threonine phosphorylation was present on the peptide. Good fragmentation coverage of the peptide sequence provides weak confirmation of phosphorylation at Y284.

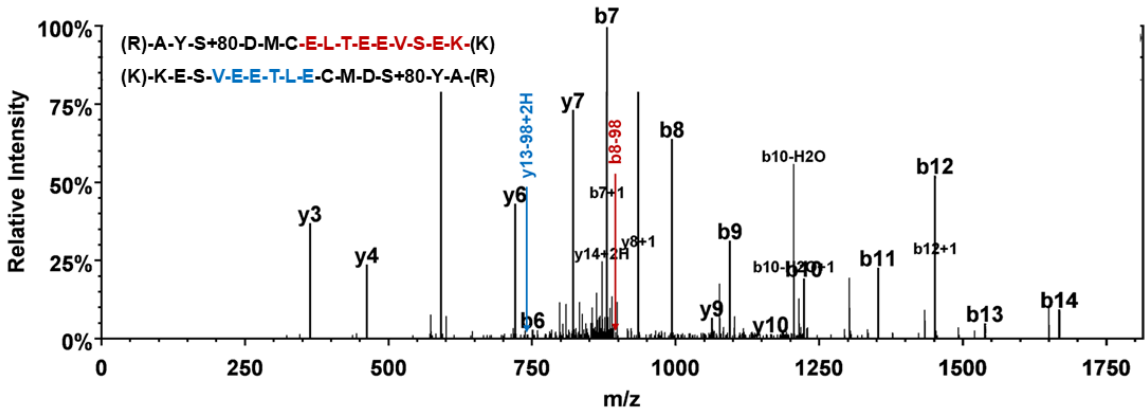

Figure 4.40: Identification of PTPIP51 S285 as a phosphorylation site by LC-MS/MS. Tandem mass spectrometry spectrum of the VAPB phosphopeptide ^{283}AYpSDMCELTEEVSEK^{297} (m/z 907.35^{2+}) fragment ion series after collision induced dissociation. The m/z of the fragment ions is plotted against intensity and the detected ions of the b- (red) and y- (blue) ion collision series are indicated on the sequence of the peptide (top left). A constant neutral loss was not detected at the parent ion. However, good fragmentation coverage of the peptide sequence and loss of phosphoric acid at the doubly charged y-13 ion and the b-8 ion (indicated by arrows on the spectrum), localizes phosphorylation to S285.

4.2.6 Identification of phosphorylation sites in VAPB in cells in which AMPK is activated

As detailed above, there is the possibility that AMPK phosphorylates serine 158 in VAPB, based on the corresponding site in VAPA which is phosphorylated by AMPK. Given this evidence and the proposed role of dysregulated AMPK activity in ALS, this study next investigated whether AMPK phosphorylated either VAPB or PTPIP51.

A number of chemical activators of AMPK have been reported, AICAR and A-769662 are two such activators. A-769662 is reported to act more specifically (Vincent et al., 2014) and studies were therefore conducted to investigate the effect of A-769662 in comparison to AICAR on AMPK activity. To do this, HEK-293 cells were treated with either vehicle (DMSO), AICAR, or A-769662 for 2 hrs. AMPK is activated either by nucleoside binding or by phosphorylation at T172. One of the most abundant targets of activated AMPK is Acetyl-CoA Carboxylase (ACC) which is primarily phosphorylated at serine 79. As such, lysates were probed on immunoblots with antibodies to total AMPK and total ACC and phospho-specific antibodies to AMPK T172 (P-AMPK) and ACC S79 (P-ACC) (Figure 4.41). AMPK has a predicted molecular weight of 63 kDa and ACC has a predicted molecular weight of 265 kDa. Neither treatment affected the expression of total AMPK or ACC. Both AICAR and A-769662 increased the phosphorylation of AMPK, but only A-769662 appeared to increased phosphorylation of ACC. For both its reported selectivity and its demonstrated activity in these experiments, A-769662 was used to enhance AMPK activity in cells in order to investigate AMPK phosphorylation of VAPB and PTPIP51.

Full length, myc-tagged VAPB was exogenously expressed in HEK-293 cells and cells were subsequently treated with either DMSO (vehicle) or A-769662 for 2 hrs. A sample of cell lysate was probed by immunoblot to confirm VAPB expression (Figure 4.42A). Myc-VAPB was immunoprecipitated from both samples via the myc tag and proteins were separated by SDS-PAGE and stained with imperial protein stain (Figure 4.42B). In this experiment, VAPB was immunoprecipitated at a higher yield from cells treated with A-769662 as can be seen by the more intense band on the SDS-PAGE gel in the A-769662 treated cells (Figure 4.42B). Although there is a low yield of VAPB from DMSO treated cells, as in 4.2.5, the experiment was carried out in triplicate and all three bands were excised to ensure sufficient material for mass spectrometric analysis. Gel bands of isolated Myc-VAPB were prepared, including digestion with trypsin, as detailed in 2.2.12 for LC-MS/MS which was carried out at the King's College London Proteomics Facility.

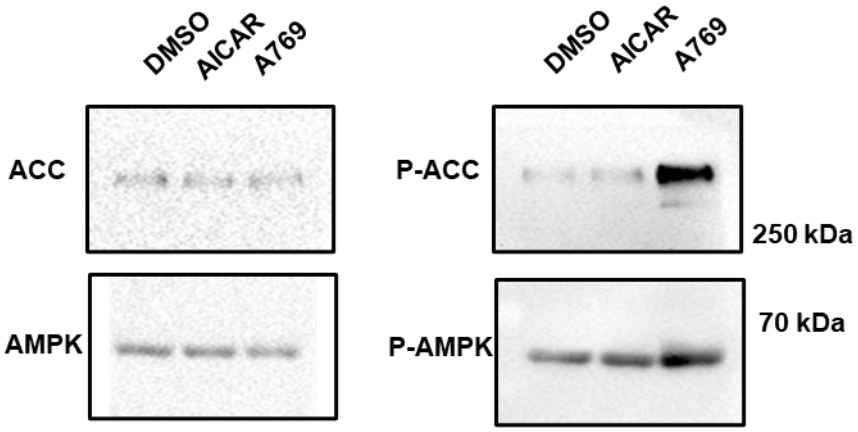

Figure 4.41: Activation of AMPK using AICAR and A-769662. HEK-293 cells were treated for 2 hrs with either DMSO vehicle control, AICAR or A-769662 (A769). Cells were lysed and probed on immunoblots for total AMPK and ACC, AMPK phosphorylated at T172 (P-AMPK) and ACC phosphorylated at S79 (P-ACC). The positions of proteins are indicated and mass markers are shown on the right.

A)

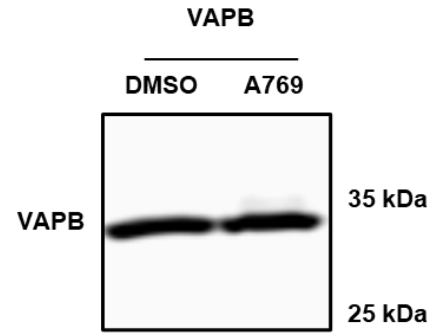

B)

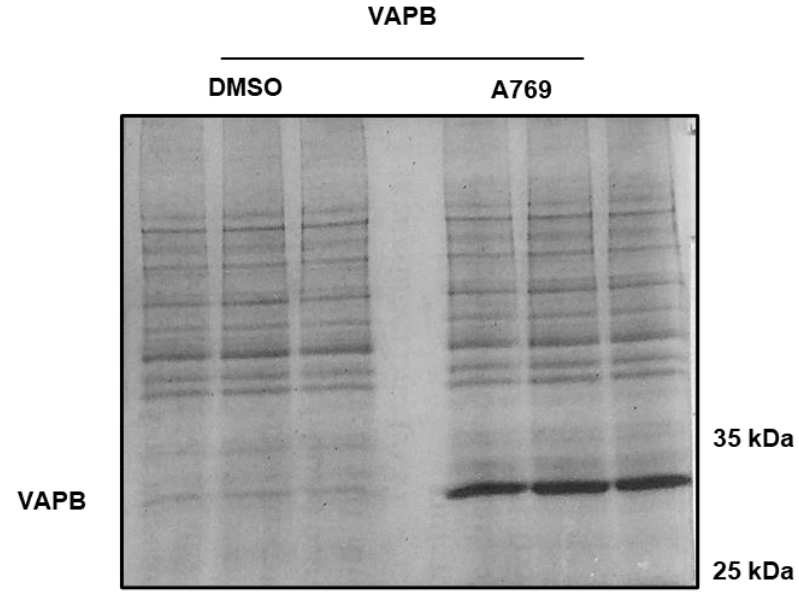

Figure 4.42: Overexpression and purification of Myc-VAPB for LC-MS/MS analysis of phosphorylation. HEK-293 cells were transfected with Myc-VAPB for 22 hrs and then treated with either DMSO vehicle control or A-769662 (A769). Cells were lysed 24 hrs after transfection and a sample was probed for VAPB expression on immunoblots (A). Myc-VAPB was immunoprecipitated using a Myc antibody, separated on an SDS-PAGE gel and stained with imperial protein stain (B). The position of VAPB is shown and molecular mass markers are shown on the right.

LC-MS/MS of myc-VAPB isolated from cells treated with vehicle control DMSO, identified peptides corresponding to myc-VAPB and provided sequence coverage of 76 % of the full-length human protein (Figure 4.43). Eight individual sites of phosphorylation were identified and analysis of the corresponding fragmentation spectra of these phosphopeptides confirmed the localisation of phosphorylation to threonine residue T143, T144, T148, T150, and serine residues S156, S158 and S159. One doubly phosphorylated peptide was identified, with phosphorylation at both S156 and S158 residues.

LC-MS/MS of myc-VAPB isolated from cells treated with the AMPK activator A-769662 identified peptides corresponding to myc-VAPB and provided sequence coverage of 72 % of the full-length human protein (Figure 4.44). Four individual sites of phosphorylation were identified and analysis of the corresponding fragmentation spectra of these phosphopeptides confirmed the localisation of phosphorylation to threonine residue T150 and serine residues S156, S158 and S159. One doubly phosphorylated peptide was identified, with phosphorylation at both S158 and S159 residues.

No phosphorylation sites were found in VAPB from cells treated with A-769662 that were not also found in VAPB from control cells. However, residues T143, T144 and T146 were found to be phosphorylated in VAPB from control cells but not in VAPB from cells treated with A-769662. The predicted AMPK phosphorylation site, S158 was found to be phosphorylated in VAPB from both samples.

One representative phosphopeptide fragmentation spectrum is shown for each of the phosphorylation sites found in VAPB from cells either treated with DMSO or A-769662 that have not yet been found in cells in this work. Representative fragmentation spectra for phosphorylation residues T144, T150, S156, S158 and S159 are shown in section 4.2.4. Representative fragmentation spectra for phosphorylation residues T143 and T148 are shown in figures 4.45 and 4.46 respectively.

A)

MAKVEQVLSLEPQHELKFRGPFTDVVTTNLKLGNPTDRNVCFKVKTTAPRRYCVRPNSGIIDAG
ASINVSVMLQPFDYDPNEKSKHKFMVQSMFAPTDTSDMEAVWKEAKPEDLMDSKLRCVFELPA
ENDKPHDVEINKIISTTASKTETPIVSKSLSSSLDDTEVKKVMEECKRLQGEVQRLREENKQFKE
EDGLRMRKTVQSNSPISALAPTGKEEGLSTRLLALVVLFFIVGVIIGKIAL

B)

Peptide Sequence	**Peptide m/z**	**Modification**
^{140}IIS**pT**TASKTETPIVSK^{155}	585.98^{3+}	T143
^{140}IIST**pT**ASKTETPIVSK^{155}	878.46^{2+}	T144
^{140}IISTTASK**pT**ETPIVSK^{155}	585.98^{3+}	T148
^{140}IISTTASKTE**pT**PIVSK^{155}	878.46^{2+}	T150
^{140}IISTTASKTETPIVSK**pS**LSSSLDDTEVK^{167}	1006.51^{3+}	S156
^{140}IISTTASKTETPIVSK**pS**L**pS**SSLDDTEVK^{167}	1148.51^{3+}	S156, S158
^{156}SL**pS**SSLDDTEVKK^{168}	744.85^{2+}	S158
^{156}SLS**pS**SLDDTEVKK^{168}	744.85^{2+}	S159

Figure 4.43: Phosphorylation sites identified in VAPB isolated from cells treated with DMSO vehicle control. (A) Sequence of full length human VAPB with the MS/MS sequence coverage of 76 % shown as underlined. Seven phosphorylation sites were identified (T143, T144, T148, T150, S156, S158, S159), shown in red. (B) VAPB phosphopeptides obtained by MS/MS sequencing with their mass/charge (m/z) ratios. Phosphorylated residues shown in red.

A)

MAKVEQVLSLEPQHELKFRGPFTDVVTTNLKLGNPTDRNVCFKVKTTAPRRYCVRPNSGIIDA
GASINVSVMLQPFDYDPNEKSKHKFMVQSMFAPTDTSDMEAVWKEAKPEDLMDSKLRCVFEL
PAENDKPHDVEINKIISTTASKTETPIVSKSLSSSLDDTEVKKVMEECKRLQGEVQRLREENKQF
KEEDGLRMRKTVQSNSPISALAPTGKEEGLSTRLLALVVLFFIVGVIIGKIAL

B)

Peptide Sequence	Peptide m/z	Modification
^{140}IISTTASKTE**pT**PIVSK^{155}	878.46^{2+}	T150
^{148}TETPIVSKSL**pSpS**SLDDTEVK^{167}	1148.52^{2+}	S158, S159
^{148}TETPIVSK**pS**LSSSLDDTEVKK^{167}	1108.54^{3+}	S156
^{156}SL**pS**SSLDDTEVKK^{168}	744.85^{2+}	S158

Figure 4.44: Phosphorylation sites identified in VAPB isolated from cells treated with AMPK activator A-769662. (A) Sequence of full length human VAPB with the MS/MS sequence coverage of 72 % shown as underlined. Four sites were identified (T150, S156, S158, S159), shown in red. (B) VAPB phosphopeptides obtained by MS/MS sequencing with their mass/charge (m/z) ratios. Phosphorylated residues shown in red.

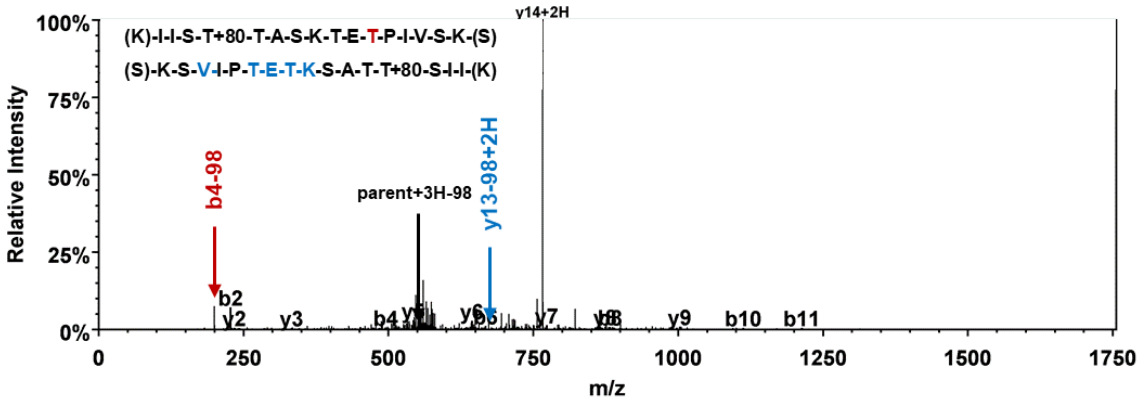

Figure 4.45: Identification of VAPB T143 as a phosphorylation site by LC-MS/MS. Tandem mass spectrometry spectrum of the VAPB phosphopeptide ^{140}IISpTTASKTETPIVSK^{155} (m/z 585.98^{3+}) fragment ion series after collision induced dissociation. The m/z of the fragment ions is plotted against intensity and the detected ions of the b- (red) and y- (blue) ion collision series are indicated on the sequence of the peptide (top left). A constant neutral loss of phosphoric acid, 98, from the parent ion was present at m/z 553.37^{3+} and is indicative of either a serine or threonine phosphorylation on the peptide. Loss of phosphoric acid from the b-4 ion and the doubly charged y-13 ion (indicated by arrows on the spectrum), localize this phosphorylation to T143.

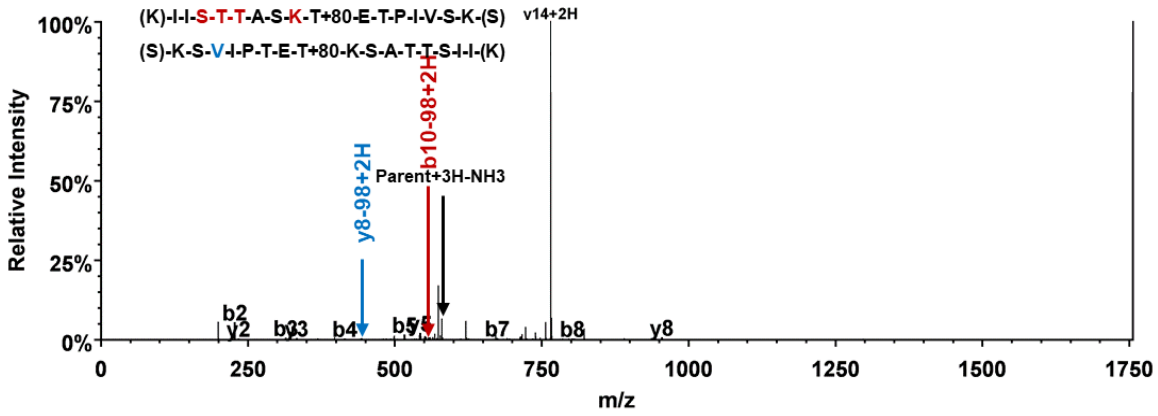

Figure 4.46: Identification of VAPB T148 as a phosphorylation site by LC-MS/MS. Tandem mass spectrometry spectrum of the VAPB phosphopeptide ^{140}IIST-TASKpTETPIVSK^{155} (m/z 585.98^{3+}) fragment ion series after collision induced dissociation. The m/z of the fragment ions is plotted against intensity and the detected ions of the b- (red) and y- (blue) ion collision series are indicated on the sequence of the peptide (top left). A constant neutral loss from the parent ion was found. However, a constant neutral loss of phosphoric acid, 98, indicative of either a serine or threonine phosphorylation on the peptide from the doubly charged b-10 and y-8 ions, localize this phosphorylation to T148.

4.2.7 Identification of phosphorylation sites in PTPIP51 in cells in which AMPK is activated

A similar study to that described above for VAPB was then conducted with PTPIP51. PTPIP51 was immunoprecipitated from HEK-293 cells in which AMPK was activated using A-769662. For comparison, cells were treated also with DMSO vehicle.

Full length, HA-tagged PTPIP51 was exogenously expressed in HEK-293 cells and cells were subsequently treated with either DMSO vehicle or A-769662 for 2 hrs. Cells were lysed and a small sample was probed by immunoblot for PTPIP51-HA (Figure 4.47). PTPIP51-HA was immunoprecipitated from both samples via the HA tag and proteins were separated by SDS-PAGE and stained with imperial protein stain (Figure 4.47). PTPIP51 was immunoprecipitated at a higher yield from cells treated with A-769662 as can be seen by the more intense PTPIP51 band on the gel (Figure 4.47) in the A-769662 condition. Although there is a low yield of PTPIP51 from DMSO treated cells, as in 4.2.6, the experiment was carried out in triplicate and all three gel bands were excised to ensure sufficient material for mass spectrometric analysis. Gel bands of isolated PTPIP51-HA was prepared, including digestion with trypsin, as detailed in 2.2.12 for LC-MS/MS which was carried out at the King's College London Proteomics Facility.

A)

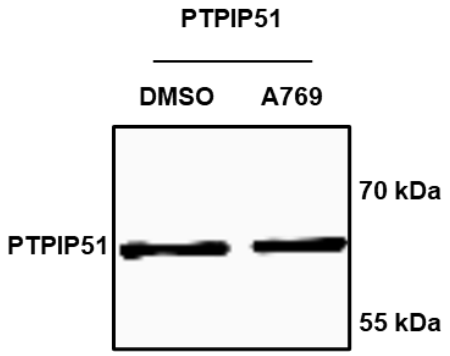

B)

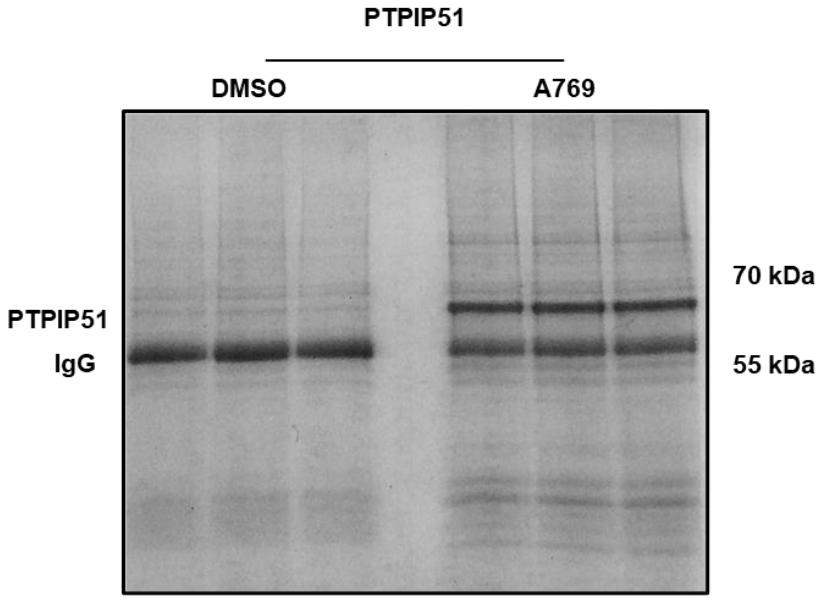

Figure 4.47: Overexpression and purification of PTPIP51-HA for LC-MS/MS analysis of phosphorylation. HEK-293 cells were transfected with PTPIP51-HA for 22 hrs and then treated with either DMSO vehicle control or A-769662 (A769). Cells were lysed 24 hrs after transfection and a sample was probed on immunoblots for PTPIP51-HA expression with HA antibody (A). PTPIP51-HA was immunoprecipitated using a HA antibody, separated on an SDS-PAGE gel and stained with imperial protein stain (B). The position of PTPIP51 and immunoglobulin heavy chain (Ig) is shown and molecular mass markers are shown on the right.

LC-MS/MS of PTPIP51-HA isolated from cells treated with vehicle control DMSO, identified peptides corresponding to PTPIP51-HA and provided sequence coverage of 61 % of the full-length human protein (Figure 4.48). Six individual sites of phosphorylation were identified and analysis of the corresponding fragmentation spectra of these phosphopeptides confirmed the localisation of phosphorylation to serine residues S44, S46, S50, S57, S77, S81. Doubly phosphorylated peptides were identified, corresponding to phosphorylation at S44 and S46, S46 and S50. Two triply phosphorylated peptides were identified, corresponding to phosphorylation at serine residues S44, S46 and S50, and S46, S50 and S57.

LC-MS/MS of PTPIP51-HA isolated from cells treated with the AMPK activator A-769662, identified peptides corresponding to PTPIP51-HA and provided sequence coverage of 72 % of the full-length human protein (Figure 4.49). Six individual sites of phosphorylation were identified and analysis of the corresponding fragmentation spectra of these phosphopeptides confirmed the localisation of phosphorylation to serine residues S44, S46, S50, S77, S81 and S212. A doubly phosphorylated peptide was identified, corresponding to phosphorylation at S46 and S50. One triply phosphorylated peptide was identified, with phosphorylation at residues S44, S46, S50. Phosphorylation at residue S212 was found in PTPIP51 from cells treated with A-769662 but not in PTPIP51 from control cells.

All of the phosphorylation sites identified in PTPIP51 from cells treated with either DMSO or A-769662 were identified in 4.2.5 of this chapter. As such, representative fragmentation spectra for each phosphorylation residue are not repeated here but instead can be found in section 4.2.5. A summary table of the phosphorylation sites which were found under each set of experimental conditions is included in the discussion of this chapter (Figure 4.50 for VAPB phosphorylation sites, Figure 4.51 for PTPIP51 phosphorylation sites).

A)

MSRLGALGGARAGLGLLLGTAAGLGFLCLLYSQRWKRTQRHGRSQSLPNSLDYTQTSDPGRHV
MLLRAVPGGAGDASVLPSLPREGQEKVLDRLDFVLTSLVALRREVEELRSSLRGLAGEIVGEVRC
HMEENQRVARRRRFPFVRERSDSTGSSSVYFTASSGATFTDAESEGGYTTANAESDNERDSDK
ESEDGEDEVSCETVKMGRKDSLDLEEEAASGASSALEAGGSSGLEDVLPLLQQADELHRGDEQ
GKREGFQLLLNNKLVYGSRQDFLWRLARAYSDMCELTEEVSEKKSYALDGKEEAEAALEKGDES
ADCHLWYAVLCGQLAEHESIQRRIQSGFSFKEHVDKAIALQPENPMAHFLLGRWCYQVSHLSWL
EKKTATALLESPLSATVEDALQSFLKAEELQPGFSKAGRVYISKCYRELGKNSEARWWMKLALEL
PDVTKEDLAIQKDLEELEVILRD

B)

Peptide Sequence	**Peptide m/z**	**Modification**
^{41}HGR**pS**Q**pS**LPNSLDYTQTSDPGR^{61}	826.01^{3+}	S44, S46
^{41}HGR**pS**Q**pS**LPN**pS**LDYTQTSDPGR^{61}	852.67^{3+}	S44, S46, S50
^{41}HGR**pS**QSLPNSLDYTQTSDPGR^{61}	799.36^{3+}	S44
^{44}SQ**pS**LPNSLDYTQTSDPGR^{61}	1023.44^{2+}	S46
^{44}SQ**pS**LPN**pS**LDYTQT**pS**DPGR^{61}	1103.41^{2+}	S46, S50, S57
^{44}SQSLPN**pS**LDYTQTSDPGR^{61}	1023.44^{2+}	S50
^{44}SQ**pS**LPN**pS**LDYTQTSDPGR^{61}	1063.43^{2+}	S46, S50
^{68}AVPGGAGDA**pS**VLPSLPR^{84}	822.41^{2+}	S77
^{68}AVPGGAGDASVLP**pS**LPR^{84}	822.41^{2+}	S81

Figure 4.48: Phosphorylation sites identified in PTPIP51 isolated from cells treated with DMSO vehicle control. (A) Sequence of full length human PTPIP51 with the MS/MS sequence coverage of 61 % shown as underlined. Six phosphorylation sites were identified (S44, S46, S50, S57, S77, S81), shown in red. (B) PTPIP51 phosphopeptides obtained by MS/MS sequencing with their mass/charge (m/z) ratios. Phosphorylated residues shown in red.

A)

MSRLGALGGARAGLGLLLGTAAGLGFLCLLYSQRWKRTQRHGRSQSLPNSLDYTQTSDPG
RHVMLLRAVPGGAGDASVLPSLPREGQEKVLDRLDFVLTSLVALRREVEELRSSLRGLAGEIV
GEVRCHMEENQRVARRRRFPFVRERSDSTGSSSVYFTASSGATFTDAESEGGYTTANAESD
NERDSDKESEDGEDEVSCETVKMGRKDSLDLEEEAASGASSALEAGGSSGLEDVLPLLQQA
DELHRGDEQGKREGFQLLLNNKLVYGSRQDFLWRLARAYSDMCELTEEVSEKKSYALDGKE
EAEAALEKGDESADCHLWYAVLCGQLAEHESIQRRIQSGFSFKEHVDKAIALQPENPMAHFL
LGRWCYQVSHLSWLEKKTATALLESPLSATVEDALQSFLKAEELQPGFSKAGRVYISKCYREL
GKNSEARWWMKLALELPDVTKEDLAIQKDLEELEVILRD

B)

Peptide Sequence	Peptide m/z	Modification
^{41}HGR**pS**QSLPNSLDYTQTSDPGR^{61}	799.36^{3+}	S44
^{44}SQ**pS**LPN**pS**LDYTQTSDPGR^{61}	1063.43^{2+}	S46, S50
^{41}HGR**pS**Q**pS**LPN**pS**LDYTQTSDPGR^{61}	825.67^{3+}	S44,S46,S50
^{44}SQ**pS**LPNSLDYTQTSDPGR^{61}	1023.44^{2+}	S46
^{44}SQSLPN**pS**LDYTQTSDPGR^{61}	1023.45^{2+}	S50
^{68}AVPGGAGDA**pS**VLPSLPR^{84}	822.41^{2+}	S77
^{68}AVPGGAGDASVLP**pS**LPR^{84}	822.41^{2+}	S81
^{210}KD**pS**LDLEEEAASGASSALEAGGSSGLEDVLPLLQQADELHR^{250}	1430.01^{3+}	S212

Figure 4.49: Phosphorylation sites identified in PTPIP51 isolated from cells treated with AMPK activator A-769662. (A) Sequence of full length human VAPB with the MS/MS sequence coverage of 72 % shown as underlined. Six phosphorylation sites were identified (S44, S46, S50, S77, S81, S212), shown in red. (B) PTPIP51 phosphopeptides obtained by MS/MS sequencing with their mass/charge (m/z) ratios. Phosphorylated residues shown in red.

4.3 Discussion

4.3.1 Summary of results

In this chapter, phosphorylation of VAPB and PTPIP51, specifically in conditions of GSK-3β and AMPK activity were investigated by mass spectrometry. In the case of GSK-3β, recombinant protein was incubated with the kinase *in vitro* to identify potential sites of direct phosphorylation. VAPB and PTPIP51 isolated from cells were also analysed to identify phosphorylation sites in cells. Over-expression of GSK-3β and pharmacological activation of AMPK were used to indicate the phosphorylation of VAPB and PTPIP51 in response to activation of these kinases.

This work identified novel potential GSK-3β phosphorylation sites in both VAPB and PTPIP51. VAPB residues T143, T148, T150 and PTPIP51 residue S77 were found to be phosphorylated by recombinant GSK-3β. Mutation of VAPB at residues T143 and T148 to mimic or preclude phosphorylation indicated that modification at T148 reduces the binding of VAPB to PTPIP51. VAPB residue T150, but not residues T143 and T148, was found to be phosphorylated in cells over-expressing GSK-3β. However, VAPB residues T143, T148 and T150 were found to be phosphorylated in control cells. PTPIP51 S77 was also found to be phosphorylated in cells in all of the conditions tested.

A number of phosphorylation sites were found in VAPB and PTPIP51 immunoprecipitated from cells. A summary of the sites found to be phosphorylated in VAPB and PTPIP51 from each condition, and a diagram of their position in the protein are shown in figures 4.50 and 4.51 for VAPB and PTPIP51, respectively. VAPB S146 was the only residue identified only in cells overexpressing GSK-3β. The predicted AMPK phosphorylation site in VAPB, residue S158, was found to be phosphorylated in all cellular conditions. A majority of PTPIP51 phosphorylation sites were found in all cellular conditions. PTPIP51 Y284 was only found to be phosphorylated in PTPIP51 from cells overexpressing GSK-3β. PTPIP51 residue S212 was phosphorylated in PTPIP51 from cells treated with AMPK activator A-769662 and in cells over-expressing GSK-3β but not in control cells. Doubly phosphorylated peptides, indicating that two residues are phosphorylated at the same time in the protein, were also found. Of these doubly phosphorylated peptides, one in each protein fits the described GSK-3β motif of priming phosphorylation 4 or 5 residues upstream of target phosphorylation (Doble and Woodgett, 2003): residues S156, S160 in VAPB and S46, S50 in PTPIP51.

Phosphorylated Residue	Recombinant protein	In Cells			
		Control	GSK-3β	DMSO	A769662
T143	x			x	
T144		x		x	
S146			x		
T148	x			x	
T150	x		x	x	x
S154		x			
S156		x	x	x	x
S158		x	x	x	x
S159		x		x	x
S160		x	x		

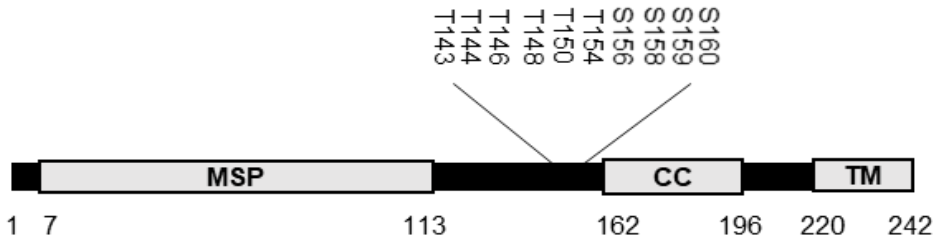

Figure 4.50: Summary of phosphorylation sites found in VAPB. Table shows the phosphorylation sites found in recombinant VAPB after incubation with GSK-3β (Recombinant protein), VAPB immunoprecipitated from cells which were transfected with control vector (Control) or GSK-3β and VAPB immunoprecipitated from cells treated with vehicle (DMSO) or A-769662. Diagram shows the position of identified phosphorylation sites on the structure of VAPB. MSP, motile sperm domain. CC, coiled coil domain, TM, transmembrane domain.

Phosphorylated Residue	Recombinant protein	In Cells			
		Control	GSK-3β	DMSO	A769662
S44		x	x	x	x
S46		x	x	x	x
S50		x	x	x	x
T54		x			
T56		x			
S57		x	x	x	
S77	x	x	x	x	x
S81		x	x	x	x
S193		x	x		
S212			x		x
S225		x			
Y284			x		
S285		x	x		

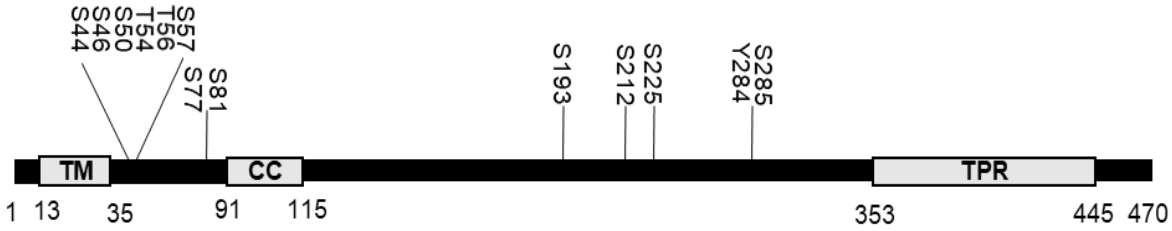

Figure 4.51: Summary of phosphorylation sites found in PTPIP51. Table shows the phosphorylation sites found in either recombinant PTPIP51 after incubation with GSK-3β (Recombinant protein), PTPIP51 immunoprecipitated from cells transfected with control vector (Control) or GSK-3β or treated with vehicle (DMSO) or A-769662. Diagram shows the position of identified phosphorylation sites on the structure of PTPIP51. TM, transmembrane domain, CC, coiled coil domain, TPR tetratricopeptide repeat domain.

4.3.2 Identification of phosphorylation sites in VAPB and PTPIP51

The study of kinases using recombinant protein is useful to identify the direct phosphorylation of a substrate, in the absence of other downstream kinases. However, this method also removes the natural modulation of kinase activity that is present in the cell, potentially leading to both false negatives and false positives. For example, false positives may arise due to the lack of competing natural kinase substrates and false negatives may arise because *E.coli* produced recombinant proteins may not fold correctly. To determine if the phosphorylation sites identified in recombinant protein in this study were false positives, VAPB and PTPIP51 from cells were also analysed. Since phosphorylation occurs dynamically in the cell, GSK-3β over-expression was used to enhance the chances of identifying phosphorylation at those residues found in recombinant experiments. Similarly, A-769662 was used to activate AMPK and increase the likelihood of identifying novel sites of phosphorylation that may be a result of AMPK activity.

Phosphorylation sites that were not identified in VAPB or PTPIP51 from control cells but were identified in protein from GSK-3β over-expressing cells or A-769662 treated cells may be deemed more likely to be targets of GSK-3β or AMPK. Quantitative mass spectrometry which compared the amounts of phosphorylation of VAPB or PTPIP51 on particular sites in control cells, or cells in which GSK-3β or AMPK were activated, would be required to demonstrate cellular targets for the two kinases. Quantitative mass spectrometry was out of the scope of this work and therefore the phosphorylation sites found are not confirmed kinase targets but instead provide direction for further investigation into the functional effects of modification on VAPB-PTPIP51 binding and ER-mitochondria signalling.

PTPIP51 residue S212 was found to be phosphorylated only in PTPIP51 from cells expressing GSK-3β or in which AMPK was activated, though it should be noted that this site was not covered in mass spectrometric analysis of PTPIP51 from DMSO treated cells. PTPIP51 S212 lies outside the core residues of PTPIP51 found to be necessary for binding to VAPB (De Vos et al., 2012) and modification at this site is therefore unlikely to alter its ability to bind to VAPB. The potential AMPK target phosphorylation site in VAPB, S158, which is the conserved residue corresponding to the AMPK target phosphorylation site in VAPA (Hoffman et al., 2015), was found to be phosphorylated in VAPB from all cellular samples. This would be a sensible next candidate for investigation for altering binding affinity to PTPIP51, and incubation of recombinant VAPB with active AMPK would be a useful way to determine that this is a direct target of AMPK.

In both VAPB and PTPIP51, a cluster of phosphorylation sites in a particular area of the protein were identified. The structure of VAPB consists of an MSP domain, a coiled coil domain, and a transmembrane domain, with unstructured regions between the main domains. The ALS-causing mutation in VAPB, P56S, is reported to reduce VAPB solubility by altering folding within the MSP domain (Shi et al., 2010). The two residues of VAPB investigated in this work, T143 and T148, reside in an unstructured region between the MSP and coiled coil domains. Indeed, all of the phosphorylation sites identified in VAPB, recombinantly and from control, GSK-3β over-expressing and A-769662 treated cells, reside in this region. It may be speculated that the multiple phosphorylation sites found in this region indicate a role for this region in modulating the structure of function of the protein. Similarly, a cluster of phosphorylation sites in PTPIP51 were found close to the transmembrane domain of the protein. The structure of PTPIP51 is yet to be reported and although the MSP domain of VAPB has been crystallised and the structure identified (Shi et al., 2010), the structure of the rest of the protein remains unsolved. Structural studies of VAPB and PTPIP51, such as NMR or crystallography investigations, particularly of VAPB in complex with PTPIP51, would enable modelling of the effect of the post translational modifications found in this study. Structural information would also provide the basis for development of molecules able to stabilise the interaction.

4.3.3 The effect of VAPB phosphorylation on binding to PTPIP51

GSK-3β target sites for phosphorylation are reported to have a priming site located 4 or 5 residues upstream of the main target site (Doble and Woodgett, 2003). VAPB T143 and T148 both fit this reported phosphorylation motif and are conserved across different species, as would be expected of residues able to regulate a prominent cellular process such as ER-mitochondrial signalling. Conversely, PTPIP51 S77 and VAPB T150 residues are not conserved between animals. As such, VAPB T143 and VAPB T148 were investigated for a potential role in regulating the binding of VAPB to PTPIP51.

Mutation of VAPB T143 or T148 indicated that T143 alone had no effect on binding to PTPIP51 but that phosphorylation of T148 may reduce the affinity of VAPB to PTPIP51. In the GAL4 2-hybrid luciferase studies there was a modest but significant decreasing in binding between VAPB-T148D and PTPIP51 compared to that of WT VAPB. Preventing phosphorylation at VAPB T148 had no effect on binding. This may be due to the majority of VAPB in the cell being non-phosphorylated at this residue. Whilst the GAL4 2-hybrid luciferase assay is a useful first indicator of protein binding, the interactions involved take place in the nucleus, requiring the removal of the transmembrane domains of VAPB and PTPIP51, and their interaction away from their natural cellular locations. Further

investigation into the binding of VAPB and PTPIP51 should include immunoprecipitation experiments in which full length proteins can be investigated in their correct locations within the cell.

In order to confer the importance of VAPB T148 in ALS, the extent of phosphorylation at this residue should be measured in ALS cell and transgenic models and in human ALS tissues. This could be performed as in this study by mass spectrometry. Quantitative mass spectrometry would allow comparison between VAPB from ALS and control tissue. Alternatively, a phospho-antibody to VAPB-T148 could be produced and used to quantify differences in the amount of phosphorylation at this specific residue between control and ALS tissue.

4.3.4 Implications for therapeutic potential

There is much evidence indicating a role for dysregulated ER-mitochondria contacts in ALS (discussed in detail in chapter 1, for review see Lau et al., 2018) and GSK-3β has been shown to mediate this dysregulation (Stoica et al., 2016; Stoica et al., 2014). GSK-3β, ER-mitochondrial signalling and VAPB-PTPIP51 binding are therefore potential therapeutic targets for ALS.

Kinases are attractive therapeutic targets because it is known that they can be modulated by small molecule drugs. GSK-3β itself has been targeted for the treatment of neurodegenerative disease (discussed in detail in chapter 1) (Ahn et al., 2012; Cohen and Goedert, 2004; Feng et al., 2008; Koh et al., 2007) with little success due to its wide-ranging roles within the cell. Therefore, there is a need to understand the mechanisms by which GSK-3β exerts its effects in ALS to identify downstream targets for therapy. There is also evidence linking AMPK to ALS (discussed in 4.1) and the phosphorylation of VAP proteins (Hoffman et al., 2015). Identification of either a GSK-3β or AMPK phosphorylation site in VAPB or PTPIP51 which disrupts ER-mitochondrial signalling would shed light on the role of GSK-3β or AMPK in ALS and enable investigation into more specific therapeutic targets.

Chapter 5: Summary and Future Directions

5.1 The role of VAPB-PTPIP51 interactions in ALS

The studies described in Chapter 3 investigated a number of ER-mitochondria signalling proteins and used PLAs to quantify the VAPB-PTPIP51 interaction in post-mortem spinal cord tissue and iPSC-MNs from ALS donors. These studies found that VAPB-PTPIP51 interactions are significantly reduced in ALS patients. This finding is in line with evidence in animal and cell models of ALS (Stoica et al., 2014; Stoica et al., 2016) and demonstrates for the first time that defective ER-mitochondria contacts are a feature of human ALS. A decrease in VAPB protein levels was also identified in ALS post-mortem spinal cord, in agreement with published studies (Anagnostou et al., 2010). VAPB protein level and PLA signal did not correlate, suggesting that VAPB amount did not necessarily account for the variation in VAPB-PTPIP51 interaction. TOM20 protein amounts were increased in ALS tissue, as reported in animal studies (Li et al., 2010) but no change in the levels of other mitochondrial or ER proteins was found. Together these findings reveal ER-mitochondria contacts and the VAPB-PTPIP51 tethers as a novel feature of human ALS and a potential therapeutic target.

5.1.1 Broken ER-mitochondria contacts: cause or consequence of cell damage?

In confirming the disruption of ER-mitochondria contacts as a feature of human ALS, this work identifies VAPB and PTPIP51 tethers as specific targets for studies aiming to rescue ER-mitochondria signalling in ALS. Chapter 3 describes a VAPB-PTPIP51 binding assay, the GAL4 2-hybrid luciferase reporter assay which presents the opportunity to screen for small molecule drugs capable of rescuing ER-mitochondria contacts.

In order to determine if such drugs would act therapeutically, future studies should seek to identify whether disruption to ER-mitochondria contacts occurs as an early ALS pathology which leads to cell damage or as a consequence of ALS-related cell damage. TDP-43 and FUS both disrupt ER-mitochondria contacts via activation of GSK-3β (Stoica et al., 2014; Stoica et al., 2016), but the mechanism by which this occurs is as yet unknown, and the possibility that it happens as a consequence of ALS-related cell damage as opposed to an early pathology should be ruled out if it is to be targeted therapeutically. This could be addressed by determining if disruption to ER-mitochondria contacts occurs early in disease, for example by measuring temporal changes in ER-mitochondria contacts in ALS transgenic mice, identifying whether they occur before the onset of symptoms. In support of the idea that disruption to MAM occurs early in disease, ER-mitochondria contacts are reported to be broken in TDP-43 and FUS transgenic mice without any change in VAPB protein levels (Stoica et al., 2014; Stoica et al., 2016), whilst VAPB protein levels are decreased at the end stage of the disease in humans, as found

in this study and by Anagnostou et al., (2010). Future studies may therefore want to measure both ER-mitochondria contacts and VAPB proteins levels in pre-symptomatic, symptomatic, and end-stage ALS transgenic animals. iPSC-MNs derived from ALS patients show increased levels of insoluble TDP-43 when matured *in vitro* (Bilican et al., 2012; Egawa et al., 2012). The findings in Chapter 3 of this thesis show reduced ER-mitochondria contacts in iPSC-MNs at a level of maturity in which TDP-43 aggregates are expected in M337V but not G298S mutant cells (unpublished data, Jenny Greig e-thesis), suggesting that disruption to ER-mitochondria signalling is likely to occur before TDP-43 aggregation. These iPSC-MNs present the opportunity to measure the development of insoluble TDP-43, damage to ER-mitochondria contacts and consequent cellular dysfunction in parallel over time.

5.1.2 Are the functions of ER-mitochondria contacts altered in ALS?

Cellular dysfunction, in particular to the processes that are regulated by ER-mitochondria signalling such as calcium signalling, ATP production, phospholipid synthesis, and inflammasome formation (Cali et al., 2013a; Missiroli et al., 2018; Rowland and Voeltz, 2012) have already been implicated in ALS (Lau et al., 2018). In order to confirm the potential of correcting ER-mitochondria contacts as a therapeutic target and to facilitate testing for compounds which rescue cellular function, future studies should measure correlate disruption to these functions with changes in the VAPB-PTPIP51 interaction and ER-mitochondria contacts in ALS. iPSC-MNs present the opportunity do this and studies could use isogenic control cell lines, in which ALS-causing mutations in patient cells are genetically modified to the wild-type gene via CRISPR methods. This would enable comparisons between ALS and control cells with the same genetic background.

5.1.2.1 Calcium signalling and energy metabolism

Calcium signalling between ER and mitochondria is mediated by IP3R and VDAC at ER-mitochondria contact sites (Szabadkai et al., 2006) and is disrupted by reduced VAPB-PTPIP51 binding (De Vos et al., 2012). Further studies could measure the interaction between IP3R and VDAC in ALS post-mortem tissue and ALS patient cells using PLAs as in this study, to determine whether this functional interaction is also affected in ALS.

In cells, changes in calcium exchange and cellular respiration have been measured as described previously (De Vos et al., 2012; Paillusson et al., 2017). Briefly, calcium exchange is measured via mitochondrial and cytosolic calcium levels upon stimulation of calcium release. Cellular respiration is investigated by measuring oxygen consumption upon treatment of electron transport chain uncouplers. These methods, used in iPSC-MNs derived from patients and in isogenic controls, would provide a functional readout

for calcium exchange and ATP production that could be utilised in a search for compounds able to restore defective ER-mitochondrial signalling.

5.1.2.2 Inflammation

In ALS, as in many neurodegenerative diseases, inflammation has been considered as both a stressor and symptom of disease (Geloso et al., 2017; Komine and Yamanaka, 2015). Formation of the inflammasome is reported to occur at MAM and subsequent inflammatory responses are therefore likely modulated by ER-mitochondria contacts (Missiroli et al., 2018; Zhou et al., 2011). This study measured VAPB-PTPIP51 interactions in the soma of motor neurons, but it would be of interest to investigate ER-mitochondria contacts in glial cells, and their role in microglia activation. This would require optimisation of glial markers and fluorescent PLA to be carried out in post-mortem tissue. Advances in iPSC differentiation mean that microglia-like cells could now be generated from ALS patient cells in which to measure ER-mitochondria contacts. These studies could compare between ALS patient and control donor or isogenic controls and between microglia-like and motor neuron cells.

5.1.2.3 Synaptic activity

VAPB-PTPIP51 binding and ER-mitochondria contact has been shown to regulate synaptic activity (Gomez-Suaga et al., 2019). Measuring VAPB-PTPIP51 interactions in synaptic regions and in response to stimulation of synaptic activity (e.g. via electrical stimulation), in ALS patient iPSC-MNs and control donor or isogenic control cells would indicate whether the regulation of synaptic activity by ER-mitochondria contact is affected in ALS.

5.1.3 How are ER and mitochondrial proteins affected in ALS?

5.1.3.1 TOM20 *and mitochondrial protein accumulation*

The levels of mitochondrial proteins PTPIP51 and VDAC were not changed between ALS and control donor spinal cord tissue in this study, but the levels of mitochondrial protein TOM20 were increased in ALS donor tissue; this is in line with studies of SOD1 ALS animal studies (Li et al., 2010). TDP-43 and FUS are both reported to bind to certain mitochondrial proteins and increase mitophagy (Davis et al., 2018; Deng et al., 2018). As discussed in 3.3.3, future studies may investigate whether mitophagy or dysfunction in mitochondrial proteins such as TOM20 is the cause of altered mitochondrial protein levels. These studies could include experimental manipulation of TOM20 function, or mitophagy, and monitoring of TOM20 protein levels in response.

5.1.3.2 Sigma1R and ER proteins

This study found that Sigma1R protein levels were not different between ALS and control donor post-mortem spinal cord tissue. Sigma1R functions to stabilise IP3R clustering (Hayashi and Su, 2007; Ryskamp et al., 2019) and the protein levels of neither IP3R nor its binding partner VDAC were altered in ALS tissues. These findings support reports that it is not changes in Sigma1R expression but altered Sigma1R function that plays a role in disease pathogenesis (Al-Saif et al., 2011; Gregianin et al., 2016; Luty et al., 2010). Future studies may investigate whether expression of functional Sigma1R can rescue calcium signalling, by enhancing IP3R clustering, in ALS models such as TDP-43 or FUS overexpressing cells.

5.2 Phosphorylation as a modulator of ER-mitochondria contacts

The studies described in Chapter 4 aimed to identify phosphorylation sites in VAPB and PTPIP51. Studies of *in vitro* phosphorylation with recombinant protein identified VAPB residues T143, T148 and T150 and PTPIP51 residue S77 as GSK-3β phosphorylation sites. A GAL4 2-hybrid assay with phospho-mimicking mutants suggested that phosphorylation of VAPB at residue T148 can alter its binding to PTPIP51, indicating that GSK-3β phosphorylation of VAPB may regulate ER-mitochondria contacts. Mass spectrometry studies of VAPB immunoprecipitated from cells confirmed the phosphorylation of these sites in cells and identified novel phosphorylation sites including the hypothesised AMPK phosphorylation site, VAPB S158, which is phosphorylated at a conserved residue in VAPA (Hoffman et al., 2015).

5.2.1 Investigating the effect of kinases on ER-mitochondria contacts in ALS

Having identified phosphorylation sites in VAPB and PTPIP51, it would next be useful to confirm whether the kinases responsible are indeed GSK-3β and AMPK. Quantitative phospho-proteomic mass spectrometry studies comparing VAPB and PTPIP51 from cells in which GSK-3β or AMPK activities have been experimentally manipulated would indicate whether GSK-3β or AMPK themselves increase phosphorylation of VAPB or PTPIP51 and at which sites. These methods involve specific labelling (e.g. isotopic labelling) of proteins in cells in which kinase activities are unaltered or elevated and/or reduced, followed by isolation and quantification of phosphorylation of the protein of interest in the different samples (Hennrich and Gavin, 2015). These studies could be complemented by investigating whether GSK-3β or AMPK activity is altered in ALS. Given that GSK-3β is activated by overexpression of TDP-43 or FUS (Stoica et al., 2014; Stoica et al., 2016), it may be hypothesised that it is increased in ALS patients. Investigating this could take the form of immunoblotting for the total and active phosphorylated forms of each protein in ALS and control donor post-mortem tissue.

GSK-3β activity has previously been shown to alter ER-mitochondria contacts (Stoica et al., 2014; Stoica et al., 2016) but the effect of AMPK activity on ER-mitochondria contacts is yet to be investigated. AMPK activity is implicated in ALS (Liu et al., 2015; Perera et al., 2014; Perera and Turner, 2016) and future studies may investigate the effect of AMPK activity on ER-mitochondria contacts. This could be investigated by measuring VAPB-PTPIP51 interactions using PLAs in cells treated with AMPK activator A-769662. It should also be determined whether modulation of AMPK activity can correct the effect of TDP-43 and FUS on ER-mitochondria contacts. Finally, there is evidence that GSK-3β and AMPK activities are linked, though the precise details are not yet fully understood (Horike et al., 2008; Suzuki et al., 2013). Investigation into the effect of AMPK activity on GSK-3β activity, and vice versa, as potential modulators of ER-mitochondria contacts could be investigated. This would involve modulation of the activity of either kinase, monitoring of the activity of the other kinase and parallel measurement of VAPB-PTPIP51 interactions.

5.2.2 Investigating the role of phosphorylation on ER-mitochondria contacts

The findings in this study provide the basis for further investigation into the effect of phosphorylation of VAPB on ER-mitochondria contacts, since phospho-mimicking at VAPB residue T148 is shown to reduce VAPB-PTPIP51 interactions. VAPB residues T148 and S158 should first be investigated for a role in ER-mitochondria contacts by the use of immunoprecipitation studies. GSK-3β activity should also be increased by over expression or reduced with selective inhibitors, and the alanine or aspartate mutants respectively transfected to determine if they rescue the effect of GSK-3β on ER-mitochondria contacts. If these studies show that such mutants do rescue the effects of GSK-3β on ER-mitochondria contacts, then phospho-specific antibodies to these sites could be used to probe whether changes in their phosphorylation occurs in ALS donor tissues and in models of ALS. Prevention of phosphorylation of these sites could then be considered a potential therapeutic strategy.

This study also found small clusters of phosphorylation sites in both VAPB and PTPIP51. These clusters may represent areas in which phosphorylation affects the structure of the protein and may be considered a basis for structural investigation into VAPB-PTPIP51 binding. Determination of the structure of this interaction, for example by crystallography or nuclear magnetic resonance studies, would facilitate modelling of the effect of post translational modifications and small molecules on the interaction. This line of investigation may lead to the identification of novel modifiers of ER-mitochondria contacts.

5.3 Conclusions

This thesis investigated two main hypotheses; that ER-mitochondria contacts are disrupted in humans with ALS and that this disruption is caused by phosphorylation of VAPB or PTPIP51, including via GSK-3β. This hypothesis is detailed in Figure 5.1, including the features of neurodegenerative disease which are affected by disruption to ER-mitochondria contacts. In the work presented in this thesis, phosphorylation sites, which may be GSK-3β targets, were identified in both VAPB and PTPIP51 and the VAPB-PTPIP51 interaction was found to be disrupted in ALS patient cells and tissue. A number of questions remain: How do ALS insults enhance GSK-3β activity? Are the phosphorylation sites identified in this work phosphorylated at higher levels in ALS patients? Finally the most important question, would preventing phosphorylation of VAPB or PTPIP51 act therapeutically for ALS patients?

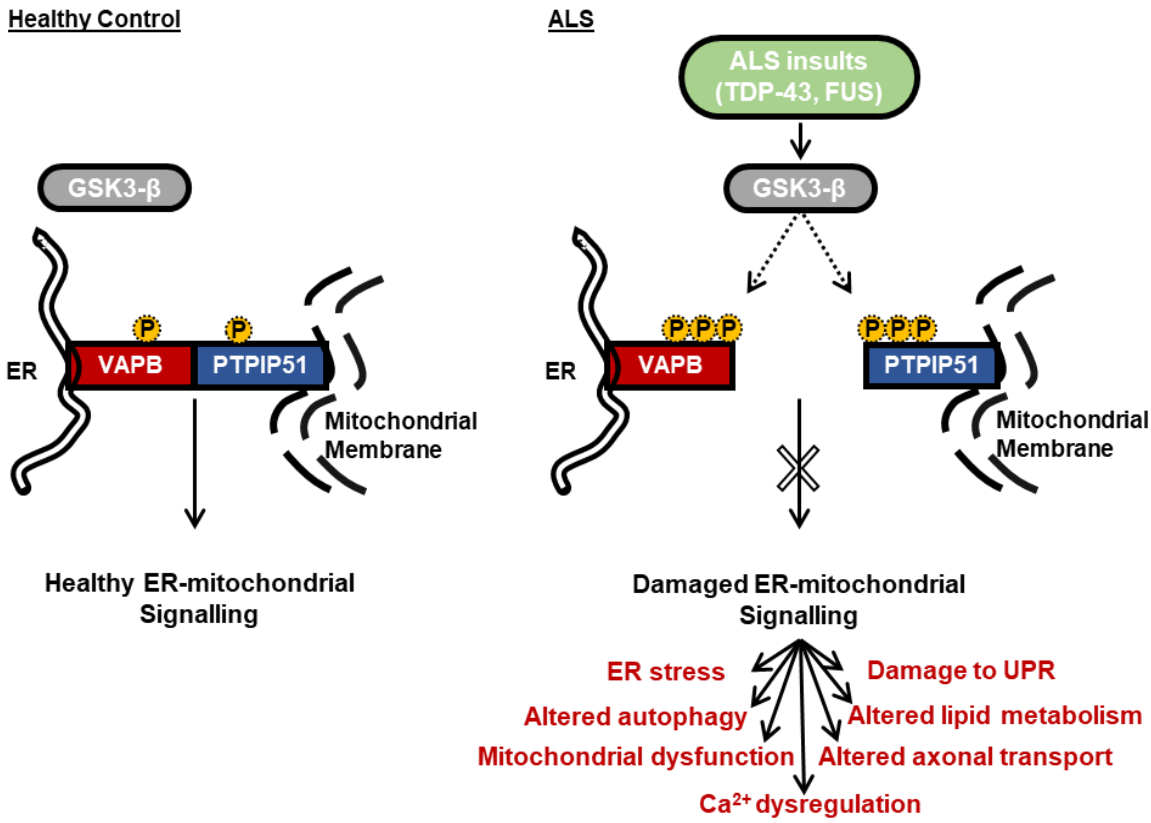

Figure 5.1: Schematic representation of the hypothesis underlying this thesis.
In healthy cells, VAPB-PTPIP51 binding facilitates contacts between ER and mitochondrial membranes which regulate healthy signaling. In ALS, insults including TDP-43 and FUS overexpression increase GSK-3β activity. The work presented in this thesis showed that VAPB-PTPIP51 interactions are reduced in human ALS and identified phosphorylation sites in VAPB and PTPIP51 which are potential GSK-3β targets and may cause disrupted VAPB-PTPIP51 binding. Disrupted ER-mitochondria contacts lead to a number of cellular dysfunctions and restoring them may be of therapeutic benefit.

In summary, the work in this thesis shows that the VAPB-PTPIP51 interaction is disrupted in ALS patient tissues and identifies novel phosphorylation sites that may affect binding of VAPB to PTPIP51. The discovery that the VAPB-PTPIP51 interaction is disrupted in ALS donor tissues and in ALS patient-derived iPSC-motor neurons recapitulates studies in ALS models and reveals a new feature of ALS in humans. As such, these findings lend strong support that correcting damaged ER-mitochondria signalling is a valid therapeutic target for ALS. Moreover, these findings reveal precise targets, VAPB and PTPIP51, suitable for drug screens to identify molecules capable of rescuing ER-mitochondria contacts in ALS.

6. References

Ackerley, S., P. Thornhill, A.J. Grierson, J. Brownlees, B.H. Anderton, P.N. Leigh, C.E. Shaw, and C.C. Miller. 2003. Neurofilament heavy chain side arm phosphorylation regulates axonal transport of neurofilaments. *J Cell Biol*. 161:489-495.

Ahn, S.W., J.E. Kim, K.S. Park, W.J. Choi, Y.H. Hong, S.M. Kim, S.H. Kim, K.W. Lee, and J.J. Sung. 2012. The neuroprotective effect of the GSK-3beta inhibitor and influence on the extrinsic apoptosis in the ALS transgenic mice. *J Neurol Sci*. 320:1-5.

Al-Saif, A., F. Al-Mohanna, and S. Bohlega. 2011. A mutation in sigma-1 receptor causes juvenile amyotrophic lateral sclerosis. *Ann Neurol*. 70:913-919.

Alam, M.S. 2018. Proximity Ligation Assay (PLA). *Curr Protoc Immunol*. 123:e58.

Anagnostou, G., M.T. Akbar, P. Paul, C. Angelinetta, T.J. Steiner, and J. de Belleroche. 2010. Vesicle associated membrane protein B (VAPB) is decreased in ALS spinal cord. *Neurobiol Aging*. 31:969-985.

Arai, T., M. Hasegawa, H. Akiyama, K. Ikeda, T. Nonaka, H. Mori, D. Mann, K. Tsuchiya, M. Yoshida, Y. Hashizume, and T. Oda. 2006. TDP-43 is a component of ubiquitin-positive tau-negative inclusions in frontotemporal lobar degeneration and amyotrophic lateral sclerosis. *Biochem Biophys Res Commun*. 351:602-611.

Area-Gomez, E., A.J. de Groof, I. Boldogh, T.D. Bird, G.E. Gibson, C.M. Koehler, W.H. Yu, K.E. Duff, M.P. Yaffe, L.A. Pon, and E.A. Schon. 2009. Presenilins are enriched in endoplasmic reticulum membranes associated with mitochondria. *Am J Pathol*. 175:1810-1816.

Area-Gomez, E., M. Del Carmen Lara Castillo, M.D. Tambini, C. Guardia-Laguarta, A.J. de Groof, M. Madra, J. Ikenouchi, M. Umeda, T.D. Bird, S.L. Sturley, and E.A. Schon. 2012. Upregulated function of mitochondria-associated ER membranes in Alzheimer disease. *EMBO J*. 31:4106-4123.

Ash, P.E., K.F. Bieniek, T.F. Gendron, T. Caulfield, W.L. Lin, M. Dejesus-Hernandez, M.M. van Blitterswijk, K. Jansen-West, J.W. Paul, 3rd, R. Rademakers, K.B. Boylan, D.W. Dickson, and L. Petrucelli. 2013. Unconventional translation of C9ORF72 GGGGCC expansion generates insoluble polypeptides specific to c9FTD/ALS. *Neuron*. 77:639-646.

Atkin, J.D., M.A. Farg, A.K. Walker, C. McLean, D. Tomas, and M.K. Horne. 2008. Endoplasmic reticulum stress and induction of the unfolded protein response in human sporadic amyotrophic lateral sclerosis. *Neurobiol Dis*. 30:400-407.

Atkins, K.M., L.L. Thomas, J. Barroso-Gonzalez, L. Thomas, S. Auclair, J. Yin, H. Kang, J.H. Chung, J.D. Dikeakos, and G. Thomas. 2014. The multifunctional sorting

protein PACS-2 regulates SIRT1-mediated deacetylation of p53 to modulate p21-dependent cell-cycle arrest. *Cell Rep*. 8:1545-1557.

Balestrino, R., and A.H.V. Schapira. 2020. Parkinson disease. *Eur J Neurol*. 27:27-42.

Bang, J., S. Spina, and B.L. Miller. 2015. Frontotemporal dementia. *Lancet*. 386:1672-1682.

Baradaran-Heravi, Y., C. Van Broeckhoven, and J. van der Zee. 2020. Stress granule mediated protein aggregation and underlying gene defects in the FTD-ALS spectrum. *Neurobiol Dis*. 134:104639.

Bartok, A., D. Weaver, T. Golenar, Z. Nichtova, M. Katona, S. Bansaghi, K.J. Alzayady, V.K. Thomas, H. Ando, K. Mikoshiba, S.K. Joseph, D.I. Yule, G. Csordas, and G. Hajnoczky. 2019. IP3 receptor isoforms differently regulate ER-mitochondrial contacts and local calcium transfer. *Nat Commun*. 10:3726.

Basso, V., E. Marchesan, C. Peggion, J. Chakraborty, S. von Stockum, M. Giacomello, D. Ottolini, V. Debattisti, F. Caicci, E. Tasca, V. Pegoraro, C. Angelini, A. Antonini, A. Bertoli, M. Brini, and E. Ziviani. 2018. Regulation of ER-mitochondria contacts by Parkin via Mfn2. *Pharmacol Res*. 138:43-56.

Beers, D.R., W. Zhao, J. Wang, X. Zhang, S. Wen, D. Neal, J.R. Thonhoff, A.S. Alsuliman, E.J. Shpall, K. Rezvani, and S.H. Appel. 2017. ALS patients' regulatory T lymphocytes are dysfunctional, and correlate with disease progression rate and severity. *JCI Insight*. 2:e89530.

Belzil, V.V., H. Daoud, W. Camu, M.J. Strong, P.A. Dion, and G.A. Rouleau. 2013. Genetic analysis of SIGMAR1 as a cause of familial ALS with dementia. *Eur J Hum Genet*. 21:237-239.

Belzil, V.V., H. Daoud, A. Desjarlais, J.P. Bouchard, N. Dupre, W. Camu, P.A. Dion, and G.A. Rouleau. 2011. Analysis of OPTN as a causative gene for amyotrophic lateral sclerosis. *Neurobiol Aging*. 32:555.e513-554.

Bernales, S., F.R. Papa, and P. Walter. 2006. Intracellular signaling by the unfolded protein response. *Annu. Rev. Cell Dev. Biol.* 22:487-508.

Bernard-Marissal, N., R. Chrast, and B.L. Schneider. 2018. Endoplasmic reticulum and mitochondria in diseases of motor and sensory neurons: a broken relationship? *Cell Death Dis*. 9:333.

Bernard-Marissal, N., J.J. Medard, H. Azzedine, and R. Chrast. 2015. Dysfunction in endoplasmic reticulum-mitochondria crosstalk underlies SIGMAR1 loss of function mediated motor neuron degeneration. *Brain*. 138:875-890.

Berning, B.A., and A.K. Walker. 2019. The Pathobiology of TDP-43 C-Terminal Fragments in ALS and FTLD. *Front Neurosci*. 13.

Bilican, B., A. Serio, S.J. Barmada, A.L. Nishimura, G.J. Sullivan, M. Carrasco, H.P. Phatnani, C.A. Puddifoot, D. Story, J. Fletcher, I.H. Park, B.A. Friedman, G.Q.

Daley, D.J. Wyllie, G.E. Hardingham, I. Wilmut, S. Finkbeiner, T. Maniatis, C.E. Shaw, and S. Chandran. 2012. Mutant induced pluripotent stem cell lines recapitulate aspects of TDP-43 proteinopathies and reveal cell-specific vulnerability. *Proc Natl Acad Sci U S A*. 109:5803-5808.

Blasco, H., S. Mavel, P. Corcia, and P.H. Gordon. 2014. The glutamate hypothesis in ALS: pathophysiology and drug development. *Curr Med Chem*. 21:3551-3575.

Bravo, R., J.M. Vicencio, V. Parra, R. Troncoso, J.P. Munoz, M. Bui, C. Quiroga, A.E. Rodriguez, H.E. Verdejo, J. Ferreira, M. Iglewski, M. Chiong, T. Simmen, A. Zorzano, J.A. Hill, B.A. Rothermel, G. Szabadkai, and S. Lavandero. 2011. Increased ER-mitochondrial coupling promotes mitochondrial respiration and bioenergetics during early phases of ER stress. *J Cell Sci*. 124:2143-2152.

Brenner, D., R. Yilmaz, K. Muller, T. Grehl, S. Petri, T. Meyer, J. Grosskreutz, P. Weydt, W. Ruf, C. Neuwirth, M. Weber, S. Pinto, K.G. Claeys, B. Schrank, B. Jordan, A. Knehr, K. Gunther, A. Hubers, D. Zeller, A.L.S.n.M.N.D.N.E.T. German, C. Kubisch, S. Jablonka, M. Sendtner, T. Klopstock, M. de Carvalho, A. Sperfeld, G. Borck, A.E. Volk, J. Dorst, J. Weis, M. Otto, J. Schuster, K. Del Tredici, H. Braak, K.M. Danzer, A. Freischmidt, T. Meitinger, T.M. Strom, A.C. Ludolph, P.M. Andersen, and J.H. Weishaupt. 2018. Hot-spot KIF5A mutations cause familial ALS. *Brain*.

Brettschneider, J., V.M. Van Deerlin, J.L. Robinson, L. Kwong, E.B. Lee, Y.O. Ali, N. Safren, M.J. Monteiro, J.B. Toledo, L. Elman, L. McCluskey, D.J. Irwin, M. Grossman, L. Molina-Porcel, V.M. Lee, and J.Q. Trojanowski. 2012. Pattern of ubiquilin pathology in ALS and FTLD indicates presence of C9ORF72 hexanucleotide expansion. *Acta Neuropathol*. 123:825-839.

Buratti, E., and F.E. Baralle. 2001. Characterization and functional implications of the RNA binding properties of nuclear factor TDP-43, a novel splicing regulator of CFTR exon 9. *J Biol Chem*. 276:36337-36343.

Cagnin, A., M. Rossor, E.L. Sampson, T. Mackinnon, and R.B. Banati. 2004. In vivo detection of microglial activation in frontotemporal dementia. *Ann Neurol*. 56:894-897.

Caldero, J., N. Brunet, O. Tarabal, L. Piedrafita, M. Hereu, V. Ayala, and J.E. Esquerda. 2010. Lithium prevents excitotoxic cell death of motoneurons in organotypic slice cultures of spinal cord. *Neuroscience*. 165:1353-1369.

Cali, T., D. Ottolini, and M. Brini. 2013a. Calcium and endoplasmic reticulum-mitochondria tethering in neurodegeneration. *DNA Cell Biol*. 32:140-146.

Cali, T., D. Ottolini, A. Negro, and M. Brini. 2013b. Enhanced parkin levels favor ER-mitochondria crosstalk and guarantee Ca(2+) transfer to sustain cell bioenergetics. *Biochim Biophys Acta*. 1832:495-508.

Cano-Cuenca, N., J.E. Solis-Garcia del Pozo, and J. Jordan. 2014. Evidence for the efficacy of latrepirdine (Dimebon) treatment for improvement of cognitive function: a meta-analysis. *J Alzheimers Dis*. 38:155-164.

Cardenas, C., and J.K. Foskett. 2012. Mitochondrial Ca(2+) signals in autophagy. *Cell Calcium*. 52:44-51.

Cardenas, C., R.A. Miller, I. Smith, T. Bui, J. Molgo, M. Muller, H. Vais, K.H. Cheung, J. Yang, I. Parker, C.B. Thompson, M.J. Birnbaum, K.R. Hallows, and J.K. Foskett. 2010. Essential regulation of cell bioenergetics by constitutive InsP3 receptor Ca2+ transfer to mitochondria. *Cell*. 142:270-283.

Carling, D. 2017. AMPK signalling in health and disease. *Curr Opin Cell Biol*. 45:31-37.

Castillo, K., M. Nassif, V. Valenzuela, F. Rojas, S. Matus, G. Mercado, F.A. Court, B. van Zundert, and C. Hetz. 2013. Trehalose delays the progression of amyotrophic lateral sclerosis by enhancing autophagy in motoneurons. *Autophagy*. 9:1308-1320.

Chang, H.Y., S.C. Hou, T.D. Way, C.H. Wong, and I.F. Wang. 2013. Heat-shock protein dysregulation is associated with functional and pathological TDP-43 aggregation. *Nat Commun*. 4:2757.

Chen, H., S.A. Detmer, A.J. Ewald, E.E. Griffin, S.E. Fraser, and D.C. Chan. 2003. Mitofusins Mfn1 and Mfn2 coordinately regulate mitochondrial fusion and are essential for embryonic development. *J Cell Biol*. 160:189-200.

Chen, S., X.J. Zhang, L.X. Li, Y. Wang, R.J. Zhong, and W. Le. 2015. Histone deacetylase 6 delays motor neuron degeneration by ameliorating the autophagic flux defect in a transgenic mouse model of amyotrophic lateral sclerosis. *Neurosci Bull*. 31:459-468.

Chou, C.C., Y. Zhang, M.E. Umoh, S.W. Vaughan, I. Lorenzini, F. Liu, M. Sayegh, P.G. Donlin-Asp, Y.H. Chen, D.M. Duong, N.T. Seyfried, M.A. Powers, T. Kukar, C.M. Hales, M. Gearing, N.J. Cairns, K.B. Boylan, D.W. Dickson, R. Rademakers, Y.J. Zhang, L. Petrucelli, R. Sattler, D.C. Zarnescu, J.D. Glass, and W. Rossoll. 2018. TDP-43 pathology disrupts nuclear pore complexes and nucleocytoplasmic transport in ALS/FTD. *Nat Neurosci*. 21:228-239.

Cirulli, E.T., B.N. Lasseigne, S. Petrovski, P.C. Sapp, P.A. Dion, C.S. Leblond, J. Couthouis, Y.F. Lu, Q. Wang, B.J. Krueger, Z. Ren, J. Keebler, Y. Han, S.E. Levy, B.E. Boone, J.R. Wimbish, L.L. Waite, A.L. Jones, J.P. Carulli, A.G. Day-Williams, J.F. Staropoli, W.W. Xin, A. Chesi, A.R. Raphael, D. McKenna-Yasek, J. Cady, J.M. Vianney de Jong, K.P. Kenna, B.N. Smith, S. Topp, J. Miller, A. Gkazi, A. Al-Chalabi, L.H. van den Berg, J. Veldink, V. Silani, N. Ticozzi, C.E. Shaw, R.H. Baloh, S. Appel, E. Simpson, C. Lagier-Tourenne, S.M. Pulst, S. Gibson, J.Q. Trojanowski, L. Elman, L. McCluskey, M. Grossman, N.A. Shneider,

W.K. Chung, J.M. Ravits, J.D. Glass, K.B. Sims, V.M. Van Deerlin, T. Maniatis, S.D. Hayes, A. Ordureau, S. Swarup, J. Landers, F. Baas, A.S. Allen, R.S. Bedlack, J.W. Harper, A.D. Gitler, G.A. Rouleau, R. Brown, M.B. Harms, G.M. Cooper, T. Harris, R.M. Myers, and D.B. Goldstein. 2015. Exome sequencing in amyotrophic lateral sclerosis identifies risk genes and pathways. *Science*. 347:1436-1441.

Cohen, P., and M. Goedert. 2004. GSK3 inhibitors: development and therapeutic potential. *Nat Rev Drug Discov*. 3:479-487.

Corcia, P., C. Tauber, J. Vercoullie, N. Arlicot, C. Prunier, J. Praline, G. Nicolas, Y. Venel, C. Hommet, J.L. Baulieu, J.P. Cottier, C. Roussel, M. Kassiou, D. Guilloteau, and M.J. Ribeiro. 2012. Molecular imaging of microglial activation in amyotrophic lateral sclerosis. *PLoS One*. 7:e52941.

Corrado, L., A. Ratti, C. Gellera, E. Buratti, B. Castellotti, Y. Carlomagno, N. Ticozzi, L. Mazzini, L. Testa, F. Taroni, F.E. Baralle, V. Silani, and S. D'Alfonso. 2009. High frequency of TARDBP gene mutations in Italian patients with amyotrophic lateral sclerosis. *Hum Mutat*. 30:688-694.

Cosson, P., A. Marchetti, M. Ravazzola, and L. Orci. 2012. Mitofusin-2 independent juxtaposition of endoplasmic reticulum and mitochondria: an ultrastructural study. *PLoS One*. 7:e46293.

Coughlan, K.S., M.R. Mitchem, M.C. Hogg, and J.H. Prehn. 2015. "Preconditioning" with latrepirdine, an adenosine 5'-monophosphate-activated protein kinase activator, delays amyotrophic lateral sclerosis progression in SOD1(G93A) mice. *Neurobiol Aging*. 36:1140-1150.

Csordas, G., C. Renken, P. Varnai, L. Walter, D. Weaver, K.F. Buttle, T. Balla, C.A. Mannella, and G. Hajnoczky. 2006. Structural and functional features and significance of the physical linkage between ER and mitochondria. *J Cell Biol*. 174:915-921.

Csordas, G., P. Varnai, T. Golenar, S. Roy, G. Purkins, T.G. Schneider, T. Balla, and G. Hajnoczky. 2010. Imaging interorganelle contacts and local calcium dynamics at the ER-mitochondrial interface. *Mol Cell*. 39:121-132.

Davis, S.A., S. Itaman, C.M. Khalid-Janney, J.A. Sherard, J.A. Dowell, N.J. Cairns, and M.A. Gitcho. 2018. TDP-43 interacts with mitochondrial proteins critical for mitophagy and mitochondrial dynamics. *Neurosci Lett*. 678:8-15.

de Brito, O.M., and L. Scorrano. 2008. Mitofusin 2 tethers endoplasmic reticulum to mitochondria. *Nature*. 456:605-610.

De Vos, K.J., G.M. Morotz, R. Stoica, E.L. Tudor, K.F. Lau, S. Ackerley, A. Warley, C.E. Shaw, and C.C. Miller. 2012. VAPB interacts with the mitochondrial protein PTPIP51 to regulate calcium homeostasis. *Hum Mol Genet*. 21:1299-1311.

DeJesus-Hernandez, M., I.R. Mackenzie, B.F. Boeve, A.L. Boxer, M. Baker, N.J. Rutherford, A.M. Nicholson, N.A. Finch, H. Flynn, J. Adamson, N. Kouri, A. Wojtas, P. Sengdy, G.Y. Hsiung, A. Karydas, W.W. Seeley, K.A. Josephs, G. Coppola, D.H. Geschwind, Z.K. Wszolek, H. Feldman, D.S. Knopman, R.C. Petersen, B.L. Miller, D.W. Dickson, K.B. Boylan, N.R. Graff-Radford, and R. Rademakers. 2011. Expanded GGGGCC hexanucleotide repeat in noncoding region of C9ORF72 causes chromosome 9p-linked FTD and ALS. *Neuron*. 72:245-256.

Del Bo, R., C. Tiloca, V. Pensato, L. Corrado, A. Ratti, N. Ticozzi, S. Corti, B. Castellotti, L. Mazzini, G. Soraru, C. Cereda, S. D'Alfonso, C. Gellera, G.P. Comi, and V. Silani. 2011. Novel optineurin mutations in patients with familial and sporadic amyotrophic lateral sclerosis. *J Neurol Neurosurg Psychiatry*. 82:1239-1243.

Del Prete, D., J.M. Suski, B. Oules, D. Debayle, A.S. Gay, S. Lacas-Gervais, R. Bussiere, C. Bauer, P. Pinton, P. Paterlini-Brechot, M.R. Wieckowski, F. Checler, and M. Chami. 2017. Localization and Processing of the Amyloid-beta Protein Precursor in Mitochondria-Associated Membranes. *J Alzheimers Dis*. 55:1549-1570.

Deng, J., P. Wang, X. Chen, H. Cheng, J. Liu, K. Fushimi, L. Zhu, and J.Y. Wu. 2018. FUS interacts with ATP synthase beta subunit and induces mitochondrial unfolded protein response in cellular and animal models. *Proc Natl Acad Sci U S A*. 115:E9678-e9686.

Dewil, M., D. Lambrechts, R. Sciot, P.J. Shaw, P.G. Ince, W. Robberecht, and L. Van den Bosch. 2007. Vascular endothelial growth factor counteracts the loss of phospho-Akt preceding motor neurone degeneration in amyotrophic lateral sclerosis. *Neuropathol Appl Neurobiol*. 33:499-509.

Di Mattia, T., L.P. Wilhelm, S. Ikhlef, C. Wendling, D. Spehner, Y. Nomine, F. Giordano, C. Mathelin, G. Drin, C. Tomasetto, and F. Alpy. 2018. Identification of MOSPD2, a novel scaffold for endoplasmic reticulum membrane contact sites. *EMBO Rep*. 19.

Doble, B.W., and J.R. Woodgett. 2003. GSK-3: tricks of the trade for a multi-tasking kinase. *J Cell Sci*. 116:1175-1186.

Dreser, A., J.T. Vollrath, A. Sechi, S. Johann, A. Roos, A. Yamoah, I. Katona, S. Bohlega, D. Wiemuth, Y. Tian, A. Schmidt, J. Vervoorts, M. Dohmen, C. Beyer, J. Anink, E. Aronica, D. Troost, J. Weis, and A. Goswami. 2017. The ALS-linked E102Q mutation in Sigma receptor-1 leads to ER stress-mediated defects in protein homeostasis and dysregulation of RNA-binding proteins. *Cell Death Differ*. 24:1655-1671.

Dukkipati, S.S., T.L. Garrett, and S.M. Elbasiouny. 2018. The vulnerability of spinal motoneurons and soma size plasticity in a mouse model of amyotrophic lateral sclerosis. *J Physiol*. 596:1723-1745.

Egawa, N., S. Kitaoka, K. Tsukita, M. Naitoh, K. Takahashi, T. Yamamoto, F. Adachi, T. Kondo, K. Okita, I. Asaka, T. Aoi, A. Watanabe, Y. Yamada, A. Morizane, J. Takahashi, T. Ayaki, H. Ito, K. Yoshikawa, S. Yamawaki, S. Suzuki, D. Watanabe, H. Hioki, T. Kaneko, K. Makioka, K. Okamoto, H. Takuma, A. Tamaoka, K. Hasegawa, T. Nonaka, M. Hasegawa, A. Kawata, M. Yoshida, T. Nakahata, R. Takahashi, M.C. Marchetto, F.H. Gage, S. Yamanaka, and H. Inoue. 2012. Drug screening for ALS using patient-specific induced pluripotent stem cells. *Sci Transl Med*. 4:145ra104.

Eidenmuller, J., T. Fath, T. Maas, M. Pool, E. Sontag, and R. Brandt. 2001. Phosphorylation-mimicking glutamate clusters in the proline-rich region are sufficient to simulate the functional deficiencies of hyperphosphorylated tau protein. *Biochem J*. 357:759-767.

Evans, C.S., and E.L.F. Holzbaur. 2019. Autophagy and mitophagy in ALS. *Neurobiol Dis*. 122:35-40.

Feng, H.L., Y. Leng, C.H. Ma, J. Zhang, M. Ren, and D.M. Chuang. 2008. Combined lithium and valproate treatment delays disease onset, reduces neurological deficits and prolongs survival in an amyotrophic lateral sclerosis mouse model. *Neuroscience*. 155:567-572.

Filadi, R., E. Greotti, G. Turacchio, A. Luini, T. Pozzan, and P. Pizzo. 2015. Mitofusin 2 ablation increases endoplasmic reticulum-mitochondria coupling. *Proc Natl Acad Sci U S A*. 112:E2174-2181.

Filadi, R., P. Theurey, and P. Pizzo. 2017. The endoplasmic reticulum-mitochondria coupling in health and disease: Molecules, functions and significance. *Cell Calcium*. 62:1-15.

Forde, J.E., and T.C. Dale. 2007. Glycogen synthase kinase 3: a key regulator of cellular fate. *Cell Mol Life Sci*. 64:1930-1944.

Fornai, F., P. Longone, L. Cafaro, O. Kastsiuchenka, M. Ferrucci, M.L. Manca, G. Lazzeri, A. Spalloni, N. Bellio, P. Lenzi, N. Modugno, G. Siciliano, C. Isidoro, L. Murri, S. Ruggieri, and A. Paparelli. 2008. Lithium delays progression of amyotrophic lateral sclerosis. *Proc Natl Acad Sci U S A*. 105:2052-2057.

Freischmidt, A., T. Wieland, B. Richter, W. Ruf, V. Schaeffer, K. Muller, N. Marroquin, F. Nordin, A. Hubers, P. Weydt, S. Pinto, R. Press, S. Millecamps, N. Molko, E. Bernard, C. Desnuelle, M.H. Soriani, J. Dorst, E. Graf, U. Nordstrom, M.S. Feiler, S. Putz, T.M. Boeckers, T. Meyer, A.S. Winkler, J. Winkelman, M. de Carvalho, D.R. Thal, M. Otto, T. Brannstrom, A.E. Volk, P. Kursula, K.M. Danzer, P.

Lichtner, I. Dikic, T. Meitinger, A.C. Ludolph, T.M. Strom, P.M. Andersen, and J.H. Weishaupt. 2015. Haploinsufficiency of TBK1 causes familial ALS and fronto-temporal dementia. *Nat Neurosci*. 18:631-636.

Freyre, C.A.C., P.C. Rauher, C.S. Ejsing, and R.W. Klemm. 2019. MIGA2 Links Mitochondria, the ER, and Lipid Droplets and Promotes De Novo Lipogenesis in Adipocytes. *Mol Cell*.

Friedman, J.R., L.L. Lackner, M. West, J.R. DiBenedetto, J. Nunnari, and G.K. Voeltz. 2011. ER tubules mark sites of mitochondrial division. *Science*. 334:358-362.

Friedman, J.R., B.M. Webster, D.N. Mastronarde, K.J. Verhey, and G.K. Voeltz. 2010. ER sliding dynamics and ER-mitochondrial contacts occur on acetylated microtubules. *J Cell Biol*. 190:363-375.

Galmes, R., A. Houcine, A.R. van Vliet, P. Agostinis, C.L. Jackson, and F. Giordano. 2016. ORP5/ORP8 localize to endoplasmic reticulum-mitochondria contacts and are involved in mitochondrial function. *EMBO Rep*. 17:800-810.

Gautier, C.A., Z. Erpapazoglou, F. Mouton-Liger, M.P. Muriel, F. Cormier, S. Bigou, S. Duffaure, M. Girard, B. Foret, A. Iannielli, V. Broccoli, C. Dalle, D. Bohl, P.P. Michel, J.C. Corvol, A. Brice, and O. Corti. 2016. The endoplasmic reticulum-mitochondria interface is perturbed in PARK2 knockout mice and patients with PARK2 mutations. *Hum Mol Genet*. 25:2972-2984.

Gelmetti, V., P. De Rosa, L. Torosantucci, E.S. Marini, A. Romagnoli, M. Di Rienzo, G. Arena, D. Vignone, G.M. Fimia, and E.M. Valente. 2017. PINK1 and BECN1 relocalize at mitochondria-associated membranes during mitophagy and promote ER-mitochondria tethering and autophagosome formation. *Autophagy*. 13:654-669.

Geloso, M.C., V. Corvino, E. Marchese, A. Serrano, F. Michetti, and N. D'Ambrosi. 2017. The Dual Role of Microglia in ALS: Mechanisms and Therapeutic Approaches. *Front Aging Neurosci*. 9:242.

Ghaffari, L.T., A. Starr, A.T. Nelson, and R. Sattler. 2018. Representing Diversity in the Dish: Using Patient-Derived in Vitro Models to Recreate the Heterogeneity of Neurological Disease. *Front Neurosci*. 12:56.

Giacomello, M., I. Drago, M. Bortolozzi, M. Scorzeto, A. Gianelle, P. Pizzo, and T. Pozzan. 2010. Ca2+ hot spots on the mitochondrial surface are generated by Ca2+ mobilization from stores, but not by activation of store-operated Ca2+ channels. *Mol Cell*. 38:280-290.

Gitcho, M.A., R.H. Baloh, S. Chakraverty, K. Mayo, J.B. Norton, D. Levitch, K.J. Hatanpaa, C.L. White, 3rd, E.H. Bigio, R. Caselli, M. Baker, M.T. Al-Lozi, J.C. Morris, A. Pestronk, R. Rademakers, A.M. Goate, and N.J. Cairns. 2008. TDP-43 A315T mutation in familial motor neuron disease. *Ann Neurol*. 63:535-538.

Gkogkas, C., S. Middleton, A.M. Kremer, C. Wardrope, M. Hannah, T.H. Gillingwater, and P. Skehel. 2008. VAPB interacts with and modulates the activity of ATF6. *Hum Mol Genet*. 17:1517-1526.

Goedert, M., and M.G. Spillantini. 2006. A century of Alzheimer's disease. *Science*. 314:777-781.

Gomez-Suaga, P., S. Paillusson, R. Stoica, W. Noble, D.P. Hanger, and C.C. Miller. 2017a. The ER-mitochondria tethering complex VAPB-PTPIP51 regulates autophagy. *Curr. Biol.* 27:371-385.

Gomez-Suaga, P., S. Paillusson, R. Stoica, W. Noble, D.P. Hanger, and C.C.J. Miller. 2017b. The ER-Mitochondria Tethering Complex VAPB-PTPIP51 Regulates Autophagy. *Curr Biol*. 27:371-385.

Gomez-Suaga, P., B.G. Perez-Nievas, E.B. Glennon, D.H.W. Lau, S. Paillusson, G.M. Morotz, T. Cali, P. Pizzo, W. Noble, and C.C.J. Miller. 2019. The VAPB-PTPIP51 endoplasmic reticulum-mitochondria tethering proteins are present in neuronal synapses and regulate synaptic activity. *Acta Neuropathol Commun*. 7:35.

Gregianin, E., G. Pallafacchina, S. Zanin, V. Crippa, P. Rusmini, A. Poletti, M. Fang, Z. Li, L. Diano, A. Petrucci, L. Lispi, T. Cavallaro, G.M. Fabrizi, M. Muglia, F. Boaretto, A. Vettori, R. Rizzuto, M.L. Mostacciuolo, and G. Vazza. 2016. Loss-of-function mutations in the SIGMAR1 gene cause distal hereditary motor neuropathy by impairing ER-mitochondria tethering and Ca2+ signalling. *Hum Mol Genet*. 25:3741-3753.

Griffiths, E.J., and G.A. Rutter. 2009. Mitochondrial calcium as a key regulator of mitochondrial ATP production in mammalian cells. *Biochim Biophys Acta*. 1787:1324-1333.

Gross, O., C.J. Thomas, G. Guarda, and J. Tschopp. 2011. The inflammasome: an integrated view. *Immunol Rev*. 243:136-151.

Group, W., and E.M.-A.S. Group. 2017. Safety and efficacy of edaravone in well defined patients with amyotrophic lateral sclerosis: a randomised, double-blind, placebo-controlled trial. *Lancet Neurol*. 16:505-512.

Guardia-Laguarta, C., E. Area-Gomez, C. Rub, Y. Liu, J. Magrane, D. Becker, W. Voos, E.A. Schon, and S. Przedborski. 2014. alpha-Synuclein is localized to mitochondria-associated ER membranes. *J Neurosci*. 34:249-259.

Guedes-Dias, P., and E.L.F. Holzbaur. 2019. Axonal transport: Driving synaptic function. *Science*. 366.

Guo, F., X. Liu, H. Cai, and W. Le. 2018. Autophagy in neurodegenerative diseases: pathogenesis and therapy. *Brain Pathol*. 28:3-13.

Guo, W., L. Fumagalli, R. Prior, and L. Van Den Bosch. 2017. Current Advances and Limitations in Modeling ALS/FTD in a Dish Using Induced Pluripotent Stem Cells. *Front Neurosci*. 11.

Hamasaki, M., N. Furuta, A. Matsuda, A. Nezu, A. Yamamoto, N. Fujita, H. Oomori, T. Noda, T. Haraguchi, Y. Hiraoka, A. Amano, and T. Yoshimori. 2013. Autophagosomes form at ER-mitochondria contact sites. *Nature*. 495:389-393.

Hardie, D.G., F.A. Ross, and S.A. Hawley. 2012. AMPK: a nutrient and energy sensor that maintains energy homeostasis. *Nat Rev Mol Cell Biol*. 13:251-262.

Hasegawa, M., T. Arai, T. Nonaka, F. Kametani, M. Yoshida, Y. Hashizume, T.G. Beach, E. Buratti, F. Baralle, M. Morita, I. Nakano, T. Oda, K. Tsuchiya, and H. Akiyama. 2008. Phosphorylated TDP-43 in frontotemporal lobar degeneration and amyotrophic lateral sclerosis. *Ann Neurol*. 64:60-70.

Hayashi, T., and T.P. Su. 2007. Sigma-1 receptor chaperones at the ER-mitochondrion interface regulate Ca(2+) signaling and cell survival. *Cell*. 131:596-610.

Hedskog, L., C.M. Pinho, R. Filadi, A. Ronnback, L. Hertwig, B. Wiehager, P. Larssen, S. Gellhaar, A. Sandebring, M. Westerlund, C. Graff, B. Winblad, D. Galter, H. Behbahani, P. Pizzo, E. Glaser, and M. Ankarcrona. 2013. Modulation of the endoplasmic reticulum-mitochondria interface in Alzheimer's disease and related models. *Proc Natl Acad Sci U S A*. 110:7916-7921.

Hennrich, M.L., and A.C. Gavin. 2015. Quantitative mass spectrometry of posttranslational modifications: keys to confidence. *Sci Signal*. 8:re5.

Hinchcliffe, M., and A. Smith. 2017. Riluzole: real-world evidence supports significant extension of median survival times in patients with amyotrophic lateral sclerosis. *Degener Neurol Neuromuscul Dis*. 7:61-70.

Hirabayashi, Y., S.K. Kwon, H. Paek, W.M. Pernice, M.A. Paul, J. Lee, P. Erfani, A. Raczkowski, D.S. Petrey, L.A. Pon, and F. Polleux. 2017. ER-mitochondria tethering by PDZD8 regulates Ca(2+) dynamics in mammalian neurons. *Science*. 358:623-630.

Hoffman, N.J., B.L. Parker, R. Chaudhuri, K.H. Fisher-Wellman, M. Kleinert, S.J. Humphrey, P. Yang, M. Holliday, S. Trefely, D.J. Fazakerley, J. Stockli, J.G. Burchfield, T.E. Jensen, R. Jothi, B. Kiens, J.F. Wojtaszewski, E.A. Richter, and D.E. James. 2015. Global Phosphoproteomic Analysis of Human Skeletal Muscle Reveals a Network of Exercise-Regulated Kinases and AMPK Substrates. *Cell Metab*. 22:922-935.

Hong, K., Y. Li, W. Duan, Y. Guo, H. Jiang, W. Li, and C. Li. 2012. Full-length TDP-43 and its C-terminal fragments activate mitophagy in NSC34 cell line. *Neurosci Lett*. 530:144-149.

Horike, N., H. Sakoda, A. Kushiyama, H. Ono, M. Fujishiro, H. Kamata, K. Nishiyama, Y. Uchijima, Y. Kurihara, H. Kurihara, and T. Asano. 2008. AMP-activated protein kinase activation increases phosphorylation of glycogen synthase kinase 3beta and thereby reduces cAMP-responsive element transcriptional activity and phosphoenolpyruvate carboxykinase C gene expression in the liver. *J Biol Chem*. 283:33902-33910.

Hung, V., S.S. Lam, N.D. Udeshi, T. Svinkina, G. Guzman, V.K. Mootha, S.A. Carr, and A.Y. Ting. 2017. Proteomic mapping of cytosol-facing outer mitochondrial and ER membranes in living human cells by proximity biotinylation. *Elife*. 6.

Hurst, S., J. Hoek, and S.S. Sheu. 2017. Mitochondrial Ca(2+) and regulation of the permeability transition pore. *J Bioenerg Biomembr*. 49:27-47.

Huttlin, E.L., L. Ting, R.J. Bruckner, F. Gebreab, M.P. Gygi, J. Szpyt, S. Tam, G. Zarraga, G. Colby, K. Baltier, R. Dong, V. Guarani, L.P. Vaites, A. Ordureau, R. Rad, B.K. Erickson, M. Wuhr, J. Chick, B. Zhai, D. Kolippakkam, J. Mintseris, R.A. Obar, T. Harris, S. Artavanis-Tsakonas, M.E. Sowa, P. De Camilli, J.A. Paulo, J.W. Harper, and S.P. Gygi. 2015. The BioPlex Network: A Systematic Exploration of the Human Interactome. *Cell*. 162:425-440.

Ilieva, E.V., V. Ayala, M. Jove, E. Dalfo, D. Cacabelos, M. Povedano, M.J. Bellmunt, I. Ferrer, R. Pamplona, and M. Portero-Otin. 2007. Oxidative and endoplasmic reticulum stress interplay in sporadic amyotrophic lateral sclerosis. *Brain*. 130:3111-3123.

Ince, P.G., J. Tomkins, J.Y. Slade, N.M. Thatcher, and P.J. Shaw. 1998. Amyotrophic lateral sclerosis associated with genetic abnormalities in the gene encoding Cu/Zn superoxide dismutase: molecular pathology of five new cases, and comparison with previous reports and 73 sporadic cases of ALS. *J Neuropathol Exp Neurol*. 57:895-904.

Israelson, A., N. Arbel, S. Da Cruz, H. Ilieva, K. Yamanaka, V. Shoshan-Barmatz, and D.W. Cleveland. 2010. Misfolded mutant SOD1 directly inhibits VDAC1 conductance in a mouse model of inherited ALS. *Neuron*. 67:575-587.

Ito, Y., D. Ofengeim, A. Najafov, S. Das, S. Saberi, Y. Li, J. Hitomi, H. Zhu, H. Chen, L. Mayo, J. Geng, P. Amin, J.P. DeWitt, A.K. Mookhtiar, M. Florez, A.T. Ouchida, J.B. Fan, M. Pasparakis, M.A. Kelliher, J. Ravits, and J. Yuan. 2016. RIPK1 mediates axonal degeneration by promoting inflammation and necroptosis in ALS. *Science*. 353:603-608.

Ivanova, H., T. Vervliet, L. Missiaen, J.B. Parys, H. De Smedt, and G. Bultynck. 2014. Inositol 1,4,5-trisphosphate receptor-isoform diversity in cell death and survival. *Biochim Biophys Acta*. 1843:2164-2183.

Iwasawa, R., A.L. Mahul-Mellier, C. Datler, E. Pazarentzos, and S. Grimm. 2011. Fis1 and Bap31 bridge the mitochondria-ER interface to establish a platform for apoptosis induction. *EMBO J*. 30:556-568.

Iyer, S., V. Subramanian, and K.R. Acharya. 2018. C9orf72, a protein associated with amyotrophic lateral sclerosis (ALS) is a guanine nucleotide exchange factor. *In* PeerJ. Vol. 6.

Jaiswal, M.K. 2019. Riluzole and edaravone: A tale of two amyotrophic lateral sclerosis drugs. *Med Res Rev*. 39:733-748.

Jara, J.H., B. Genc, M.J. Stanford, P. Pytel, R.P. Roos, S. Weintraub, M.M. Mesulam, E.H. Bigio, R.J. Miller, and P.H. Ozdinler. 2017. Evidence for an early innate immune response in the motor cortex of ALS. *J Neuroinflammation*. 14:129.

Jesse, C.M., E. Bushuven, P. Tripathi, A. Chandrasekar, C.M. Simon, C. Drepper, A. Yamoah, A. Dreser, I. Katona, S. Johann, C. Beyer, S. Wagner, M. Grond, S. Nikolin, J. Anink, D. Troost, M. Sendtner, A. Goswami, and J. Weis. 2017. ALS-Associated Endoplasmic Reticulum Proteins in Denervated Skeletal Muscle: Implications for Motor Neuron Disease Pathology. *Brain Pathol*. 27:781-794.

Jiang, H.Q., M. Ren, H.Z. Jiang, J. Wang, J. Zhang, X. Yin, S.Y. Wang, Y. Qi, X.D. Wang, and H.L. Feng. 2014. Guanabenz delays the onset of disease symptoms, extends lifespan, improves motor performance and attenuates motor neuron loss in the SOD1 G93A mouse model of amyotrophic lateral sclerosis. *Neuroscience*. 277:132-138.

Jiang, Z., W. Wang, G. Perry, X. Zhu, and X. Wang. 2015. Mitochondrial dynamic abnormalities in amyotrophic lateral sclerosis. *Transl Neurodegener*. 4:14.

Kabashi, E., P.N. Valdmanis, P. Dion, D. Spiegelman, B.J. McConkey, C. Vande Velde, J.P. Bouchard, L. Lacomblez, K. Pochigaeva, F. Salachas, P.F. Pradat, W. Camu, V. Meininger, N. Dupre, and G.A. Rouleau. 2008. TARDBP mutations in individuals with sporadic and familial amyotrophic lateral sclerosis. *Nat Genet*. 40:572-574.

Kaidanovich-Beilin, O., and J.R. Woodgett. 2011. GSK-3: Functional Insights from Cell Biology and Animal Models. *Front Mol Neurosci*. 4:40.

Kanekura, K., I. Nishimoto, S. Aiso, and M. Matsuoka. 2006. Characterization of amyotrophic lateral sclerosis-linked P56S mutation of vesicle-associated membrane protein-associated protein B (VAPB/ALS8). *J Biol Chem*. 281:30223-30233.

Kanekura, K., H. Suzuki, S. Aiso, and M. Matsuoka. 2009. ER Stress and unfolded protein response in amyotrophic lateral sclerosis. *Mol. Neurobiol.* 39:81-89.

Kato, S., M. Takikawa, K. Nakashima, A. Hirano, D.W. Cleveland, H. Kusaka, N. Shibata, M. Kato, I. Nakano, and E. Ohama. 2000. New consensus research on

neuropathological aspects of familial amyotrophic lateral sclerosis with superoxide dismutase 1 (SOD1) gene mutations: inclusions containing SOD1 in neurons and astrocytes. *Amyotroph Lateral Scler Other Motor Neuron Disord*. 1:163-184.

Kim, H.J., and J.P. Taylor. 2017. Lost in Transportation: Nucleocytoplasmic Transport Defects in ALS and Other Neurodegenerative Diseases. *Neuron*. 96:285-297.

Kim, J.Y., A. Jang, R. Reddy, W.H. Yoon, and J.L. Jankowsky. 2016. Neuronal overexpression of human VAPB slows motor impairment and neuromuscular denervation in a mouse model of ALS. *Hum Mol Genet*. 25:4661-4673.

Kipanyula, M.J., L. Contreras, E. Zampese, C. Lazzari, A.K. Wong, P. Pizzo, C. Fasolato, and T. Pozzan. 2012. Ca2+ dysregulation in neurons from transgenic mice expressing mutant presenilin 2. *Aging Cell*. 11:885-893.

Koh, S.H., Y. Kim, H.Y. Kim, S. Hwang, C.H. Lee, and S.H. Kim. 2007. Inhibition of glycogen synthase kinase-3 suppresses the onset of symptoms and disease progression of G93A-SOD1 mouse model of ALS. *Exp Neurol*. 205:336-346.

Komine, O., and K. Yamanaka. 2015. Neuroinflammation in motor neuron disease. *Nagoya J Med Sci*. 77:537-549.

Kornmann, B., E. Currie, S.R. Collins, M. Schuldiner, J. Nunnari, J.S. Weissman, and P. Walter. 2009. An ER-mitochondria tethering complex revealed by a synthetic biology screen. *Science*. 325:477-481.

Kornmann, B., C. Osman, and P. Walter. 2011. The conserved GTPase Gem1 regulates endoplasmic reticulum-mitochondria connections. *Proc Natl Acad Sci U S A*. 108:14151-14156.

Korobova, F., V. Ramabhadran, and H.N. Higgs. 2013. An actin-dependent step in mitochondrial fission mediated by the ER-associated formin INF2. *Science*. 339:464-467.

Koshiba, T., S.A. Detmer, J.T. Kaiser, H. Chen, J.M. McCaffery, and D.C. Chan. 2004. Structural basis of mitochondrial tethering by mitofusin complexes. *Science*. 305:858-862.

Krols, M., G. van Isterdael, B. Asselbergh, A. Kremer, S. Lippens, V. Timmerman, and S. Janssens. 2016. Mitochondria-associated membranes as hubs for neurodegeneration. *Acta Neuropathol*. 131:505-523.

Kwiatkowski, T.J., D.A. Bosco, A.L. LeClerc, E. Tamrazian, C.R. Vanderburg, C. Russ, A. Davis, J. Gilchrist, E.J. Kasarskis, T. Munsat, P. Valdmanis, G.A. Rouleau, B.A. Hosler, P. Cortelli, P.J.d. Jong, Y. Yoshinaga, J.L. Haines, M.A. Pericak-Vance, J. Yan, N. Ticozzi, T. Siddique, D. McKenna-Yasek, P.C. Sapp, H.R. Horvitz, J.E. Landers, and R.H. Brown. 2009. Mutations in the FUS/TLS Gene on Chromosome 16 Cause Familial Amyotrophic Lateral Sclerosis.

Lau, D.H.W., N. Hartopp, N.J. Welsh, S. Mueller, E.B. Glennon, G.M. Morotz, A. Annibali, P. Gomez-Suaga, R. Stoica, S. Paillusson, and C.C.J. Miller. 2018. Disruption of ER-mitochondria signalling in fronto-temporal dementia and related amyotrophic lateral sclerosis. *Cell Death Dis*. 9:327.

Leal, N.S., B. Schreiner, C.M. Pinho, R. Filadi, B. Wiehager, H. Karlstrom, P. Pizzo, and M. Ankarcrona. 2016. Mitofusin-2 knockdown increases ER-mitochondria contact and decreases amyloid beta-peptide production. *J Cell Mol Med*. 20:1686-1695.

Lewis, S.C., L.F. Uchiyama, and J. Nunnari. 2016. ER-mitochondria contacts couple mtDNA synthesis with mitochondrial division in human cells. *Science*. 353:aaf5549.

Li, Q., C. Vande Velde, A. Israelson, J. Xie, A.O. Bailey, M.Q. Dong, S.J. Chun, T. Roy, L. Winer, J.R. Yates, R.A. Capaldi, D.W. Cleveland, and T.M. Miller. 2010. ALS-linked mutant superoxide dismutase 1 (SOD1) alters mitochondrial protein composition and decreases protein import. *Proc Natl Acad Sci U S A*. 107:21146-21151.

Liao, B., W. Zhao, D.R. Beers, J.S. Henkel, and S.H. Appel. 2012. Transformation from a neuroprotective to a neurotoxic microglial phenotype in a mouse model of ALS. *Exp Neurol*. 237:147-152.

Ling, S.C., M. Polymenidou, and D.W. Cleveland. 2013. Converging mechanisms in ALS and FTD: disrupted RNA and protein homeostasis. *Neuron*. 79:416-438.

Liu, Y., X. Ma, H. Fujioka, J. Liu, S. Chen, and X. Zhu. 2019. DJ-1 regulates the integrity and function of ER-mitochondria association through interaction with IP3R3-Grp75-VDAC1. *Proc Natl Acad Sci U S A*. 116:25322-25328.

Liu, Y.J., T.C. Ju, H.M. Chen, Y.S. Jang, L.M. Lee, H.L. Lai, H.C. Tai, J.M. Fang, Y.L. Lin, P.H. Tu, and Y. Chern. 2015. Activation of AMP-activated protein kinase alpha1 mediates mislocalization of TDP-43 in amyotrophic lateral sclerosis. *Hum Mol Genet*. 24:787-801.

Luo, J. 2012. The role of GSK3beta in the development of the central nervous system. *Front Biol (Beijing)*. 7:212-220.

Luty, A.A., J.B. Kwok, C. Dobson-Stone, C.T. Loy, K.G. Coupland, H. Karlstrom, T. Sobow, J. Tchorzewska, A. Maruszak, M. Barcikowska, P.K. Panegyres, C. Zekanowski, W.S. Brooks, K.L. Williams, I.P. Blair, K.A. Mather, P.S. Sachdev, G.M. Halliday, and P.R. Schofield. 2010. Sigma nonopioid intracellular receptor 1 mutations cause frontotemporal lobar degeneration-motor neuron disease. *Ann Neurol*. 68:639-649.

Macaskill, A.F., J.E. Rinholm, A.E. Twelvetrees, I.L. Arancibia-Carcamo, J. Muir, A. Fransson, P. Aspenstrom, D. Attwell, and J.T. Kittler. 2009. Miro1 is a calcium

sensor for glutamate receptor-dependent localization of mitochondria at synapses. *Neuron*. 61:541-555.

Mancuso, R., S. Olivan, A. Rando, C. Casas, R. Osta, and X. Navarro. 2012. Sigma-1R agonist improves motor function and motoneuron survival in ALS mice. *Neurotherapeutics*. 9:814-826.

Mandrioli, J., R. D'Amico, E. Zucchi, A. Gessani, N. Fini, A. Fasano, C. Caponnetto, A. Chiò, E. Dalla Bella, C. Lunetta, L. Mazzini, K. Marinou, G. Sorarù, S. de Biasi, D. Lo Tartaro, M. Pinti, and A. Cossarizza. 2018. Rapamycin treatment for amyotrophic lateral sclerosis: Protocol for a phase II randomized, double-blind, placebo-controlled, multicenter, clinical trial (RAP-ALS trial). *Medicine (Baltimore)*. 97.

Mandrioli, J., L. Mediani, S. Alberti, and S. Carra. 2019. ALS and FTD: Where RNA metabolism meets protein quality control. *Semin Cell Dev Biol*.

Mann, D.M.A., and J.S. Snowden. 2017. Frontotemporal lobar degeneration: Pathogenesis, pathology and pathways to phenotype. *Brain Pathol*. 27:723-736.

Mao, D., G. Lin, B. Tepe, Z. Zuo, K.L. Tan, M. Senturk, S. Zhang, B.R. Arenkiel, M. Sardiello, and H.J. Bellen. 2019. VAMP associated proteins are required for autophagic and lysosomal degradation by promoting a PtdIns4P-mediated endosomal pathway. *Autophagy*:1-20.

Martino Adami, P.V., Z. Nichtova, D.B. Weaver, A. Bartok, T. Wisniewski, D.R. Jones, S. Do Carmo, E.M. Castano, A.C. Cuello, G. Hajnoczky, and L. Morelli. 2019. Perturbed mitochondria-ER contacts in live neurons that model the amyloid pathology of Alzheimer's disease. *J Cell Sci*. 132.

Maruyama, H., H. Morino, H. Ito, Y. Izumi, H. Kato, Y. Watanabe, Y. Kinoshita, M. Kamada, H. Nodera, H. Suzuki, O. Komure, S. Matsuura, K. Kobatake, N. Morimoto, K. Abe, N. Suzuki, M. Aoki, A. Kawata, T. Hirai, T. Kato, K. Ogasawara, A. Hirano, T. Takumi, H. Kusaka, K. Hagiwara, R. Kaji, and H. Kawakami. 2010. Mutations of optineurin in amyotrophic lateral sclerosis. *Nature*. 465:223-226.

Mathis, S., C. Goizet, A. Soulages, J.M. Vallat, and G.L. Masson. 2019. Genetics of amyotrophic lateral sclerosis: A review. *J Neurol Sci*. 399:217-226.

Maury, Y., J. Come, R.A. Piskorowski, N. Salah-Mohellibi, V. Chevaleyre, M. Peschanski, C. Martinat, and S. Nedelec. 2015. Combinatorial analysis of developmental cues efficiently converts human pluripotent stem cells into multiple neuronal subtypes. *Nat Biotechnol*. 33:89-96.

McCauley, M.E., and R.H. Baloh. 2019. Inflammation in ALS/FTD pathogenesis. *Acta Neuropathol*. 137:715-730.

Miller, R.G., J.D. Mitchell, M. Lyon, and D.H. Moore. 2003. Riluzole for amyotrophic lateral sclerosis (ALS)/motor neuron disease (MND). *Amyotroph Lateral Scler Other Motor Neuron Disord*. 4:191-206.

Missiroli, S., S. Patergnani, N. Caroccia, G. Pedriali, M. Perrone, M. Previati, M.R. Wieckowski, and C. Giorgi. 2018. Mitochondria-associated membranes (MAMs) and inflammation. *Cell Death Dis*. 9:329.

Mitchell, J.C., R. Constable, E. So, C. Vance, E. Scotter, L. Glover, T. Hortobagyi, E.S. Arnold, S.C. Ling, M. McAlonis, S. Da Cruz, M. Polymenidou, L. Tessarolo, D.W. Cleveland, and C.E. Shaw. 2015. Wild type human TDP-43 potentiates ALS-linked mutant TDP-43 driven progressive motor and cortical neuron degeneration with pathological features of ALS. *Acta Neuropathol Commun*. 3:36.

Mitchell, J.C., P. McGoldrick, C. Vance, T. Hortobagyi, J. Sreedharan, B. Rogelj, E.L. Tudor, B.N. Smith, C. Klasen, C.C. Miller, J.D. Cooper, L. Greensmith, and C.E. Shaw. 2013. Overexpression of human wild-type FUS causes progressive motor neuron degeneration in an age- and dose-dependent fashion. *Acta Neuropathol*. 125:273-288.

Mitne-Neto, M., M. Machado-Costa, M.C.N. Marchetto, M.H. Bengtson, C.A. Joazeiro, H. Tsuda, H.J. Bellen, H.C.A. Silva, A.S.B. Oliveira, M. Lazar, A.R. Muotri, and M. Zatz. 2011. Downregulation of VAPB expression in motor neurons derived from induced pluripotent stem cells of ALS8 patients. *Human Molecular Genetics*. 20:3642-3652.

Moller, A., C.S. Bauer, R.N. Cohen, C.P. Webster, and K.J. De Vos. 2017. Amyotrophic lateral sclerosis-associated mutant SOD1 inhibits anterograde axonal transport of mitochondria by reducing Miro1 levels. *Hum Mol Genet*. 26:4668-4679.

Moore, A.S., and E.L. Holzbaur. 2016. Dynamic recruitment and activation of ALS-associated TBK1 with its target optineurin are required for efficient mitophagy. *Proc Natl Acad Sci U S A*. 113:E3349-3358.

Mori, K., T. Arzberger, F.A. Grasser, I. Gijselinck, S. May, K. Rentzsch, S.M. Weng, M.H. Schludi, J. van der Zee, M. Cruts, C. Van Broeckhoven, E. Kremmer, H.A. Kretzschmar, C. Haass, and D. Edbauer. 2013a. Bidirectional transcripts of the expanded C9orf72 hexanucleotide repeat are translated into aggregating dipeptide repeat proteins. *Acta Neuropathol*. 126:881-893.

Mori, K., S.M. Weng, T. Arzberger, S. May, K. Rentzsch, E. Kremmer, B. Schmid, H.A. Kretzschmar, M. Cruts, C. Van Broeckhoven, C. Haass, and D. Edbauer. 2013b. The C9orf72 GGGGCC repeat is translated into aggregating dipeptide-repeat proteins in FTLD/ALS. *Science*. 339:1335-1338.

Mori, M., and K. Terada. 1998. Mitochondrial protein import in animals. *Biochim Biophys Acta*. 1403:12-27.

Morotz, G.M., K.J. De Vos, A. Vagnoni, S. Ackerley, C.E. Shaw, and C.C. Miller. 2012. Amyotrophic lateral sclerosis-associated mutant VAPBP56S perturbs calcium homeostasis to disrupt axonal transport of mitochondria. *Hum Mol Genet*. 21:1979-1988.

Morton, S., L. Hesson, M. Peggie, and P. Cohen. 2008. Enhanced binding of TBK1 by an optineurin mutant that causes a familial form of primary open angle glaucoma. *FEBS Lett*. 582:997-1002.

Moujalled, D., J.L. James, S.J. Parker, G.E. Lidgerwood, C. Duncan, J. Meyerowitz, T. Nonaka, M. Hasegawa, K.M. Kanninen, A. Grubman, J.R. Liddell, P.J. Crouch, and A.R. White. 2013. Kinase Inhibitor Screening Identifies Cyclin-Dependent Kinases and Glycogen Synthase Kinase 3 as Potential Modulators of TDP-43 Cytosolic Accumulation during Cell Stress. *PLoS One*. 8:e67433.

Munch, C., A. Rosenbohm, A.D. Sperfeld, I. Uttner, S. Reske, B.J. Krause, R. Sedlmeier, T. Meyer, C.O. Hanemann, G. Stumm, and A.C. Ludolph. 2005. Heterozygous R1101K mutation of the DCTN1 gene in a family with ALS and FTD. *Ann Neurol*. 58:777-780.

Munch, C., R. Sedlmeier, T. Meyer, V. Homberg, A.D. Sperfeld, A. Kurt, J. Prudlo, G. Peraus, C.O. Hanemann, G. Stumm, and A.C. Ludolph. 2004. Point mutations of the p150 subunit of dynactin (DCTN1) gene in ALS. *Neurology*. 63:724-726.

Naon, D., M. Zaninello, M. Giacomello, T. Varanita, F. Grespi, S. Lakshminaranayan, A. Serafini, M. Semenzato, S. Herkenne, M.I. Hernandez-Alvarez, A. Zorzano, D. De Stefani, G.W. Dorn, 2nd, and L. Scorrano. 2016. Critical reappraisal confirms that Mitofusin 2 is an endoplasmic reticulum-mitochondria tether. *Proc Natl Acad Sci U S A*. 113:11249-11254.

Naruse, H., Y. Takahashi, T. Kihira, S. Yoshida, Y. Kokubo, S. Kuzuhara, H. Ishiura, M. Amagasa, S. Murayama, S. Tsuji, and J. Goto. 2012. Mutational analysis of familial and sporadic amyotrophic lateral sclerosis with OPTN mutations in Japanese population. *Amyotroph Lateral Scler*. 13:562-566.

Neumann, M., U.H.o.Z. 1 Institute of Neuropathology, Zürich, Switzerland, R. Rademakers, J. 2 Mayo Clinic – Neuroscience, FL, USA, S. Roeber, L.-M.-U. 3 Center for Neuropathology and Prion Research, Muenchen, Germany, M. Baker, J. 2 Mayo Clinic – Neuroscience, FL, USA, H.A. Kretzschmar, L.-M.-U. 3 Center for Neuropathology and Prion Research, Muenchen, Germany, I.R.A. Mackenzie, and U.o.B.C. 4 Department of Pathology, Vancouver, British Columbia, Canada. 2019. A new subtype of frontotemporal lobar degeneration with FUS pathology. *Brain*. 132:2922-2931.

Neumann, M., D.M. Sampathu, L.K. Kwong, A.C. Truax, M.C. Micsenyi, T.T. Chou, J. Bruce, T. Schuck, M. Grossman, C.M. Clark, L.F. McCluskey, B.L. Miller, E.

Masliah, I.R. Mackenzie, H. Feldman, W. Feiden, H.A. Kretzschmar, J.Q. Trojanowski, and V.M. Lee. 2006. Ubiquitinated TDP-43 in frontotemporal lobar degeneration and amyotrophic lateral sclerosis. *Science*. 314:130-133.

Neumann, M., C.F. Valori, O. Ansorge, H.A. Kretzschmar, D.G. Munoz, H. Kusaka, O. Yokota, K. Ishihara, L.C. Ang, J.M. Bilbao, and I.R. Mackenzie. 2012. Transportin 1 accumulates specifically with FET proteins but no other transportin cargos in FTLD-FUS and is absent in FUS inclusions in ALS with FUS mutations. *Acta Neuropathol*. 124:705-716.

Nicolas, A., K.P. Kenna, A.E. Renton, N. Ticozzi, F. Faghri, R. Chia, J.A. Dominov, B.J. Kenna, M.A. Nalls, P. Keagle, A.M. Rivera, W. van Rheenen, N.A. Murphy, J. van Vugt, J.T. Geiger, R.A. Van der Spek, H.A. Pliner, Shankaracharya, B.N. Smith, G. Marangi, S.D. Topp, Y. Abramzon, A.S. Gkazi, J.D. Eicher, A. Kenna, G. Mora, A. Calvo, L. Mazzini, N. Riva, J. Mandrioli, C. Caponnetto, S. Battistini, P. Volanti, V. La Bella, F.L. Conforti, G. Borghero, S. Messina, I.L. Simone, F. Trojsi, F. Salvi, F.O. Logullo, S. D'Alfonso, L. Corrado, M. Capasso, L. Ferrucci, C.A.M. Moreno, S. Kamalakaran, D.B. Goldstein, A.D. Gitler, T. Harris, R.M. Myers, H. Phatnani, R.L. Musunuri, U.S. Evani, A. Abhyankar, M.C. Zody, J. Kaye, S. Finkbeiner, S.K. Wyman, A. LeNail, L. Lima, E. Fraenkel, C.N. Svendsen, L.M. Thompson, J.E. Van Eyk, J.D. Berry, T.M. Miller, S.J. Kolb, M. Cudkowicz, E. Baxi, M. Benatar, J.P. Taylor, E. Rampersaud, G. Wu, J. Wuu, G. Lauria, F. Verde, I. Fogh, C. Tiloca, G.P. Comi, G. Soraru, C. Cereda, P. Corcia, H. Laaksovirta, L. Myllykangas, L. Jansson, M. Valori, J. Ealing, H. Hamdalla, S. Rollinson, S. Pickering-Brown, R.W. Orrell, K.C. Sidle, A. Malaspina, J. Hardy, A.B. Singleton, J.O. Johnson, S. Arepalli, P.C. Sapp, D. McKenna-Yasek, et al. 2018. Genome-wide Analyses Identify KIF5A as a Novel ALS Gene. *Neuron*. 97:1268-1283.e1266.

Nishimura, A.L., M. Mitne-Neto, H.C. Silva, A. Richieri-Costa, S. Middleton, D. Cascio, F. Kok, J.R. Oliveira, T. Gillingwater, J. Webb, P. Skehel, and M. Zatz. 2004. A mutation in the vesicle-trafficking protein VAPB causes late-onset spinal muscular atrophy and amyotrophic lateral sclerosis. *Am J Hum Genet*. 75:822-831.

Nishimura, A.L., V. Zupunski, C. Troakes, C. Kathe, P. Fratta, M. Howell, J.M. Gallo, T. Hortobagyi, C.E. Shaw, and B. Rogelj. 2010. Nuclear import impairment causes cytoplasmic trans-activation response DNA-binding protein accumulation and is associated with frontotemporal lobar degeneration. *Brain*. 133:1763-1771.

Nixon, A., Y. Jia, C. White, and N.A. Bradbury. 2013. Fluorescence protease protection reveals the topology of the integral membrane protein Lemur Tyrosine Kinase 2 (LMTK2). *Am. J. Physiol. Cell Physiol.* 304:C164-169.

Nozaki, I., M. Arai, K. Takahashi, T. Hamaguchi, H. Yoshikawa, T. Muroishi, M. Noguchi-Shinohara, H. Ito, M. Itokawa, H. Akiyama, A. Kawata, and M. Yamada. 2010. Familial ALS with G298S mutation in TARDBP: a comparison of CSF tau protein levels with those in sporadic ALS. *Intern Med*. 49:1209-1212.

Oakes, J.A., M.C. Davies, and M.O. Collins. 2017. TBK1: a new player in ALS linking autophagy and neuroinflammation. *Mol Brain*. 10:5.

Oda, Y. 1999. Choline acetyltransferase: the structure, distribution and pathologic changes in the central nervous system. *Pathol Int*. 49:921-937.

Ono, Y., H. Tanaka, M. Takata, Y. Nagahara, Y. Noda, K. Tsuruma, M. Shimazawa, I. Hozumi, and H. Hara. 2014. SA4503, a sigma-1 receptor agonist, suppresses motor neuron damage in in vitro and in vivo amyotrophic lateral sclerosis models. *Neurosci Lett*. 559:174-178.

Paillusson, S., P. Gomez-Suaga, R. Stoica, D. Little, P. Gissen, M.J. Devine, W. Noble, D.P. Hanger, and C.C.J. Miller. 2017. alpha-Synuclein binds to the ER-mitochondria tethering protein VAPB to disrupt Ca(2+) homeostasis and mitochondrial ATP production. *Acta Neuropathol*. 134:129-149.

Paillusson, S., R. Stoica, P. Gomez-Suaga, D.H. Lau, S. Mueller, T. Miller, and C.C. Miller. 2016. There's Something Wrong with my MAM; the ER-Mitochondria Axis and Neurodegenerative Diseases. *Trends Neurosci*. 39:146-157.

Perera, N.D., R.K. Sheean, J.W. Scott, B.E. Kemp, M.K. Horne, and B.J. Turner. 2014. Mutant TDP-43 deregulates AMPK activation by PP2A in ALS models. *PLoS One*. 9:e90449.

Perera, N.D., and B.J. Turner. 2016. AMPK Signalling and Defective Energy Metabolism in Amyotrophic Lateral Sclerosis. *Neurochem Res*. 41:544-553.

Pesiridis, G.S., V.M. Lee, and J.Q. Trojanowski. 2009. Mutations in TDP-43 link glycine-rich domain functions to amyotrophic lateral sclerosis. *Hum Mol Genet*. 18:R156-162.

Pizzasegola, C., I. Caron, C. Daleno, A. Ronchi, C. Minoia, M.T. Carri, and C. Bendotti. 2009. Treatment with lithium carbonate does not improve disease progression in two different strains of SOD1 mutant mice. *Amyotroph Lateral Scler*. 10:221-228.

Puri, R., X.T. Cheng, M.Y. Lin, N. Huang, and Z.H. Sheng. 2019. Mul1 restrains Parkin-mediated mitophagy in mature neurons by maintaining ER-mitochondrial contacts. *Nat Commun*. 10:3645.

Qiao, X., S. Jia, J. Ye, X. Fang, C. Zhang, Y. Cao, C. Xu, L. Zhao, Y. Zhu, L. Wang, and M. Zheng. 2017. PTPIP51 regulates mouse cardiac ischemia/reperfusion through mediating the mitochondria-SR junction. *Sci Rep*. 7:45379.

Rapizzi, E., P. Pinton, G. Szabadkai, M.R. Wieckowski, G. Vandecasteele, G. Baird, R.A. Tuft, K.E. Fogarty, and R. Rizzuto. 2002. Recombinant expression of the voltage-

dependent anion channel enhances the transfer of Ca2+ microdomains to mitochondria. *J Cell Biol*. 159:613-624.

Renton, A.E., E. Majounie, A. Waite, J. Simon-Sanchez, S. Rollinson, J.R. Gibbs, J.C. Schymick, H. Laaksovirta, J.C. van Swieten, L. Myllykangas, H. Kalimo, A. Paetau, Y. Abramzon, A.M. Remes, A. Kaganovich, S.W. Scholz, J. Duckworth, J. Ding, D.W. Harmer, D.G. Hernandez, J.O. Johnson, K. Mok, M. Ryten, D. Trabzuni, R.J. Guerreiro, R.W. Orrell, J. Neal, A. Murray, J. Pearson, I.E. Jansen, D. Sondervan, H. Seelaar, D. Blake, K. Young, N. Halliwell, J.B. Callister, G. Toulson, A. Richardson, A. Gerhard, J. Snowden, D. Mann, D. Neary, M.A. Nalls, T. Peuralinna, L. Jansson, V.M. Isoviita, A.L. Kaivorinne, M. Holtta-Vuori, E. Ikonen, R. Sulkava, M. Benatar, J. Wuu, A. Chio, G. Restagno, G. Borghero, M. Sabatelli, D. Heckerman, E. Rogaeva, L. Zinman, J.D. Rothstein, M. Sendtner, C. Drepper, E.E. Eichler, C. Alkan, Z. Abdullaev, S.D. Pack, A. Dutra, E. Pak, J. Hardy, A. Singleton, N.M. Williams, P. Heutink, S. Pickering-Brown, H.R. Morris, P.J. Tienari, and B.J. Traynor. 2011. A hexanucleotide repeat expansion in C9ORF72 is the cause of chromosome 9p21-linked ALS-FTD. *Neuron*. 72:257-268.

Ringel, S.P., J.R. Murphy, M.K. Alderson, W. Bryan, J.D. England, R.G. Miller, J.H. Petajan, S.A. Smith, R.I. Roelofs, F. Ziter, and et al. 1993. The natural history of amyotrophic lateral sclerosis. *Neurology*. 43:1316-1322.

Ringholz, G.M., S.H. Appel, M. Bradshaw, N.A. Cooke, D.M. Mosnik, and P.E. Schulz. 2005. Prevalence and patterns of cognitive impairment in sporadic ALS. *Neurology*. 65:586-590.

Rosen, D.R., T. Siddique, D. Patterson, D.A. Figlewicz, P. Sapp, A. Hentati, D. Donaldson, J. Goto, J.P. O'Regan, H.X. Deng, and et al. 1993. Mutations in Cu/Zn superoxide dismutase gene are associated with familial amyotrophic lateral sclerosis. *Nature*. 362:59-62.

Rothstein, J.D. 2017. Edaravone: A new drug approved for ALS. *Cell*. 171:725.

Rowland, A.A., and G.K. Voeltz. 2012. Endoplasmic reticulum-mitochondria contacts: function of the junction. *Nat Rev Mol Cell Biol*. 13:607-625.

Rubinsztein, D.C., P. Codogno, and B. Levine. 2012. Autophagy modulation as a potential therapeutic target for diverse diseases. *Nat. Rev. Drug Discov.* 11:709-730.

Rusinol, A.E., Z. Cui, M.H. Chen, and J.E. Vance. 1994. A unique mitochondria-associated membrane fraction from rat liver has a high capacity for lipid synthesis and contains pre-Golgi secretory proteins including nascent lipoproteins. *J Biol Chem*. 269:27494-27502.

Rutherford, N.J., Y.J. Zhang, M. Baker, J.M. Gass, N.A. Finch, Y.F. Xu, H. Stewart, B.J. Kelley, K. Kuntz, R.J.P. Crook, J. Sreedharan, C. Vance, E. Sorenson, C. Lippa, E.H. Bigio, D.H. Geschwind, D.S. Knopman, H. Mitsumoto, R.C. Petersen, N.R. Cashman, M. Hutton, C.E. Shaw, K.B. Boylan, B. Boeve, N.R. Graff-Radford, Z.K. Wszolek, R.J. Caselli, D.W. Dickson, I.R. Mackenzie, L. Petrucelli, and R. Rademakers. 2008. Novel Mutations in TARDBP (TDP-43) in Patients with Familial Amyotrophic Lateral Sclerosis. *PLoS Genet*. 4.

Ryskamp, D.A., S. Korban, V. Zhemkov, N. Kraskovskaya, and I. Bezprozvanny. 2019. Neuronal Sigma-1 Receptors: Signaling Functions and Protective Roles in Neurodegenerative Diseases. *Front Neurosci*. 13:862.

Sadowski, I., B. Bell, P. Broad, and M. Hollis. 1992. GAL4 fusion vectors for expression in yeast or mammalian cells. *Gene*. 118:137-141.

Sadowski, I., J. Ma, S. Triezenberg, and M. Ptashne. 1988. GAL4-VP16 is an unusually potent transcriptional activator. *Nature*. 335:563-564.

Sangwan, S., and D.S. Eisenberg. 2016. Perspective on SOD1 mediated toxicity in Amyotrophic Lateral Sclerosis. *Postepy Biochem*. 62:362-369.

Saotome, M., D. Safiulina, G. Szabadkai, S. Das, A. Fransson, P. Aspenstrom, R. Rizzuto, and G. Hajnoczky. 2008. Bidirectional Ca2+-dependent control of mitochondrial dynamics by the Miro GTPase. *Proc Natl Acad Sci U S A*. 105:20728-20733.

Sarkar, S., R.A. Floto, Z. Berger, S. Imarisio, A. Cordenier, M. Pasco, L.J. Cook, and D.C. Rubinsztein. 2005. Lithium induces autophagy by inhibiting inositol monophosphatase. *J Cell Biol*. 170:1101-1111.

Saxton, W.M., and P.J. Hollenbeck. 2012. The axonal transport of mitochondria. *J Cell Sci*. 125:2095-2104.

Schellenberg, G.D., and T.J. Montine. 2012. The genetics and neuropathology of Alzheimer's disease. *Acta Neuropathol*. 124:305-323.

Scheper, W., and J.J. Hoozemans. 2015. The unfolded protein response in neurodegenerative diseases: a neuropathological perspective. *Acta Neuropathol*. 130:315-331.

Schreiner, B., L. Hedskog, B. Wiehager, and M. Ankarcrona. 2015. Amyloid-beta peptides are generated in mitochondria-associated endoplasmic reticulum membranes. *J Alzheimers Dis*. 43:369-374.

Selvaraj, B.T., M.R. Livesey, C. Zhao, J.M. Gregory, O.T. James, E.M. Cleary, A.K. Chouhan, A.B. Gane, E.M. Perkins, O. Dando, S.G. Lillico, Y.B. Lee, A.L. Nishimura, U. Poreci, S. Thankamony, M. Pray, N.A. Vasistha, D. Magnani, S. Borooah, K. Burr, D. Story, A. McCampbell, C.E. Shaw, P.C. Kind, T.J. Aitman, C.B.A. Whitelaw, I. Wilmut, C. Smith, G.B. Miles, G.E. Hardingham, D.J.A. Wyllie,

and S. Chandran. 2018. C9ORF72 repeat expansion causes vulnerability of motor neurons to Ca(2+)-permeable AMPA receptor-mediated excitotoxicity. *Nat Commun*. 9:347.

Shaw, P.J. 1999. Motor neurone disease. *BMJ*. 318:1118-1121.

Shi, J., S. Lua, J.S. Tong, and J. Song. 2010. Elimination of the native structure and solubility of the hVAPB MSP domain by the Pro56Ser mutation that causes amyotrophic lateral sclerosis. *Biochemistry*. 49:3887-3897.

Simmen, T., J.E. Aslan, A.D. Blagoveshchenskaya, L. Thomas, L. Wan, Y. Xiang, S.F. Feliciangeli, C.H. Hung, C.M. Crump, and G. Thomas. 2005. PACS-2 controls endoplasmic reticulum-mitochondria communication and Bid-mediated apoptosis. *EMBO J*. 24:717-729.

Simmen, T., E.M. Lynes, K. Gesson, and G. Thomas. 2010. Oxidative protein folding in the endoplasmic reticulum: tight links to the mitochondria-associated membrane (MAM). *Biochim Biophys Acta*. 1798:1465-1473.

Simon, D.K., C.M. Tanner, and P. Brundin. 2020. Parkinson Disease Epidemiology, Pathology, Genetics, and Pathophysiology. *Clin Geriatr Med*. 36:1-12.

Sleigh, J.N., A.M. Rossor, A.D. Fellows, A.P. Tosolini, and G. Schiavo. 2019. Axonal transport and neurological disease. *Nat Rev Neurol*.

Smith, E.F., P.J. Shaw, and K.J. De Vos. 2017. The role of mitochondria in amyotrophic lateral sclerosis. *Neurosci Lett*.

Soderberg, O., M. Gullberg, M. Jarvius, K. Ridderstrale, K.J. Leuchowius, J. Jarvius, K. Wester, P. Hydbring, F. Bahram, L.G. Larsson, and U. Landegren. 2006. Direct observation of individual endogenous protein complexes in situ by proximity ligation. *Nat Methods*. 3:995-1000.

Sreedharan, J., I.P. Blair, V.B. Tripathi, X. Hu, C. Vance, B. Rogelj, S. Ackerley, J.C. Durnall, K.L. Williams, E. Buratti, F. Baralle, J.d. Belleroche, J.D. Mitchell, P.N. Leigh, A. Al-Chalabi, C.C. Miller, G. Nicholson, and C.E. Shaw. 2008. TDP-43 Mutations in Familial and Sporadic Amyotrophic Lateral Sclerosis.

Starr, A., and R. Sattler. 2018. Synaptic dysfunction and altered excitability in C9ORF72 ALS/FTD. *Brain Res*. 1693:98-108.

Stewart, H.G., I.R. Mackenzie, A. Eisen, T. Brannstrom, S.L. Marklund, and P.M. Andersen. 2006. Clinicopathological phenotype of ALS with a novel G72C SOD1 gene mutation mimicking a myopathy. *Muscle Nerve*. 33:701-706.

Stoica, R., K.J. De Vos, S. Paillusson, S. Mueller, R.M. Sancho, K.F. Lau, G. Vizcay-Barrena, W.L. Lin, Y.F. Xu, J. Lewis, D.W. Dickson, L. Petrucelli, J.C. Mitchell, C.E. Shaw, and C.C. Miller. 2014. ER-mitochondria associations are regulated by the VAPB-PTPIP51 interaction and are disrupted by ALS/FTD-associated TDP-43. *Nat Commun*. 5:3996.

Stoica, R., S. Paillusson, P. Gomez-Suaga, J.C. Mitchell, D.H. Lau, E.H. Gray, R.M. Sancho, G. Vizcay-Barrena, K.J. De Vos, C.E. Shaw, D.P. Hanger, W. Noble, and C.C. Miller. 2016. ALS/FTD-associated FUS activates GSK-3beta to disrupt the VAPB-PTPIP51 interaction and ER-mitochondria associations. *EMBO Rep*. 17:1326-1342.

Stone, S.J., and J.E. Vance. 2000. Phosphatidylserine synthase-1 and -2 are localized to mitochondria-associated membranes. *J Biol Chem*. 275:34534-34540.

Suzuki, H., K. Kanekura, T.P. Levine, K. Kohno, V.M. Olkkonen, S. Aiso, and M. Matsuoka. 2009. ALS-linked P56S-VAPB, an aggregated loss-of-function mutant of VAPB, predisposes motor neurons to ER stress-related death by inducing aggregation of co-expressed wild-type VAPB. *Journal of Neurochemistry*. 108:973-985.

Suzuki, T., D. Bridges, D. Nakada, G. Skiniotis, S.J. Morrison, J.D. Lin, A.R. Saltiel, and K. Inoki. 2013. Inhibition of AMPK catabolic action by GSK3. *Mol Cell*. 50:407-419.

Szabadkai, G., K. Bianchi, P. Varnai, D. De Stefani, M.R. Wieckowski, D. Cavagna, A.I. Nagy, T. Balla, and R. Rizzuto. 2006. Chaperone-mediated coupling of endoplasmic reticulum and mitochondrial Ca2+ channels. *J Cell Biol*. 175:901-911.

Takeuchi, R., Y. Toyoshima, M. Tada, A. Shiga, H. Tanaka, M. Shimohata, K. Kimura, T. Morita, A. Kakita, M. Nishizawa, and H. Takahashi. 2013. Transportin 1 accumulates in FUS inclusions in adult-onset ALS without FUS mutation. *Neuropathol Appl Neurobiol*. 39:580-584.

Tambini, M.D., M. Pera, E. Kanter, H. Yang, C. Guardia-Laguarta, D. Holtzman, D. Sulzer, E. Area-Gomez, and E.A. Schon. 2016. ApoE4 upregulates the activity of mitochondria-associated ER membranes. *EMBO Rep*. 17:27-36.

Teuling, E., S. Ahmed, E. Haasdijk, J. Demmers, M.O. Steinmetz, A. Akhmanova, D. Jaarsma, and C.C. Hoogenraad. 2007. Motor neuron disease-associated mutant vesicle-associated membrane protein-associated protein (VAP) B recruits wild-type VAPs into endoplasmic reticulum-derived tubular aggregates. *J Neurosci*. 27:9801-9815.

Tiryaki, E., and H.A. Horak. 2014. ALS and other motor neuron diseases. *Continuum (Minneap Minn)*. 20:1185-1207.

Toft, M.H., O. Gredal, and B. Pakkenberg. 2005. The size distribution of neurons in the motor cortex in amyotrophic lateral sclerosis. *J Anat*. 207:399-407.

Toyofuku, T., Y. Okamoto, T. Ishikawa, S. Sasawatari, and A. Kumanogoh. 2019. LRRK2 regulates endoplasmic reticulum-mitochondrial tethering through the PERK-mediated ubiquitination pathway. *Embo j*:e100875.

Tsao, W., Y.H. Jeong, S. Lin, J. Ling, D.L. Price, P.M. Chiang, and P.C. Wong. 2012. Rodent models of TDP-43: recent advances. *Brain Res*. 1462:26-39.

Tumer, Z., B. Bertelsen, O. Gredal, M. Magyari, K.C. Nielsen, Lucamp, K. Gronskov, and K. Brondum-Nielsen. 2012. Novel heterozygous nonsense mutation of the OPTN gene segregating in a Danish family with ALS. *Neurobiol Aging*. 33:208.e201-205.

Turner, M.R., A. Cagnin, F.E. Turkheimer, C.C. Miller, C.E. Shaw, D.J. Brooks, P.N. Leigh, and R.B. Banati. 2004. Evidence of widespread cerebral microglial activation in amyotrophic lateral sclerosis: an [11C](R)-PK11195 positron emission tomography study. *Neurobiol Dis*. 15:601-609.

Ullah, M.I., A. Ahmad, S.I. Raza, A. Amar, A. Ali, A. Bhatti, P. John, A. Mohyuddin, W. Ahmad, and M.J. Hassan. 2015. In silico analysis of SIGMAR1 variant (rs4879809) segregating in a consanguineous Pakistani family showing amyotrophic lateral sclerosis without frontotemporal lobar dementia. *Neurogenetics*. 16:299-306.

van Blitterswijk, M., P.W. van Vught, M.A. van Es, H.J. Schelhaas, A.J. van der Kooi, M. de Visser, J.H. Veldink, and L.H. van den Berg. 2012. Novel optineurin mutations in sporadic amyotrophic lateral sclerosis patients. *Neurobiol Aging*. 33:1016.e1011-1017.

Van Deerlin, V.M., J.B. Leverenz, L.M. Bekris, T.D. Bird, W. Yuan, L.B. Elman, D. Clay, E.M. Wood, A.S. Chen-Plotkin, M. Martinez-Lage, E. Steinbart, L. McCluskey, M. Grossman, M. Neumann, I.L. Wu, W.S. Yang, R. Kalb, D.R. Galasko, T.J. Montine, J.Q. Trojanowski, V.M. Lee, G.D. Schellenberg, and C.E. Yu. 2008. TARDBP mutations in amyotrophic lateral sclerosis with TDP-43 neuropathology: a genetic and histopathological analysis. *Lancet Neurol*. 7:409-416.

van Es, M.A., P.W. Van Vught, H.M. Blauw, L. Franke, C.G. Saris, P.M. Andersen, L. Van Den Bosch, S.W. de Jong, R. van 't Slot, A. Birve, R. Lemmens, V. de Jong, F. Baas, H.J. Schelhaas, K. Sleegers, C. Van Broeckhoven, J.H. Wokke, C. Wijmenga, W. Robberecht, J.H. Veldink, R.A. Ophoff, and L.H. van den Berg. 2007. ITPR2 as a susceptibility gene in sporadic amyotrophic lateral sclerosis: a genome-wide association study. *Lancet Neurol*. 6:869-877.

Vance, C., B. Rogelj, T. Hortobágyi, K.J.D. Vos, A.L. Nishimura, J. Sreedharan, X. Hu, B. Smith, D. Ruddy, P. Wright, J. Ganesalingam, K.L. Williams, V. Tripathi, S. Al-Saraj, A. Al-Chalabi, P.N. Leigh, I.P. Blair, G. Nicholson, J.d. Belleroche, J.-M. Gallo, C.C. Miller, and C.E. Shaw. 2009. Mutations in FUS, an RNA Processing Protein, Cause Familial Amyotrophic Lateral Sclerosis Type 6.

Vance, C., E.L. Scotter, A.L. Nishimura, C. Troakes, J.C. Mitchell, C. Kathe, H. Urwin, C. Manser, C.C. Miller, T. Hortobagyi, M. Dragunow, B. Rogelj, and C.E. Shaw.

2013. ALS mutant FUS disrupts nuclear localization and sequesters wild-type FUS within cytoplasmic stress granules. *Hum Mol Genet*. 22:2676-2688.

Vance, J.E. 1990. Phospholipid synthesis in a membrane fraction associated with mitochondria. *J Biol Chem*. 265:7248-7256.

Vande Velde, C., K.K. McDonald, Y. Boukhedimi, M. McAlonis-Downes, C.S. Lobsiger, S. Bel Hadj, A. Zandona, J.P. Julien, S.B. Shah, and D.W. Cleveland. 2011. Misfolded SOD1 associated with motor neuron mitochondria alters mitochondrial shape and distribution prior to clinical onset. *PLoS One*. 6:e22031.

Vincent, E.E., P.P. Coelho, J. Blagih, T. Griss, B. Viollet, and R.G. Jones. 2014. Differential effects of AMPK agonists on cell growth and metabolism. *Oncogene*. 34:3627-3639.

Walker, A.K., and J.D. Atkin. 2011. Stress signaling from the endoplasmic reticulum: A central player in the pathogenesis of amyotrophic lateral sclerosis. *IUBMB Life*. 63:754-763.

Wang, P.T., P.O. Garcin, M. Fu, M. Masoudi, P. St-Pierre, N. Pante, and I.R. Nabi. 2015. Distinct mechanisms controlling rough and smooth endoplasmic reticulum contacts with mitochondria. *J Cell Sci*. 128:2759-2765.

Wang, W., L. Li, W.L. Lin, D.W. Dickson, L. Petrucelli, T. Zhang, and X. Wang. 2013. The ALS disease-associated mutant TDP-43 impairs mitochondrial dynamics and function in motor neurons. *Hum Mol Genet*. 22:4706-4719.

Watanabe, S., H. Ilieva, H. Tamada, H. Nomura, O. Komine, F. Endo, S. Jin, P. Mancias, H. Kiyama, and K. Yamanaka. 2016. Mitochondria-associated membrane collapse is a common pathomechanism in SIGMAR1- and SOD1-linked ALS. *EMBO Mol Med*. 8:1421-1437.

Woollacott, I.O., and J.D. Rohrer. 2016. The clinical spectrum of sporadic and familial forms of frontotemporal dementia. *J Neurochem*. 138 Suppl 1:6-31.

Wroe, R., A. Wai-Ling Butler, P.M. Andersen, J.F. Powell, and A. Al-Chalabi. 2008. ALSOD: the Amyotrophic Lateral Sclerosis Online Database. *Amyotroph Lateral Scler*. 9:249-250.

Wu, D., and W. Pan. 2010. GSK3: a multifaceted kinase in Wnt signaling. *Trends Biochem Sci*. 35:161-168.

Wu, W., W. Li, H. Chen, L. Jiang, R. Zhu, and D. Feng. 2016a. FUNDC1 is a novel mitochondrial-associated-membrane (MAM) protein required for hypoxia-induced mitochondrial fission and mitophagy. *Autophagy*. 12:1675-1676.

Wu, W., C. Lin, K. Wu, L. Jiang, X. Wang, W. Li, H. Zhuang, X. Zhang, H. Chen, S. Li, Y. Yang, Y. Lu, J. Wang, R. Zhu, L. Zhang, S. Sui, N. Tan, B. Zhao, J. Zhang, L. Li, and D. Feng. 2016b. FUNDC1 regulates mitochondrial dynamics at the ER-mitochondrial contact site under hypoxic conditions. *EMBO J*. 35:1368-1384.

Yang, Z., X. Zhao, J. Xu, W. Shang, and C. Tong. 2018. A novel fluorescent reporter detects plastic remodeling of mitochondria-ER contact sites. *J Cell Sci*. 131.

Yedavalli, V.S., A. Patil, and P. Shah. 2018. Amyotrophic Lateral Sclerosis and its Mimics/Variants: A Comprehensive Review. *J Clin Imaging Sci*. 8:53.

Yoshino, H. 2019. Edaravone for the treatment of amyotrophic lateral sclerosis. *Expert Rev Neurother*. 19:185-193.

Youker, R.T., U. Shinde, R. Day, and G. Thomas. 2009. At the crossroads of homoeostasis and disease: roles of the PACS proteins in membrane traffic and apoptosis. *Biochem J*. 421:1-15.

Zhang, F., W. Wang, S.L. Siedlak, Y. Liu, J. Liu, K. Jiang, G. Perry, X. Zhu, and X. Wang. 2015a. Miro1 deficiency in amyotrophic lateral sclerosis. *Front Aging Neurosci*. 7:100.

Zhang, K., J.G. Daigle, K.M. Cunningham, A.N. Coyne, K. Ruan, J.C. Grima, K.E. Bowen, H. Wadhwa, P. Yang, F. Rigo, J.P. Taylor, A.D. Gitler, J.D. Rothstein, and T.E. Lloyd. 2018. Stress Granule Assembly Disrupts Nucleocytoplasmic Transport. *Cell*. 173:958-971 e917.

Zhang, K., C.J. Donnelly, A.R. Haeusler, J.C. Grima, J.B. Machamer, P. Steinwald, E.L. Daley, S.J. Miller, K.M. Cunningham, S. Vidensky, S. Gupta, M.A. Thomas, I. Hong, S.L. Chiu, R.L. Huganir, L.W. Ostrow, M.J. Matunis, J. Wang, R. Sattler, T.E. Lloyd, and J.D. Rothstein. 2015b. The C9orf72 repeat expansion disrupts nucleocytoplasmic transport. *Nature*. 525:56-61.

Zhang, X., S. Chen, L. Song, Y. Tang, Y. Shen, L. Jia, and W. Le. 2014. MTOR-independent, autophagic enhancer trehalose prolongs motor neuron survival and ameliorates the autophagic flux defect in a mouse model of amyotrophic lateral sclerosis. *Autophagy*. 10:588-602.

Zhao, W., D.R. Beers, B. Liao, J.S. Henkel, and S.H. Appel. 2012. Regulatory T lymphocytes from ALS mice suppress microglia and effector T lymphocytes through different cytokine-mediated mechanisms. *Neurobiol Dis*. 48:418-428.

Zhou, R., A.S. Yazdi, P. Menu, and J. Tschopp. 2011. A role for mitochondria in NLRP3 inflammasome activation. *Nature*. 469:221-225.